UNIVERSITY OF SOUTHAMPTON

FACULTY OF ENGINEERING AND PHYSICAL SCIENCES

Airbus Noise Technology Centre

Aerodynamics and acoustics of aerofoils in simulated grid turbulence

by

Stefan Andreas Petrikat

Thesis for the degree of Doctor of Philosophy

Supervisor: Dr. David Angland

28th February 2021

UNIVERSITY OF SOUTHAMPTON

ABSTRACT

FACULTY OF ENGINEERING AND PHYSICAL SCIENCES
Aeronautics and Astronautics

Thesis for the degree of Doctor of Philosophy

AERODYNAMICS AND ACOUSTICS OF AEROFOILS IN SIMULATED GRID TURBULENCE

by Stefan Andreas Petrikat

The interaction of turbulence with the leading edges of blades or vanes is a prominent and often dominant noise source in many applications. Although it is reasonably well understood for infinite aerofoils, the noise production of finite aerofoils has not been extensively investigated to date. This thesis presents a methodology to investigate the interaction of complex geometries, such as finite aerofoils, with homogeneous turbulent flows. A turbulence creation method for large eddy simulations, capable of generating evolving homogeneous turbulent flows, is investigated. It is shown that the method is capable of creating turbulent flows similar to those found in grid turbulence experiments and allows the turbulence production processes and development of anisotropy to be investigated. A spectral criterion to quantify the anisotropy of the energy carrying scales is presented and is shown to provide a more comprehensive description of the anisotropy than other criteria. For the purpose of validation, and to establish a baseline for the investigation of the interaction of a finite aerofoil with a turbulent flow, the problem of a thick, infinite aerofoil immersed in turbulence is studied. Results are compared against experimental and analytical methods. It is found that the numerical method is capable of capturing thickness and non-compactness effects on the far-field noise, demonstrating, for the first time, the applicability of a compressible large eddy simulation on an unstructured mesh for the investigation of aerofoil interaction noise with an evolving turbulent flow. Finally, the first investigation of a finite, thick, loaded aerofoil in a turbulent flow is presented. By comparing the distortion of the turbulent flow at the leading edge of the finite aerofoil to that of a corresponding infinite aerofoil, indications are found that the tip effects are limited to the immediate vicinity of the tip. The aerodynamics of the tip vortex interaction with the turbulence are assessed. It is found that the simulated tip vortex exhibits vortex wandering, and a wrapping of turbulent structures around the tip vortex is observed. Present results indicate that the tip vortex has an asymmetric structure in the vicinity of the aerofoil. The analysis of surface pressure spectra and cross-correlations, as well as the far-field noise emissions of subsets of spanwise sections of the finite aerofoil, suggests that while the leading edge noise is not significantly affected by the finiteness of the geometry, the tip vortex leads

to a considerable attenuation of the pressure fluctuations on the suction side close to the trailing edge, and thus to a reduction of the non-compactness effects of the aerofoil sections closest to the tip.

Contents

List of Figures

List of Tables

List of Accompanying Materials

All data supporting this study are openly available from the University of Southampton repository at https://doi.org/10.5258/SOTON/D1756.

Declaration of Authorship

I, **Stefan Andreas Petrikat**, declare that this thesis, entitled *Aerodynamics and acoustics of aerofoils in simulated grid turbulence*, as well as the work presented in it are my own and have been generated by me as the result of my own original research. I confirm that:

- this work was done wholly or mainly while in candidature for a research degree at this University;
- where any part of this thesis has previously been submitted for a degree or any other qualification at this University or any other institution, this has been clearly stated;
- where I have consulted the published work of others, this is always clearly attributed;
- where I have quoted from the work of others, the source is always given. With the exception of such quotations, this thesis is entirely my own work;
- I have acknowledged all main sources of help;
- where the thesis is based on work done by myself jointly with others, I have made clear exactly what was done by others and what I have contributed myself;
- parts of this work have been published, or are under review, as:
    1. S. A. Petrikat, R. Karve, and D. Angland, "Broadband leading edge interaction noise prediction using simulated grid turbulence", in *24th AIAA/CEAS Aeroacoustics Conference*, no. AIAA 2018-3286, 2018.
    2. S. A. Petrikat and D. Angland, "Anisotropy development in the near-grid flow region of grid turbulence", *submitted to Physics of Fluids*, 2019.

Signed: .....

Date: .....

Acknowledgements

Firstly, I would like to thank my supervisor, Dr. David Angland, for his invaluable support and advice throughout my PhD studies, as well as his many words of encouragement during the difficult final time of this work. A great thanks also goes to Dr. Ravish Karve, as well as Dr. Fernando Gea-Aguilera and Dr. James Gill, who helped me find the right track and answered uncountable questions. I would also like to thank Dr. David Marshall for his aid in designing the aerofoil test rig.

This research has been possible thanks to financial support from the University of Southampton through the Airbus Noise Technology Centre (ANTC). The IRIDIS 4 and 5 High Performance Computing Facilities, as well as the associated IT services at the University of Southampton are also acknowledged in the completion of this work.

No PhD can succeed in isolation, and mine was no different. Thank you to all my friends in Southampton and abroad, Daryl, Sylvain, Tim, Ardi, Maria, Panos, Daniel, Stefania, Andreas and Aline, who were there part or all of the way. Thank you also to Hamideh, who led me to this path and supported me through much of it.

Finally, I would like to thank my family, who have shaped me to be this person capable of doing this thesis in more ways than I could ever know. Ich danke euch allen, es bedeutet mir die Welt dass ich euch habe.
I wish my father was here to witness this, and I hope that in some ways he is.

Nomenclature

Roman letters

A_p	Boundary patch area
A_{ii}	Autocorrelation of component i
a_{ij}	Deviatoric anisotropic Reynolds stress component i, j
b_{ij}	Normalized deviatoric anisotropic Reynolds stress component i, j
C_s	Smagorinsky coefficient
c	Chord length
c_0	Speed of sound
c_{DES}	Detached eddy simulation adjustable modelling constant
c_p	Pressure coefficient
d	Aerofoil semi span
d_c	Distance from cell centre to cell face
d_s	Cell distance to surface
E_{ij}	One-dimensional energy spectrum of components i, j
E	Energy spectrum function
E^*	Conjugate of the Fresnel integral
e	Internal energy per unit mass
$\mathfrak{f}$	Longitudinal autocorrelation
f	Frequency
f_b	Frequency band
$f_{c,0}$	Non-compactness base frequency
f_{cT}	Highpass cut-off frequency due to finite signal
f_{cv}	Mesh cut-off frequency for vortical waves
f_l	Lower bound of frequency band
f_u	Upper bound of frequency band
f_{TE}	Frequency where trailing edge noise is assumed to be dominant
f_w	Wake oscillation frequency
G_p	Grid period
H	Hankel function
$\mathfrak{g}$	Transverse autocorrelation

I_r	Resolved turbulence intensity
I_t	Integral time scale
I_ϕ	Inhomogeneity of quantity ϕ
I_{ii}	Integral length scale of component i
II	Second invariant of anisotropic Reynolds stress tensor
III	Third invariant of anisotropic Reynolds stress tensor
J	Bessel function
k	Turbulent kinetic energy
k_{iso}	Isotropic part of the turbulent kinetic energy
k_{rel}	Field relaxation coefficient
$\tilde{k}$	Thermal conductivity
$\mathcal{L}$	Acoustic lift integral
l	Extent of computational domain in streamwise direction
l_∞	Relaxation length scale
M	Mach number
M_0	Far-field Mach number
n	Turbulence decay coefficient
n_p	Number of times the vortex core coincided with a given grid point
n_r	Refinement level
$\mathcal{P}$	Turbulence production
$\mathcal{P}_{ref}$	Reference power
p	Pressure
p'	Unsteady pressure
p_0	Mean far-field pressure
p_{RMS}	Root mean square of unsteady pressure
p_{ref}	Acoustic reference pressure
Q	Q-criterion
R_{ij}	Two-point velocity correlation
R_{pp}	Two-point pressure correlation
r_{cc}	Distance between cross-correlation origin and maximum
r	Displacement in mean flow direction
$\mathbf{r}_d$	Displacement vector
r_{LE}	Leading edge radius
r_{LE-O}	Distance between observer and leading edge
r_{TE-O}	Distance between observer and trailing edge
r^*	Tip vortex core radius
r_0	Distance to the observer
S_{ij}	Strain rate tensor
S_{pp}	Sound power spectral density
S_f	Patch face area vector
S_λ	Largest eigenvalue of strain rate tensor

s	Span width
s_G	Grid solidity
T	Temperature
T_l	Throughflow time
t	Time
t_a	Aerofoil thickness
U_i	Local mean flow velocity component i
U_0	Axial far-field mean flow velocity
U_c	Eddy convection velocity
U_θ	Circumferential velocity
u_i	Unsteady velocity component i
u_{ij}	Reynolds stress tensor component i, j
u_{RMS}	RMS value of the fluctuating velocity
$\mathbf{x}$	Position vector
x	Streamwise coordinate
y	Transverse coordinate
y_v	Deviation of the vortex centre from its mean position in the transverse direction
z	Spanwise coordinate
z_v	Deviation of the vortex centre from its mean position in the spanwise direction

Greek letters

α	Angle of attack
β	Compressibility factor
Γ	Gamma function
Γ_0	Vortex circulation
γ_{ij}	Anisotropy parameter
γ_{LE}	Angle between streamwise direction and line connecting leading edge and observer
γ_{TE}	Angle between streamwise direction and line connecting trailing edge and observer
Δ_b	Cell base size
Δ_i	Mesh cell size in direction i
Δt	Numerical time step
δ_{ij}	Kronecker delta
ε	Dissipation of turbulent kinetic energy
ε_{Diss}	Dissipative error
ε_{Disp}	Dispersive error
ε_r	Resolved dissipation

ε_{SGS}	Sub-grid scale dissipation
η	Abscissa of the anisotropic invariant map
η_K	Kolmogorov scale
Θ_{cc}	Angle between vector of cross-correlation origin and maximum and spanwise direction
θ	Angle to observer
$\boldsymbol{\kappa}$	Wavenumber vector
κ_c	Mesh cutoff wavenumber
κ_i	Wavenumber in direction i
λ	Taylor microscale
μ	Molecular viscosity
μ_a	Acoustic reduced frequency
μ_h	Hydrodynamic reduced frequency
μ_2	Bulk viscosity
ν	Kinematic viscosity
ν_t	Turbulent viscosity
ν_{SGS}	Sub-grid scale viscosity
ξ	Ordinate of the anisotropic invariant map
ρ	Density
ρ_0	Far-field density
σ	Flow corrected distance to observer
τ	Time delta
τ_{LE}	Propagation time of signal travelling from leading edge to observer
τ_{TE}	Propagation time of signal travelling from trailing edge to observer
Φ_{ij}	Velocity spectrum tensor
ϕ	Arbitrary flow variable
ϕ_p	Patch face flux
ψ_p	Patch compressibility
Ω_{ij}	Rotation tensor
ω	Angular frequency
ω_i	Vorticity component in direction i

Symbols

$\langle . \rangle$	Ensemble average operator
$\lvert . \rvert$	Magnitude of a vector
∇	Gradient operator
$\overline{(.)}$	Spatial average in one direction
$\overline{\overline{(.)}}$	Spatial average in two directions
$\tilde{(.)}$	Favre-filtered variable

Abbreviations

ACARE	Advisory Council for Aviation Research and Innovation in Europe
AIM	Anisotropic Invariant Map
ANTC	Airbus Noise Technology CentreInvariants
aRST	anisotropic Reynolds stress tensor
CAA	Computational AeroAcoustics
CFD	Computational Fluid Dynamics
CFL	Courant-Friedrichs-Lewy
CROR	Contra-Rotating Open Rotor
DES	Detached Eddy Simulation
DNS	Direct Numerical Simulation
FSM	Forward-Stepwise Method
FW-H	Ffowcs-Williams and Hawkings
LEE	Linearised Euler Equations
LES	Large Eddy Simulation
OASPL	Overall Sound Pressure Level
PIV	Particle Image Velocimetry
PISO	Pressure-Implicit with Splitting of Operators
PPW	Points Per Wavelength
PSD	Power Spectral Density
PWL	Sound Power Level
RANS	Reynolds-Averaged Navier-Stokes
RFG	Random Flow Generation
RMS	Root Mean Square
RPM	Random Particle Mesh
RST	Reynolds Stress Tensor
RTI	Return To Isotropy
SIMPLE	Semi-Implicit Method for Pressure Linked Equations
SPL	Sound Pressure Level
S-A	Spalart-Allmaras
URANS	Unsteady Reynolds-Averaged Navier-Stokes
VM	Vortex method

Chapter 1

Introduction

As the civil aviation sector expands, its environmental impact on the growing urban society is felt to an ever-increasing degree. A combination of ecological and economical concerns have led to calls for aircraft to be less damaging to the environment, as measured by emissions of carbon dioxide and nitrogen oxide, and to exhibit a higher propulsive efficiency. At the same time, construction of airports has been held up, and approach routes have been made more complicated by a population unwilling to suffer from noise pollution caused by air traffic. Recognizing these demands, the Advisory Council for Aviation Research and Innovation in Europe (ACARE) has set strict targets to be reached by 2050: A 75% reduction of carbon dioxide, a 90% reduction of nitrogen oxide, and a 65% reduction of perceived noise emission relative to the state of the art of the year 2000 [1].

In many applications, the noise produced by the interaction of turbulence with the leading edges of blades and vanes of turbomachinery is a significant, and in some cases the dominant source, of noise. Examples of such cases are the interaction between the wakes of blades and the downstream vanes in the bypass ducts of shrouded fans, interactions between pylon wakes and open rotors, or the significant noise being produced when a boundary layer is ingested by a rotor.

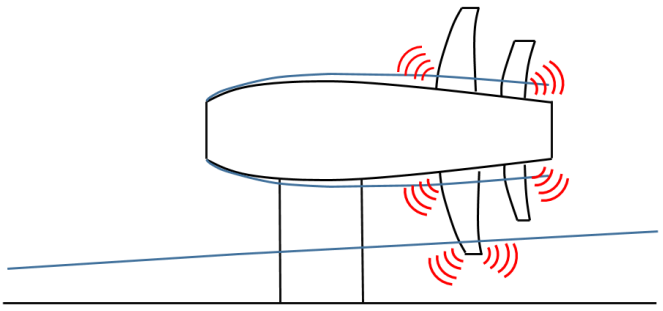

Figure 1.1: Possible boundary layer interactions in case of a CROR.

In particular the latter case has been found to be a prohibitive noise source of Counter Rotating Open Rotors (CROR), which are often installed at the rear fuselage, where the boundary layers developing on the fuselage have grown to appreciable sizes. Figure 1.1 illustrates the different noise sources which may occur during the operation of a CROR, and which have so far prohibited their use in general aviation. Beside the interactions between boundary layer of the nacelle and the rotor, which cannot be avoided, there is in some cases also the fuselage boundary layer to consider, which may extend into the rotor disk. As the blades pass through this boundary layer, they experience unsteady loading, which leads to additional noise emissions.

Due to the large potential of CRORs, as well as other technologies such as engines capable of boundary layer ingestion, to contribute to significant fuel savings [2], the scientific community has been tasked to investigate the processes responsible for noise production, and to optimize the design of next-generation engines. After significant advances have been made in the understanding of tonal noise sources [3], a number of researchers have contributed to the explanation and mitigation of blade self-noise and wake interaction noise in steady flows [4; 5; 6; 7; 8]. However, the assumption that the rotor is operating in a steady environment is not always applicable. Especially when the CROR is installed, pylon, fuselage and under some circumstances wing root vortices, as well as wing downwash, will all contribute to a considerably unsteady operating regime. The influence of the pylon was identified quite early, and investigated by, among others, Hoff [5], Ricouard *et al.* [9] and Sinnige *et al.* [10; 11]. However, much is still unknown about the interactions between the boundary layers and the rotor, in particular in the vicinity of large geometry changes, such as the tip of the blade.

Although analytical and numerical prediction methods exist for the interaction of blades with turbulent flow, they are often limited to simple geometries, or require prohibitive computational resources. Thus, for the development of capable and efficient analytical prediction tools, a better understanding of the development of turbulent flows as well as their interaction with aerofoils immersed in them is required.

As can be seen in Figure 1.1, a CROR contains a large number of sources. Without an understanding of the majority of them, it is impossible to draw conclusions about the remaining unknown sources when investigating a full CROR interacting with its installation environment. In order to isolate the sources for unambiguous identification and characterization, the problem will be simplified to a single blade of constant aerofoil with a round tip, interacting with a turbulence. This approach is well suited for rotors where the solidity is low, such as open rotors [12]. The only potential noise sources then become leading edge noise, where the unsteady flow of the boundary layer interacts with the leading edge, trailing edge noise, as well as aerofoil tip vortex formation noise.

For the remainder of this thesis, the single blade of constant aerofoil, i.e. the finite-span wing, will be referred to as the “finite aerofoil”. Conversely, the term “infinite aerofoil” will be used for a wing of essentially infinite span, which is realised using periodic boundary conditions.

1.1 Aims of the research

This research presented in this thesis is aimed to answer the following questions:

1. How is the anisotropy of the energy carrying scales produced and how does it develop as it approaches an aerofoil?
2. Are large eddy simulations using unstructured grids a tool suitable for the investigation of broadband leading edge interaction noise?
3. What are the characteristics of the tip vortex in a strongly turbulent flow?
4. How large are the impacts of the aerofoil tip geometry on turbulence statistics, and therefore on noise production?

By doing so, this thesis aims to increase the understanding of anisotropic flows, and investigate the applicability of large eddy simulations for aeroacoustic investigations for the investigation of leading edge turbulence interaction noise. Finally, this thesis aims to provide a proof of concept for the versatility of using LES on unstructured meshes for aeroacoustic purposes by demonstrating the first numerical investigation of a finite aerofoil, i.e. a finite-span wing, immersed in a turbulent flow.

1.2 Original contributions

1. The method of inlet-grid turbulence creation, previously proposed by Blackmore [13], is applied to investigate the origin of anisotropy in turbulent flows produced by grid-like turbulence generators.
2. A method to quantify the anisotropy of the energy carrying scales on a scale-by-scale basis is proposed and applied to demonstrate the physical causes of the complex development of the anisotropy in the vicinity of grid-like turbulence generators.
3. The inlet-grid method is applied to generate a turbulent flow in a compressible, unstructured large eddy simulation with an infinite aerofoil immersed in turbulence, demonstrating the capability of this approach to predict leading edge interaction noise.
4. The inlet-grid method is applied for the simulation of a finite aerofoil immersed in turbulence, allowing an in-depth investigation of the leading edge turbulence interaction and noise emission of a finite aerofoil geometry. Additionally, first results of the interaction of the tip vortex with surrounding turbulence in the vicinity of an aerofoil are presented.

A conference paper containing item 3 has been presented at the 24th AIAA/CEAS Aeroacoustic Conference [14]. Items 1 and 2 have been submitted for review to the Journal Physics of Fluids.

1.3 Thesis structure

This thesis presents the application of a flexible turbulence creation method for the investigation of the development of the anisotropy close to the grid, for a proof-of-concept case of an infinite aerofoil interacting with a strongly turbulent flow, as well as for the investigation of a finite aerofoil immersed in homogeneous turbulence. The thesis is structured as follows:

- Chapter 2 first introduces the basic concepts and nomenclature used in this thesis and provides a review of the one of the most common methods to produce turbulent flows, the turbulence grid. The state of the art of current understanding of leading edge noise is discussed, and the literature concerning finite aerofoil aerodynamics and aeroacoustics is summarized.
- Chapter 3 introduces the theory underpinning the simulation method of large eddy simulation, as well as the basics of the hybrid methodology used to compute far-field noise radiation. The effects of various changes in terms of numerical schemes and solvers as well as boundary conditions are investigated to establish comparability between the various simulations presented in this thesis.
- Chapter 4 demonstrates the relevance of the inlet-grid turbulence creation technique for the investigation of grid-generated turbulent flows and investigates the development of the anisotropy of the energy carrying scales both qualitatively and quantitatively. For the latter, the method of computing a spectral anisotropic Reynolds stress tensor is proposed and applied. Finally, a discussion of Reynolds effects is presented.
- Chapter 5 presents the use of the inlet-grid turbulence creation method for the simulation of a leading edge turbulence interaction problem of a thick, infinite aerofoil, using a compressible large eddy solver on an unstructured grid. The development of the anisotropy towards the leading edge is compared to literature. Aeroacoustic results are computed using a hybrid approach and compared against the analytical method of Amiet [15]. Additionally, a comparison with an incompressible simulation as well as with a case of an aerofoil at a small angle of attack is conducted
- Chapter 6 presents the simulation case of a thick and loaded finite aerofoil immersed in a turbulent flow. The aerodynamic phenomena of the interaction of the

turbulent structures with the leading edge, as well as the interaction of the tip vortex with the turbulence are investigated. Acoustic results are computed and compared to the corresponding case of a thick and loaded infinite aerofoil.

- Chapter 7 presents the conclusions, and an outlook to potential future work.

Chapter 2

Literature review

This literature preview will establish the basic theory behind the description and analysis of turbulent flows, and provide a review of the research conducted using one of the most common methods to produce turbulence, the turbulent grid, in Sections 2.1 and 2.2, respectively. The state of the art of knowledge concerning leading edge turbulence interaction noise is reviewed in Section 2.4. Finally, the literature on finite aerofoils is discussed in Section 2.5, with a focus on the interaction of tip vortices with turbulent flows, as well as prior studies investigating the noise emissions of finite aerofoils.

2.1 Basics of turbulence

As the physics of turbulent flows is a vast topic, a comprehensive discussion is beyond the scope of this literature research. For the purpose of this thesis, a review of the basic concepts is provided only, with a more complete discussion given in textbooks such as by Pope [16]. This section will review some of these concepts important when discussing turbulence, and establish the nomenclature used in this thesis.

2.1.1 The statistical description of turbulence

Since turbulence is a highly complex phenomenon, it cannot be described as straightforward as mean or laminar flows. In order to be able to characterize it, it is necessary use the methods of statistics. Given a velocity signal U, the signal can be split into a steady and an unsteady part:

$$U_i = u_i + \langle U_i \rangle, \tag{2.1}$$

where u is the unsteady or fluctuating velocity, and $\langle U \rangle$ is the ensemble average of U over time. The index i has the values $1, 2, 3$ for the three flow components u_1, u_2 and

u_3 of streamwise, transverse and spanwise velocity fluctuations, respectively.
Similarly, the pressure p can be decomposed as:

$$p = p' + \langle p \rangle, \tag{2.2}$$

with p' as the unsteady or fluctuating pressure and $\langle p \rangle$ as the ensemble average of p over time.
An important quantity to describe the turbulent flow are the correlations, which quantify the extent of coherent structures in time and space. For a homogeneous, statistically stationary flow, the spatial two-point correlation of components i and j in direction k is defined as the ensemble average of the product of the random variable evaluated at two points in space, i.e.

$$R_{ij}^{k}(\mathbf{r_d}) = \langle u_i(\mathbf{x} + \mathbf{r_d}, t) u_j(\mathbf{x}, t) \rangle, \tag{2.3}$$

where $\mathbf{r_d}$ is the displacement vector from the position vector $\mathbf{x}$. The spatial two-point correlation provides information about the size of the turbulent eddies in the flow.
Conversely, the temporal correlation is defined as the average of the product of the random variable at two points in time. Assuming a homogeneous, statistically stationary flow, this quantity is only depending on the time difference τ between two arbitrary moments in time. Therefore, it can be defined as:

$$A_{ij}(\tau) = \langle u_i(\mathbf{x}, t) u_j(\mathbf{x}, t + \tau) \rangle, \tag{2.4}$$

For $i = j$, the autocorrelation A_{ii} is obtained, which can be understood as a measure of the "memory" of the signal. It quantifies the longevity of coherent structures in the signal.
An important assumption, often made during investigation of turbulence, is to consider the eddies to be frozen as they are convected downstream. In other words, the statistics of the turbulent structures are assumed to not evolve rapidly enough in the time they are convected past a measurement point. When doing so, it is possible to derive the spatial structure of the turbulence from a temporal signal by multiplying it with the mean flow velocity. This concept is known as Taylor's hypothesis [17], and has been shown most recently by Djenidi *et al.* [18] to be accurate in grid turbulence with $u_{RMS}/\langle U \rangle \ll 1$, where u_{RMS} is the root mean square of the fluctuating velocity, whereas it fails especially in free shear flows, as shown by Tong and Warhaft [19]. The error can be of the order of $u_{RMS}/\langle U \rangle$, and it is thus imperative to be cautious when using this assumption. Lumley [20] investigated the applicability of Taylor's hypothesis by considering several criteria, such as the criterion of Lin [21], and provided a lower bound for the assumption of frozen turbulence. Lumley stated that provided Lin's criterion,

$$\langle U \rangle \gg \frac{\mathrm{d}\langle U \rangle}{\mathrm{d}x_i} 2\pi/\kappa_i, \tag{2.5}$$

holds true, with κ_i being the wavenumber in direction i, then the effect of different convection effects on the wavenumber components can be disregarded. If additionally, the one-dimensional spectral energy $E_{ii}(\kappa)$ fulfils

$$E_{ij}(\kappa) \lll \langle U^2 \rangle / \kappa_i, \tag{2.6}$$

then the eddies can be assumed to be frozen in the sense of Taylor.
Assuming statistic stationarity, and taking advantage of the assumption of frozen turbulence, the longitudinal and transverse correlations for displacements r in the streamwise direction, $\mathfrak{f}(r)$ and $\mathfrak{g}(r)$, respectively, can be obtained by normalizing the autocorrelation of the axial and transverse component by the mean square velocity fluctuation, since:

$$\mathfrak{f}(r) = A_{11}(\tau)/\langle u_1^2 \rangle = R_{11}^1(r)/\langle u_1^2 \rangle, \tag{2.7}$$

$$\mathfrak{g}(r) = A_{22}(\tau)/\langle u_2^2 \rangle = R_{22}^1(r)/\langle u_2^2 \rangle. \tag{2.8}$$

Von Kármán and Howarth [22] showed that the two correlation functions are related by

$$\mathfrak{g}(r) = \mathfrak{f}(r) + \frac{1}{2} r \frac{\partial}{\partial r} \mathfrak{f}(r), \tag{2.9}$$

in isotropic turbulence. From $\mathfrak{f}$ and $\mathfrak{g}$ two important length scales can be calculated: the longitudinal integral length scale I_{ii} and the longitudinal Taylor micro scale λ:

$$I_{ii} = \int_0^\infty \mathfrak{f}(r)\, \mathrm{d}r, \tag{2.10}$$

$$\lambda = \sqrt{-\frac{1}{2} \mathfrak{f}\,''(0)}, \tag{2.11}$$

where $\mathfrak{f}''$ is the second derivative of $\mathfrak{f}$. While the integral length scale provides information about the size of the largest eddies, the Taylor micro scale gives an indication of how fast the flow evolves, i.e. how quickly large eddies dissipate into smaller eddies. In this thesis, the common practice [23; 24; 25] of computing the integral length scale by integrating the correlation function up to the point where it first crosses horizontal axis was adopted.

2.1.2 Energy spectra and the energy cascade

When the two-point correlation is known for all values of the displacement vector $\mathbf{r}_d$, the velocity spectrum tensor can be computed by [16]:

$$\Phi_{ij}(\boldsymbol{\kappa}, t) = \frac{1}{(2\pi)^3} \iiint_{-\infty}^{\infty} e^{-i\boldsymbol{\kappa}\cdot\mathbf{r_d}} R_{ij}(\mathbf{r_d}, t)\, \mathrm{d}\mathbf{r_d}. \tag{2.12}$$

It describes the energy content of the turbulence as a function of the wavenumber vector $\boldsymbol{\kappa}$. As it is a second order tensor function of a vector, it contains a considerable amount of information. A more simplified description of the turbulence is provided by the energy spectrum function $E(|\boldsymbol{\kappa}|$, which is a scalar function of the wavenumber magnitude $|\boldsymbol{\kappa}|$. In order to remove the directional information, only half of the trace of the velocity spectrum, i.e. $\frac{1}{2}\Phi_{ii}(\boldsymbol{\kappa})$, is considered. The energy spectrum function is then obtained by integrating $\frac{1}{2}\Phi_{ii}(\boldsymbol{\kappa})$ over spheres S with radius $|\boldsymbol{\kappa}|$, as given by [16]:

$$E(|\boldsymbol{\kappa}|) = \oint \frac{1}{2}\Phi_{ii}(\boldsymbol{\kappa})\,\mathrm{d}S(|\boldsymbol{\kappa}|). \tag{2.13}$$

Since $E(|\boldsymbol{\kappa}|)$ is easier accessible by experimental measurements, it has been extensively studied. It has been found that the energy contained in the turbulent fluctuations follows the so-called energy cascade. In virtually all turbulent flows, most of the energy is contained in eddies of scales within the energy carrying range, i.e. up to the limit of $l_{EI} = I_{ii}/6$. These eddies are considered anisotropic and large and are assumed to be responsible for all large-scale flow phenomena. Below this limit, the energy spectra obtain a universal shape, as was shown in many different experiments [26; 27; 28; 29]. Thus, eddies of these scales are commonly described as being within in the universal equilibrium range. At a certain threshold in this range, viscous effects become dominant over the inertial effects, and the turbulent motions are transformed into heat. This threshold is commonly referred to as the Kolmogorov scales:

$$\eta_K = (\nu^3/\varepsilon)^{1/4}, \tag{2.14}$$

with the viscosity ν and the dissipation of turbulent kinetic energy ε. An intermediate scale region, above the Kolmogorov scales yet below the energy carrying range, is the inertial subrange. It is characterized by a distinct and universal decay following the so-called Kolmogorov $-5/3$ spectrum, defined as [16]:

$$E(\kappa) = C\varepsilon^{2/3}\kappa^{-5/3}, \tag{2.15}$$

with the constant C. The correct representation of this decay, as well as the larger scales, is a crucial part when developing analytical or numerical methods or models for turbulence simulation [30]. A number of models were suggested based on modelling the spectral energy transfer rate, such as the proposals of Obukhov [31], Heisenberg [32] and Pao [33]. Panchev [34] reviewed those among numerous others, finding that Pao's model is in better agreement with experimental data than the majority of alternatives. However, in a later review, Pope [16] concluded that the model of von Kármán [22] is superior to Pao's model. Yet another alternative model was developed by Liepmann [35]. It has been found that while the Liepmanns spectrum provides an adequate description of the energy containing range, the von Kármán spectrum provides an adequate description of both the energy containing range and the inertial subrange [36]. Consequently, the

von Kármán spectrum was chosen as a reference spectrum for isotropic turbulence in this study and was implemented for this work following the notation given by Amiet [15]:

$$E(|\boldsymbol{\kappa}|) = \frac{I|\boldsymbol{\kappa}|^4}{(1+(|\boldsymbol{\kappa}|/\kappa_e)^2)^{17/6}}, \tag{2.16}$$

where

$$I = \frac{55}{9\sqrt{\pi}}\frac{\Gamma(5/6)\langle u_1^2\rangle}{\Gamma(1/3)\kappa_e^5}, \quad \kappa_e = \frac{\sqrt{\pi}}{I_{11}}\frac{\Gamma(5/6)}{\Gamma(1/3)}, \tag{2.17}$$

where $|\boldsymbol{\kappa}|$ is the magnitude of the wave number vector, Γ is the gamma function, and I_{11} is the axial integral length scale. The wave number is related to the frequency f by $\kappa = 2\pi f/U_0$. Following Pope [16], the one-dimensional velocity spectrum can then be obtained from $E(|\boldsymbol{\kappa}|)$ by numerical integration of Eqn. (2.16) using,

$$E_{ii}(\kappa_1) = \int\!\!\int_{-\infty}^{\infty} \frac{E(|\boldsymbol{\kappa}|)}{2\pi|\boldsymbol{\kappa}|^2}\left(1-\frac{\kappa_i^2}{|\boldsymbol{\kappa}|^2}\right)\mathrm{d}\kappa_2\,\mathrm{d}\kappa_3. \tag{2.18}$$

2.1.3 The Reynolds-stress tensor and the Lumley triangle

The importance of the Reynolds-stresses in the description of turbulent flows arises from the mean-momentum, or Reynolds equations, which are obtained when the Navier-Stokes equations are decomposed into mean and fluctuating parts. The Reynolds equations are then obtained as [16]:

$$\frac{\overline{\mathrm{D}}\langle U_j\rangle}{\overline{\mathrm{D}}t} = \nu\nabla^2\langle U_j\rangle - \frac{\partial\langle u_i u_j\rangle}{\partial x_i} - \frac{1}{\rho}\frac{\partial\langle p\rangle}{\partial x_j}, \tag{2.19}$$

where $\frac{\overline{\mathrm{D}}}{\overline{\mathrm{D}}t}$ is the mean substantial derivative, ν is the kinematic viscosity, and ∇ is the gradient operator. The evolution of the mean flow quantities is therefore dependent on the Reynolds-stress tensor term $\partial\langle u_i u_j\rangle$. In the following, for the purpose of brevity, the convention

$$u_{ij} = \langle u_i u_j\rangle, \tag{2.20}$$

will be adopted for the components of the Reynolds Stress Tensor (RST). The RST can be further distinguished into an isotropic and deviatoric anisotropic contribution. With the isotropic stress defined as $\frac{2}{3}k\delta_{ij}$, where k is the turbulent kinetic energy, and δ_{ij} is the Kronecker delta, the deviatoric anisotropic Reynolds-stresses is obtained as:

$$a_{ij} = u_{ij} - \frac{2}{3}k\delta_{ij}. \tag{2.21}$$

As the proper description of the development of a_{ij} is critical to many turbulence modelling approaches, the investigation of the governing principles for the development of the Reynolds-stresses has received considerable interest [16; 37]. Reasonably successful models have been developed based on the assumption that the mean rate of strain $\overline{S}_{ij}$

and the anisotropic Reynolds-stresses are directly proportional to each other:

$$a_{ij} = 2\rho\nu_t \overline{S}_{ij}, \tag{2.22}$$

with ν_t being the turbulent viscosity, and ρ the density. This assumption, also known as Boussinesq eddy-viscosity approximation, is the basis for the most common turbulent flow simulation methods, the class of Reynolds Averaged Navier-Stokes (RANS) with a modelled turbulent viscosity. The turbulent viscosity is obtained in these methods either by a simple algebraic model, or by the solving of one or two transport equations for the turbulent quantities. As discussion of these methods is beyond the scope of this thesis, only an introduction to the turbulence model used in the presented Large Eddy Simulation (LES), which was developed by Spalart and Allmaras [38] is provided in Section 3.1.2.2.

The anisotropic Reynolds-stress tensor is a convenient quantity to investigate the return to isotropy of turbulence. A very descriptive way of coupling the special states of the invariants to the corresponding shape of the RST was suggested by Lumley and Newman [39]. They introduced the so-called Lumley triangle, or anisotropy invariant map (AIM) technique, which will be used extensively in Chapter 4. The normalized anisotropic Reynolds-stress tensor (aRST), given by

$$b_{ij} = \frac{a_{ij}}{2k}, \tag{2.23}$$

has zero trace, and has thus only two independent invariants:

$$II = \frac{1}{2}((b_{ii})^2 - b_{ii}^2) = \frac{1}{2}((\mathrm{trace}(b_{ij}))^2 - \mathrm{trace}(b_{ij}^2)), \tag{2.24}$$

$$III = \frac{1}{6}(b_{ii})^3 - \frac{1}{2}\cdot b_{ii}\cdot b_{jj}^2 + \frac{1}{3}b_{ii} = \det(b_{ij}), \tag{2.25}$$

following the notation in Pope [16], where trace denotes the trace, and det denotes the determinant. Although Lumley and Newman [39] defined the AIM purely in terms of II and III, the coordinates

$$\eta = \sqrt{-II/3}, \tag{2.26}$$

$$\xi = \sqrt[3]{III/2}, \tag{2.27}$$

are used in the current analysis, yielding straight lines for the lower limits of the triangle. On the Lumley triangle, several special states can be identified, as summarized in Table 2.1.

	State of turbulence	Invariants	Shape of RST ellipsoid
1)	Isotropic	$\xi = \eta = 0$	Sphere
2)	Two-component axisymmetric	$\xi = -\frac{1}{6}, \eta = \frac{1}{6}$	Disk
3)	One-component	$\xi = \frac{1}{3}, \eta = \frac{1}{3}$	Line
4)	Axisymmetric, negative ξ	$\eta = -\xi$	Prolate spheroid (pancake shaped)
5)	Axisymmetric, positive ξ	$\eta = \xi$	Oblate spheroid (cigar shaped)
6)	Two-component	$\eta = \left(\frac{1}{27} + 2\xi^3\right)^{(1/2)}$	Ellipse

Table 2.1: Special states of the Reynolds-stress tensor [16].

In $\eta - \xi$ coordinates, Figure 2.1 (a) shows the extent of the AIM in which all states of the RST must fall for physical flows. The lower two diagonal borders represent the axisymmetric limits, with $\xi < 0$ being associated with a pancake-shaped RST, i.e. with two main directions of stress, whereas $\xi > 0$ denotes states which are characterized by a cigar-shaped RST, i.e. where the stress in one direction dominates.

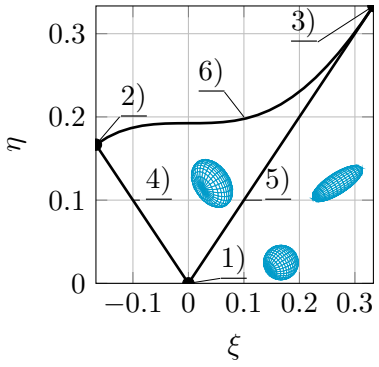

(a) Shapes of the aRST in the AIM. 3D aRST shapes (blue meshes): Upper left: Pancake shape; Upper right: cigar shape; lower middle: Isotropic shape.

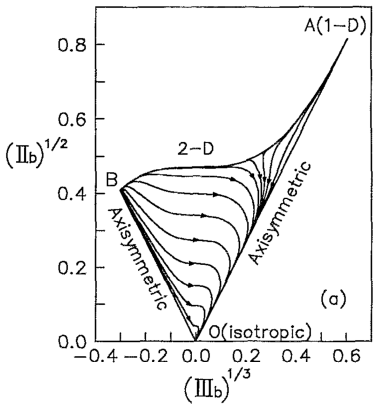

(b) The model of Chung and Kim [37].

Figure 2.1: The Lumley triangle.

In the past, efforts were undertaken to develop models able to predict the development of the trajectories in the AIM which decaying turbulence follows as it develops towards isotropy. A first, linear, model was introduced by Rotta [40], but a review of various experimental data conducted by Chung and Kim [37] revealed a trend towards the axisymmetric state with ξ positive, as shown in Figure 2.1 b). This was confirmed by the later experiments of Choi and Lumley [41], who also showed that the rate of Return

To Isotropy (RTI) was much lower for turbulence with a greater III. More recently, Djenidi and Tardu [42] performed a Direct Numerical Simulation (DNS) with a grid-like turbulence generator consisting of floating square grid elements, showing that the spatial averages of the invariants in the transverse direction follow a perfectly axisymmetric expansion on the RTI.
In order to study the effect of different starting states of the anisotropy invariants on the trajectories on the AIM, Zusi and Perot [43] conducted several DNS where they used axisymmetric expansion or contraction to achieve target values for II and III. They find that their simulations do not show a RTI, but a return to the background level of statistical anisotropy that the simulations began with. Furthermore, it is found that the RTI occurs in two stages, a recovery stage immediately after removing the strain, and a return stage where the velocity fluctuation anisotropy tends to zero.

2.2 Turbulence grids

One of the most common methods used in experiments to create turbulent flow are turbulence grids. Their method of operation is quite simple: By installing several square or round bars in a grid pattern in the flow, turbulence is created by the large number of interacting wakes. Historically, the study of grid turbulence has attracted considerable interest. This is partly due to the ease of its experimental creation, but also since there is no remaining mean shear, the decay of the turbulence can be studied in isolation. Furthermore, as grid turbulence is considered to be the closest approximation to homogeneous and isotropic turbulence, it is well suited to testing new theories, as Taylor recognized in 1935 [44].

2.2.1 The decay of turbulence

Research in grid turbulence has, in many cases, focused on the determination of universal scaling laws for the dissipation of turbulence. Considerations based on the self-preservation of the correlation functions lead to the prediction that the turbulent kinetic energy of homogeneous, isotropic turbulence decays according to a power law [22; 45]. Comte-Bellott and Corrsin [26] define it as

$$\frac{u_{11}}{U_0^2} = \frac{1}{A}\left(\frac{x - x_0}{G_p}\right)^{-n}, \tag{2.28}$$

with U_0 as the mean streamwise velocity, n as the decay factor, x as the flow development length in streamwise direction, x_0 as a virtual origin, G_p as the grid period and A as a constant. Since the actual grid position is irrelevant in fully developed flow [26], the many investigations have focused on finding universally valid values for the exponent n, resulting in a wide range of values [46]. This has led George [47] to suggest that

there may not be a universal self-preserving state for grid-generated flows, i.e. a_1 and n both vary on initial conditions. Physically, this has the implication that there are mechanisms by which the turbulence "remembers" its production processes, which is in stark contrast to the established theories postulating the independence of the development of turbulence from the initial conditions. Considering the dependence of virtually all turbulence modelling approaches on the assumed universality of scalings such as $\varepsilon = C_\varepsilon \overline{u_1^3} L_{11}$, where C_ε is a positive constant [48], this open question is of great interest to the research community. Experiments by Lavoie *et al.* [24] were aimed at determining the relationship between the initial conditions and the power-law exponent n, and to evaluate the equilibrium similarity approach suggested by George [49], which allows different similarity scales for second and third order velocity structure functions. It was found that while initial conditions did affect n, the importance of the initial conditions is diminished when the created turbulence has a more isotropic character. Furthermore, the development of the second and third-order structure functions was found to only approximately agree with the predictions of equilibrium similarity theory. It was concluded that the influence of the initial conditions is primarily expressed via anisotropy in the largest scales, which tend to increase the magnitude of the decay coefficient.

Recently, the advent of fractal grids has opened new pathways to the role of the various scales in setting the level of dissipation in turbulent flows. Seoud and Vassilicos [50] showed experimentally that fractal grids generate a region where the decay is locked into a single length scale. As such, in this region, the classical high Reynolds number scaling of the dissipation rate $\varepsilon = C_\varepsilon \overline{u^3} L$ does not hold, and the Taylor-based Reynolds number Re_λ is not proportional to the integral scale L divided by the Taylor microscale λ. This non-classical decay behaviour was further investigated by Valente and Vassilicos [51], who found that in these regions, an approximate proportionality between the L and λ exists. The same authors showed subsequently [52] that this non-classical decay behaviour is also exhibited by classical grids, provided the grid Reynolds number R_{G_p} is high enough.

Inspired by these results, Krogstad and Davidson [53] used multi-scale grids as well as a classical grid to investigate whether the very high decay components of turbulence produced by fractal grids are caused by the significant inhomogeneity of the turbulence, that persists far downstream the grid. While they concluded from their analysis that the turbulence behind the used multi-scale grids is virtually identical to an equivalent classical grid, in a re-analysis of their results Valente and Vassilicos [54] argued the turbulence created by the two types of grid differs considerably. Furthermore, Valente and Vassilicos argued that dependencies on the inflow conditions related to anisotropy are unlikely to be causal for the observed differences, as the turbulence exhibited very small levels of anisotropy throughout.

Most recently, a comprehensive experimental work concerning the evolution of the anisotropic turbulence and the effects of spatial confinement, i.e. when the integral length scale is on the scale of the domain, on the decay was conducted by Esteban *et al.* [25]

. In order to avoid invoking Taylor's hypothesis, they used a zero-mean flow facility, where the turbulence is created by arrays of randomly activated turbulent jets. They observed two different decay regimes, and related the more rapidly decaying regime to the "near-field" region a few integral length scales downstream of the grid, which is likely strongly affected by turbulence production mechanisms and hence facility dependent. Conversely, a second region of logarithmically decaying turbulence was related to the "far-field" decay, with a decay exponent well within the range observed in wind-tunnel experiments. Finally, an increasing spatial confinement of the largest scales was observed to lead to an increasing decay coefficient.

2.2.2 Homogeneity and isotropy of grid turbulence

In order to unambiguously compare the experimental results from grid turbulence measurements to analytical theories for homogeneous isotropic turbulence, it is of great importance that the flow is as homogeneous and isotropic as possible. However, it was soon realized that grid turbulence deviates from homogeneity and isotropy significantly, if no countermeasures are taken, as shown by Grant and Nisbet [55]. As a measure to neutralize the effect of the remaining transverse inhomogeneity, they proposed taking the transverse average of flow quantities. In order to improve the isotropy of the flow, Comte-Bellot and Corrsin [26] proposed the use of a contraction, which they showed to be effective in equalizing the axial and transverse turbulent kinetic energies.
However, due to space constraints in experimental setups, this is not always possible, and some inhomogeneity and anisotropy remains in the flow. This was most recently illustrated by Ertunc *et al.* [56], who showed experimentally and using DNS that even after the mean velocity field has obtained a state of homogeneity, significant inhomogeneity persists in the distribution of the Reynolds-stresses. They explain this behaviour with the fast decay of the spatial inhomogeneity of the mean velocity, which reduces the turbulence production and, consequently, the viscous diffusion, thereby preventing homogenization of the Reynolds-stresses in the flow. Laizet and Vassilicos [57] presented a first large-scale DNS of fractal and classical grids, focussing on homogeneity, vorticity and intensity of the simulated turbulence. They found that fractal grids generate far larger inhomogeneities than classical grids, which persist a significant distance downstream, while the turbulence vorticity and intensity is larger. Furthermore, they find a clear dependence of the energy spectra on the position within the production regions near the grid.
The reason for the anisotropy of grid generated turbulence remains poorly investigated, as the highly inhomogeneous flow regime in the near-field of the grid represents a great challenge for experimental investigation. However, over the years, a number of observations have been made. From the data of Comte-Bellot and Corrsin [26], a small trend towards anisotropy with increasing grid Reynolds number is observed. Gad-el-Hak and Corrsin [58] note that their active jet grid can reduce the anisotropy of the flow, if the

jets are used in a coflow configuration, however at the expense of the turbulence intensity. While the experiments of Lavoie *et al.* [23; 59; 24] extensively studied the effects of initial conditions on grid turbulence, as discussed in Section 2.2.1, their investigations did not cover the near-grid flow regime $x/M < 20$.
Discetti *et al.* [60], investigating the flow physics of fractal grids using PIV, showed that the isotropy of the flow downstream of such grids is reduced as the wake of the largest bar is approached. Valente and Vassilicos [61], also studying fractal grids, make a similar conclusion from their study of the development of various integral length scales using two-component hot-wire anemometry. An interesting study using DNS and a "grid-like" turbulence generator, consisting of floating square elements, was conducted by Djenidi and Tardu [42]. For the case of low-Reynolds number turbulence, they showed that the return to isotropy is fast and follows a perfectly axisymmetric expansion.

2.3 Turbulence creation methods for large eddy simulations

In order to investigate turbulent flows in simulations, methods are required which can create realistic turbulence in the numerical domain. This is a complex problem, since turbulence exhibits a random nature, but is also characterized by statistical correlations in space and time which must be reproduced in order for the simulated turbulence to behave like "real" turbulence. Roughly, the various proposed methods for turbulence generation in LES can be classified into synthesis approaches, where a random fluctuation is superimposed to the mean flow at the inlet, precursor methods where the turbulence is precomputed prior to the main simulation and then introduced at the inlet, and concurrent methods, where the turbulence is created directly in the domain through suitable means at runtime.

2.3.1 Synthetic turbulence methods

The field of synthetic turbulence methods is both large and quickly evolving, as showcased by recent reviews such as Wu [62] and Dhamankar [63]. Within the class of synthetic turbulence methods, a number of families may be identified:

- Fourier mode based methods produce a periodically fluctuating velocity field through the superposition of appropriately weighted sinusoidal functions. With an increasing number of modes, an increasingly broadband spectral content is achieved, albeit one made up of a finite number of modes and often at a considerable computational expense. However, as these methods are relatively simple to implement, they have become popular and are widely available in industrial CFD codes.

- Methods based on digital filters generate turbulent flows by filtering a random source, such as white noise signals, in order to reproduce the target turbulent statistics. The resulting velocity field is aperiodic and exhibits a broadband spectral content.
- Synthetic eddy based methods create turbulent flows by summation of ideal eddies, which may be described by velocity fields shaped according to Gaussian or Mexican-Hat profiles. The produced turbulence is aperiodic and of a continuous spectral density.

In particular for aeroacoustic purposes, an important aspect of a given turbulence generation method is that it should satisfy the divergence-free, or solenoidal, property for an incompressible flow, i.e.:

$$\nabla \cdot \mathbf{U} = 0. \tag{2.29}$$

Any method which violates this condition will lead to large erroneous pressure fluctuations being introduced to the domain, as the LES procedure will generate pressure variations to ensure that the velocity field inside the domain is divergence-free [64]. In addition, synthetic turbulence methods may exhibit fluctuations in terms of the instantaneous mass flux across the inlet, since the velocity fluctuations prescribed by the method may not have a mean of zero across the inlet[64]. This creates a significant noise source with monopole characteristics [65]. Conversely, if the synthetic turbulence generation method is applied to a plane within the domain, the sudden appearance of vortical structures is also associated with the creation of significant spurious noise [66], if no remediating measures are applied.

2.3.1.1 Fourier based methods

Using Fourier modes to generate a divergence-free turbulent flow was first proposed by Kraichnan [67]. As Kraichnan's model produces a Gaussian energy spectrum, which is centred at a given wavenumber and thus fails to reproduce the turbulent energy content at higher wavenumbers, Karweit *et al.* [68] modified the method to obtain the von Kármán spectrum. Kraichnan's model was subsequently also adapted to the random flow generation (RFG) method proposed by Smirnov *et al.* [69], which is capable of prescribing a required Reynolds stress tensor by a tensor-scaling operation and a subsequent orthogonal transformation of the velocity correlation tensor. While not divergence-free in all cases, the RFG method has been implemented into the commercial CFD package ANSYS Fluent, spurring the use of this method in various applications [70; 71; 72].
A major simplification of the RFG model was proposed by Batten *et al.* [73], who suggested Cholesky decomposing of the Reynolds stress tensor, thereby obtaining a procedure which is both highly efficient and relatively straightforward to implement.
In order to allow use of the RFG model for non-Gaussian energy spectra such as often

encountered in wind engineering applications, Huang *et al.* [74] suggested the generation of several independent velocity fields. More recently, Castro and Paz [75] expanded the method proposed by Huang *et al.* to improve the control of statistical properties of the turbulence. A divergence-free variant of the RFG method was proposed by Yu and Bai [76], who suggested to take the curl of the potential field to achieve the solenoidal property.
In practice, it has often been found that Fourier based methods require a significant development length until the turbulence can be considered fully developed [77; 78]. An example of an application of a Fourier based methods to a LES used for aeroacoustic purposes is the study by Shur *et al.* , who used it in a zonal simulation to study the noise of a trailing edge as well as the noise produced by a two-element aerofoil configuration[66].

2.3.1.2 Digital filter methods

One of the first digital filter methods for LES was proposed by Klein *et al.* [79]. By applying digital filters, designed to establish a Gaussian two-point correlation function, to random data, they were able to produce spatially correlated velocity fields, which reproduce given Reynolds stress tensors, as well as the locally given autocorrelation function. The method was subsequently generalized by di Mare *et al.* [80], who showed that the use of an arbitrary correlation function, combined with a simplified method of obtaining the filter coefficients, lead to a better agreement of the produced turbulent flows with DNS.
Since the digital filter method developed by Klein *et al.* [79] involved an expensive 3D filtering step of a volume of random data, Xie and Castro [81] proposed a modification, in which the filtering is applied to transverse planes of random data only, and two subsequent planes are then correlated using an exponential function. This approach, also known as the Forward-Stepwise method (FSM), has been shown to be very promising in terms of its capability to generate synthetic turbulence for LES and DES [82] in applications where time averaged pressure and aerodynamic forces are of interest.
A drawback of the models of Klein [79] and Xie and Castro [81] is that the produced velocity fields are not divergence free. Thus, it was observed by Kim *et al.* [65] that the FSM in particular results in a considerable over-prediction of the pressure fluctuations. Consequently, for aeroacoustic applications, Kim *et al.* proposed the use of a modified inlet condition, which prescribes the velocity perturbations related to the turbulence not to the inlet patch directly, but to a transverse patch near the domain inlet, where the divergence-free criterion can be satisfied by a suitably altered velocity-pressure coupling step. Both the modified inlet condition and an alternative correction of the instantaneous mass flux at the inlet were shown to result in significant improvements of the computed pressure fluctuations.

2.3.1.3 Synthetic eddy approach

One of the early proposals to synthesize turbulence from individual vortices was made by Sergent [83], who was able to prescribe two-dimensional velocity fluctuations of a broadband spectrum at the inlet using this method. Known as the vortex method (VM), it was later extended by Benhamadouche *et al.* [84] to three-dimensional turbulence by the use of a one-dimensional Langevin equation for the streamwise component. It since has been implemented in the commercial code Fluent. However, a fundamental drawback of the VM approach is that the streamwise fluctuations are generated by a separate equation, and are therefore uncorrelated with the other components [64]. A method capable of accounting for the correlations of all flow components was proposed by Jarrin *et al.* [85; 86] who suggested the use of arbitrarily shaped 3D vortices with a prescribed Reynolds stress tensor. They reported superior performance in terms of development length when compared to Batten's Fourier based model [73], and good agreement in the case of a turbulent flow over an aerofoil trailing edge between the simulation and experimental reference data.
However, while the original method of Sergent [83] is divergence-free, the approach adopted by Jarrin *et al.* [85] can violate the solenoidal condition. A modification of their model was proposed by Poletto *et al.* [64], who redefined the shape functions with constraints designed to create a divergence-free velocity field.
To date, digital filter methods have been found to lead to adaption distances on the order of ten boundary layer thicknesses [81; 87].

2.3.1.4 Conclusions on the state of the art of turbulence generation methods for LES

As outlined in the preceding sections, there has been a considerable amount of progress in the field of synthetic turbulence methods in the recent years. However, in particular for aeroacoustic purposes using hybrid methods, more work needs to be done to establish these methods for the investigation of turbulence interaction noise. A method satisfying the stringent requirements of aeroacoustic investigations is yet to be implemented in more widely available CFD codes, even though several promising concepts exist, such as the methods of Kim *et al.* [65] as well as Poletto *et al.* [64]. As a consequence, most applications of synthetic turbulence methods in LES have so far been focused on the investigation of the aerodynamic aspects of turbulent flows, as documented in the reviews of Tabor and Baba-Ahmadi [30], as well as Dhamankar *et al.* [63].

2.3.2 Precursor and concurrent turbulence creation approaches

As noted by Tabor and Baba-Ahmadi [30], precursor simulation methods dominate in terms of their capability to produce accurate results. However, they are often associated

with a considerable computational expense, both in terms of generating the turbulence as well as in terms of the storage requirements for the library of the turbulent velocity field. In order to reduce the storage space, the stored turbulence is often reused, which however may lead to an artificial repetitive behaviour at low frequency in the flow [30]. Another fundamental issue is the requirement to read large amounts of data each time step, which can have an significant impact on simulation runtime [63].

A generally more efficient approach are flow recycling methods, which can be classified as concurrent turbulence creation approaches. The turbulence generation is conducted within the same domain as the object of interest. By mapping the flow through the outlet of the domain onto the inlet, a fully developed state of the turbulence is achieved relatively quickly. However, similar to the case of reusing the data as in precursor type methods, spurious low-frequency behaviour has been found to negatively influence noise level predictions when flow recycling is applied [88]. Nevertheless, when used in a hybrid approach for the prediction of trailing edge noise with LES, flow recycling has been shown to be a promising turbulence generation method [89].

The most straightforward way of creating turbulence in a simulation are the transition-based methods. Depending on the approach, transition is stimulated by artificial instability waves, or by geometrical features. Examples of the latter approach are the periodic blowing and suction features employed by Fasel *et al.* [90], the high aspect ratio step such as used by Gloerfelt and Berland [91] as well as the wall-mounted cubes proposed by Yang *et al.* [92] suitable for the creation of a turbulent boundary layer.

A method capable of creating a homogeneous turbulent flow comparable to that produced by the grids commonly used in wind tunnel experiments was proposed by Blackmore *et al.* [13]. By dividing the inlet of a domain into wall and inlet patches, a system of wakes and jets is created, which produces turbulence in a very similar fashion to that of a turbulence grid. Due to the grid geometry being approximated by a 2D pattern on the inlet only, computationally expensive meshing of the grid geometry is avoided. However, the production of the turbulence is different from the conditions in experiment as the upstream conditions, e.g. boundary layer development, do not influence the eddy shedding behind the "bars" through potential effects, as there is no upstream domain. By changing the development length of the turbulence, grid dimensions and flow speeds, integral length scales and energy spectra can be varied. In their paper, Blackmore *et al.* [13] describe a parameter study for grid generated turbulence in an incompressible flow and state a number of conditions for the production of realistic turbulence. Similar devices were also used by Ertunc *et al.* [56] as well as Djenidi and Tardu [42] for the study of turbulent flows.

As noted by Dhamankar *et al.* [63], the drawback of transition-based approaches consists in the relatively long development distances required by them. In addition, it is often not possible to precisely control the parameters of the produced turbulent flow. However, in particular for aeroacoustic applications, they have been recognized as being preferable to synthetic, precursor or flow-recycling methods [66; 91].

As the inlet grid turbulence method proposed by Blackmore *et al.* [13] does not involve any modelling steps, unlike many synthetic turbulence generation methods [30], does not necessitate a computationally expensive precursor simulation to generate a library of turbulent data for injection, is relatively simple to apply to existing CFD packages, and can be expected to be reasonably devoid of spurious noise at low Mach number, it was selected for this study.

2.4 The aeroacoustics of aerofoils

An isolated aerofoil in a steady flow will produce noise solely through the interaction of the fluctuations within the turbulent boundary layer in the vicinity of the trailing edge. In the absence of a turbulent incident flow, this is the total noise produced by an aerofoil [4]. However, if the aerofoil is immersed in a turbulent flow, additional noise is produced by the interaction of the turbulent eddies with the leading edge. The physical cause for the leading edge noise was stated by Roger and Moreau [12] to be the rapid change experienced by the turbulent motions as they are convected onto the leading edge. Due to fluid compressibility, part of the inertia of the vortical motion is converted into sound, which has a broadband character owing to the random nature of turbulent flow. As the turbulent fluctuations interacting with the leading edge are often more energetic than the turbulence in the boundary layer, the overall noise emissions levels are in many cases dominated by the leading edge noise [93; 94; 95]. Consequently, the investigation and prediction of leading edge noise has attracted considerable interest in the past.

2.4.1 Experimental studies of leading edge noise

One of the earliest experimental investigations of leading edge noise was conducted by Hersh and Meecham [96] in 1973. Investigating primarily the directivity pattern, they showed that a small aerofoil in a turbulent flow radiates like a point dipole, provided the dimension of the aerofoil is small relative to the wavelength of the radiated sound. An extensive experimental campaign dedicated to the measurement of the far-field noise of an aerofoil in a turbulent flow was conducted by Paterson and Amiet in 1976 [97]. Using a NACA 0012 aerofoil in an open-jet anechoic wind tunnel, they investigated the noise emissions over a wide range of mean flow velocities and two different angles of attack. The turbulence was created by means of a grid upstream of the nozzle, and a reasonable level of isotropy and homogeneity was achieved. Noise levels and directivity were measured by placing a number of microphones on an arc in the mid-span plane, and corrections were applied to remove the background noise. They reported reasonable agreement with the analytical leading edge noise theory formulated earlier by Amiet [15], if a suitable correction for the effects of the jet shear layer is applied. They concluded

that the inclusion of compressibility and source non-compactness in any theoretical formulation is necessary for accurate amplitude and directivity predictions to be obtained. Additionally, they observed that the effects of aerofoil thickness on the noise becomes important at high frequency and low mean flow velocity. Furthermore, although they reported a small angle of attack effect, they concluded that further investigations were necessary before the angle of attack may be considered to be a small factor in terms of leading edge noise emissions.

The effects of angle of attack as well as of the aerofoil shape were further investigated by Moreau, Roger and Jurdic [98]. They reported no significant angle of attack effects, and a considerable reduction of the turbulence interaction noise with increasing aerofoil thickness. To account for the thickness effect, the authors presented semi-empirical corrections to analytical methods. A later study of Moreau and Roger [95] was focused on the comparison of trailing edge noise and leading edge noise and confirmed the earlier finding of Paterson and Amiet [97] that over most of the frequency range, the leading edge is the dominant source of noise. The self-noise of the aerofoil was reported to only become significant at high angles of attack close to flow separation. Their results also showed that the boundary layer driven pressure fluctuations, which cause the trailing edge noise, are largely independent from the turbulence intensity of the external flow. As such, the boundary layer was shown to be the sole source of the trailing edge noise, while leading edge noise was associated with the interaction of external eddies only. Thus, the two noise sources were reported to be uncorrelated.

Experiments conducted by Staubs [99] in a closed wind tunnel with a test section enclosed by Kevlar panels, allowing measurements with minimal shear layers, showed angle of attack effects especially for aerofoils where the ratio of turbulence integral length scale to aerofoil chord is small. However, a later study in the same facility by Devenport, Staub and Glegg [100] showed that while the angle of attack has a strong effect on the aerofoil response function, the averaging effect of the isotropic turbulence spectrum reduces its impact on the emitted noise. They illustrated with a panel method that angle of attack effects may be significant provided the turbulence is anisotropic. Additionally, they reported that the noise reductions of thicker aerofoils are not only determined by leading edge radius and overall thickness.

The effects of aerofoil geometry were investigated extensively by Chaitanya *et al.* [94], who confirmed the earlier finding of Paterson and Amiet [93] that the aerofoil thickness, and the leading edge radius, are the main geometric parameters controlling turbulence interaction noise. Conversely, angle of attack and camber were found to have only a minor impact on the interaction noise, suggesting that mean loading does not affect the distortion effects of the leading edge to a large degree. By performing Particle Image Velocimetry (PIV) measurements, Chaitanya *et al.* were able to show that a sharper leading edge is associated with stronger transverse velocity fluctuations than if the leading edge is blunter.

An in-depth investigation of the development of unsteady quantities such as the Reynolds-stresses at the leading edge was conducted by Santana *et al.* [101], who showed that the distortion effects on the turbulence are concentrated in a narrow region immediately upstream the stagnation point of the leading edge. Within a distance on the order of the leading edge radius, the turbulence intensity was reported to grow substantially, with the axial and spanwise component increasing by the same amount, while the transverse component increases by a factor of two more. It should be noted that simulations of this region generally result in a significant increase of the transverse components, and a strong decrease of the axial components [102; 103]. Based on these results, Santana *et al.* proposed a modified turbulence spectrum to be used for noise prediction with Amiets [15] theory.

Most recently, the investigation of the reduction of leading edge interaction noise by the use of wavy leading edges has attracted considerable interest [104; 105; 106; 107]. The underlying mechanism is that the sinusoidal variations of the chord length introduces a spanwise correlation loss and modifies the response of the leading edge to the impinging gusts from parallel cut-on modes to oblique cut-off modes [104]. Simulations of Haeri *et al.* [105] showed this to be the case, with the correlation length of the fluctuation pressure on the leading edge decreasing as a function of serration amplitude. A corresponding noise reduction of up to 10 dB has been reported from experimental measurements of Narayanan *et al.* [106].

2.4.2 Analytical models for leading edge noise

The first analytical work to describe the aerodynamic response from a flat plate interacting with a parallel harmonic gust was developed by Sears [108]. A more comprehensive model for oblique gusts, including the effects of compressibility, was later developed by Amiet [109]. In his seminal paper in 1975, Amiet [15] used these models to predict the noise emissions from a thin, unloaded aerofoil in a turbulent flow, modelling the leading edge noise as a dipole.

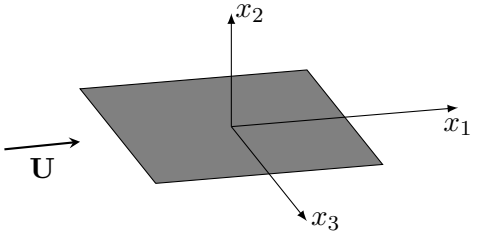

Figure 2.2: Aerofoil coordinate system.

For the purpose of illustration, the coordinate system as used for the subsequent discussion of Amiet's model is shown in Figure 2.2 superimposed to a flat plate immersed in a turbulent flow as indicated by the instantaneous velocity vector **U**. The aerofoil is located in the x_1-x_3 plane, where x_1 is defined as the streamwise direction and x_3 is

parallel to the span. In the following, the direction x_1 will be referred to as chordwise, and x_2 as well as x_3 as the transverse and spanwise directions, respectively.
By arguing that the only relevant fluctuations are the transverse velocity fluctuations, Amiet [15] first derived an equation for the cross power spectral density (PSD) of the surface pressure jump on two points on the aerofoil, S_{QQ}, due to incoming isotropic turbulence, as given by:

$$S_{QQ}(x_a, x_b, y_a, y_b, \omega) = (2\pi\rho_0 c)^2 U_0 \int_{-\infty}^{\infty} g^*(x_a, K_0, \kappa_3) g(x_b, K_0, \kappa_3) \Phi_{22}(K_0, \kappa_3) e^{i\kappa_3(y_b - y_a)} \, \mathrm{d}\kappa_3, \quad (2.30)$$

where x_a, y_a and x_b, y_b are the coordinates along x_1 and x_3 of two points on the aerofoil surface, κ_3 is the spanwise wavenumber, g and g^* are the transfer functions between turbulent velocity and aerofoil pressure jump at the two points respectively, $K_0 = -\omega/U_0$ where ω is a given angular frequency of the pressure jump, and Φ_{22} is the energy spectrum of the transverse velocity fluctuations as a function of the wavevector components. Subsequently, with reference to the theories of Kirchhoff [110] and Curle [111], Amiet [15] related the acoustic PSD in the far-field, S_{pp}, to a distribution of dipoles on the aerofoil surface, where the dipoles exhibit a strength equal to the force on the surface:

$$S_{pp}(x_1, x_2, x_3, \omega) = \left(\frac{\omega x_2}{4\pi c_0 \sigma^2}\right)^2 \iiiint S_{QQ}(x_a, x_b, y_a, y_b, \omega) e^{\frac{i\omega}{c_0}\left[\beta^{-2}(x_a - x_b)(M - x_1/\sigma) + x_3 \cdot (y_b - y_a)/\sigma\right]} \, \mathrm{d}x_a \, \mathrm{d}x_b \, \mathrm{d}y_a \, \mathrm{d}y_b, \quad (2.31)$$

with x_1, x_2, x_3 being the coordinates of a far-field observer, c_0 is the speed of sound, $\sigma = \sqrt{x_1^2 + \beta^2(x_2^2 + x_3^2)}$ and $\beta = \sqrt{1 - M}$, and M as the Mach number. The quadruple integral of Eqn. (2.31) can be simplified by defining the chordwise integral of the surface loading as

$$\mathcal{L}(x_1, K_0, \kappa_3) = \int_{-c/2}^{c/2} g(x_0, K_0, \kappa_3) e^{\frac{-i\omega x_0 (M - x_1/\sigma)}{c_0 \beta^2}} \, \mathrm{d}x_0. \quad (2.32)$$

As noted by Amiet [15], Eqn. (2.32) introduces the effects of non-compactness into the acoustic solution. For small frequencies, the imaginary exponent is small as well, and the integral is reduced to the sectional lift of the aerofoil, allowing use of distinct high- and low frequency solutions for the aerofoil unsteady load response, equivalent to the approach chosen by Paterson and Amiet [97]. This approach was also used in the implementation of Amiet's model for this thesis. As the ability to capture the non-compactness effects was considered an important aspect of the simulation method investigated in this thesis, the non-compactness effects are discussed in more detail in Section 2.4.2.1.
The general expression derived by Amiet [15], Eqn. (2.31), is applicable to a large variety

of cases. However, as Santana [101] pointed out, even in cases where the assumption of a constant aerofoil section in the spanwise direction is true, the homogeneity of the turbulence statistics in the spanwise direction may be compromised. This observation is of particular interest for finite wings at an angle of attack, where the spanwise loading distribution as well as the presence of the tip vortex may affect the development of the turbulence upstream of the leading edge.

While the definition of $\mathcal{L}$ allows to compute the far-field PSD by integrating over the spanwise wavenumber only, it requires the specification of a two-dimensional velocity spectrum, which is difficult to obtain experimentally [16]. Facilitating the evaluation of Eqn. (2.31) even further, Amiet [15] observed that as the aerofoil span increases, i.e. when the spanwise extent becomes much larger than the spanwise turbulent length scale, the contribution of skewed gusts diminishes, allowing to use a two-dimensional compressible-flow aerofoil theory in the large span limit.

For the observer position defined in polar coordinates, as illustrated by Figure 2.4 with the assumption of applicability of the two-dimensional compressible-flow aerofoil theory and using a 2D Green's function, Blandeau *et al.* [112] derived the PSD of the acoustic pressure in the far-field per unit span as:

$$S_{pp}(r_0, \theta, \omega) = \frac{\pi \rho_0^2 c^2 U_0 \omega \sin^2 \theta}{8 c_0 r_0 A(\theta, M)^3} |\mathcal{L}(\theta, \kappa_1, 0)|^2 \Phi_{22}(\kappa_1, \kappa_3 = 0), \tag{2.33}$$

where ρ_0 is the density, and $\mathcal{L}(\Theta, \kappa_1)$ is the acoustic lift integral as a function of observer angle and chordwise wavenumber, which is further discussed in Section 2.4.2.1. Since the use of Eqn. (2.33) is the most amenable for experimental investigations, it has been chosen also as a base of comparison for the noise results in this thesis.

For the practical evaluation of Eqn. (2.33), Φ_{22} is related to the energy spectrum as a function of the magnitude of the wavevector $E(|\boldsymbol{\kappa}|)$ by,

$$\Phi_{22}(\kappa_1, \kappa_2, \kappa_3) = \frac{E(|\boldsymbol{\kappa}|)}{4\pi\kappa^2}(1 - \kappa_2^2/\kappa^2). \tag{2.34}$$

As discussed in Section 2.1.2, various model spectra are available for $E(|\boldsymbol{\kappa}|)$, of which the von Kármánmodel [22] was selected for this study.

While Amiet's model [15] has been recognized as being reasonably accurate for flat plates, it fails to account for thickness and angle of attack effects, as was shown in the experiments of Paterson and Amiet [97]. Subsequently, a number of authors suggested corrections for the thickness effect, which is generally more dominant than angle of attack effects [97; 12; 113]. Gershfeld [114] developed a method to compute leading edge noise predictions for symmetric thick aerofoils. Following earlier studies of Hunt [115], who computed the influence of a body in the flow on the turbulent spectrum using a generalized rapid distortion theory, and based on their own experiments, Moreau, Roger and Jurdic [98] proposed several semi-empirical corrections to Amiets [15] model to account for aerofoil thickness and camber.

2.4.2.1 Non-compactness effects

As discussed in the previous Section, the non-compactness effects are a consequence of the two distinct solutions for the chordwise loading integral given by Eqn. (2.32), which have been derived for two distinct ranges of the acoustic reduced frequency $\mu_a = \frac{\omega c}{2c_0\beta^2}$. For $\mu_a < \pi/4$, the aerofoil can be considered compact, and the low frequency response function as formulated by Amiet [109] is valid. In this range, Eqn. (2.32), for an observer in polar coordinates r_0, θ as illustrated in Figure 2.4, becomes [112]:

$$\mathcal{L}_{low}(\theta, \kappa_1) = \frac{S(\mu_h)}{\beta} e^{i\mu_h f(M)} \left\{ J_0\left(\mu_a \frac{\cos\theta}{A(\theta, M)}\right) - iJ_1\left(\mu_a \frac{\cos\theta}{A(\theta, M)}\right) \right\}, \tag{2.35}$$

with

$$\begin{aligned} S(\mu_h) =& \frac{2}{\pi\mu_h[H_0^{(2)}(\mu_h) - iH_1^{(2)}(\mu_h)]}, \\ f(M) =& (1-\beta)\ln(M) + \beta\ln(1+\beta) - \ln(2), \\ A(\theta, M) =& \sqrt{1 - M^2\sin^2\theta}, \end{aligned}$$

where $\mu_h = \mu_a/M$, J_0 and J_1 are Bessel functions of the first kind while H_0 and H_1 are Hankel functions of the second kind.
Conversely, for reduced frequencies $\mu_a > \pi/4$, the assumption of compactness does no longer apply to the aerofoil, which is taken into account by splitting the response function into two terms:

$$\mathcal{L}_{high}(\theta, \kappa_1) = \mathcal{L}_1(\theta, \kappa_1) + \mathcal{L}_2(\theta, \kappa_1). \tag{2.36}$$

where the function $\mathcal{L}_1$ represents the leading edge scattering contribution, while the function $\mathcal{L}_2$ represents the trailing edge back-scattering contribution to the far-field noise. By defining the conjugate of the Fresnel integral $E^*(z)$ following Amiet [116] as:

$$E^*(z) = \frac{1}{\sqrt{2}} \int_0^2 \frac{e^{-i\zeta}}{\sqrt{\zeta}} \, \mathrm{d}\zeta, \tag{2.37}$$

$\mathcal{L}_1$ and $\mathcal{L}_2$ are obtained as [112]:

$$\mathcal{L}_1(\theta, \kappa_1) = \frac{\sqrt{2}}{\pi\beta\sqrt{\mu_h(1+M)\Theta_1}} E^*(2\Theta_1) e^{i\Theta_2}, \tag{2.38}$$

$$\begin{aligned} \mathcal{L}_2(\theta, \kappa_1) = & \frac{e^{i\Theta_2}}{\pi\Theta_1\beta\sqrt{2\pi\mu_h(1+M)}} \left[i(1 - e^{-i2\Theta_1}) + (1-i) \right. \\ & \left. \times \left\{ E^*(4\mu_a\beta^2) - \sqrt{\frac{2}{1 + \frac{\cos\theta}{A(\theta,M)}}} e^{-i2\Theta_1} E^*(2\Theta_3) \right\} \right], \end{aligned} \tag{2.39}$$

with

$$\Theta_1 = \mu_a \left(1 - \frac{\cos\theta}{A(\theta, M)}\right)$$

$$\Theta_2 = \beta^2 \mu_h + \mu_a \left(M - \frac{\cos\theta}{A(\theta, M)}\right) - \frac{\pi}{4},$$

$$\Theta_3 = \mu_a \left(1 + \frac{\cos\theta}{A(\theta, M)}\right).$$

The effect of using either Eqn. (2.35) or (2.36) to compute the far-field SPL is illustrated in Figure 2.3 (a).

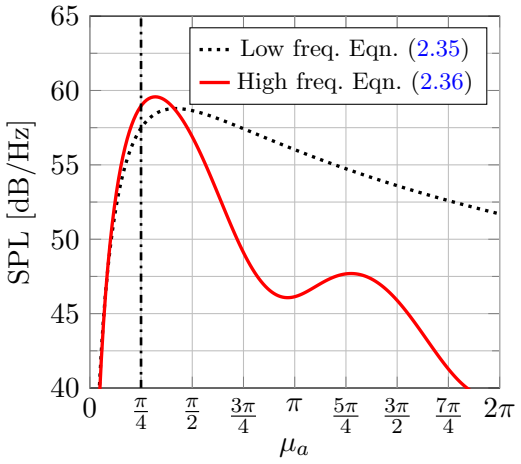

(a) High and low frequency noise solution for $\theta = 90°$.

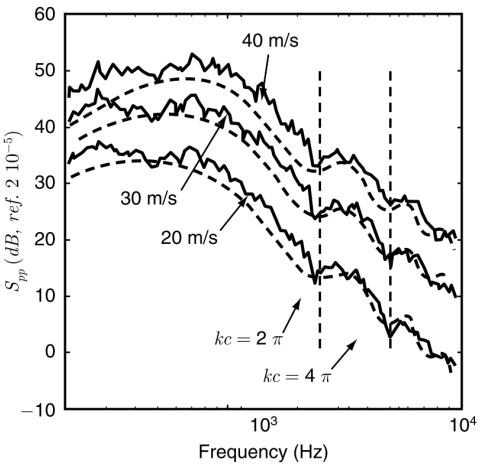

(b) Example of non-compactness effects in the acoustic emissions of a thin aerofoil [12]. Experimental results at three flow speeds (solid), Amiet's model [15] Eqn. (2.33) (dashed), Non-compactness dips (vertical dashed).

Figure 2.3: Illustration of non-compactness effects.

From Figure 2.3 (a), it is apparent that for $\mu_a > \pi/2$, the effects of non-compactness are considerable, with the low frequency solution predicting noise levels up to 15 dB higher than the high frequency solution.

An example of the observation of these effects in experiment is shown in Figure 2.3 (b), where the dips associated with the non-compactness are clearly visible for a thin aerofoil. As noted by Roger and Moreau [12], at low Mach numbers, for an observer located directly above the aerofoil, the dips coincide with the reduced frequencies $\kappa c = 2\pi$ and $\kappa c = 4\pi$.

For the more general case of an observer at an arbitrary position in the mid-span plane, the frequencies of the local minima associated with the non-compactness effects are approximated in the following, using the definition of the observer position as illustrated in Figure 2.4. It is assumed that the connecting line between leading and trailing edge

aligns with the direction of flow, and that the effects on sound propagation due to non-uniform mean flow around the aerofoil are negligible.

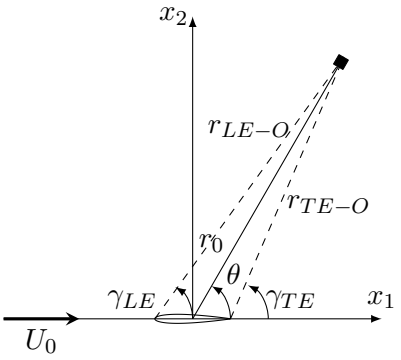

Figure 2.4: Coordinate system for observer positions.

The observer position relative to the aerofoil mid-chord position is defined by the angle θ and the radius r_0. The radii and angles of the connecting lines between leading and trailing edge, r_{LE-O}, r_{TE-O}, γ_{LE} and γ_{TE} are defined as shown in Figure 2.4. Geometric considerations are then used to relate the leading edge and trailing edge radii to θ and r_0:

$$r_{LE-O} = \sqrt{(r_0 \cdot \cos\theta + c/2)^2 + \beta^2 (r_0 \sin\theta)^2}, \tag{2.40}$$

$$r_{TE-O} = \sqrt{(r_0 \cdot \cos\theta - c/2)^2 + \beta^2 (r_0 \sin\theta)^2}. \tag{2.41}$$

The angles for the lines connecting leading and trailing edge and the observer positions are then:

$$\gamma_{LE} = \arccos\left(\frac{r_0 \cos\theta + c/2}{r_{LE-O}}\right), \tag{2.42}$$

$$\gamma_{TE} = \arccos\left(\frac{r_0 \cos\theta - c/2}{r_{TE-O}}\right). \tag{2.43}$$

The propagation times along the lines are now computed as:

$$\tau_{LE} = \frac{r_{LE-O}}{c_0 + U_0 \cos\gamma_{LE}}, \tag{2.44}$$

$$\tau_{TE} = \frac{r_{TE-O}}{c_0 + U_0 \cos\gamma_{TE}}. \tag{2.45}$$

The frequencies $f_{c,1}, f_{c,2} \ldots f_{c,n}$ of the non-compactness dips in the aerofoil far-field spectra are now given as integer multiples of the base frequency $f_{c,0}$ defined as:

$$f_{c,0} = \frac{1}{\frac{c}{c_0+U_0} + \tau_{TE} - \tau_{LE}}. \tag{2.46}$$

2.4.3 Numerical investigations of leading edge noise

While numerical studies of leading edge noise can investigate more complex geometries than many analytical methods, due to the requirement of simulating the interaction of inherently unsteady turbulent flows with objects in the flow, they are often associated with considerable computational expense. The two main approaches used for the simulation of leading-edge noise are hybrid methods and Computational AeroAcoustic (CAA) methods that solve the Linearised Euler Equations (LEEs).
Hybrid methods split noise generation and radiation by the use a Computational Fluid Dynamics (CFD) solver to compute the acoustic sources, and then use an acoustic analogy such as those put forward by Lighthill [117], Curle [111] and Ffowcs-Williams and Hawkings [118] in a post processing step to compute the radiation to the far-field. Commonly, a free field Green's function is used to describe the response of the problem geometry and physics to a perturbation, which carries the implicit assumption that scattering effects are negligible.
Conversely, CAA methods allow to directly compute noise generation and radiation. However, in addition to neglecting the effects of viscosity, depending on the formulation of the LEEs and the underpinning assumptions, mean flow gradients as well as finite frequency effects may not be accounted for by the CAA method.

2.4.3.1 CAA studies of leading edge noise

Since the generation of realistic turbulence in the numerical domain represents a considerable challenge on its own [30], early studies focused on the interaction of harmonic gusts with leading edges and the associated noise [119; 120]. Using a multi-frequency harmonic gust approach in a CAA solver, Gill, Zhang and Joseph [121] investigated the influence of a non-uniform mean flow, as is caused by the presence of an aerofoil in the flow due to its potential effects, as well as the influence of viscosity. For this purpose, mean flow results were computed with a commercial RANS solver, and interpolated on the acoustic grid as a boundary condition for the subsequent LEE simulation. They reproduced the expected decreases of noise emissions with thickness and leading edge radius and showed that the non-uniform mean flow is essential to avoid over-predicting the noise. This was shown to be related to the increased distortion of the gust wavefront as the thickness of the aerofoil is increased, which leads to a reduction in the peak transverse unsteady velocity values relative to those observed in thin aerofoils. In a later study of Gill [7], it was concluded that while the accurate representation of the potential flow surrounding an aerofoil is essential, the effect of viscosity on the background mean flow is negligible for the purposes of the leading edge noise if the angle of attack is small. The distortion of the energy spectrum by the aerofoil leading edge was investigated further by Hainaut, Gabard and Clair [102]. Using stochastically synthesized turbulence in a LEE solver, they found that the distortion of the transverse energy spectrum

is wavenumber dependent and is affected by nose radius as well as the position and magnitude of the maximum thickness.

2.4.3.2 Studies using hybrid methods

One of the earliest applications of a hybrid methodology to a leading edge turbulence interaction problem was reported by Casalino, Jacob, and Roger [122]. They used an Unsteady RANS (URANS) solver to simulate the oscillating wake of a rod interacting with an aerofoil and computed the far-field radiation using the analogy of Ffowcs-Williams and Hawkings (FW-H). Acoustic results were shown to be in good agreement with experimental measurements. They concluded that for applications at low Mach number, volume sources are negligible, and thus physical surfaces are best suited as integration surfaces for the FW-H solver.
The rod-aerofoil problem was subsequently used as a benchmark problem for hybrid approaches by several authors, an overview of which was provided by Giret *et al.* [123]. In their work, they investigated the effects of using unstructured meshes on acoustic results of complex geometries, albeit at the expense of numerical accuracy. They reported acceptable agreement with the experimental values, with some discrepancies at high frequencies where quadrupole sources were observed to become significant.
A simulation of true broadband turbulence interacting with a leading edge using a hybrid approach was conducted by Christophe [124]. The case consisted of an incompressible LES of an infinite aerofoil, interacting with turbulence created by an upstream jet, as shown in Figure 2.5.

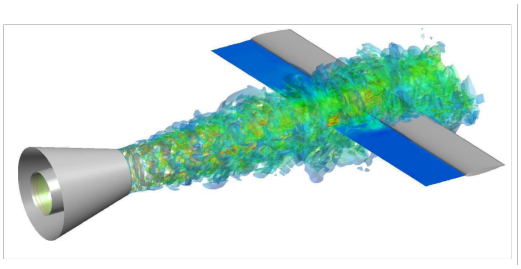

Figure 2.5: Simulation setup of Christophe [124].

Unsteady surface pressure data was stored, and the far-field radiation was computed using Curle's analogy. Non-compactness effects were neglected, as the cut-off frequency of the most resolved simulation was approximately 1 kHz, for which the aerofoil was considered compact. The results were shown to be in agreement with experiments.
A first compressible LES, using a zonal approach, was conducted by Deniau *et al.* [125]. By treating the far-field with a RANS solver and restricting the LES domain to the immediate vicinity of their thick, cambered aerofoil, they reduced computational expense considerably. A divergence-free Fourier mode method was used to synthesize the turbulence at the LES inflow boundary, with energy spectra based on experimental data.

Although the LES was found to produce a large recirculation bubble close to the leading edge, contaminating the acoustic results with additional trailing edge noise, acceptable agreement was reported with experimental data when the sources were restricted to the leading edge area during the acoustic post processing step.

2.4.4 Investigations of anisotropic turbulence

All the work discussed above assumed or investigated isotropic turbulence. This mostly due to the fact that anisotropic turbulence is difficult to model and measure. Furthermore, in many applications, prediction methods modelling the energy spectrum with isotropic models such as the von Kármán[16] and the Liepmann [35] model show reasonable agreement with experimental results. However, there are cases where the use of an isotropic model will lead to inaccuracies. Such a case was first encountered by Sevik [126], who investigated the sound radiation from a rotor subjected to turbulence. Since he used a simplified cascade prediction model for the sound emissions, which did not account for blade-to-blade correlation effects, he was not able to reproduce the broadening of the tones around the blade passing frequency and harmonics, which creates distinct humps in the spectrum. These correlation effects are caused by turbulent structures being stretched by the streamline curvature upstream of the rotor. The necessity of accounting for the anisotropy was also shown by Ganz *et al.* [127] who investigated the broadband noise emissions of a representative 18-inch fan rig. By comparing noise emissions of the fan with and without boundary layer suction in the fan inlet, they concluded that the rotor-boundary layer interaction is a significant source mechanism, which is characterized by distinct humps in the noise spectra. They report that the turbulent component in the streamwise direction is roughly twice as large the one in the transverse direction.

In 1981, Kerschen and Gliebe [128] presented a model for anisotropic turbulence. Their model is based on the theory of axisymmetric turbulence, which assumes that the vortices in anisotropic turbulence still show a symmetry about the streamwise axis. This is a reasonable assumption for turbulent boundary layers, as well as for rotor inflows, where the vortices are stretched by streamline contraction [129]. The Kerschen and Gliebe spectrum was subsequently used in a study by Posson *et al.* [130], focused on broadband noise prediction of fan outlet guide vanes, to investigate the effect of different turbulence models. They found that their noise prediction model is highly sensitive to the parameters of the anisotropic model. They recommended that if the anisotropic turbulence model cannot be conditioned by proper characterization of the turbulence from experimental measurements, a simpler isotropic model should be used.

An extensive CAA study on the influence of anisotropy on leading edge noise was conducted by Gea-Aguilera *et al.* [113]. They produced anisotropic turbulence by means of the superposition of anisotropic Gaussian eddies and computed the noise by using a LEE solver. Thickness effects are assessed, and similar trends are reported for both

isotropic and moderately anisotropic flows, i.e. noise was observed to reduce at high frequencies with increasing aerofoil thickness, and the angle of attack effects were found to be small for both isotropic and moderately anisotropic turbulence. In a later work, Gea-Aguilera [103] reported that the redistribution of energy in the velocity spectra, by which anisotropic turbulent flows are characterized, affects the amount of energy which produces leading edge noise.

2.5 Finite aerofoil aerodynamics and aeroacoustics

Finite aerofoils have attracted considerable interest in the past, as they produce tip vortices responsible for the induced drag of aircraft wings, which represent a significant danger for following aircraft. Furthermore, the interaction of the tip vortices with downstream leading edges represents a considerable source of noise, in particular in the case of CRORs. However, the numerical simulation of the wing tip vortices is associated with appreciable difficulties due to the strong unsteadiness of the tip vortex, combined with the requirement of meshing the relatively complicated geometry of the wing tip. Historically, most simulations have been attempted using the Reynolds Averaged Navier-Stokes (RANS) equations, as the Reynolds numbers encountered in engineering applications often leads to prohibitive costs when LES is used. However, as RANS computations require the use of a model for the turbulence to provide closure, uncertainties are introduced.

Due to the high cost of LES of a finite aerofoil geometry, only a few simulations have been reported to date. The development of a multi-block LES method with overset grid capability was reported by Uzun, Hussaini and Streett [131] who used it for the study of the tip vortex in a steady flow, finding good qualitative agreement between experiment and numerical predictions. A hybrid RANS-LES simulation was conducted by Kolomenskiy, Paoli and Boussuge [132], which takes advantage of a RANS approach in the near field of the aerofoil, whereas LES is used to predict the decay of the wing tip vortex more accurately. An implicit LES, serving as a proof of concept for the application of this method for these problems, was presented by Lombard *et al.* [133].

Conversely, several experimental studies have been conducted on finite aerofoils, both in steady flow conditions [134; 135; 136], and when immersed in turbulence [137; 138; 139; 140]. As a complete summary of the vast literature on this topic is beyond the scale of this work and can be found in reviews such as by Rossow [141] and more recently by Hallock [142], only the main findings on tip vortex aerodynamics are summarized here, followed by a discussion of studies focused on the noise emissions of finite aerofoils.

Following Bailey [140], the research topics commonly associated with the trailing vortex problem are: Formation of vortex and roll-up phenomena, its velocity profiles, the vortex wandering phenomena, the presence of turbulence in the vortex as well as the interaction of the vortex with external turbulence.

2.5.1 Vortex formation

The wing tip shape has considerable influence on the formation and downstream behaviour of the wing tip vortex. In the simplest case, with a rounded tip, it was shown by Green [143] that the flow separates from the pressure surface and reattaches on the surface section by the mid-chord location, whereas sharp edges may lead to the merging of multiple smaller vortices forming from separating shear layers, as observed by Katz and Galdo [144]. Further downstream, the wing wake rolls up in a spiral around the vortex. This roll-up process was considered by Philips [145] to not be complete until the wake spiral is indistinguishable from the vortex core, and thus roll-up was stated to persist several wingspans downstream of the wing. Conversely, Shekarriz *et al.* [146] considered roll-up complete when maximum vorticity is attained, which they found to be the case directly downstream the trailing edge. Yet another definition, used by Ramaprian and Zheng [147] relates the roll-up process to the symmetry of the vortex core. They reported that the vortex core exhibits near-axisymmetry within two chord lengths downstream the trailing edge, concluding that this type of roll-up process is completed relatively quickly.

2.5.2 Vortex velocity profiles

Once the vortex core has attained near-axisymmetry, the typical radial profile of the circumferential velocity U_Θ of a vortex with a circulation strength Γ_0 follows the well-known Lamb-Oseen model, as illustrated in Figure 2.6.

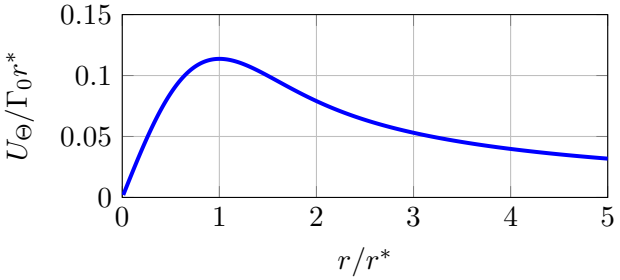

Figure 2.6: Radial profile of axisymmetric tip vortex following Lamb-Oseen model.

Close to the centre of the vortex, the velocity profile is nearly linear, similar to a solid body rotation. This region is commonly referred to the viscous core of the vortex, as it is dominated by viscous effects. As the radius of maximum circumferential velocity at r^* is approached, the velocity gradient inverses until the profile resembles that of a potential vortex.
While the circumferential velocity profile is approximated fairly accurately by the Lamb-Oseen model for many tip vortices, the axial velocity profile is more dependent on vortex formation processes. Studies conducted by Batchelor [148] showed that the axial velocity

may exhibit either a jet-like or a wake-like behaviour. There are strong indications that this phenomenon is Reynolds number dependent [135]. More recently, Anderson and Lawson [149] investigated the axial flow and found that high angles of attack and rounded tips produce jet-like flow, whereas lower angles of attack and square wing tips were associated with wake-like flows. In the experimental study of Bailey [140], a wake-like profile of the mean axial velocity was found for all investigated levels of turbulence intensity, which was significantly affected by the vortex wandering.

2.5.3 Vortex wandering

Vortex wandering describes the phenomenon that in most experiments, the vortex core tends to wander in a chaotic manner in the flow-normal plane, severely affecting measurement quality. This has been most commonly attributed to free-stream turbulence [136; 137]. Beninati and Marshall [139] found evidence in their experiments supporting earlier computational results of Melander and Hussain [150] that the external turbulence induces bending waves on the vortex.
Devenport [136] used an analytical approach to determine the magnitude of vortex wandering and to correct the effects of it on their point measurements. They found that there was a significant effect of wandering only on the point statistics measured within the vortex core, and that the wandering occurred predominantly in a broad-band, low frequency range. Bailey [140] reported indications that the vortex wandering is caused by convective transport due to large-scale free-stream eddies.

2.5.4 Turbulence and instability in the vortex

The vortex core has been found in experiment to rapidly lead to relaminarization by Chow [151], and later Devenport [136]. This had been attributed by Bradshaw [152] to the high level of streamline curvature within the vortex core, which act in a stabilizing way by impeding radial motions and increasing turbulence decay. While turbulence does not persist in the core, the vortex frequently exchanges fluid with the surrounding flow, partially relaminarizing it before ejecting it again, as shown in flow visualizations by Bandyopadhyay *et al.* [153].
Recently, the investigation of turbulent fluctuations within the vortex has been found to be a particular problem in the context of numerical studies, as many eddy-viscosity based turbulence models are unable to properly reproduce the stabilizing effects of the rotation in the tip vortex [154]. Corrections have been introduced to some models, such as to the Baldwin-Barth model [154], as well as to the Spalart-Allmaras model [155], but still significant inaccuracies remain, as shown for instance by Churchfield and Blaisdell [156]. Furthermore, as by Holzäpfel pointed out [157], LES methods have significant shortcomings when modelling vortex core evolution, since the development

of turbulence in this region of very high vorticity is often not appropriately modelled by the subgrid model, which is particularly critical as the vortex core regions are often under-resolved. In addition, strongly rotating turbulent flows may exhibit an inverse energy cascade, where energy is transported from the small to the large scales by the successive merging of vortices [150]. This process, first described by Kraichnan [158] is a phenomenon produced by turbulent flows of a quasi two-dimensional nature in the large scales, and cannot be captured by strictly dissipative subgrid-scale models.
Considering these problems, exhibited by the majority of commonly used LES modelling approaches [159], it is apparent that the prediction of the turbulence development within the core regions of the tip vortex is associated with considerable uncertainties. However, since prior studies of rotating flows in pipes showed the ability of even relatively simple LES models to reproduce the main flow features [160; 161], it is expected that this shortcoming is of negligible effect on the main focus of the thesis, which is the analysis of the leading edge turbulence interaction noise of finite aerofoil geometries. In future investigations, the problem geometry as used in Chapter 6 may be used to validate advanced subgrid scale models such as proposed by Holzäpfel [162].

2.5.5 The interaction between a vortex and turbulence

A number of studies have been conducted to investigate the effect of a vortex on a surrounding turbulent flow and vice versa. Melander and Hussain [150] used DNS to observe that small-scale non-coherent turbulence was reorganized by the vortex, and stretched by it, leading to an increase of the magnitude of the azimuthal component of vorticity. Organized secondary structures, arranged in spirals around the vortex, resulted. An example is shown in Figure 2.7, reproduced from the simulation of Marshall and Beninati [163].

Melander and Hussain [150] observed that for low turbulence levels, the structures would form, but decay together with the free-stream turbulence. For medium levels, the turbulence within the secondary structures would be sustained, and the vortex coexisted with them. At high levels, bending waves were induced in the vortex, which corrupted the axisymmetry of the secondary structures.
A distinction of the effect of large and small turbulent eddies on the vortex tube was first shown by Risso *et al.* in their DNS [164]. They state that while the large eddies of the surrounding turbulence, by their deformation around the vortex axis, slow down and straighten the curvature of the vortex significantly and are therefore causal for the collapse of the vortex, the small eddies enhance the diffusion of vorticity out of the vortex core. In the context of the incompressible Euler equations, i.e. the Navier-Stokes equations in the limit of infinite Reynolds number and low Mach number, this observation can be understood as a consequence of the transition from a quasi two-dimensional flow,

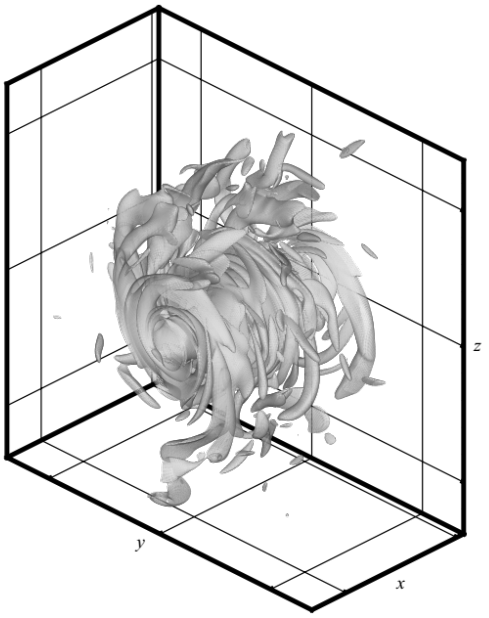

Figure 2.7: Turbulent structures wrapping around a vortex core [163].

i.e. the isolated vortex, to a three-dimensional flow by the interaction with the free-stream turbulence. When the Euler equations are written in terms of vorticity, vorticity is conserved in the 2D case, whereas in 3D the additional terms on the right hand side of the vorticity equation, which are associated with vortex stretching and vortex tilting due to the presence of secondary eddies, lead to vorticity no longer being conserved. Finally, in their DNS simulations, Marshall and Beninati [163] found little evidence of stripping of core fluid into the free-stream, except for immediately before the break-up of the vortex in very high free-stream turbulence conditions.

2.5.6 The state of the art of the aeroacoustics of finite aerofoils

A limitation of many analytical and numerical tools for aeroacoustic noise prediction is the assumption of an infinite span. The most widely used noise prediction method of Amiet [15], given by Eqn. (2.31), requires both the aerofoil response to turbulent gusts, as well as the turbulence statistics, to be constant at least on the order of the spanwise turbulence length scale. Although this allows treatment of spanwise changing flow conditions, as would be the case for finite aerofoils, by a strip theory approach [165], this has led to most of the experimental and numerical investigations to feature infinite aerofoil problems. Exceptions were the aeroacoustic investigations of a finite aerofoil with a tripped boundary layer, conducted by Moreau *et al.* [166]. They compared their noise measurements with predictions of a semi-analytical model by Brooks, Pope and Marcolini [4; 167]. They showed that tip-vortex formation noise is a dominant noise source, especially at higher angles of attack. Earlier experiments with a rounded tip were conducted by Brooks and Marcolini [167]. Yet another experiment was conducted

by Giez *et al.* [8]. Investigating an isolated, non-rotating aerofoil, data in support for an analytical model for predicting interaction noise of an open rotor was acquired. They showed that in the case of a swept aerofoil, a clear monotonic increase of noise level with angle of attack can be observed. This is explained to be most likely due to the leading edge vortex triggering the developing boundary layers.

2.6 Summary

This Chapter has introduced important concepts for the description of turbulence, with a focus on the properties of the energy spectra as well as the description of the anisotropy using the Reynolds-stress tensor and the Lumley triangle, both of which will be used extensively in Chapter 4. A review of the literature regarding turbulence grids was conducted, as the inlet grid turbulence creation method proposed by Blackmore [13] produces turbulence in a very similar way. It was found that while a considerable number of investigations have been conducted in the past, there are still open research questions, such as the development and generation of turbulence anisotropy in the immediate vicinity of the grid, as well as the long term development of the anisotropy. Both of these problems will be addressed in Chapter 4.
The state of the art regarding leading edge turbulence interaction noise was discussed, and it was found that the interaction of infinite aerofoils has been exhaustively investigated using both analytical and numerical tools. However, these method are often limited to simple geometries. This thesis will address this problem by demonstrating the use of a highly versatile approach of a compressible LES on an unstructured mesh for the investigation of a leading edge turbulence interaction problem of an infinite aerofoil in Chapter 5. Subsequently, the methodology will be applied to the problem of a loaded, thick, finite aerofoil in Chapter 6, allowing the investigation of the effects of the tip vortex on the far-field noise emissions of an aerofoil in a turbulent flow for the first time.

Chapter 3

Numerical methodology

The investigation of turbulence development with the inlet grid turbulence creation method proposed by Blackmore [13] is possible using a very uniform, isotropic mesh. Under such circumstances, errors arising from inhomogeneities in the mesh are small, and thus, highly accurate, albeit only conditionally stable numerical schemes can be used. However, in most applied cases, such as the infinite and finite aerofoil interaction cases, the geometry of interest makes the generation of a high quality mesh difficult, if not impossible. At the same time, accurate results from LES is still desired. In these situations, it is often difficult to assess the impact of using less accurate, yet stable schemes, and to take the effects of the changing mesh quality into account.
This Chapter aims to conduct a sensitivity study to investigate the consequences of changing case geometry and numerical schemes on the solution result. Due to the large number of possible numerical schemes, boundary conditions and mesh quality criteria, not all effects can be investigated. Analysis is concentrated on those changes which were made during this research project. Therefore, dependence of the results on mesh, boundary conditions and numerical schemes is presented.
The Chapter is structured as follows. In Section 3.1.1, the numerical methods of Large Eddy Simulation (LES) and Detached Eddy Simulation (DES) are introduced, and the governing equations for LES of incompressible and compressible flows are given. Additionally, the method chosen for aeroacoustic post processing is discussed. The effect of conducting compressible or incompressible turbulent LES at relatively low Mach numbers is investigated in Section 3.2, as well as the effect of choosing more stable, but less accurate upwind biased schemes over highly accurate, but oscillatory central schemes for the discretisation of the convective term. Finally, the impact of different boundary conditions on the development of the simulated turbulent flow is investigated in Section 3.3. Finally, the Chapter is summarized, and conclusions are given in Section 3.4.

3.1 Numerical background

For the selection of the simulation method used in this study, a number of factors were considered. Primarily, the method should be able to capture the relevant physics for the prediction of broadband noise, however it should also be computationally affordable, it should be versatile to support complex geometries such as finite aerofoils and it should be accessible.
Considering the review documented in Section 2.4.3, CAA methods were deselected based on the reasoning that while they are able to capture the relevant physics and predict noise emissions to a high level of accuracy, they are inflexible in terms of which geometries may be considered due to their very high mesh quality requirements.
Conversely, URANS methods, while computationally affordable and more versatile than CAA methods, are in general limited to the prediction of tonal noise sources, where they have been applied quite successfully [168; 169]. Most recently, some research groups [170; 171] have been successful by combining URANS methods with synthetic turbulence creation methods such as the random particle method (RPM) and fRPM methods proposed by Ewert [172] and Siefert and Ewert [173] to create broadband turbulence, and compute the noise emissions via a subsequent CAA step. However, these methods have yet to find wider adoption outside of proprietary academic codes, and are furthermore fundamentally limited, since the turbulent quantities for the RPM/fRPM turbulence synthesizing are extracted from a URANS simulation with its associated modelling assumptions.
The simulation method of LES has been shown in a number of prior investigations to be both an accurate as well as versatile tool for aeroacoustic purposes, in particular if the broadband noise is of interest [125; 169; 174; 175; 176], as it resolves the turbulent fluctuations up to the cut-off frequency. Furthermore, as it is computationally relatively affordable using modern research clusters and widely accessible, it was selected for this study.

3.1.1 LES for turbulence development and aeroacoustic research

The simulation method of LES, first proposed by Smagorinsky in 1963 [177], has been actively used by the scientific community for a wide range of applications. There are four steps in a LES [16]:

1. A filtering operation, decomposing the velocity field into a filtered, or resolved component, and a subgrid-scale component. The filtered velocity field represents the motion of the large eddies, hence the name LES. This filter can be applied in wavenumber space, or in physical space, using the numerical grid of the domain.

2. The evolution of the filtered velocity field is computed using equations derived from the Navier-Stokes equations. The contribution of the subgrid-scale components

is accounted for with the momentum equation, which contains the subgrid-scale stress tensor.

3. In order to close the system of equations, modelling is necessary. This is most commonly done with an eddy-viscosity model, like the Smagorinsky model [177].

4. Finally, the filtered equations are solved numerically, and an approximation of the large-scale motions of one realization of the turbulent flow is obtained.

The fundamental assumption of this method is that the energy contained in the small eddies is a negligible fraction of the overall turbulent kinetic energy. In addition, the majority of common subgrid models is unable to properly reproduce inverse energy cascades, such as present in strongly rotating flows, and consequently it is assumed that the subgrid scales act exclusively as an energy sink. If these assumptions hold true, the modelling error incurred is small. It is up to the user to ensure that this is the case, and that LES is used appropriately. Typically, it is assumed that a LES is physical once at least 80% of the energy is resolved [16].
While a LES incurs some accuracy loss compared to DNS due to the modelling of the small scales, it has a major advantage. Whereas the computational cost for a DNS, due to it resolving all scales, grows with $0.55Re_\lambda^6$ [16], the computational cost for LES is, depending on the application, less than 5% of a corresponding DNS [178], with little impact on the accuracy. For the case of a boundary layer, Piomelli [179] estimated the cost of a resolved LES to scale as $Re^{0.6}$ for the outer layer, and as $Re^{2.4}$ for the inner layer. Thus, for the investigation of decaying turbulence, LES represents a promising approach. This was recognized by Okong'o, Knight and Zhou [180], and later by Kang, Chester, and Meneveau [181], who both evaluated several LES models in terms of their capability to replicate low-order statistics of isotropic turbulence during decay.
For incompressible flows, the filtered Navier-Stokes equations underpinning the LES methodology reduce to:

$$\frac{\partial \overline{U_i}}{\partial x_i} = 0, \tag{3.1}$$

$$\frac{\partial \overline{U_i}}{\partial t} + \partial \overline{U_j} \frac{\partial \overline{U_i}}{\partial x_j} = -\frac{1}{\rho}\frac{\partial \overline{p}}{\partial x_i} + \frac{\partial}{\partial x_j}\left([\nu + \nu_{SGS}] \frac{\partial \overline{U_i}}{\partial x_j} \right). \tag{3.2}$$

with ν_{SGS} being the subgrid-scale viscosity. The overbar represents filtered, grid-scale components. From left to right, the terms in Eqn. (3.2) are commonly referred to as the transient, convective, pressure as well as the viscous term. The viscous term includes a term for the residual stresses ν_{SGS}, which are introduced by the filtering operation. These stresses are commonly approximated by a subgrid model. A large number of variants exist, and reviews of recent progress have been conducted by Georgiadis [174] as well as Piomelli [182]. One of the most widely used subgrid scale models was proposed

by Smagorinsky [177], and is defined as:

$$\nu_{SGS} = (C_s \Delta_i)^2 \sqrt{2 \overline{S_{ij} S_{ij}}}, \tag{3.3}$$

$$\overline{S_{ij}} = \frac{1}{2} \left(\frac{\overline{U_i}}{\partial x_j} + \frac{\overline{U_j}}{\partial x_i} \right). \tag{3.4}$$

with C_s being the Smagorinsky coefficient. Although the Smagorinsky model is known to be overly dissipative, and its coefficient has only been accurately validated for decaying turbulence [174], it has been recognized as sufficiently accurate in many applications since the impact of the subgrid-scale motions on the low-order statistics of the larger eddies is often negligible [178]. As such, it is used for the turbulence development investigations of Chapter 4, where the development and decay of the large scales is of primary interest.

In order to capture the non-compactness effect discussed in Section 2.4.2.1, the assumption of incompressibility has to be abandoned, as the speed of sound in an incompressible medium is infinite. Thus, the compressible Navier-Stokes equations have to be solved. To facilitate the notation of the compressible Navier-Stokes equations for LES, Favre filtering [183] is adopted. A Favre-filtered variable is then defined as

$$\tilde{f} = \overline{\rho f} / \overline{\rho}. \tag{3.5}$$

Under the common assumptions reported by Piomelli [184], the filtered, compressible Navier-Stokes equations for a perfect gas of constant molecular viscosity μ then take on the form:

$$\frac{\partial \overline{\rho}}{\partial t} + \frac{\partial \overline{\rho} \tilde{U}_j}{\partial x_i} = 0, \tag{3.6}$$

$$\frac{\partial \overline{\rho} \tilde{U}_i}{\partial t} + \frac{\partial \overline{\rho} \tilde{U}_i \tilde{U}_j}{\partial x_j} = -\frac{\partial \overline{p}}{\partial x_i} + \frac{\partial \tilde{\sigma}_{ji}}{\partial x_j} - \frac{\partial \tau_{ji}}{\partial x_j} \tag{3.7}$$

$$\frac{\overline{\rho} \tilde{e}}{\partial t} + \frac{\partial}{\partial x_k} (\overline{\rho} \tilde{U}_j \tilde{e}) + \frac{\partial \tilde{q}_j}{\partial x_j} = -\overline{p} \tilde{S}_{kk} + \tilde{\sigma}_{ji} \tilde{S}_{ij} - \frac{\partial}{\partial x_j} (\overline{\rho} (\widetilde{U_j e} - \tilde{U}_j \tilde{e})), \tag{3.8}$$

with the additional definitions

$$\tau_{ij} = \overline{\rho} (\widetilde{U_i U_j} - \tilde{U}_i \tilde{U}_j), \tag{3.9}$$

$$\tilde{\sigma}_{ij} = 2 \nu \tilde{S}_{ij} + \left(\tilde{\nu}_2 - \frac{2}{3} \tilde{\nu} \right) \delta_{ij} \tilde{S}_{kk}, \tag{3.10}$$

$$\tilde{q}_j = -\tilde{k} \frac{\partial \tilde{T}}{\tilde{x}_j}, \tag{3.11}$$

where $\tilde{S}_{ij}$ is the filtered strain-rate tensor, μ_2 is the bulk viscosity, e is the internal energy per unit mass, and $\tilde{k}$ is the thermal conductivity at the filtered temperature $\tilde{T}$.

3.1.2 The near wall region treatment in LES

An area of particular concern when conducting LES is the treatment of any walls in the domain. Towards the wall, the energy carrying scales becomes progressively smaller, which leads to excessive resolution requirements [38; 179; 185]. Since wall-resolved LES is infeasible for many practical applications, a number of proposals have been made to reduce the cost of computing a turbulent boundary layer by means of modelling. Larsson *et al.* [185] categorize wall-modelled LES in their recent review into wall stress models and hybrid LES/RANS approaches.

3.1.2.1 Wall stress models

In wall stress models, the LES methodology is extended all the way to the wall, and a model is used to adjust the wall stress based on information from the LES to allow the number of grid points to be reduced. Examples are the two-layer model proposed by Balaras and Benocci [186], the approach based on suboptimal control theory suggested by Nicoud *et al.* [187], and the model developed by Schumann [188], which assumes the existence of an equilibrium layer in a manner similar to wall functions used by common RANS turbulence models.
In terms of accuracy and computational cost, Piomelli [179] concludes that the computational cost of hybrid LES/RANS methods is higher than of the different types of wall stress models, with accuracy depending significantly on the application. Conversely, Larsson *et al.* [185] argue that wall stress-models where the derefinement is limited to the inner layer of the boundary layer have the potential to be significantly more accurate than hybrid LES/RANS approaches where this is not strictly required, albeit at a much increased computational cost.

3.1.2.2 Hybrid LES/RANS approaches

Hybrid LES/RANS approaches reduce the computational cost by computing the inner layer of the boundary layer using RANS, and then using the wall shear stress as computed by the RANS as input for the LES of the surrounding domain. The most well-known hybrid LES/RANS approach was proposed by Spalart *et al.* [155]. In the so-called detached eddy simulation approach, they suggested the use of the Spalart-Allmaras (S-A) [38] turbulence model as a subgrid scale model, allowing for a straightforward coupling of LES and RANS mode in the simulation. In the classic S-A turbulence model, the

equation for the evolution of the eddy viscosity is given as [178]:

$$\nu_t = \tilde{\nu} f_{v1}, \tag{3.12}$$

$$\frac{\partial \tilde{\nu}}{\partial t} + U_j \frac{\partial \tilde{\nu}}{\partial x_j} = c_{b1} \tilde{S} \tilde{\nu} - c_{w1} f_w \left(\frac{\tilde{\nu}}{d}\right)^2 + \frac{1}{\sigma} \frac{\partial}{\partial x_k} \left[(\nu + \tilde{\nu}) \frac{\partial \tilde{\nu}}{\partial x_k} \right] + \frac{c_{b2}}{\sigma} \frac{\partial \tilde{\nu}}{\partial x_k} \frac{\partial \tilde{\nu}}{\partial x_k} \tag{3.13}$$

with

$$\tilde{S} = S + \frac{\tilde{\nu}}{\kappa^2 d^2} f_{v2}, \tag{3.14}$$

$$S = \sqrt{2 \Omega_{ij} \Omega ij}, \tag{3.15}$$

where $\Omega_{ij} = 0.5(\partial U_i / \partial x_j - \partial U_j \partial x_i)$ as the rotation tensor, and d_s as the distance from the closest surface. The remaining constants of the S-A model are omitted here and can be found in Wilcox [178]. It follows from Eqn. (3.13) and Eqn. (3.15) that the evolution of the eddy viscosity equation in the classical S-A model depends on the distance from the closest surface, as well as the gradients of $\tilde{\nu}$. Thus, the eddy viscosity does not decay to zero in a free-stream, which can lead to non-physical diffusion [178].
For the purpose of using Eqn. (3.13) as a subgrid scale model, the distance d is replaced with $\tilde{d}$, defined as

$$\tilde{d} = \min(d, C_{DES} \Delta_i), \tag{3.16}$$

where C_{DES} is an adjustable constant, which is set in accordance with measurements from homogeneous turbulence [155], and Δ_i is cell size, which is determined in the presented work using the cube root procedure. With this modification, the model returns the classical value of the S-A model for the eddy viscosity near a surface, whereas at large distances the cell spacing is used for the computation of $\tilde{\nu}$, yielding a behaviour equivalent [189] to the classical model of Smagorinsky [177], given in Eqn. (3.4).
It is noted that, following Eqn. (3.13) and (3.16), the common practice of gradual derefinement of the mesh with distance from the surfaces results in a non-zero value of the subgrid-scale eddy viscosity even far away from the surfaces. However, since a LES is performed, the dissipation is the sum of subgrid-scale dissipation ε_{SGS}, which is a function of the subgrid-scale eddy viscosity, and the resolved, or grid-scale, dissipation ε_r, which is not. Estimations by Leonard [190] show that ε_r amounts to at minimum of 20 to 40% of the total dissipation, with the subgrid dissipation representing the remainder of the total dissipation. While the dissipation of the subgrid scales is modelled to be isotropic, the resolved dissipation may not, and thus allow the LES to exhibit anisotropic dissipation in a manner equivalent to observation from experimental flows [61].
Furthermore, it has been observed [191], that in meshes with ambiguous grid densities, the standard formulation of DES will lead to grid induced separation, especially in thick boundary layers. However, it is not expected that for the case of aerofoils at a small angle of attack, as is investigated in this research, thick boundary layers will be created.

For future investigations, which may feature larger angle of attacks to analyse the effect of stronger tip vortices, it may be advisable to use advanced formulations of DES, such as delayed DES [192], which is better able to prevent grid induced separation, or improved delayed DES [193], which incorporates a better reproduction of the log-layer. DES has been shown to be superior to RANS and URANS particularly when used for the prediction of strongly separated flows [194], albeit its performance regarding the accurate simulation of boundary layers is case dependent [195], and will necessarily lag behind that of wall-resolved LES and DNS, which however are will not become feasible to use at realistic Reynolds numbers even on large research clusters in the near future [155].

3.1.3 Aeroacoustic post processing

As the created turbulence is not divergence-free, the noise emissions of the aerofoil cannot be extracted directly from the unsteady pressure field, since the noise caused by the hydrodynamic pressure fluctuations of the turbulence interferes with the acoustic response of the aerofoil [113]. Furthermore, the relatively low order schemes of the used finite volume code are not suitable for the accurate simulation of the acoustic waves to the far-field.

Thus, a hybrid approach was adopted for the computation of the turbulence interaction noise. In a first step, the unsteady pressure data, generated by the DES run using the OpenFOAM CFD package was sampled on the aerofoil surface. The far-field radiation was then computed using the commercial software FLUENT^{TM}, which contains an implementation of the acoustic analogy of Ffowcs-Williams and Hawkings (FW-H) [118], according to the formulation 1A of Farassat [196]. For this purpose, the data output of the DES was converted to FLUENT readable files using scripts written in the commercial programming language Matlab^{TM}. A free-field Green's function is used, and a uniform mean flow is assumed. Mesh information and observer positions were supplied, and the post processing step was conducted in parallel on the computer clusters Iridis 4 and 5 of the University of Southampton.

By making use of an extraction of the unsteady pressure data directly on the aerofoil surface, an impermeable sampling surface was realized. Thus, additional noise being created by eddies passing through the FW-H surface is avoided [197]. The contribution of the quadrupole sources in the boundary layer of the aerofoil was, due to its very limited size considering the small angle of attack and limited chord length, considered to be negligible. Since the aerofoil is at rest relative to the observer, the use of the FW-H analogy corresponds in this case to the analogy of Curle [111].

The analytical model chosen for validation was Amiets thin aerofoil model [15] according to Eqn. (2.33), which was implemented using scripts written in MATLAB^{TM}. In this work, the von Kármán spectrum, as defined in Eqn. (2.16), was used in Amiets model as input for the energy spectrum.

3.2 Effects of numerical schemes and solvers

When conducting simulations, numerical schemes and solvers are chosen according to the physics of the problem, which determine the type of partial differential equation which needs to be solved. Subsequently, it is highly desirable that numerical schemes and solvers are kept unchanged to facilitate comparison across cases.
In this thesis, the two areas of interest pose unique requirements to the numerical procedure.

- The first area of interest, the analysis of the turbulence development behind the inlet grid boundary condition, is a strictly incompressible problem, as it is restricted by design to low Mach numbers and the acoustic aspect is not considered. As such, the incompressible Navier-Stokes equations may be solved on a homogeneous grid of exclusively hexahedral cells, allowing the use of cell-centred schemes for the discretisation of the convective term with minimal dissipative error, which is considered best practice for LES [174].
- The second area of interest, the study of turbulence interaction noise of finite and infinite aerofoils, in particular for frequencies and observer angles where the aerofoil cannot be acoustically considered compact, is a compressible problem with the additional complication of a solid body in the domain. Consequently, the compressible Navier-Stokes equations have to be solved on a mesh capable of accommodating a finite aerofoil, which exhibits a blunt trailing edge. For these types of meshes, cell-centred schemes have been found to be unstable for the discretisation of the convective term, and second order upwind biased schemes have been used instead.

As it is furthermore intended to be able to relate the findings of Chapter 4, which deals with the first area of interest, to those of Chapters 5 and 6, which deal with the second area of interest, the effect of changing the schemes for the discretisation of the convective term, as well as conducting an incompressible Navier-Stokes LES as opposed to a compressible LES is investigated in this Section.
The solvers used for all parts of this work are part of the well validated [198; 199; 200] open source computational fluid dynamics package OpenFOAM 3.0. All simulations were computed on the IRIDIS 4 and 5 computer clusters of the University of Southampton.

3.2.1 Numerical setup for methodology comparison study turbulence development case

Figure 3.1 illustrates the setup chosen for the comparison of solvers and schemes, as well as the "offset" plane and lines along which data sampling was conducted. Additionally, the definition of the grid period G_p is given.

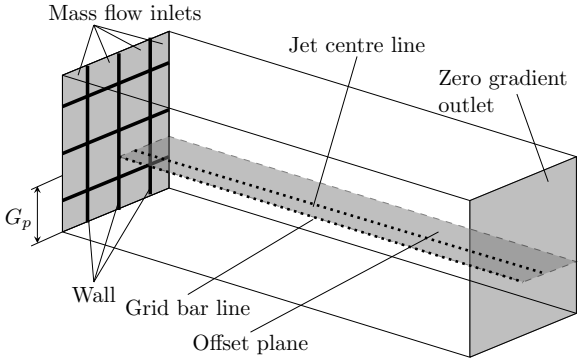

Figure 3.1: Boundary conditions and probe positions. Illustration not to scale.

Figure 3.1 shows the data sampling positions. Velocity data for computation of correlations and energy spectra was sampled on one plane, designated "Offset", as it is offset to the symmetry plane by $G_p/2$. On this plane, two lines are illustrated by the dotted lines, the "Grid bar line" and the "Jet centre line", for which in depth analysis will be presented in Chapter 4. The centreline is illustrated with a dotted line. The sampling frequency was greater than 5 kHz. Turbulent stresses were computed at all cell centres at runtime, allowing to conduct analysis of turbulent stress based quantities at all positions of the simulated domain.
As shown in Figure 3.1, the inlet was divided into wall and mass flow inlet patches according to the methodology described by Blackmore *et al.* [13]. Boundary conditions for the setup are given in Table 3.1.

Patch	Variable	Type	Definition
Wall	U	Dirichlet	$\mathbf{U} = (0, 0, 0)$
	p	Neumann	$\mathrm{d}p/\,\mathrm{d}x = 0$
Inlet	U	Dirichlet	$U_1 = \dot{m}/(A_p\rho_0), U_2 = U_3 = 0$
	p	Neumann	$\mathrm{d}p/\,\mathrm{d}x = 0$
Outlet[1]	U	Mixed	Eqn. (3.17)
	p	Neumann	$\mathrm{d}p/\,\mathrm{d}x = 0$
Sides	U, p	Periodic	1:1 field mapping to opposite boundary

Table 3.1: Boundary conditions of turbulence development setup

The outlet was set to a zero gradient condition, i.e. $\mathrm{d}p/\,\mathrm{d}x = 0$, also known as Neumann boundary condition, as a constant value pressure boundary conditions would not be appropriate considering the expected convection of eddies through the outlet. The

[1] In case of the incompressible simulations, a simpler Neumann boundary condition was used for the velocity, as the primary investigation was focussed on the near-grid region.

pressure is thus fixed in the domain by specifying a density in the mass flow inlet boundary condition. A mixed boundary condition, which would set Neumann or a Dirichlet boundary condition for flux out or into the domain, respectively, was applied for the velocity at the outlet, and is given by

$$\mathbf{U} = \begin{cases} \mathrm{d}U/\,\mathrm{d}x = 0 & \text{if } \phi_p > 0, \\ \mathbf{U} = (U_0, 0, 0) & \text{if } \phi_p < 0. \end{cases} \tag{3.17}$$

where $\phi_p > 0$ indicates flow out of the domain, $\phi_p < 0$ indicates into the domain. On each face of the inlet boundary patches, the velocity is set through the mass inlet boundary conditions as a function of mass flow $\dot{m}$, patch area A_p, and the fixed density ρ_0. Period boundary conditions were chosen for all boundaries normal to the transverse directions.

The grid setup chosen had a solidity of $s_G = 0.6$, with a grid period of $G_p = 0.06$ m. The mesh for the turbulence development simulations was created using the *blockMesh* utility provided within OpenFOAM v3.0, generating a high quality isotropic hexahedral mesh of 17.7×10^6 cells. The size of every cell in the domain was $\Delta_c = \Delta_1 = \Delta_2 = \Delta_3 = 1.875 \times 10^{-3}$ m, corresponding to 32 cells per grid period, which was chosen following the recommendations of the parameter study of Blackmore [13]. The time step Δt was chosen to satisfy the Courant-Friedrichs-Lewy (CFL) condition,

$$\mathrm{CFL} = \frac{|\mathbf{U}|\Delta t}{\Delta_c} \leq 0.9, \tag{3.18}$$

where $\mathbf{U}$ is the mean flow velocity vector in a given cell. For the incompressible LES, the *pisoFoam* solver implemented in OpenFOAM was used, which is transient and uses the PISO algorithm proposed by Issa [201] for velocity-pressure coupling. Conversely, for the compressible LES presented in this thesis, the solver *rhoPimpleFoam* was chosen, which conducts pressure-velocity coupling with the merged PISO and SIMPLE [202] algorithms. Similarly to SIMPLE, the PIMPLE algorithm solves the momentum equations repeatedly, and applies corrector steps as in the PISO algorithm. This allows to use under-relaxation in the solving of the equations, which enhances stability by reducing the change of the flow variables from one iterative step to the next. Although this leads to an increase of convergence times, the gain in stability is considerable.

An analysis of the dissipation and dispersion error characteristics of the chosen numerical schemes was conducted, and is documented in Appendix B.3. It was found that CFL numbers lower than 0.5 are advisable to minimize the dissipation error, while CFL numbers lower than 0.3 are advisable to minimize the dispersion error. Thus, for all simulations presented in this thesis, a CFL number smaller than 0.5 was used once quasi-steady state was achieved, which is furthermore considered best practice in order to increase stability and decrease temporal numerical dissipation [174].

3.2.2 Numerical convergence

The convergence of the numerical solution for a physical quantity is an important quality criterion, without which accurate and reliable analysis cannot be undertaken. In experiment, the convergence of a certain quantity is often assured, since it is possible to acquire data over an extended time period. Thereby, is ensured that sufficient statistically uncorrelated samples are acquired [203]. Numerical simulations, however, are limited in how much physical time can be simulated. Consequently, some quantities, in particular the higher statistical moments of the turbulence, are affected from imperfect convergence.

Compared to numerical simulations solving the compressible Navier-Stokes equations, simulations solving the incompressible Navier-Stokes equations are associated with a significantly lower computational cost, as the highest characteristic speed in an incompressible problem is much lower than the speed of sound, and consequently a larger time step can be used. Consequently, for the investigation of the convergence of the axial turbulent stress component u_{11}, as defined by Eqn. (2.20), as well as of the axial integral length scale I_{11}, as defined by Eqn. (2.10), the turbulence development case at low Reynolds number was used, which was computed using an incompressible LES. Figures 3.2 (a) and (b) shows the development of u_{11} and I_{11}, respectively, at three points on the centreline in the domain, when data over an increasingly larger time period is used for the computation. The convergence time was non-dimensionalised by multiplying it by the mean velocity at outlet, U_0, divided by the final value of the integral length scale, $I_{11}|_{final}$.

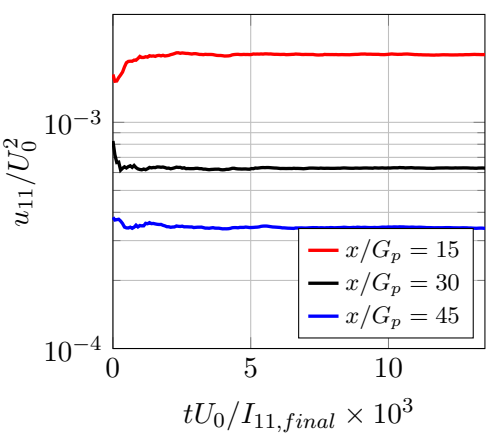

(a) Convergence of u_{11}.

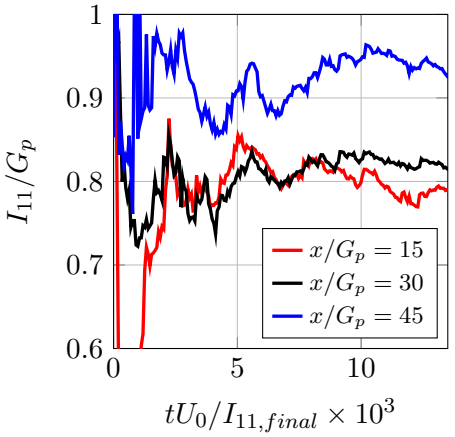

(b) Convergence of I_{11}.

Figure 3.2: Convergence of Reynolds stresses and integral length scale.

From Figure 3.2 (a) it is apparent that the values obtained for the turbulent stresses converge with data sampled for more than 2000 integral time scales, while Figure 3.2 (b) shows that the integral time scales themselves require data to be sampled for at least 5000 integral time scales. Based on the values shown above, the uncertainty of the turbulent stresses and the integral length scales is estimated to be less than 0.2% and 0.8%,

respectively.

It is concluded that an extensive time scale is necessary for u_{11} and I_{11} to converge, in particular in case of the latter. This is due to the fact that the longest scales, which carry most of the energy, will only be sufficiently represented in a temporal average if the time period over which it is computed is long enough. Consequently, experimental and numerical investigations often acquire data over time periods equal to at least 10^5 times the integral time scale.

As discussed above, numerically solving the compressible Navier-Stokes equations is associated with considerably increased computational cost due to the higher characteristic speeds involved. Considering the significantly increased cell count of the turbulence interaction cases, discussed in Chapters 5 and 6, it was found infeasible with the available computational resources to run the simulation for sufficient time to allow in particular the integral length scale to converge. However, in these cases the quantities of interest for which a converged solution is required are the aeroacoustic quantities.

In order to establish the time period sufficient for the convergence of aeroacoustic quantities, the OverAll Sound Pressure Level (OASPL) of the infinite aerofoil case was computed for an increasing time period, with the time non-dimensionalised by the streamwise mean flow velocity U_0 and the aerofoil chord length c. The results are shown in Figure 3.3.

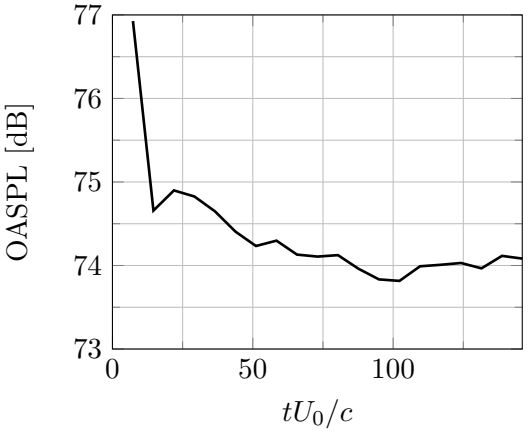

Figure 3.3: Convergence of OASPL levels of the infinite aerofoil simulation at an observer angle of $\theta = 90$.

From Figure 3.3, it is apparent that for times larger than $tU_0/c \geq 50$, the OASPL does not deviate more than 0.25 dB from the final result for this observer angle.

3.2.3 Impact of the assumption of compressibility on LES of highly turbulent flows at low Mach number

In order to study the effect of the assumption of compressibility on the turbulence produced by the inlet-grid methodology, and hence allow comparison of the results of Chapter 4 to those of the Chapters 5 and 6, a study was conducted on the turbulence development domain illustrated in Figure 3.1.

A second order backward-biased stepping scheme was used for the temporal discretization. Gradient terms were computed using a second order accurate scheme based on Gauss' theorem, while the convection and diffusion terms are computed using a second order central differencing scheme. Numerical oscillations were prevented by the use of gradient limiter functions. These limiters react to excessive gradients by switching to a lower order scheme, i.e. first order upwind [204]. Although this locally reduces the accuracy, the benefit of suppressing oscillations is substantial. An analysis of the effect of the use of these limiters was conducted and is documented in Appendix B. No effect on dissipative or dispersive was found for the present levels of turbulence and Mach number.

Figures 3.4 (a), (c) and (e) show the one-dimensional axial energy spectrum $\overline{E_{11}}$ for mean Mach numbers $M_0 = 0.018$, 0.088 and 0.177 respectively, while Figures 3.4 (b), (d) and (f) show the one-dimensional transverse energy spectrum $\overline{E_{22}}$. In order to facilitate comparison between the Mach numbers, the spectra are given as a function of wavenumber obtained for the position $x/G_p = 30$, where the mixing processes can be assumed to be completed and transverse averaging can be used to reduce noise in the spectra. This is necessary as the significantly more computationally expensive compressible simulations prohibit sampling times of the same length as the incompressible simulations, and therefore require the averaging over space to produce equivalently smooth spectral shapes. The spectra compared here are obtained by post processing data acquired to a physical time equal to 10 throughflow times T_l for all Mach numbers. T_l is defined as

$$T_l = l/U_0, \tag{3.19}$$

where l is the length of the domain in the streamwise direction. The analytical model spectra of von Kármán, provided as a reference, were computed with integral length scale and axial stress extracted from the incompressible simulations at much longer physical times, as shorter physical times led to a mismatch between analytical spectrum and LES spectra. The cut-off wavenumber of the grid $\kappa_c = 134$ m^{-1}, using the criterion of 25 points per wavenumber as established in Appendix B, is illustrated by the vertical dash dotted lines in Figures 3.4 (a) - (f).

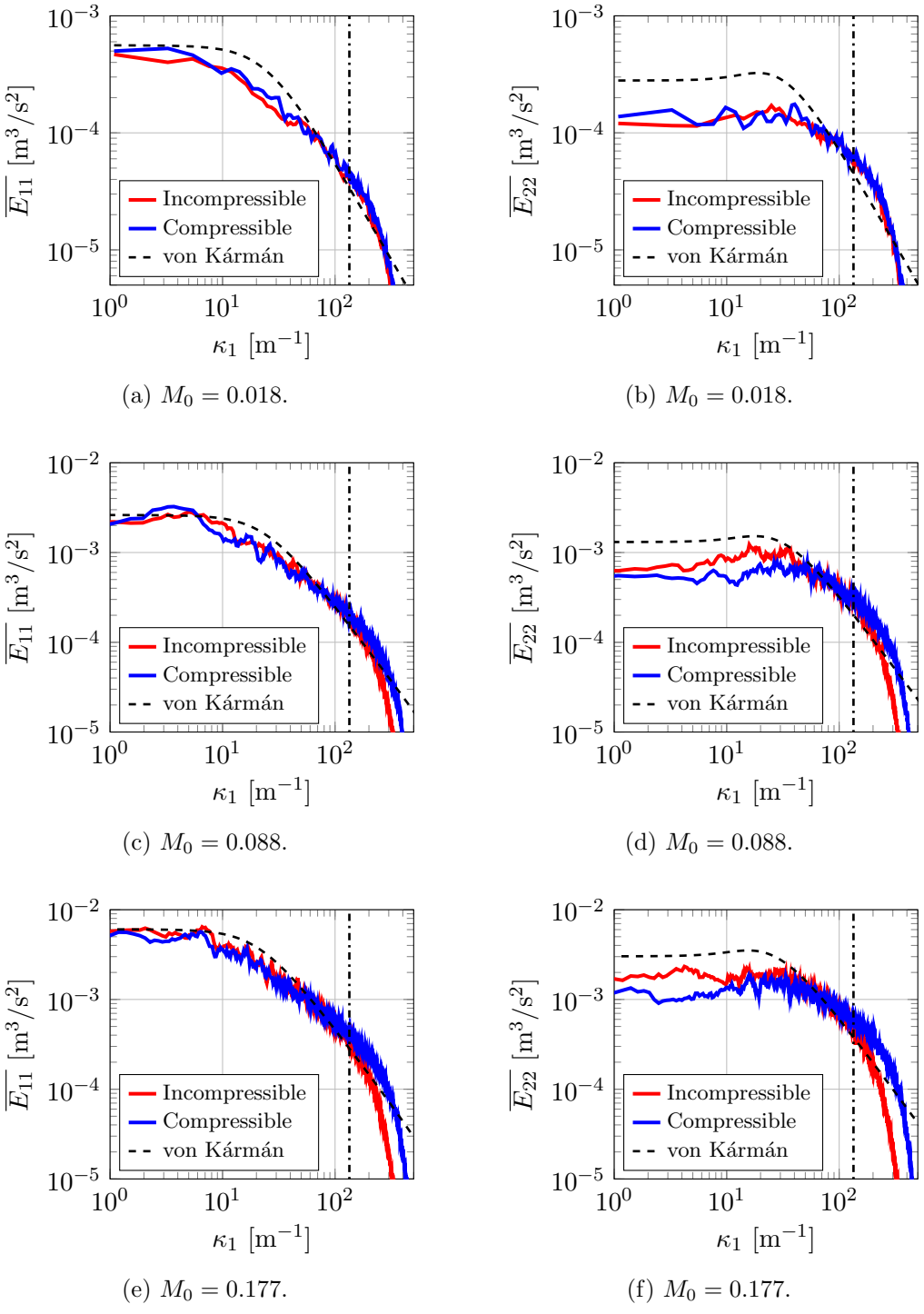

(a) $M_0 = 0.018$. (b) $M_0 = 0.018$.

(c) $M_0 = 0.088$. (d) $M_0 = 0.088$.

(e) $M_0 = 0.177$. (f) $M_0 = 0.177$.

Figure 3.4: Comparison of energy spectra from incompressible LES against compressible LES. Mesh cut-off wavenumber illustrated by dash dotted line.

As Figures 3.4 (a) - (f) show, the principal effect of conducting a compressible LES for the Mach number range investigated appears to be an increase in energy at the high wavenumbers as the Mach number is increased. However, as this effect is beyond the cut-off wavenumber, this is attributed to differences in the numerical dissipation and dispersion characteristics. Close examination of the simulation output revealed small

differences in the mean CFL numbers of the simulations, which will affect the dissipation and dispersion error of the used numerical schemes, as discussed in Appendix B. Below the cut-off wavenumber the spectra are observed to virtually collapse, which is expected for turbulence at low Mach numbers such as the range investigated here.
The energy at low wavenumbers, which constitutes the majority of turbulent kinetic energy, appears largely unaffected by the choice of a compressible or an incompressible LES. In order to ascertain this observation, the development of the kinetic turbulent energy over the length of the domain is shown in Figures 3.5.

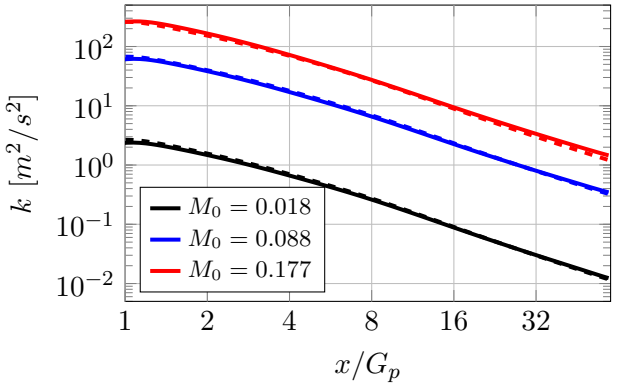

Figure 3.5: Development of k with mean flow Mach number. Comparison of incompressible (solid) and compressible (dashed) LES.

It is apparent that the curves do, for all intents and purposes, collapse for all investigated Mach numbers. Remaining uncertainties are likely due to the better convergence of the incompressible LES.

3.2.4 Impact of using central versus upwind biased schemes

In the finite volume method, the convective term in Eqn. (3.2) is computed by applying Gauss' theorem to the cell, thereby converting the volume integral into the sum of the convective fluxes through the faces of cell. As the values for an arbitrary flow quantity are known only at the cell centre, the face values of the flow quantities are then approximated with a numerical scheme. When conducting LES, it is best practice to use numerical schemes of at least second order [174]. Furthermore, it is an area of contention whether upwinded methods can be used for the convective term of Eqn. (3.2), as their inherent dissipation introduces numerical error into the simulation. As shown by Beaudan and Moin [205], even high order upwind biased numerical schemes show significant dissipation, although advanced schemes such as the non-dissipative and neutrally stable upwind scheme proposed by Karabasov and Goloviznin [206] have been shown to be promising for noise prediction with LES [207]. However, they have yet to be implemented in more widely available CFD packages.
While central schemes are preferred for LES due to their very low dissipation error, the sensitivity of such schemes to grid stretching and outflow boundary conditions

[208] makes the use of central schemes for more complex geometries, which often require unstructured meshes, difficult, if not impossible. Most recently, the application of high order discontinuous Galerkin schemes [174] and schemes of the Taylor-Galerkin family [123; 209] has shown promise. However, outside a small number of academic codes, they have found little implementation to date.

The open source solver package OpenFOAM v3.0, while supporting a wide variety of second order schemes, does not offer these advanced schemes yet. As such, the most accurate scheme for the convective term available in OpenFOAM v3.0 is the second-order central differencing scheme, which was found to be stable on the very regular, high quality, isotropic mesh used for the turbulence development simulations of Chapter 4. Using this scheme, the face values of an arbitrary quantity ϕ_f on the cell i are computed as

$$\phi_{f,i} = \frac{\phi_{c,i-1} - \phi_{c,i+1}}{2\Delta_i}, \tag{3.20}$$

with $\phi_{c,i-1}$ and $\phi_{c,i+1}$ being the values of the quantity at the cell centres of the neighbouring cells, and Δ_i is the spacing of grid points in the direction of discretization.

Conversely, on the unstructured meshes for the turbulence interaction simulations, a second-order upwind-biased scheme had to be used for reasons of stability. In this case, the cell face value $\phi_{f,i}$ is computed using the value and the cell gradient of ϕ in the upwind cell, as given by [210]:

$$\phi_{f,i} = \begin{cases} \phi_{c,i} + (\nabla\phi_{c,i}) \cdot d_{c,i} & \text{if } U > 0, \\ \phi_{c,i+1} + (\nabla\phi_{c,i+1}) \cdot d_{c,i+1} & \text{if } U < 0. \end{cases} \tag{3.21}$$

where $d_{c,i}$ is the distance from the cell centre to the face of cell i.

Since the choice of the less accurate upwind biased scheme was only necessary for the turbulence interaction cases, investigation of the effect of changing the schemes is conducted using for the compressible LES only, as it was used extensively for the turbulence interaction simulations. An investigation of the linear wave dissipation and dispersion properties was conducted, and is documented in Appendix B.

In all simulations presented in this thesis the three-level, second order accurate, implicit "backward" scheme, given by

$$\frac{\partial\phi}{\partial t} = \frac{3\phi - 4\phi^n + \phi^{n-2}}{2\Delta t}, \tag{3.22}$$

where n indicates the time level, was used for the transient term of Eqn. (3.2).

In order to quantify the effect of the increased numerical dissipation due to the upwind scheme, the energy spectra for the axial and transverse components at the position $x/G_p = 30$, obtained from simulations conducted with the central scheme for the convective term, are compared with those with the upwind biased schemes in Figures 3.6 (a) and (b). Comparison is conducted for the highest Mach number only, i.e. $M_0 = 0.177$. The physical time simulated was equal to 10 throughflow cycles. Transverse averaging

was used to reduce spectral noise.

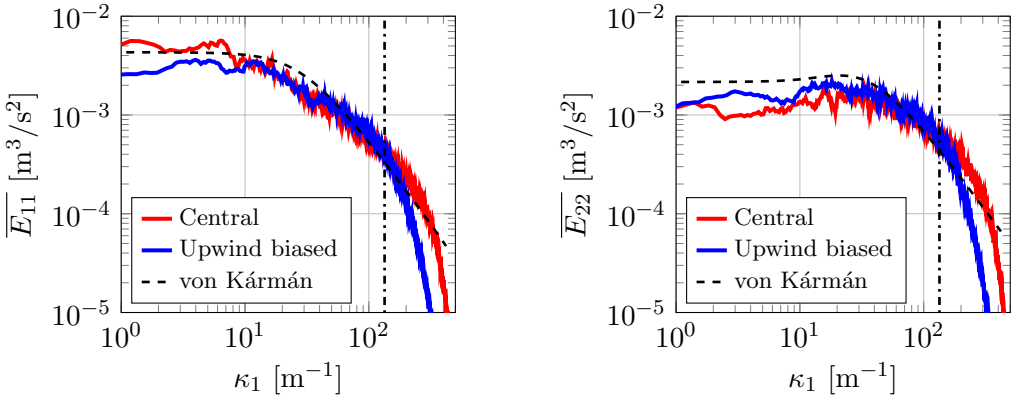

(a) Axial energy spectrum.

(b) Transverse energy spectrum.

Figure 3.6: Comparison of energy spectra at $x/G_p = 30$ of obtained from a compressible LES when using central or upwind biased numerical schemes. Mesh cut-off wavenumber illustrated by dash dotted line.

It is apparent that the choice of the central scheme has two effects. The energy content at the low wavenumbers is closer to the isotropic ratio of $E_{11}/E_{22} = 2$, and the spectra drop off more rapidly past the grid cut-off wavenumber. Considering the analysis of the linear wave propagation properties documented in Appendix B, the latter effect is related to the higher dissipative error of the upwind biased scheme. While the central scheme does exhibit a considerable dispersive error, it is found here in agreement with the observations of Mittal and Moin [208] that this does not affect the energy spectrum due to the very homogeneous mesh, which does not feature any grid stretching. Thus, the apparent mesh cut-off frequency is increased.

The effect of the choice of the numerical schemes on the Reynolds stresses and the anisotropy is investigated in more detail in Figures 3.7 (a) and (b). Illustrated are the development of the RST component u_{11} and of the anisotropy parameter $\gamma_{12} = \sqrt{u_{11}}/\sqrt{u_{22}}$, respectively, for both the central and upwind biased schemes, over the length of the numerical domain.

As Figure 3.7 (a) shows now quantitatively, the decay of the turbulence is significantly accelerated when using the upwind biased scheme. While both simulations exhibit a linear region past distances of $x/G_p = 16$, the slope is steeper when the upwind biased scheme is used, which is attributed to the higher dissipative error of the upwind biased scheme as discussed in Appendix B. However, in terms of the magnitude of the RST component u_{11}, large differences appear only very close and very far from the grid, illustrating that the differences in terms of the energy contained in the large and the small scales have only a small effect on the magnitude of the Reynolds stresses, in agreement with findings of Mittal and Moin [208] as well as Cao and Tamura [210].

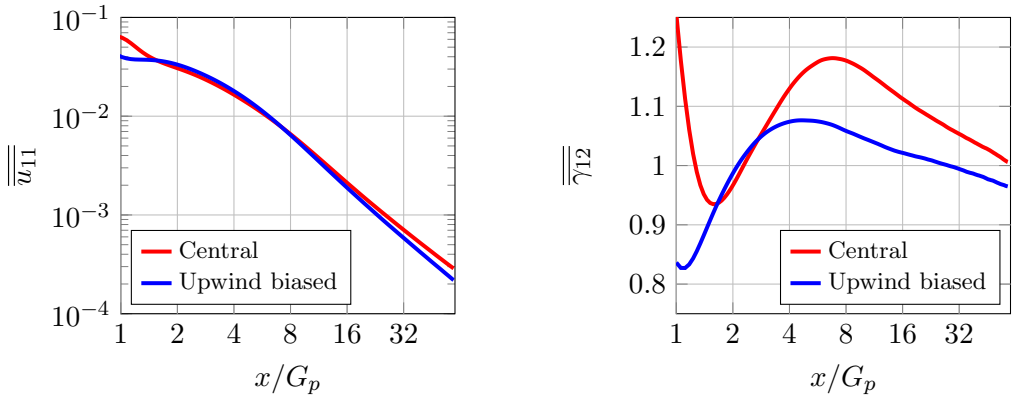

(a) Development of axial Reynolds stress.

(b) Development of anisotropy parameter.

Figure 3.7: Development of RST based quantities with distance to inlet grid for central and upwind biased schemes.

From Figure 3.7 (b) it is apparent that while the impact of the numerical schemes on the magnitude of the Reynolds stresses is relatively minor, the effect observed in Figures 3.6 (a) and (b) that the axial and transverse scales are affected leads to differences of the anisotropy parameter of approximately 10%, which is twice the spread observed in the experiments of Comte-Bellot and Corrsin [26] for typical isotropic turbulence. Additionally, the return to isotropy is accelerated when the upwind biased scheme is used. At very large distances to the grid, the anisotropy parameter attains a value smaller than unity for the simulation with the upwind biased scheme. While the anisotropy is contained, as shown in Figures 3.6 (a) and (b), predominantly in the large scales, with wavenumbers significantly below the cut-off frequency, leading to the dissipativeness of the upwind biased schemes having less of an impact, it is observed that over long flow distances, the larger dissipation error relative to the central schemes leads to an un-physical development of the turbulence in the present LES. It is concluded that the dissipative properties of the upwind biased schemes may lead to an underestimation of the anisotropy in a flow, and its long-term development.

Considering the conclusions of Figures 3.6 (a) and (b) as well as of Figure 3.7 (b), indications exist that the correlation of the largest scales is significantly reduced by the choice of an upwinded scheme. At $x/G_p = 30$, Taylor's frozen turbulence hypothesis [17] can be invoked, and the spatial correlation of the scales can be investigated using the autocorrelations of the unsteady velocities. Figure 3.8 (a) and (b) compare the autocorrelations for the axial and the transverse component at $x/G_p = 30$ of the two simulations with central and with upwind biased schemes. The time shift axis is non-dimensionalised by using the temporal integral time scale of the simulation using central schemes, which is deemed to be the more accurate. In order to provide context on the isotropy of the flow, the analytical relation according to von Kármán-Howarth [22] is indicated by the dashed lines.

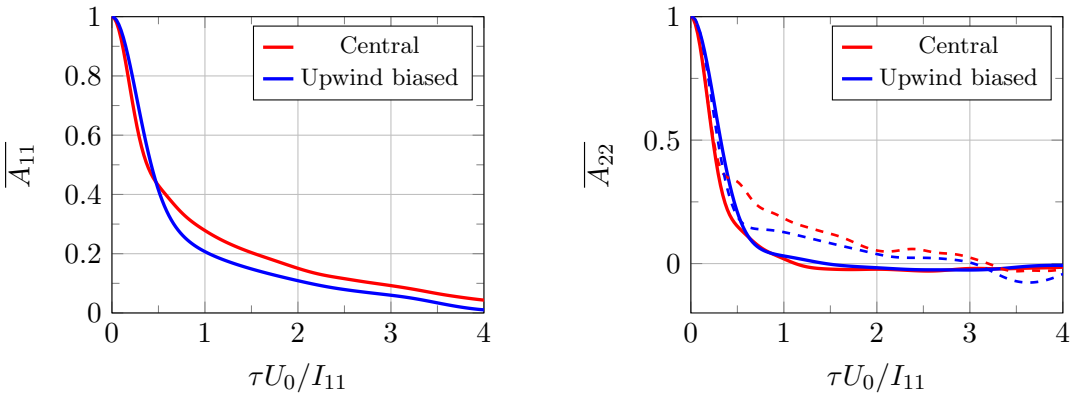

(a) Axial autocorrelation A_{11}.

(b) Transverse correlation A_{22}.

Figure 3.8: Comparison of correlation functions for central scheme against upwind biased scheme, when used in a compressible solver. Analytical relation according to von Kármán-Howarth [22], given in Eqn. (2.9) shown dashed.

From Figures 3.8 (a) and (b) it is apparent that when central schemes are used for the convective term, the turbulence exhibits a more anisotropic character at the large scales, considering that the integrals of the two autocorrelations up to the zero crossing point are larger and lower, for the axial and the transverse component, respectively, than when upwind biased schemes are used. At the same time, the comparison of the von Kármán-Howarth relations to the actual autocorrelations of the transverse component reveals that the simulation using central schemes exhibits a more isotropic flow at the small scales, as the analytical relation collapses completely with the autocorrelation for time shifts $\tau U_0/I_{11} < 0.2$.

While the use of gradient limiters has been known to introduce additional dissipation errors, a linear wave propagation analysis conducted to investigate this did not show any effect of the gradient limiters, as is documented in Appendix B.

It is concluded that in the present numerical setup, upwind biased schemes appear to be associated with a reduced large scale anisotropy, and an increased small scale anisotropy relative to the more accurate central schemes. The former leads to a considerable deviation in terms of the turbulent stress anisotropy, with the axial stress decreased in magnitude and the transverse stress increased in the magnitude. The latter has the implication that one of the core premises of the LES, i.e. the isotropy of the small scales, is met less accurately. While the von Kármán-Howarth relation is met close to the origin of the autocorrelation function, the fact that it deviates almost immediately from A_{22} indicates that this is more an artefact from the subgrid model forcing isotropy, rather than the simulation being able to accurately replicate the trend of the smaller scales to evolve towards isotropy. As such, the behaviour of the smallest resolved scales is considerably affected by the subgrid modelling. However, as the smallest scales constitute a very small part of the total kinetic energy contained in the turbulent flow, the resulting error is considered acceptable.

An additional conclusion from Figure 3.8 (a) is that simulations with upwind biased

schemes benefit from a faster convergence, as the time between decorrelated samples is reduced.

3.3 Impact of boundary conditions

The turbulence development case investigated so far, exclusively consisting of a rectangular cuboid domain with the boundary conditions of inlet grid, outlet and the periodic conditions, represents a very simple problem. When the inlet grid turbulence creation method is applied to the more complex turbulence interaction problem, boundary conditions in the transverse direction must be adapted. This section is dedicated to evaluating the effects of this change, in order to ensure comparability between the cases.
Comparison is conducted between cases of comparable numerical settings, i.e. of compressible LES and using the upwind biased scheme for the convection term, as the more accurate central scheme was found to be unstable on more complex meshes. Following the conclusions of Section 3.2.4, this is expected to lead to a decrease in the observed anisotropy of the turbulence.
The introduction of an aerofoil, and the requirement to use the setup for aeroacoustic investigations, necessitates a change of the boundary conditions normal to the span-chord plane, as well as for the downstream direction. From geometry considerations it follows that a periodic or symmetric setup is no longer appropriate, and that the domain is significantly enlarged in order to capture the physics of an isolated aerofoil. Additionally, the requirement that the boundary conditions do not reflect waves arises. The meshing setup, as well as the boundary conditions chosen for the infinite aerofoil interaction cases is discussed in Section 5.1.1.

3.3.1 Flow inhomogeneities

The effect of the change in boundary condition is expected to be most visible in the homogeneity of the turbulent flow. Ertunc *et al.* [56] introduced the inhomogeneity parameter I_ϕ for the quantification of a temporally averaged flow scalar $\langle\phi\rangle$, defined as

$$I_\phi = 100 \cdot \frac{\langle\phi(x,y)\rangle - \overline{\langle\phi\rangle}}{\overline{\langle\phi\rangle}}, \tag{3.23}$$

where the overline indicates the additional averaging of $\langle\phi\rangle$ in space. In order to establish a baseline of the achievable homogeneity when using the inlet grid turbulence creation method proposed by Blackmore [13], Figures 3.9 (a) - (c) show, for the "offset" plane in the turbulence development setup as defined in Figure 3.1 (a), the inhomogeneities of the axial mean velocity $\langle U_1\rangle$, the axial RST component u_{11} as defined in Eqn. (2.20) as well as of the anisotropy parameter $\gamma_{12} = \sqrt{u_{11}}/\sqrt{u_{22}}$.

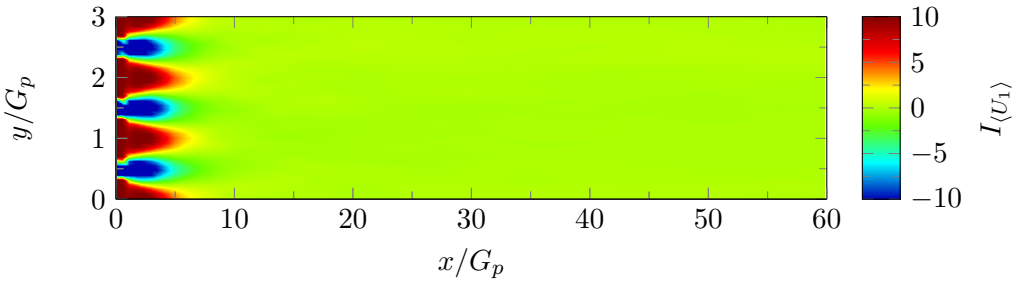

(a) Inhomogeneity of mean axial velocity.

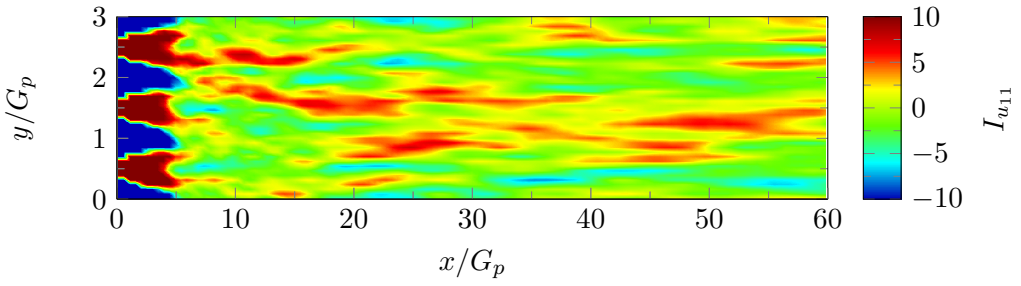

(b) Inhomogeneity of axial RST component.

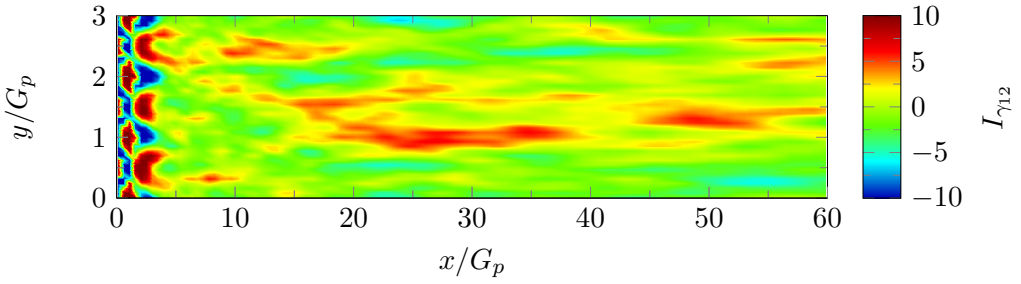

(c) Inhomogeneity of anisotropy parameter γ_{12}.

Figure 3.9: Flow inhomogeneity in the "offset" plane of the turbulence development case.

As can be seen in Figure 3.9, significant inhomogeneities of the mean velocities persist in the flow up to a distance of $10G_p$. Further downstream, however, the flow is quite homogeneous. The inhomogeneities of the higher moments, such as the axial turbulent stresses and of the anisotropy γ_{12}, persist far longer in the flow, and can be stated to never completely disappear. This result is in agreement with the measurements and simulations of Ertunc *et al.* [56] and demonstrates the necessity of transverse averaging to achieve quantitative results. Further assessment of the flow homogeneity, supporting the results shown above, was conducted for three planes normal to the streamwise direction and is documented in Appendix E.1.

In order to assess the homogeneity of the flow in the turbulence interaction setup, the homogeneity parameter is computed in a slightly altered way. While the analysis is conducted for a xy plane offset to the grid bar by half a grid period, the transverse average $\overline{\langle\phi\rangle}$ is taken for the xz plane at $y = 0$, which corresponds to the symmetry plane of the case. This allows the transverse deviation of the flow quantities from the plane of the prospective aerofoil position to be quantified. Figures 3.10 (a) - (c) show the contour

plots for the inhomogeneity parameters $I_{\langle U_1 \rangle}$, $I_{u_{11}}$ and $I_{\gamma_{12}}$. Dotted lines illustrate the position of the prospective aerofoil, which was placed $16G_p$ downstream of the inlet grid. This position was established in prior parameter studies to be associated with a suitable turbulent intensity as well as integral length scale to facilitate comparison of the aeroacoustic predictions with the experimental results of Paterson and Amiet [97], which is conducted in Chapter 5.

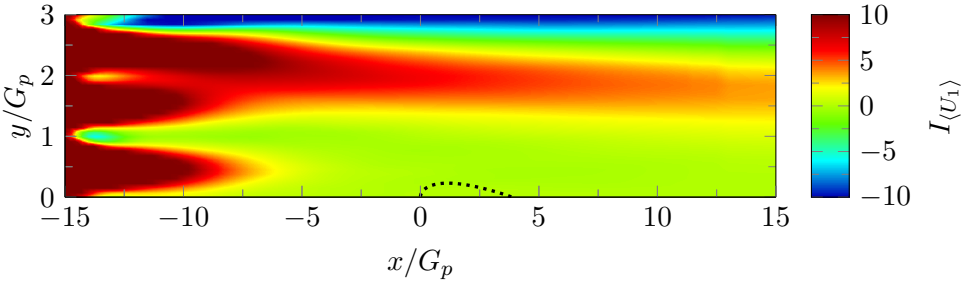

(a) Inhomogeneity of mean axial velocity.

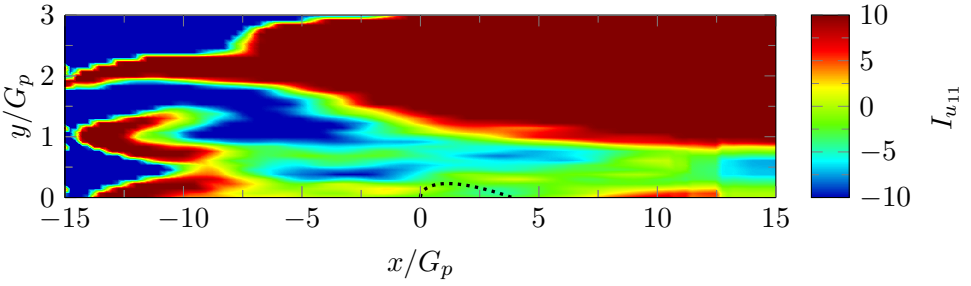

(b) Inhomogeneity of axial Reynolds stress.

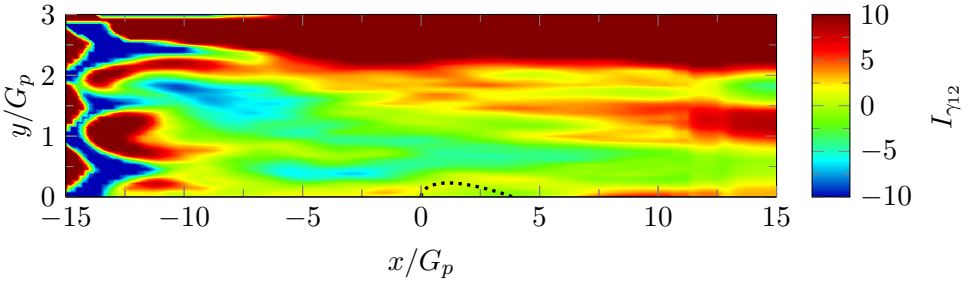

(c) Inhomogeneity of anisotropy parameter γ_{12}.

Figure 3.10: Flow inhomogeneity in the spanwise normal plane of the turbulence interaction case. Dotted lines indicate the position of the aerofoil.

As shown by Figures 3.10 (a) - (c), the homogeneity of the three quantities $\langle U_1 \rangle$, u_{11} and γ_{12} is qualitatively equivalent to that exhibited by the simple turbulence development setup to within one grid period of the symmetry plane for all downstream distances. The aerofoil is well separated from a region of larger mean velocity and turbulence intensity which exists towards the edge of the turbulent flow. This shear layer is caused by two effects, the mixing of the turbulent eddies with the laminar flow of the far-field, and a mismatch of $\langle U_1 \rangle$ of the turbulent domain relative to the far-field steady domain, which proved very difficult and time intensive to minimize.

Additional analysis of the flow homogeneity of the turbulence interaction case setup, supporting the results shown above, was conducted for three planes normal to the streamwise direction and is documented in Appendix E.1.
A potential matter of concern is the presence of the derefinement zone between turbulence domain and buffer domain, shown in Figure 5.1, which may lead to non-physical turbulent fluctuations, if eddies repeatedly pass through the transverse interface. However, as Figures 3.10 (a) - (c) show, the turbulent shear layer is wholly contained in the finely resolved domain, making potential interactions between the derefinement zone and the shear layer unlikely up to the point where the turbulent jet passes through the downstream interface. Further investigation of the shear layer and its potential interaction with the derefinement zones was conducted and is documented in Appendix D.1, showing that effects of the presence of the transverse derefinement zones are negligible. Furthermore, it was found that no reflection of acoustic waves from the derefinement layer takes place, allowing to use the presented domain setup for aeroacoustic purposes.

3.3.2 Development of turbulent stresses and anisotropy with streamwise distance

Typically, for the purpose of investigating noise created by the interaction of turbulence with an aerofoil leading edge, the characteristics of the turbulence determining the acoustic emissions are extracted in the plane of the aerofoil at the position of the leading edge, i.e. $x, y, z = 0$. Consequently, in order to investigate the capability of the simpler turbulence development, used in Chapter 4, to be used to establish suitable grid parameters to create turbulence of desired characteristics for the subsequent investigation of turbulence interaction noise, as conducted in Chapters 5 and 6, the comparison is restricted to the plane of the aerofoil, i.e the xz plane. In order to eliminate the effect of remaining flow inhomogeneity, the quantities are additionally averaged in the transverse direction.
Figures 3.11 (a) and (b) show the development of $\overline{u_{11}}$ as well as of the anisotropy parameter $\overline{\gamma_{ij}}$, respectively, for the turbulence development (TD) case in red, and for the turbulence interaction (TI) case with the aerofoil omitted in blue. Both simulations were conducted solving the full compressible Navier-Stokes equations and using upwind-biased schemes for the convective term.
It is apparent from Figure 3.11 (a) that in comparison to the turbulence development case, the turbulence interaction case is characterized by lower initial axial turbulent stress, and a slightly decreased decay at larger distances to the grid. However, at distances $x/G_p > 8$, the deviations become minor, both in terms of axial stress and anisotropy in both transverse direction, as illustrated by Figure 3.11 (b). This indicates that for the purpose of establishing the desired flow conditions by parameter studies, the simpler and less computationally expensive turbulence development setup can be used in parameter studies.

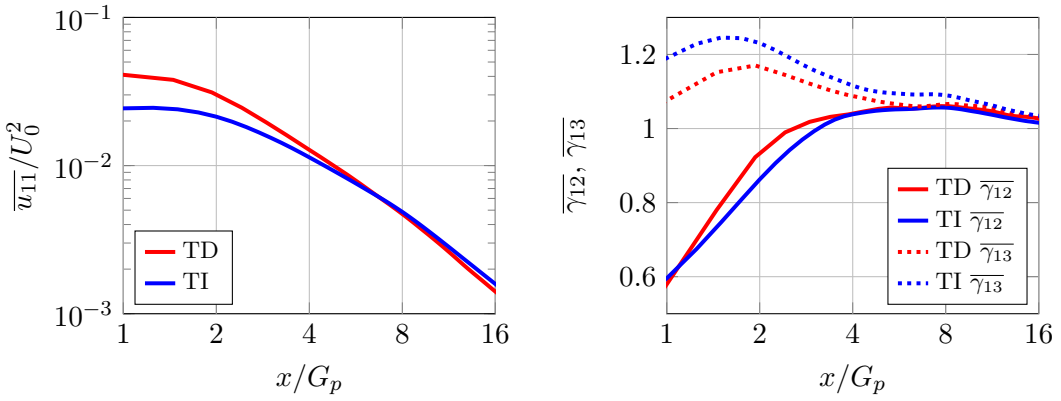

(a) Development of $\overline{u_{11}}$.

(b) Development of $\overline{\gamma_{ij}}$.

Figure 3.11: Development of Reynolds stress based quantities (dashed) with distance to grid for Turbulence Development (TD) and Turbulence Interaction (TI) cases. U_0 from turbulence interaction case.

While the development of the Reynolds stresses at large distances to the grid indicates that the turbulence is not significantly influenced by the change of boundary conditions for one of the transverse directions, the effect of the changed boundary conditions on the large scales is further analysed by comparing the autocorrelation of the unsteady velocity at the point of the prospective aerofoil, i.e. $x/G_p = 16$. Figures 3.12 (a) - (c) show the autocorrelation for the axial, the transverse and the spanwise component, respectively, for the turbulence development case and the turbulence interaction case.

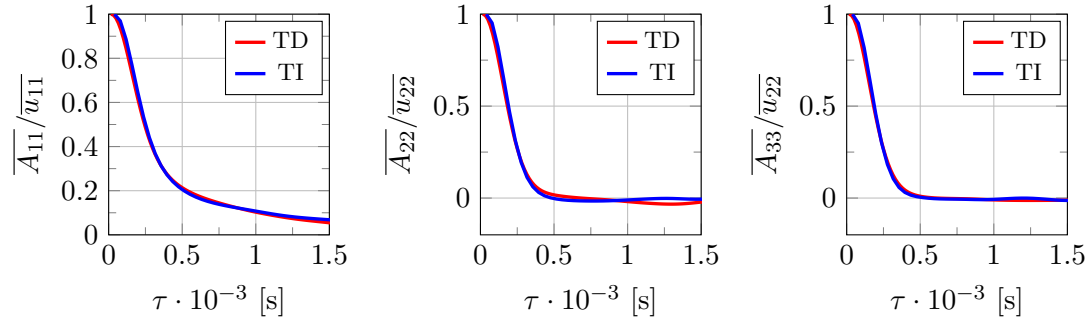

(a) Normalised A_{11}.

(b) Normalised A_{22}.

(c) Normalised A_{33}.

Figure 3.12: Comparison of correlation functions of the Turbulence Development (TI) case with the Turbulence Development (TD) case at the point of prospective aerofoil at $x/G_p = 16$.

From Figures 3.12 (a) - (c), it is apparent that the autocorrelations of the turbulence development case and the turbulence interaction case are virtually identical. It follows that the Taylor length scale, as well as the integral length scale, will display only very minor differences. Thus, the largest scales are shown not to be influenced by changing boundary conditions at distances reasonably close to the grid, and it is possible to use the simpler turbulence interaction case for parameter studies to establish the link between grid parameters and turbulence quantities.

In terms of application, Figure 3.11 (a) demonstrates how the user may exploit the evolving nature of the turbulent flow created by the inlet grid method of Blackmore *et al.* [13] to achieve the desired flow conditions for the simulation of a body with a turbulent flow by placing the geometry of interest at suitable distances from the grid. This approach was used to attain a flow condition suitable for the validation of the aeroacoustic results presented in Chapter 5.

3.4 Summary

This Chapter has given a brief overview of the method of LES for the investigation of turbulence development and aeroacoustic research. A particular focus was dedicated to the issue of the near wall region treatment, which is often a major complication when conducting LES. It was concluded that the simulation methodology of DES, as proposed by Spalart *et al.* [155] which uses an adapted Spalart-Allmaras turbulence model both for a RANS simulation close the walls to reduce computational cost, and for the subgrid scales in the areas far from the wall, is the most appropriate tool for this study.
Subsequently, investigations have been presented in this Chapter to establish the link between the relatively simple turbulence development case, as discussed in Chapter 4, and the more complex turbulence interaction case as used in Chapters 5 and 6. While the former, due to its simple geometry and lack of compressible phenomena, allows the use of non-dissipative central schemes for the convective term and of a solver of the incompressible Navier-Stokes equations, the latter require the use of less oscillatory, albeit more dissipative upwind-biased schemes, and, as the investigation of non-compactness effects is required, the use of a solver of the compressible Navier-Stokes equations. As the turbulence development case is less computationally expensive than the turbulence interaction case, and is therefore ideal for parameter studies to establish grid parameters appropriate for turbulence of target intensities and length scales, it is essential that the results of the turbulence development case can be related to the more complex turbulence interaction cases.
The main conclusions of these parameter studies, presented in this Chapter, are:

- Using a compressible LES as opposed to an incompressible LES for turbulent flows of the Mach number ranges investigated results in minor differences in terms of energy spectra for the transverse component and beyond the cut-off wavenumber. However, it is found that the effect on the total energy at low wavenumbers is not affected by the choice of the type of LES, and thus the development total turbulent kinetic energy is unaffected. It is noted that when the compressible Navier-Stokes equations are being solved, a considerable increase in terms of computational expense is observed, and consequently the convergence of statistics of higher order is impacted as less physical time can be simulated with the available computational resources.

- The use of stable, albeit dissipative upwind biased schemes for the convective term instead of the less dissipative central scheme resulted in the decrease of both the energies at low wavenumber, as well as a lower mesh cut-off frequency. While the latter is consistent with results in literature [205; 208], the reason of the former is hypothesized to be the increased dissipation of the numerical scheme, which lead to a more rapid decay of the largest scales. The anisotropy of the flow is affected in particular, as the largest scales exhibit the largest anisotropy. These findings were further supported by the analysis of the linear wave propagation properties of the central and upwind biased schemes, documented in Appendix B, where it was shown that the upwind biased schemes are associated with a higher dissipative error, although they are superior in terms of their dispersive error compared to central schemes.

- The effect of changing boundary conditions was assessed. As expected, large differences in the homogeneity of the flow were found when the grid turbulence flow is restricted to only parts of a numerical domain, but a core region of homogeneous turbulent flow was shown to exist were the assumption of homogeneity is reasonably fulfilled. In this core region, investigation of complex turbulence interaction problems with homogeneous turbulence is possible. Further assessment of the transverse homogeneity was conducted and is documented in Appendix E.1. It was observed that while the absolute values of the turbulent stresses differ to a limited degree in particular close to the grid when boundary conditions are changed, mean flow quantities as well as the correlation lengths at distances representative of a fully developed flow were unaffected, indicating that the simple geometry used in Chapter 4 can be used for parameter studies to achieve desired values of turbulent intensities and length scales in an applied case. Additional analysis of the potential effect of the derefinement zones is conducted in Appendix D.1.

This Chapter has established essential, and novel, links between a setup of the inlet-grid turbulence creation method amenable to parameter studies and more complex cases where this turbulence creation method is used to study turbulence interaction problems.

Chapter 4

The inlet grid turbulence creation method for LES

The effect of various changes to numerical schemes, solvers and boundary conditions on the turbulence generated by the inlet grid turbulence creation method proposed by Blackmore [13] were discussed in Chapter 3. While Blackmore conducted an extensive parameter study on the effects of changing domain size, discretization and flow speeds, an in-depth investigation on the anisotropy produced by the method as well as the decay processes was not conducted. In order to assess the capability of the LES method to accurately model the production and decay processes of grid turbulence, the turbulence development setup is revisited and a closer examination of the turbulent flow in the vicinity of the grid is conducted in the present Chapter, with a focus on the anisotropy of the energy carrying scales. By doing so, the inlet-grid turbulence creation method is established as an appropriate tool for the reproduction of turbulent flows often used in experiment, and as a method to investigate near-grid turbulence development, in particular the origin of the anisotropy of the turbulence, with low computational cost compared to DNS.
The main aims of this Chapter are:

- To demonstrate the applicability of the inlet-grid turbulence creation method, coupled with the simulation method of LES for the investigation of anisotropic flows produced by grid turbulence.
- To improve the understanding of the creation processes of the anisotropy of the energy carrying scales.
- To assess the impact of Reynolds number on the anisotropy of the energy carrying scales.
- To study the turbulent decay and return to isotropy in the case of an isotropic dissipation tensor, as enforced by the LES subgrid-scale model.

The Chapter is structured as follows. Relevance of this approach to actual grid turbulence is shown in Section 4.1 by discussion of the most commonly used quantities for the characterization of turbulence. A qualitative investigation of the relationship between eddy shedding processes in the grid bar wakes and the resulting anisotropy is conducted in Section 4.2. In order to quantify these processes, energy spectra and spectral invariant maps are computed for probes along two representative lines of the flow and presented in Section 4.3. Additionally, a procedure to quantify the anisotropy of the energy carrying scales by linking the Reynolds-stress tensor invariant approach with the energy spectra is proposed. The investigation of Reynolds effects, with a focus on the ability of LES to capture constrained turbulence decay, is presented in Section 4.4. Finally, the conclusions of the Chapter are given in Section 4.5.

4.1 Relevance to the grid turbulence problem

Typically, grid turbulence is most commonly produced by the introduction of a passive obstacle into the flow, which consists of a grid of cylindrical and square bars. However, many variants are documented in the literature, such as active grids [58; 211] and most recently, fractal grids [52; 50; 51]. Thus, grid turbulence is generally understood to describe any type of turbulence generated by an upstream obstacle which may or may not be active, and which can be described downstream a certain distance to the grid by the root mean square of the turbulent fluctuations and their decay rates, the integral scales of the flow and its anisotropy.
Due to the large variety of grid turbulence generators, the reported values for these quantities show a considerable variation. In order to establish the relevance of the inlet grid turbulence generation method to the problem of grid generated turbulence, the development of the turbulence as quantified by the turbulent stresses, the correlations as well as the energy spectra, is discussed in this section. While an extensive investigation of these parameters was also presented by Blackmore *et al.* [13], the results for these quantities are shown here to for the purpose of reproduction, and to expand on the report of Blackmore *et al.*

4.1.1 Numerical setup of the turbulence development case

Figure 4.1 illustrates the setup chosen for the analysis of the development of the turbulence, which is the same setup as used in Section 3.2.1 to study the effect of using different schemes for the convective term as well the effect of using a compressible or an incompressible LES to compute turbulent flows at low Mach number.

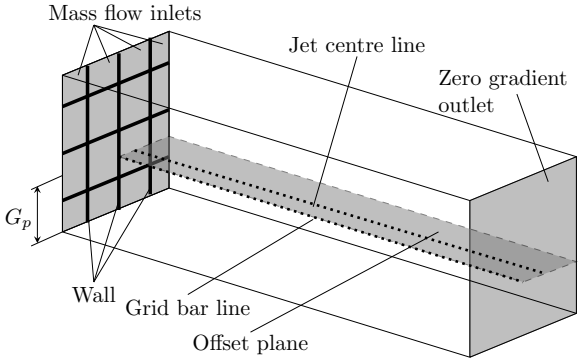

Figure 4.1: Boundary conditions and probe positions. Illustration not to scale.

Velocity data for computation of correlations and energy spectra was sampled on one plane, designated "Offset" in Figure 4.1, as it is offset to the symmetry plane by $G_p/2$. On this plane, two lines are illustrated by the dotted lines, the "Grid bar line" and the "Jet centre line", which are reference lines for the analysis conducted in Section 4.3. The centreline is illustrated with a dotted line. The sampling frequency was greater than 5 kHz. Turbulent stresses were computed at all cell centres over the runtime, allowing to conduct analysis of turbulent stress based quantities at all positions of the domain.
As shown in Figure 4.1, the inlet was divided into wall and mass flow inlet patches according to the methodology described by Blackmore *et al.* [13]. Boundary conditions for the setup are given in Table 4.1.

Patch	Variable	Type	Definition
Wall	U	Dirichlet	$\mathbf{U} = (0, 0, 0)$
	p	Neumann	$\mathrm{d}p/\,\mathrm{d}x = 0$
Inlet	U	Dirichlet	$U_1 = \dot{m}/(A_p\rho_0), U_2 = U_3 = 0$
	p	Neumann	$\mathrm{d}p/\,\mathrm{d}x = 0$
Outlet[1]	U	Mixed	Eqn. (3.17)
	p	Neumann	$\mathrm{d}p/\,\mathrm{d}x = 0$
Sides	U, p	Periodic	1:1 field mapping to opposite boundary

Table 4.1: Boundary conditions of turbulence development setup.

The outlet was set to a zero gradient condition, i.e. $\mathrm{d}p/\,\mathrm{d}x = 0$, also known as Neumann boundary condition, as a constant value pressure boundary conditions would not be appropriate considering the expected convection of eddies through the outlet. The pressure is thus fixed in the domain by specifying a density in the mass flow inlet boundary condition. A mixed boundary condition, which would set Neumann or a Dirichlet

[1] In case of the incompressible simulations, a simpler Neumann boundary condition was used for the velocity, as the primary investigation was focussed on the near-grid region.

boundary condition for flux out or into the domain, respectively, was applied for the velocity at the outlet, and is given by Eqn. (3.17). On each face of the inlet boundary patches, the velocity is set through the mass inlet boundary conditions as a function of mass flow $\dot{m}$, patch area A_p, and the fixed density ρ_0. Periodic boundary conditions were chosen for all boundaries normal to the transverse directions. The solver *pisoFoam*, implemented in OpenFOAM v3.0, was used, which conducts pressure-velocity coupling using the PISO algorithm proposed by Issa [201]. The case discussed here had a grid Reynolds number of $Re_{G_p} = 23 \cdot 10^3$, which, at a position of $x/G_p = 30$, corresponded to Reynolds numbers based on the Taylor length scale of $Re_\lambda = 10$.

4.1.2 Turbulence decay

The most well-investigated property of grid turbulence is its decay at distances where no mean velocity gradients, and therefore no production, exist. Figures 4.2 (a) and (b) illustrate the development of the turbulent stresses, as well as the development of the isotropy of the flow as determined using the anisotropy parameter $\gamma_{12} = \sqrt{u_{11}}/\sqrt{u_{22}}$, respectively. The values are computed with data along the centreline of the domain, as illustrated by Figure 3.1 (a).

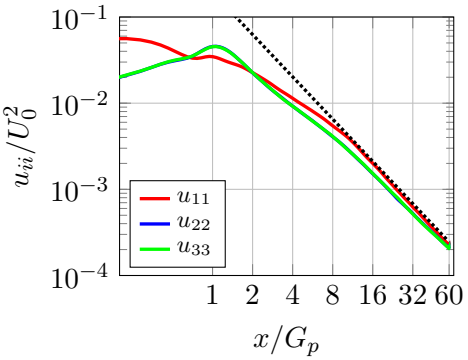

(a) LES (solid), analytical decay law Eqn. (2.28) (densely dashed).

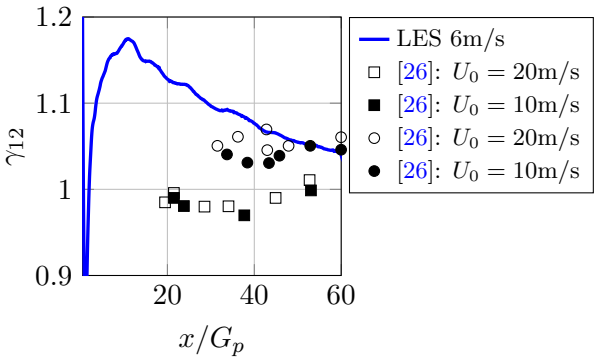

(b) Development of γ_{12} in the streamwise direction: LES at $U_0 = 5$m/s, (solid, blue), experimental values [26] with $G_p = 0.05$m (symbols: Square rods: □, ■; Disk rods: ○,●).

Figure 4.2: Decay of turbulence and development of isotropy according to ratio of turbulent components.

As Figure 4.2 (a) shows, the Reynolds-stresses are obtained at $x/G_p \approx 1$, with the axial component exhibiting a maximum slightly upstream of the transverse components. This is in good agreement with the development of the turbulent kinetic energy obtained by Ertunc *et al.* [56] in their DNS on the line coinciding with a grid bar and wake, which is to be expected as the centreline coincides with it most upstream position with an intersection of two grid bars.

Both u_{22} and u_{33} collapse over the entire length of the simulated domain, which is expected considering the symmetry of the case. The values of the axial mean squared

velocity u_{11} are larger than u_{22} and u_{33} over a significant part of the domain. A proper collapse of the three components, constituting isotropy, can only be observed for values of $x/G_p > 30$. Past $x/G_p = 15$, it is possible to fit the power law developed by Comte-Bellot and Corrsin [26], given in Eqn. (2.28) to the values from the LES. In their investigation, Comte-Bellot and Corrsin found values of $1.15 \leq n < 1.34$ and $7.1 \leq A < 35$ depending on mean flow velocity, grid period size, type of grid and location of a contraction which was used to enhance isotropy of the flow. Using a least-squares nonlinear fit method implemented in Matlab, equivalent to method IV of Valente and Vassilicos [51], a best fit to the data obtained from the current LES is achieved with values of $n = 1.56$ and $A = 15.33$, shown in Figure 4.2 (b). This value of the decay coefficient is high compared to the values commonly found in experiment and simulation, which range from $1.15 \leq n < 1.45$. However, since the decay coefficient has been found to be influenced by a large number of factors [48], a more in-depth investigation is required to find the potential causes for this high decay coefficient, which is conducted in Section 4.4.

In terms of flow anisotropy, the values of γ_{12} from the LES shown in Figure 4.2 (b) show that a significant level of anisotropy persists for almost all of the domain, confirming the earlier conclusions drawn in Figure 4.2 (a). However, when put into context with values of this ratio given for reasonably isotropic turbulence, e.g. by Comte-Bellot and Corrsin [26], who measured, for a range of downstream distances, mean flow speeds and grid geometries, values of $0.95 \leq \gamma_{12} < 1.05$, it can be stated that approximate isotropy is exhibited by the flow by a distance of 25 G_p to the grid.

Furthermore, from Figure 4.2 (b) it is observed that the levels of anisotropy are closer to the values obtained by Comte-Bellot and Corrsin [26] for a grid with disk rods, rather than square rods. While it is noted that the inlet-grid turbulence creation method, due to its lack of upstream domain, is not designed to replicate the exact turbulence creation mechanisms of either type of grid, it is apparent that the turbulence development is more representative of turbulence created by a round-rod grid, which predominantly sheds its vortex streets in in-phase mode [59]. Further discussion of the turbulence creation mechanisms is conducted in Section 4.2.

4.1.3 Two point correlations and energy spectra

In grid turbulence, but also in many other applications, the correlation lengths exhibited by a turbulent flow play an important role. In Figures 4.3 (a) and (b), the longitudinal and lateral autocorrelations, as defined in Eqn. (2.8), as computed from the resolved fluctuations of the simulation are compared to the von Kármán-Howarth relation at two points in the flow, at a distances $x/G_p = 30$ and $x/G_p = 58$, which is generally considered sufficient for grid turbulence to have obtained a well-developed state.

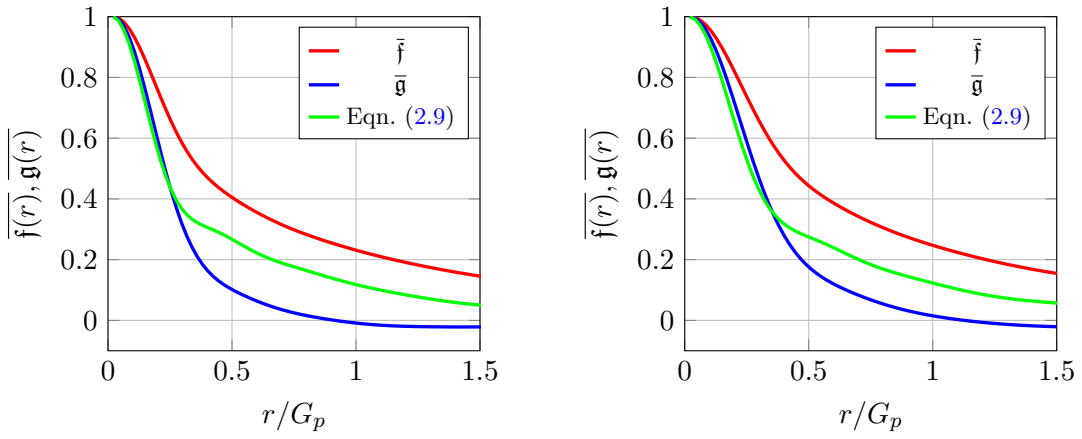

(a) $x/G_p = 30$. (b) $x/G_p = 58$.

Figure 4.3: Development of the longitudinal and transverse autocorrelations.

As shown by Figures 4.3 (a) and (b), the transverse autocorrelation $\overline{\mathfrak{g}}$ begins to deviate from the von Kármán-Howarth relation fairly quickly, so much so that by $r/G_p \approx 0.15$ at $x/G_p = 30$ and by $r/G_p \approx 0.25$ at $x/G_p = 58$ the two curves no longer collapse. This is indicative of a significant amount of large-scale anisotropy in the flow, similar to the conclusions drawn from Figures 4.2 (a) and (b). The almost perfect collapse for small values of r/G_p, on the other hand, indicates isotropy in the small scales, following the arguments of Valente and Vassilicos [51] and Discetti *et al.* [60], which is an important requirement for the applicability of the LES method.

In order to assess the distribution of the anisotropy across the energy carrying scales in more detail, the energy spectra obtained from the LES are compared to the isotropic model spectra of von Kármán, given by Eqn. (2.16) and Eqn. (2.18), in Figures 4.4 (a) and (b), for the positions $x/G_p = 30$ and $x/G_p = 58$ respectively, for E_{11} and E_{22}. I_{11} and u_{11} used for the computation of the model spectra are extracted directly from the LES. In order to provide context on the influence of numerical dissipation and dispersion error on the results, the cut-off wavenumber κ_c is indicated by the vertical black dash dotted line. A criterion of 25 points per wavelength is used, leading to $\kappa_c = 134.04\ \mathrm{m}^{-1}$, as established in Appendix B.

As shown by Figure 4.4 (a), good agreement is obtained between the axial energy spectra and the corresponding model spectra, with some minor deviation from the model spectrum in the mid-frequency range. However, the deviation of the transverse spectra is significant, especially at low- to mid-wavenumbers. Clearly, a significant amount of anisotropy is present at the large scales, which is an expected result as the energy spectra and the two-point correlations represent a Fourier-transform pair.

The match between model spectra and the turbulence spectra does improve with distance to the grid, as shown by Figure 4.4 (b), indicating a return to isotropy of the large scales. Still, a certain degree of anisotropy remains, which is a result often encountered in untreated grid turbulence [26].

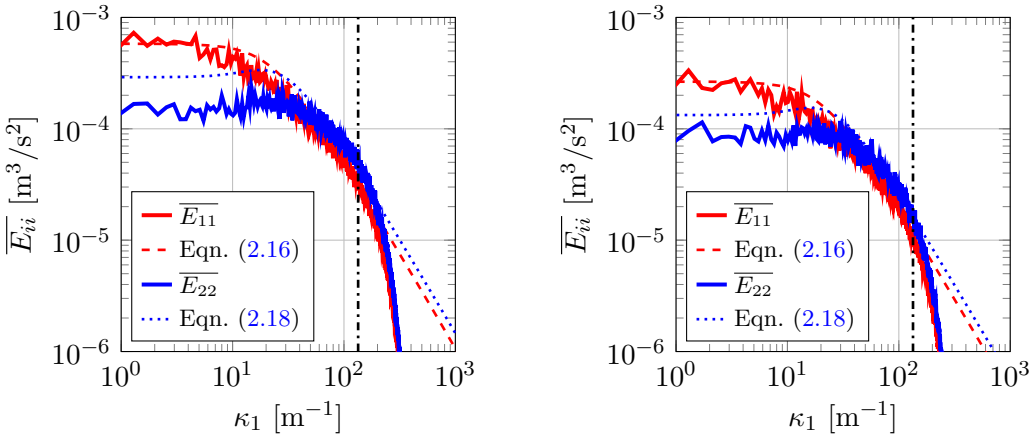

(a) $x/G_p = 30$. (b) $x/G_p = 58$.

Figure 4.4: Comparison of energy spectra from LES (solid) against model Eqn. (2.16) (dashed) and Eqn. (2.18) (dotted). κ_c indicated by vertical dash dotted line.

Considering the potential influence of numerical dissipative and dispersive error, it is observed that the wavenumber range associated with the majority of the anisotropy is smaller by almost a decade than κ_c. Thus, the influences of the dissipative and dispersive error on the large-scale anisotropy are considered negligible.

4.1.4 The development of the invariants averaged across flow normal planes

The method chosen for the investigation of turbulence anisotropy is the computation of the invariants of the anisotropic Reynolds-stress tensor (aRST), and their visualization in the so-called Lumley triangle. The development of the transverse averages of the two invariants II and III, as defined by Eqn. (2.24) and Eqn. (2.25), respectively, computed on planes normal to the flow is shown in Figures 4.5 (a) and (b). Due to a relative dearth of data in the literature regarding the development of the invariants of turbulence downstream a grid, validation of the results is difficult. A qualitative comparison is conducted with the results obtained by Djenidi and Tardu [42], who used floating square elements as turbulence generators in their DNS. As this is, essentially, an inverted grid, results can be compared, but some differences can be expected. Since the computation method used to compute the invariants involves first a time-averaging step to obtain the Reynolds-stress tensors, before spatial averaging is used to account for effects of local inhomogeneity, temporally averaged values from the DNS are used as comparison. Since these were not spatially averaged by Djenidi and Tardu, some differences must be anticipated.

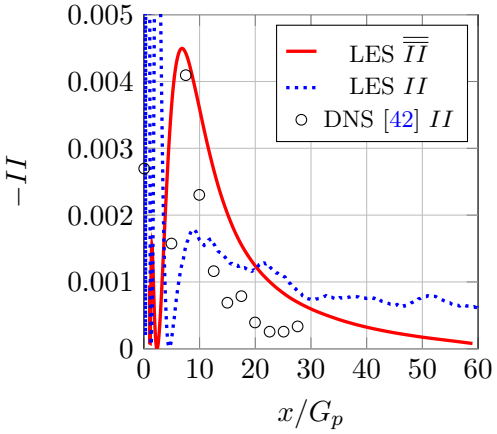

(a) Development of the second invariant of the RST.

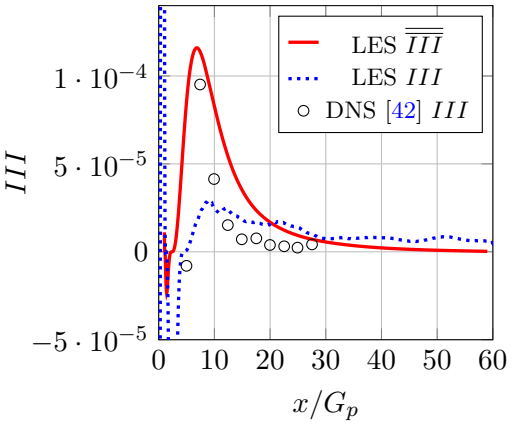

(b) Development of the third invariant of the RST.

Figure 4.5: Temporally averaged second (a) and third (b) invariants of the turbulent stress tensor over x/G_p. Transversally and temporally averaged invariants obtained from the LES (solid red), temporally averaged invariants from LES (dotted blue).

It is readily apparent from Figures 4.5 (a) and (b) that the two invariants of the anisotropy tensor evolve very similarly in the axial direction. A region with very steep gradients exists very close to the grid, which is associated with the eddy shedding immediately behind the bars. It is followed by a gradual increase of the anisotropy, which peaks just before $x/G_p = 10$. After this, both invariants first rapidly decay towards zero, but the return to isotropy slows with decreasing values of the invariants. It is noted that the development of the local values from the LES, shown by the dotted blue line in Figures 4.5 (a) and (b) for which only averaging in time was conducted, are associated with an apparently irregular development. This is caused by the remaining levels of inhomogeneity in the streamwise direction, which have been shown by Ertunc *et al.* [56] to be a feature of grid-generated turbulence in general. These can also be observed in the development of the values of II and III from the DNS of Djenidi and Tardu [42], which have equally been computed by averaging only in time, thus retaining the influence of inhomogeneity.

As shown by Figures 4.5 (a) and (b), the general trend of the invariants as obtained from DNS is replicated, but the LES values are consistently above the DNS values. The return to isotropy in particular appears to be happening at a faster rate, however this might be due to the position of the probe points chosen by Djenidi and Tardu [42] used for time averaging, relative to the grid elements. An analysis of the effect of the effect of different probe positions on the values of the invariants is conducted in Section 4.3.

While the DNS of Djenidi and Tardu [42] can be expected to contain significantly lower levels of both dissipative and dispersive error than the present simulation, it is observed from Figures 4.4 (a) and (b) that the anisotropy is predominantly contained in wavenumbers significantly smaller than the mesh cut-off frequency, which indicates that

the contribution of excessive dissipation and dispersion to the observed differences is small. As such, it is concluded that the mesh is sufficiently refined to resolve the energy carrying range relevant for the development of the invariants.

It is furthermore noted that due to the definitions of II and III, given by Eqn. (2.24) and Eqn. (2.25), respectively, there are different levels of uncertainty associated with the the invariants. Based on the uncertainty established by the analysis of the convergence of the RST components u_{ij}, discussed in Section 3.2.2, an uncertainty of 0.4% and 0.6% is estimated for II and III, respectively, as II is a squared and III a cubed function of the RST. As these uncertainties are very small, error bars have been omitted from plots showing the invariants.

The transversally averaged shapes of the aRST as a function of distance to the grid are shown in Figure 4.6. In order to simplify the analysis, points closer than two grid periods to the grid were omitted. This is due to planes closer to the grid than $x/G_p = 2$ are expected to include points where no turbulence exists yet, i.e. in the centre of the grid jets, and where turbulence is recirculating, i.e. directly behind grid bars. When these points are omitted, the resulting states of the anisotropy stress tensor lie in an area close to the isotropic corner. Thus, only the area of the isotropic corner is plotted.

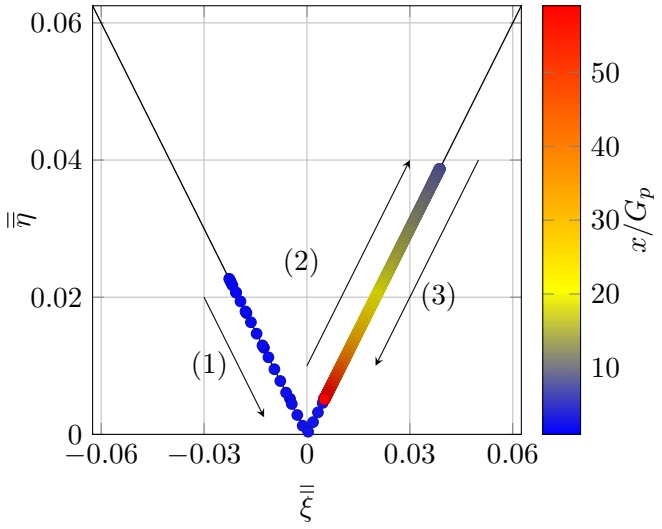

Figure 4.6: Shape of the aRST with growing distance to the grid x/G_p. Arrows highlight direction of aRST shape development: (1) for the region $x/G_p < 2$, (2) for the region $2 < x/G_p \leq 7$, and (3) for $x/G_p > 7$.

From Figure 4.6 it is immediately apparent that when plotted in the Lumley triangle, the global averages of the invariants, $\overline{\overline{II}}$ and $\overline{\overline{III}}$, of the Reynolds-stress ellipsoid are on the axisymmetric limits. Taking the shapes of the RST on the limits of the Lumley triangle into account, as discussed in Section 2.1.3, it follows that beside some points very closely to the grid, which are characterized by a pancake-shaped Reynolds-stress ellipsoid, all remaining states are found on the limit for cigar-shaped Reynolds-stress ellipsoids. It appears that both the growing values of anisotropy close to the grid as well as the return to isotropy are, on average, associated with a cigar shaped Reynolds-stress

ellipsoid, as the states of the return to isotropy completely cover those of the growing anisotropy. A similar result was also found by Djenidi and Tardu [42], however in their case the flow area with growing values of the invariants was more restricted to very close grid distances ($x/G_p \leq 3$), which is likely due to geometry differences in the turbulence generator, and corresponding changes in the mixing behaviour.

4.2 Wake mixing and turbulence production

The near-grid flow region is, due to the inhomogeneity and anisotropy of the produced turbulence, highly complex. An analysis of spatially averaged flow quantities will invariably mask the local phenomena responsible for the flow development. At the same time, localized analysis will only capture parts of the flow. This section provides a first qualitative insight into the near-grid flow phenomena of the grid-like turbulence generator used in this investigation, in order to investigate the origins of the complex development of the anisotropy of the spatially averaged flow.

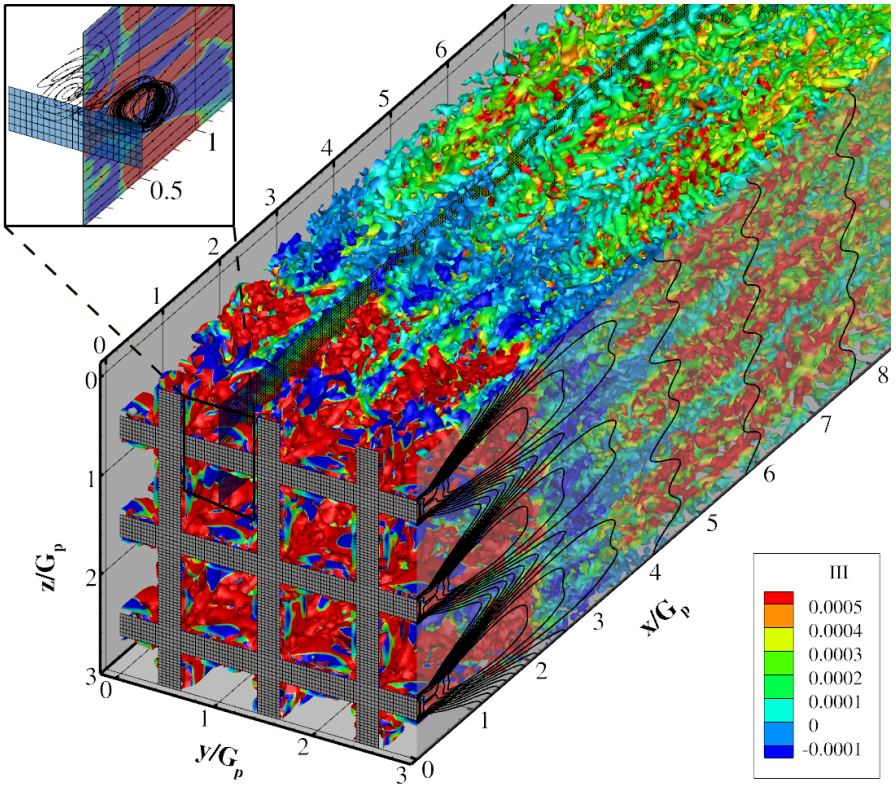

Figure 4.7: Turbulence development in the near-grid vicinity. Q-criterion isosurfaces coloured by III. Isolines of k given by black lines on plane with $y/G_p = 3$. Left upper detail: Streamlines of the time averaged flow, superimposed on grid bar and intersecting plane, coloured in III.

Figure 4.7 shows the development of the isosurface for a singular value of the Q-criterion for the entire volume of the simulation. The distribution of the anisotropy in the flow

is illustrated by using III as the variable for the colour on the isosurfaces of Q. III was chosen as it develops in a manner very similar to II, as shown in Figure 4.5 (a) and is additionally more indicative of the shape of the aRST, as it can take positive and negative values. In order to provide additional context, the values of the turbulent kinetic energy k were computed and are shown as isolines on the plane with $y/M = 3$. A detail in the upper left shows the streamlines of the time averaged flow superimposed to the instantaneous quantities in the immediate vicinity of a grid bar.

As shown by Figure 4.7, although the individual wakes of the grid bars become indistinguishable from each other within a very short distance, the values of the invariants display significant inhomogeneities for a much longer distance from the grid. The immediate vicinity of the grid, $x/G_p < 1$, is dominated by large flow features, as shown by the Q-criterion isosurfaces. The mean streamlines in the upper detail show that they are caused by recirculation zones. By $x/G_p > 1$, however, the mean streamlines are essentially parallel. This region of the flow is dominated by very large values of III, indicating highly anisotropic turbulence, which is expected considering the large mean flow gradients.

Close examination of Figure 4.7 shows that the majority of the turbulence production appears to be associated with the detachment of large eddies from the grid bar wake at distances $x/G_p < 2$, rather than by the interaction of the wakes, as shown by the isocontours of k. In order to investigate the turbulence production in more detail, the "offset" plane, as defined in Figure 4.1, is investigated using both instantaneous and time-averaged quantities in Figure 4.8. Illustrated are the vorticity component ω_z in the upper half and the aRST invariant III as a measure of anisotropy in its lower half, with the isolines of k superimposed. Black bars indicate the position of the grid bars.

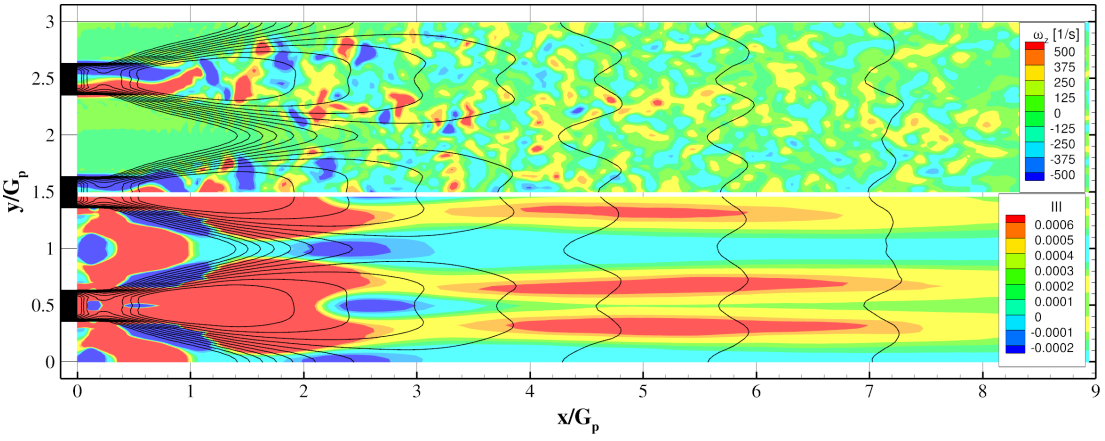

Figure 4.8: Turbulence development in the near-grid vicinity. Upper half: Vorticity component ω_z, lower half: aRST invariant III. Superimposed isolines of k.

Considering the maxima in the distribution of the vorticity component ω_z in Figure 4.8, it is apparent that the wakes directly behind the grid bars do not fluctuate, before oscillation and shedding sets in further downstream. It is noted that the near field wake

is highly dependent on the upstream conditions, and the present conditions of constant velocity at the inlet grid patches and zero velocity at the bar patches cannot be considered to be representative of any experimental conditions. However, qualitatively the appearance of the wake can still be likened to wakes behind rectangular cylinders at low Reynolds numbers [212]. While the flow Reynolds number of this simulation would lead to a significantly differing mode for the eddy shedding of an isolated rectangular cylinder, Lavoie [59] found in experimental investigations that the three dimensionality of a grid appears to have a strong effect on the vortex shedding mechanism of square bars, potentially leading to reattachment of the flow to the side faces of the cylinder and thus leading to a initially more steady wake.

An additional factor leading to the observed low Reynolds number-like behavior are the effects of grid resolution, which may lead to an excessive damping of the larger scales by the dissipation and dispersion errors if the resolution is too low. Additionally, a too dissipative subgrid-scale model may lead to a reduction of the effective Reynolds number in LES simulations, as shown by Bogey and Bailly [213], who advise against using eddy-viscosity based models for the study of flow phenomena where the Reynolds number is a major factor, which is not the case for the investigation of the anisotropy in grid turbulence [26; 214; 215]. Since the exact replication of the mechanisms responsible for the turbulence generation is not the main object of the inlet-grid turbulence creation method, and a strongly periodic component is still present, the findings of this work are still considered relevant to other turbulence generators which exhibit the production of periodic eddies.

As the isolines of k in Figure 4.8 show now conclusively, the points of largest turbulent kinetic energy in the flow, at $x/G_p = 1$ and $y/G_p = 0.5$, 1.5 and 2.5, are associated with the point of shedding, i.e. where eddies detach from the fluctuating recirculation zones. More downstream, k is continuously decreasing, indicating that production has ceased to be a large factor. This finding compares well with the DNS results of Ertunc *et al.* [56], who found peak production at positions of less than $x/G_p = 2$.

As the wake spreads, indicated by the scattering of the zones of high ω_z and the decreasing levels of k past $x/G_p = 2$, anisotropy as measured by III is reduced, i.e. the RST attains a more isotropic shape. Interestingly, this is true across the entire grid period, even in regions where wake mixing begins to take place. This is in apparent contradiction to the common assumption that the vortex stretching taking place during the interaction of the wakes is the primary cause for the anisotropy [59]. From $x/G_p = 3$ onwards, however, the values of III increase, i.e. one or two components of the RST become dominant. At this point, the wake interaction process appears to have overcome the processes responsible for the equalization of the Reynolds-stresses. A more detailed investigation of these processes is conducted in Section 4.3.

In order to support this statement, the mean flow gradients were computed, and the components of the mean rate of strain tensor $\overline{\overline{S_{ij}}}$ were derived, averaged over planes

normal to the axial direction, in a manner similar to the computation of the invariants of the turbulent stress tensor. In addition, the production $|\overline{\overline{\mathcal{P}}}|$ was estimated by computing their upper bound $|\overline{\overline{\mathcal{P}}}| \leq 2k\overline{\overline{S_\lambda}}$ [16], with $\overline{\overline{S_\lambda}}$ being the largest eigenvalue of $\overline{\overline{S_{ij}}}$.

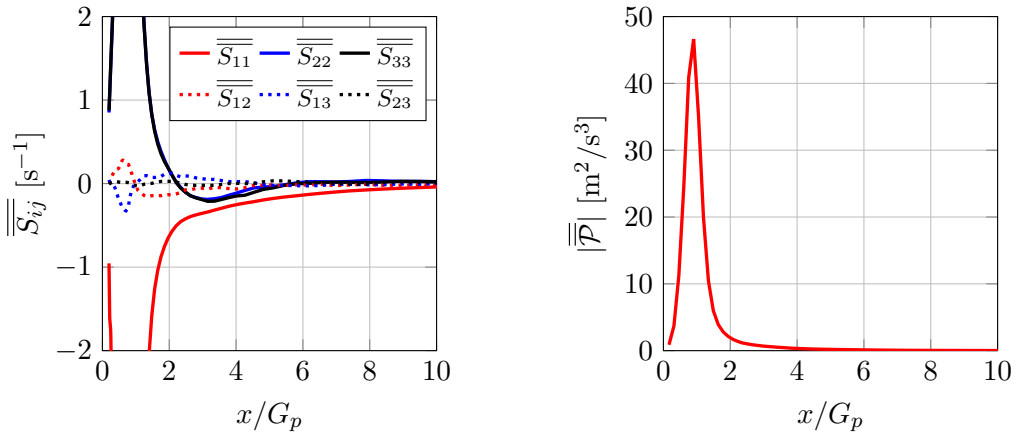

(a) Development of mean gradients.

(b) Development of production.

Figure 4.9: Transverse averages of mean rate of strain tensor components and their effect on production.

From Figure 4.9 (a) it is apparent that the components of the mean rate of strain tensor $\overline{\overline{S_{ij}}}$ attain a maximum upstream of $x/G_p = 2$, and are essentially zero for $x/G_p > 4$, confirming the qualitative analysis of Figure 4.7. The remaining strain $\overline{\overline{S_{11}}}$ can be associated with the wake mixing processes, but as Figure 4.9 (b) shows, production has ceased past $x/G_p = 4$. These results are in qualitative agreement with the findings of Ertunc *et al.* [56], whose DNS simulations of grid turbulence showed peak production being reached within two grid periods of the mesh, followed by a rapid reduction of turbulence production.

While the analysis of flow anisotropy by means of the invariant analysis delivers valuable insight, it cannot strictly be used to make statements about the shape of the eddies, as Simonsen and Krogstadt point out [216]. A method more suitable for this purpose is the ratio of the longitudinal integral length scales of the axial and transverse components, which should be $2I_{22}/I_{11} = 1$ for isotropic turbulence [16]. It is noted here that while the ratio of the longitudinal integral length scale of the axial component to the transverse integral length scale of the corresponding transverse component is 1 for isotropic turbulence, the ratio of the longitudinal integral length scales is investigated here as it is easier accessible since it allows the invocation of Taylor's hypothesis.

The distribution of the temporal integral length scale I_{11}, as well as of $2I_{22}/I_{11}$ is shown in Figures 4.10 (a) and (b), respectively, on the "offset" plane illustrated in Figure 3.1 (a). When conducting analysis of this quantity, two important caveats need to be respected: Firstly, in the immediate grid vicinity, periodic eddy shedding will cause the autocorrelation to develop a large negative loop, which will lead to the integral length scale losing its usual meaning as spatial extent of largest correlation [61]. This

is related to the formulation of the autocorrelation, which will return a sinusoid when the input signal is a sinusoid, and then becomes representative of very long correlation scales, which in turn leads to a very slow convergence of the autocorrelation integral or prohibits the convergence altogether. Secondly, as the parameter study of Blackmore *et al.* [13], which also investigated whether the inlet grid method allows for realistic development of the largest eddies, was restricted up to $x/G_p = 20$, constriction of the growth of the integral length scales at very large distances to the grid $x/G_p > 40$ cannot be completely ruled out. Therefore, analysis of the integral length scales is restricted to $1.5 < x/G_p < 20$.

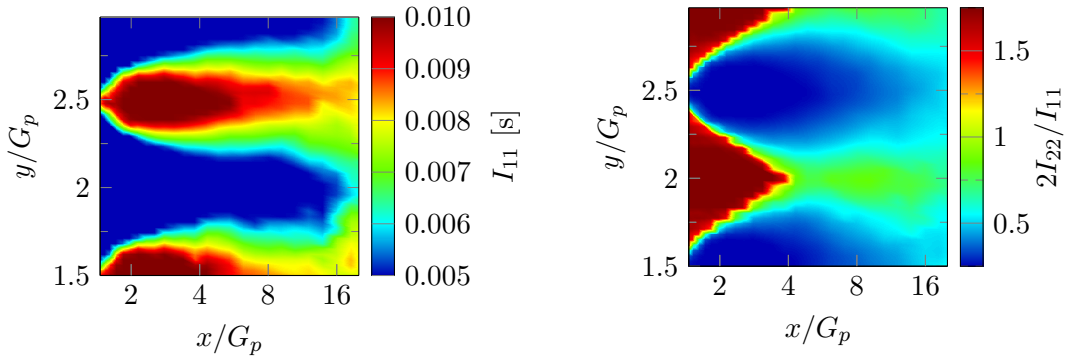

(a) I_{11}. (b) $2I_{22}/I_{11}$.

Figure 4.10: Distribution of values of the integral length scale, and large-scale anisotropy.

As Figure 4.10 (a) shows, large inhomogeneities of I_{11} persist for an extended time in the flow. Interestingly, the integral length scale does not show monotonically increasing behaviour throughout the flow. In particular downstream the grid bars at $y/G_p = 1.5$, 2.5, i.e. in the oscillating wake region, I_{11} appears to decrease between $4 < x/G_p \leq 20$. A potential explanation for this observation is that the wake mixing process decreases correlation due to large-scale eddies downstream of the grid bars as smaller scale eddies from neighbouring bars are convected into them with the spreading wakes. Conversely, axial correlation lengths along the jet centre lines, i.e. $y/G_p = 2$, 3 remain small until wake mixing is largely completed, and typical increase of correlation due to the decay of turbulence sets in. The experimental investigation of integral length scales in the wakes of regular and fractal grids by Valente and Vassilicos [61] found similar results, however these results showcase the spatial distribution of the integral length scale more clearly. It is found that the integral length scale retains the inhomogeneity caused by the upstream geometry for a considerable distance to the grid. The mixing process appears to not complete entirely within the examined domain, and larger simulations may be necessary to establish whether homogeneity is eventually established. However, considering the relationship [16]:

$$L_{ii} = \frac{\pi E_{ii}(\kappa_i = 0)}{2u_{ii}}, \tag{4.1}$$

and the finding of Ertunc *et al.* [56] relating to the persistence of inhomogeneity of the turbulent stresses, it may be hypothesized that the inhomogeneity of the integral length scale is caused by the same root cause which lead to the inhomogeneity of the turbulent stresses, i.e. the lack of dissipation and viscous diffusion processes as a means for homogenization [56]. As the turbulent stresses retain a certain level of inhomogeneity due to lack of homogenizing processes, and the energy spectra at the largest scales κ_i will be effected by the boundary conditions, a long term inhomogeneity of the integral length scales may remain in the flow even for very large domains.
Comparing the conclusions drawn from the isotropy parameter $2I_{22}/I_{11}$ and the invariants of the aRST, it appears that for the majority of this type of flow, the latter are a good proxy for the relative extent of correlation of the flow the spatial directions. However, in the region $x/G_p < 4$, conflicting results are obtained. Regions in the early wake development, where the shape of the aRST indicates an almost isotropic state, are shown in Figure 4.10 to exhibit a strongly axisymmetric state with $2I_{22} < I_{11}$. As it is, as discussed above, not entirely clear where the integral length scale becomes a reliable indicator of the extent of correlation in the flow, and furthermore the assessment using integral lengthscales does not allow to exclude potential effects of grid resolution or the numerical transition to turbulence, a more detailed investigation is conducted in Section 4.3.

4.3 Local anisotropy development

As discussed in Section 4.2, the shape of the aRST as well as the ratio of integral length scales have both shortcomings in terms of providing a physical explanation for the observed anisotropy. Therefore, further analysis is now conducted by computing the 1D energy spectra at 4 points along the two lines defined in Figure 4.1: One centred behind a vertical bar, and one centred in the middle of a jet. The four positions were chosen to coincide with the following points: $x/G_p = 1.46$ is equal to a distance representative of the highly turbulent region directly behind the grid. $x/G_p = 3.44$ is equal to the distance of highest turbulent kinetic energy along the line coinciding with the centre of the jet. $x/G_p = 7.07$ is equal to the distance of highest anisotropy according to the peaks of $\overline{\overline{II}}$ and $\overline{\overline{III}}$ in Figures 4.5 (a) and (b), while $x/G_p = 24.76$ represents a point sufficiently removed from the grid so that transverse gradients of k are small.

4.3.1 Energy spectra and local shapes of the anisotropic Reynolds-stress tensor

Figures 4.11 (a) - (d) shows the energy spectra E_{11}, E_{22} and E_{33} at the four positions $x/G_p = 1.46$, 3.44, 7.07 and 24.76 along the line downstream the grid bar, and within a jet centre, shown in Figure 4.1. The algorithm according to Welch, was chosen to

compute the auto spectral densities. In order to reduce noise, the signal was divided into 32 windows, using the windowing according to Hanning. The mesh cut-off frequency f_{cv}, beyond which dissipative and dispersive error of the grid resolution affect the numerical solution to an increasing degree, is indicated by the vertical dash-dotted line. For the present case, using a criterion of 25 points per wavelength as established in Appendix B, the cut-off frequency for vortical waves is determined to be $f_{cv} = 128$ Hz.

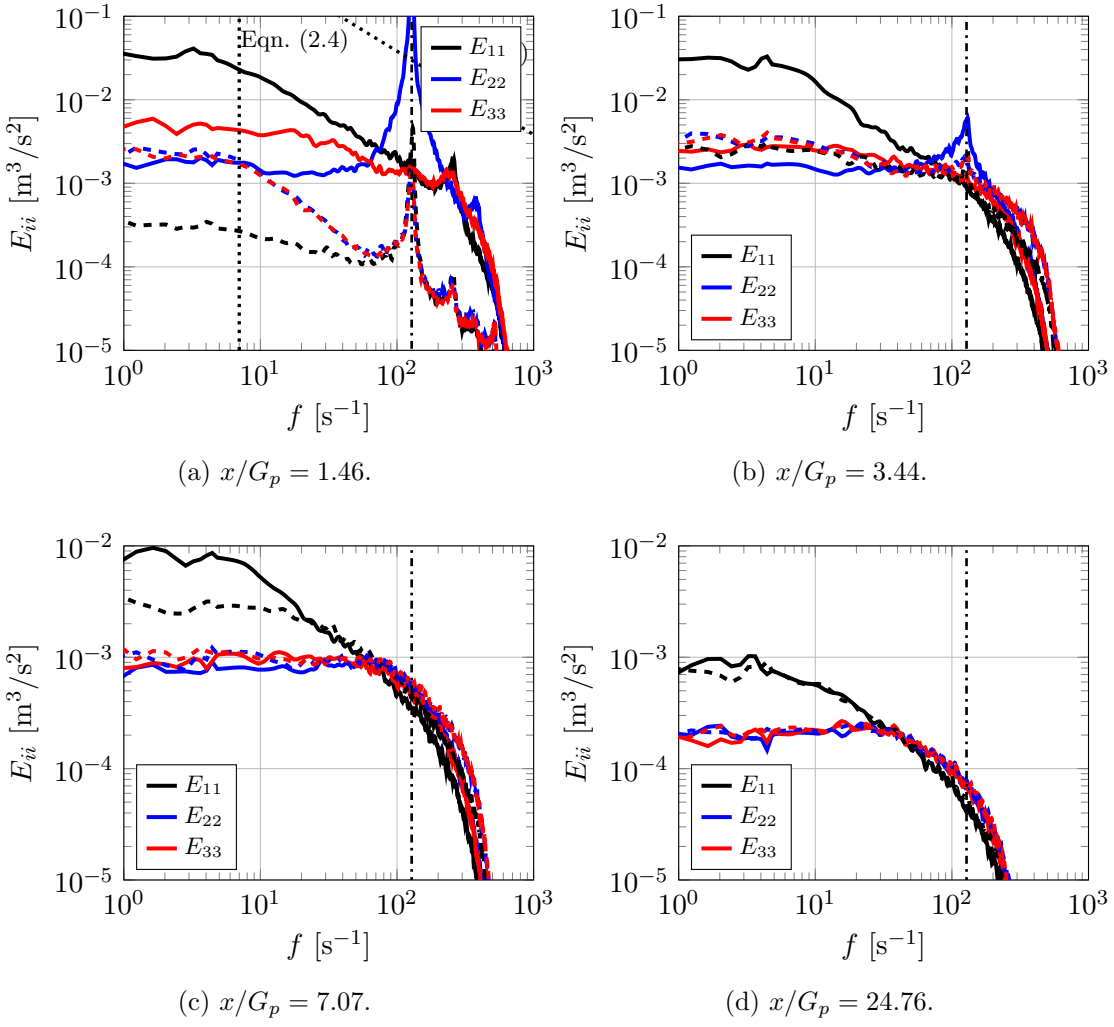

(a) $x/G_p = 1.46$. (b) $x/G_p = 3.44$.

(c) $x/G_p = 7.07$. (d) $x/G_p = 24.76$.

Figure 4.11: Comparison of energy spectra behind grid bar (solid lines) and in jet centre (dashed lines). Mesh cut-off frequency f_{cv} indicated by vertical dash-dotted black line.

The analysis of the energy spectra at the point $x/G_p = 1.46$ is in terms of assuming the equivalency of temporal and spatial scales according to Taylor [44] the most problematic. In order to assess the applicability of the frozen turbulence assumption, the criteria given by Lumley [20] were computed, with particular attention to the criterion of Lin [21], which provides a lower bound for the applicability of Taylor's hypothesis. The criteria were computed following the procedure given by Lumley [20], i.e. by replacing a set of $\ll$ with a factor of three on the larger side, and evaluating the equation using an equality sign. Eqn. (2.6) is shown in Figure 4.11 (a) by the dashed line. Evaluation of

Eqn. (2.6) yields a lower limit of $\kappa = 7.3$ m^{-1}, which is shown by a dashed vertical line. Since the turbulence intensity at the points $x/G_p > 1.46$ is greatly reduced, it can be safely assumed that conditions Eqn. (2.5) and Eqn. (2.6) are satisfied for all positions further downstream, thus, the corresponding lines are omitted. Analysis is conducted for the parts of the spectra only which are within the valid zone, i.e. below Eqn. (2.5) and above Eqn. (2.6). In this area, it is possible to relate the spatial structure of the turbulence to the temporal structure with an uncertainty of less than 30% [20].

As shown in Figure 4.11 (a), for all components, the spectra of the jet flow are significantly below the spectra obtained behind the grid bar, with the exception of the frequency associated with the oscillation of the wake, $f_w = 130$ Hz, shown in Figure 4.8, which initiate the numerical transition to turbulence. It is concluded that at the position $x/G_p > 1.46$, the point in the jet centre line is primarily influenced by the potential core of the jet. However, the presence of a pronounced peak at f_w indicates that the periodic fluctuations of the wake have an effect already at a position where no significant wake mixing has taken place.

Interestingly, E_{22} and E_{33} tend to the same value at low frequencies for both the jet centre and the grid bar positions. This is related to the periodicity of the grid, which will, at the large scales, introduce a limit to the correlation in the transverse directions, and thus to the size and energy of the eddies. Conversely, streamwise correlation of the axial component is affected only by the streamwise inhomogeneity, i.e. the spreading of the grid bar wakes and the related mean flow gradients. Thus, much larger scales and energies may be exhibited by the turbulent fluctuations in the axial direction.

With $f_w = 130$ Hz and a grid bar width of $d = 0.011$, a Strouhal number of 0.24 is obtained, which is considerably higher than the value of 0.17 measured by Lavoie *et al.* [59] for their rectangular bar grid. Considering the findings of Mukhopadhyay and Sundarajan [217] regarding the effects of flow constrainment on the Strouhal numbers of rectangular cylinders, this may be related to the artificial uniform flow imposed by the inlet boundary condition, which acts as if the flow as constrained upstream. Thus, a larger Strouhal number may be obtained.

As shown in Figure 4.11 (b), the spectra downstream of the grid bar and the jet centre equalize rapidly at high frequencies. However, notable exception are the low frequencies of E_{11}, as well as remaining peaks at f_w. The strong reduction in the energy of the periodic eddies indicates that they mix out rapidly, and their kinetic energy is transferred to eddies of other length scales.

Towards the higher frequencies, a certain trend can be observed where the jet-centre spectra exceed those of the position downstream the grid bar. This is related to the prevalence of wake interaction events at this position, which would produce a surplus of small-scale eddies relative to the grid bar position.

By the point of maximum anisotropy, at $x/G_p = 7.07$, no peak attributable to periodic eddies can be detected any more, as shown by Figure 4.11 (c). Except for E_{11} at low frequencies, the spectra have, to a large degree, collapsed, indicating that the mixing

process is largely completed.

Finally, at the most downstream point investigated here, $x/G_p = 24.76$, shown in Figure 4.11 (d), the spectra of the grid bar and the jet centre positions essentially collapse over most of the frequency range except below $f < 3$ Hz, indicating homogeneity at all but the largest scales.

It is noted that the frequency associated with the oscillation of the grid bar wakes, f_w, coincides with the mesh cut-off frequency almost perfectly. While the criterion of 25 grid points is likely conservative in terms of the dissipative error for the central schemes used in the simulations of this Chapter, as discussed in Appendix B, the dispersive error is likely to contribute to the rapid decay of the energy contained in the main peak at f_w and in particular to its harmonics, which can be observed in Figure 4.11 (a) only. Since these peaks contain only a small percentage of the total turbulent kinetic energy, the effect of this error is considered negligible for the present investigation. Further mesh refinement studies are recommended to establish the influence of the dispersive error on the decay of the energy peak at f_w.

For the purpose of quantifying the anisotropy, the development of the shape of the aRST is shown in Figure 4.12. The trajectory of the Reynolds-stress tensor in the AIM along the centre jet line is shown dotted, while the trajectory along the line downstream the grid bar is shown dashed. The values of the invariants at the positions investigated in Figures 4.11 (a) - (d) are highlighted with triangles for the development behind the bar, whereas circles illustrate the states along the centre of the grid jet.

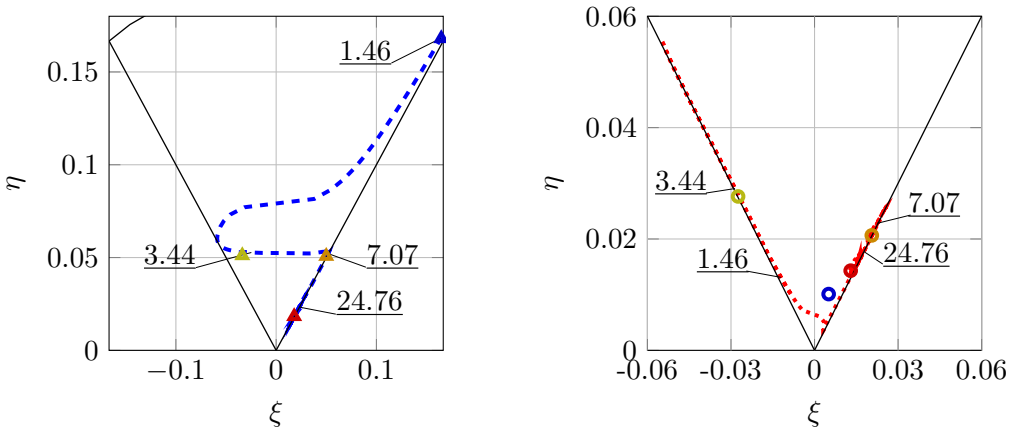

(a) Grid bar positions.

(b) Jet centre positions.

Figure 4.12: Shape of the aRST at the four positions $x/G_p = 1.46, 3.44, 7.07$ and 24.76. Triangles and dashed line indicate shapes downstream the grid bar, circles and dotted line indicate shapes within grid jet.

As Figure 4.12 (a) shows, an axisymmetric shape tending towards the one-dimensional limit is computed directly downstream the grid bar at $x/M = 1.46$. For the equivalent position in the jet centre, shown in Figure 4.12 (b), a shape on the pancake-shaped axisymmetric limit, albeit very close to isotropy is obtained. By relating this to the energy spectra shown in Figure 4.11 (a), it is found that the one-component shape behind

the grid bar is caused by the dominating energy content in E_{22} at f_w. The cause of the shape within the jet centre is found to be a slight surplus of energy contained in E_{22} and E_{33} relative to E_{11}, as the two former exhibit sufficient energy below $f < 80$Hz to surpass the contribution to E_{11} at f_w. It appears that this "isotropic" shape of the aRST in the jet centre is the consequence of a temporary equality of energies only, and consequently limited to a very short development length of the flow.

At $x/M = 3.44$, a state close to or on the axisymmetric limit for a pancake-shaped aRST is obtained for the position downstream the grid bar and the position within the jet centre in Figures 4.12 (a) and (b), respectively. As Figure 4.11 (b) shows, in case of the position downstream of the grid bar, this is caused by an approximate equality between the energy contained in the low frequencies of E_{11}, and the energy contained at f_w in E_{22}. In the case of the position within the jet, the spectra indicate a state closer to isotropy in general, however the transverse spectra display a higher energy content at low frequencies than their isotropic value of $E_{11}/2$. Thus, the temporary trend towards a pancake-shaped aRST is caused by the strong periodic content in the transverse spectra in case of the grid bar positions, and by the transverse periodicity of the grid in case of the jet centre positions.

Further downstream at $x/M = 7.07$, a state on the axisymmetric limit for cigar-shaped aRSTs is obtained for both positions, as shown by Figures 4.12 (a) and (b). Considering the corresponding spectra, shown in Figure 4.11 (c), this can clearly be related to the large energy content in the low frequencies of E_{11} both within the jet and behind the grid bar.

Finally, at $x/M = 24.76$, the shapes obtained for the aRST almost collapse if Figures 4.12 (a) and (b) were to be superimposed. This is expected, as the energy spectra at this position, presented in Figure 4.11 (d), collapse almost perfectly, with the exception of the very largest scales. As the Reynolds stresses are obtained by taking the integral of the respective energy spectra, such a collapse would lead to almost identical values of the aRST. Clearly, a well-developed flow is retained at these distances to the turbulence generator, and inhomogeneities become minimal.

It is concluded from this analysis that the local areas of apparent isotropic or pancake-shaped aRSTs exhibited by grid-like turbulence generators is primarily caused by a shift in the dominance of the aRST from one or two transverse components towards the axial components. It is found that while the axial energy spectra exhibit a large energy content in the low frequencies even quite close to the grid, the oscillating wake contributes sufficient energy to the transverse components in the mid to high frequencies to result in an apparently isotropic aRST. However, as these eddies are short-lived and mix out quickly, as shown by Figures 4.11 (a) - (c), the energy content of the axial component in the low frequencies eventually dominates and produces the state of cigar-shaped axisymmetric anisotropy well known in grid turbulence.

4.3.2 Scale-to-scale anisotropy in the energy carrying range

In order to support the qualitative analysis conducted in Section 4.3.1, the anisotropy is assessed by combining the spectral analysis with the invariant analysis. For this purpose, a spectral Reynolds-stress tensor is defined as:

$$u_{ij}(f_b) = \int_{f_l}^{f_u} E_{ij}(f)\,\mathrm{d}f. \tag{4.2}$$

with f_u, f_l being the upper and lower bounds of the frequency band with the central frequency f_b, respectively. To obtain the deviatoric anisotropic part of this spectral RST, an expression for the isotropic spectral RST has to be defined, since the respective contribution of the spectral normal stresses to the kinetic energy contained in one frequency band is a function of the frequency. For this purpose, the isotropic model spectra of von Kármán is used for the normal stresses, while the shear stress spectra are zero, since the shear stresses of the isotropic RST are also zero [16]. A normalized turbulent kinetic energy is defined as:

$$k_{iso} = 0.5\left(\frac{u_{11}}{u_{11,vK}} + \frac{u_{22}}{u_{22,vK}} + \frac{u_{33}}{u_{33,vK}}\right), \tag{4.3}$$

with $u_{ii,vK}$ being the spectral normal stress components as obtained from the model of von Kármán. In order to obtain a traceless anisotropic spectral stress tensor, the components are computed as:

$$b_{ij}(f_b) = \begin{cases} \frac{u_{ij}(f_b)}{u_{ij,vK}(f_b)2k_{iso}(f_b)} - 1/3 & \text{if } i = j, \\ \frac{u_{ij}(f_b)}{2k(f_b)} & \text{if } i \neq j. \end{cases} \tag{4.4}$$

with $u_{ij,vK}(f_b)$ being the isotropic spectral tensor based on the model spectra of von Kármán, and $k(f_b)$ and $k_{vK}(f_b)$ are the kinetic energies as a function of frequency for the spectral aRST and the isotropic spectral tensor, respectively. Normalization is conducted separately for the measured and the model spectral RST in order to reduce the impact of the model spectra to an information on the stress ratios only.

An important caveat of this method is that the model spectra of von Kármán relies on the axial integral length scale as an input. As such, it cannot be used for flows where a strong periodic content is present in the axial component, since the integral length scale then loses its typical meaning as a measure for the spatial correlation of the flow [61]. Consequently, points very close to the grid, such as the earlier investigated $x/G_p = 1.46$, are omitted from the following analysis, due to the dominating periodic content in the spectra of E_{11} in the jet centre positions.

Figures 4.13 (a) - (f) show the distribution of the invariants on the AIM for the three positions $x/G_p = 3.44$, $x/G_p = 7.07$ and $x/G_p = 24.76$. Spectral bandwidth was $f_u - f_l = 16$ Hz, yielding 13 distinct frequency bands up to the low-pass cut-off frequency of 200 Hz. While in (a), (c) and (e), the colours of the shapes indicate the central

frequency of a band, in (b), (d) and (f) the shapes are coloured by their energy content as a fraction of the total turbulent kinetic energy. Triangles indicate the shape of the spectral aRST exhibited by the turbulence downstream a grid bar, while circles indicate the shapes of the spectral aRST in the centre of a grid jet.

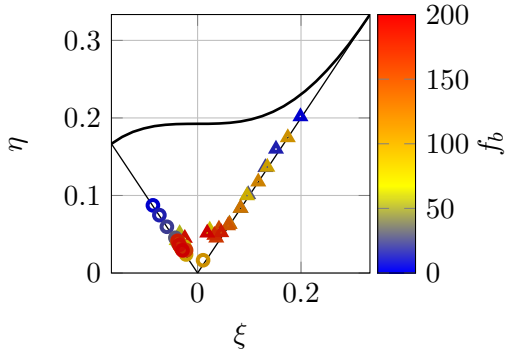

(a) Shapes per frequency at $x/G_p = 3.44$.

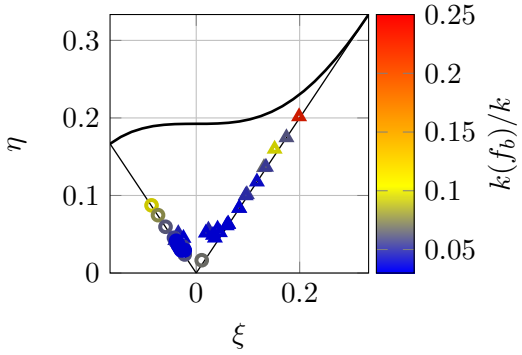

(b) Shapes per energy content at $x/G_p = 3.44$.

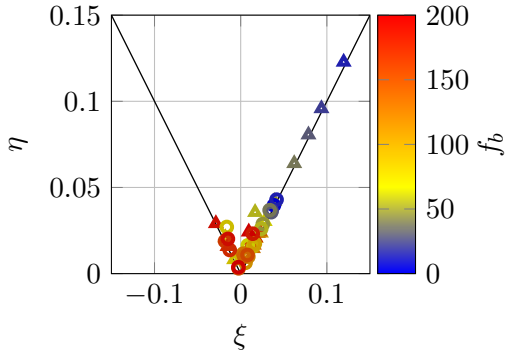

(c) Shapes per frequency at $x/G_p = 7.07$.

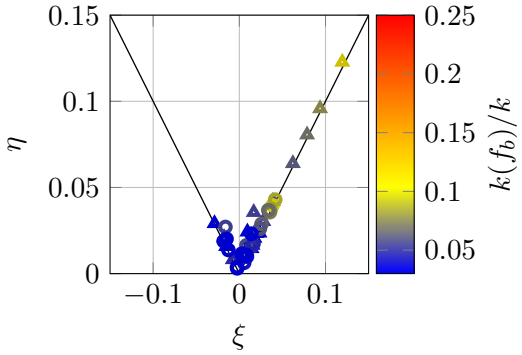

(d) Shapes per energy content at $x/G_p = 7.07$.

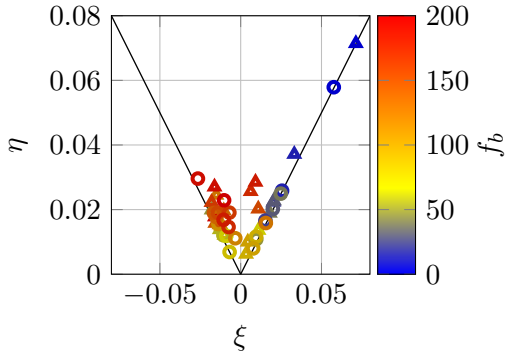

(e) Shapes per frequency at $x/G_p = 24.76$.

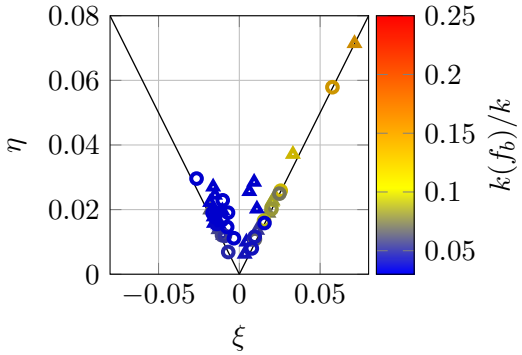

(f) Shapes per energy content at $x/G_p = 24.76$.

Figure 4.13: Spectral Reynolds-stress tensor shapes as a function of frequency band and energy content, shown for positions behind grid bar (triangles) and in jet centre (circles).

For the grid bar position at $x/G_p = 3.44$, shown by Figure 4.13 (a), a result is obtained which is, at first sight, at odds with the total shape of the aRST, shown in Figure 4.12. Rather than being on the pancake-shaped limit, the spectral aRST shapes are on the

cigar-shaped limit. However, as shown in Figure 4.11 (b), depending on f_b, either the axial or the transverse velocity component dominates in terms of energy component. Thus, a cigar shape is obtained for each frequency band, albeit one which is oriented in either the axial or the transverse direction. While the energy contained in the low frequencies $f < 50$, which is dominated by E_{11}, represents a large fraction of the total k, the dominance of E_{22} at frequencies $f > 80$ Hz results in the energies contained in E_{11} and E_{22} to be roughly equal, as shown by Figure 4.13 (b). Combined with the large anisotropy of eddies of these smaller scales, the resulting total aRST shape shown in Figure 4.12 is obtained.

The spectral shapes of the aRST in the grid jet are all on the pancake shaped limit, which fits the qualitative analysis conducted in Section 4.3.1. A strong trend towards isotropy and lower energy content with growing frequency is obtained, which is a well-known behaviour of turbulent flows.

As shown in Figure 4.13 (c), further downstream at $x/G_p = 7.07$, the anisotropy has decreased for all spectral shapes of the aRST. At this point, the lowest frequency bands dominate both in terms of their energy content and their anisotropy, resulting in the shape of the total aRST coinciding with the axisymmetric limit for a cigar shaped aRST. Finally at the largest downstream distance investigated here at $x/G_p = 24.76$, shown in Figures 4.13 (e) and (f), the spectral shapes are all quite close to the isotropic corner, with the spectral aRST downstream the grid bar and within the jet centre only deviating from the isotropic shape at the lowest frequencies. It is concluded that the flow has obtained a homogeneous state for much of the energy carrying range, with the return to isotropy well under way. Significant anisotropy and inhomogeneity is only present at the largest scales, which is in agreement with findings of Chasnov [218] and Ertunc *et al.* [56], respectively.

It is of note that the shape of the aRST at the lowest frequency bands returns for all investigated positions a state of the anisotropy with one component dominating, qualitatively equivalent to the conclusions which can be drawn from the ratio of the integral length scales, shown in Figure 4.10 (b). However, the ratio of integral length scales in isolation would not provide information on the transition of energy dominance occurring in flows with a strong transverse energy component at scales other than the integral length scale. It is concluded with the analysis of Figures 4.13 (a) - (f) that the invariants of the spectral aRST are a more comprehensive approach to investigate the anisotropy of the energy carrying scales than either the invariants of the total aRST, or the ratio of integral length scales.

4.4 Investigation of Reynolds number effects

While the investigation of the flow phenomena at low Reynolds numbers facilitates comparison between simulation and experiment, in many applications, the Reynolds number is substantially higher. In this section, the effect of increasing the Reynolds number on the flow behind the inlet-grid turbulence generator is investigated. This is in support of and supplementary to the findings of Blackmore *et al.* [13], who reported than an increase in Reynolds number led to a higher growth rate for the integral length scale, and a corresponding increase in the energy contained in the lower frequency velocity fluctuations. Additionally, they found that the turbulence intensity decay rate is independent of the Reynolds number.
The dependence on Reynolds number is investigated by comparing various flow quantities of the case at the lowest Reynolds number $Re_\lambda = 10$, which was investigated in detail in the previous Section, to the results for two cases at $Re_\lambda = 112$ and $Re_\lambda = 303$, respectively. All results were computed using a compressible LES, and the second order accurate central scheme as given by Eqn. (3.20) was used for the convective term.

4.4.1 Dependency of the anisotropy on the Reynolds number

The development of the transversally averaged turbulent stresses and the corresponding anisotropy parameter $\overline{\overline{\gamma_{12}}}$ for simulations with a Reynolds number of $Re_\lambda = 10$, 112 and 303 is shown in Figures 4.14 (a) and (b).

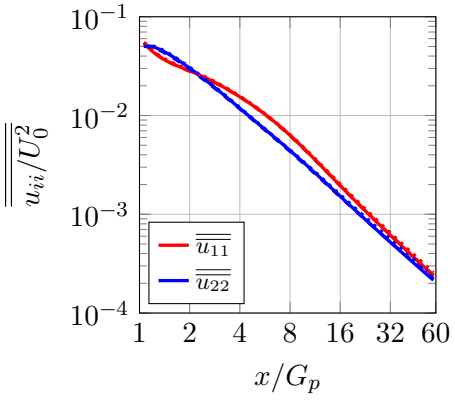

(a) Development of axial and transverse turbulent stresses. $Re_\lambda = 10$ (solid), $Re_\lambda = 112$ (dotted), $Re_\lambda = 303$ (dashed).

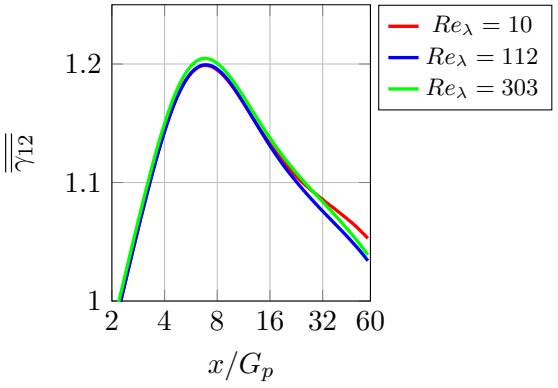

(b) Development of $\overline{\overline{\gamma_{12}}}$ in the streamwise direction for growing Reynolds number.

Figure 4.14: Development of turbulent stresses and anisotropy parameter $\overline{\overline{\gamma_{12}}}$ with Reynolds number.

As can be seen in Figure 4.14 (a), the normal Reynolds-stress components collapse almost completely. This collapse is reflected in the anisotropy parameter γ_{12}, where no clear trend of the anisotropy with changing Reynolds number is detected. Considering

Figures 4.4 (a) and (b), where it was observed that the anisotropy in the turbulence produced by the inlet-grid turbulence creation method is predominantly contained at wavenumbers much smaller than the mesh cut-off wavenumber, effects of the LES mesh refinement are considered to be negligible. As experiments have shown a trend towards lower anisotropy with higher Reynolds number [26; 215], it is hypothesized that the size of the numerical domain is insufficient to contain the largest eddies carrying the majority of the anisotropy, in particular at large distances to the grid. The potential influence of domain size will be further investigated in Section 4.4.2. Figures 4.15 (a) and (b) show the development of the transverse averaged invariants $\overline{\overline{II}}$ and $\overline{\overline{III}}$ with increasing Reynolds number.

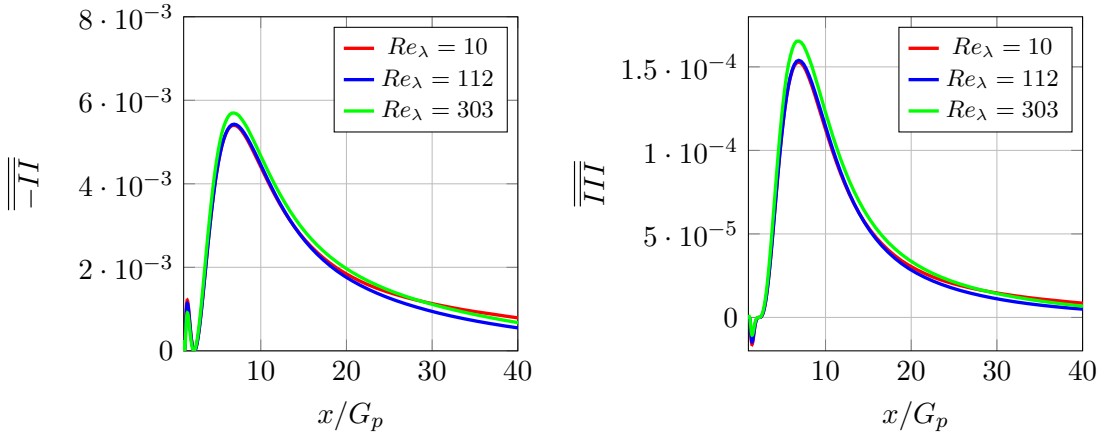

(a) Second invariant.

(b) Third invariant.

Figure 4.15: Development of the invariants of the aRST as a function of the Reynolds number.

Besides a very minor effect on the maximum anisotropy, the development of the Reynolds-stress invariants is almost identical for all investigated Reynolds numbers. By $x/G_p > 15$, the differences between the values of the invariants are negligible. Due to the qualitatively very similar development of the transversally averaged Reynolds-stress invariants, it is concluded that the mechanisms leading to the complex return to isotropy of the low Reynolds number case are similarly prevalent at higher Reynolds numbers. Therefore, a discussion of the development of the aRST close to the grid is omitted.

In order to obtain a better insight into the distribution of anisotropy over the energy carrying scales at large distances to the grid, the spectral aRST, defined by Eqn. (4.4), is computed for the three Reynolds number cases at $x/G_p = 30$, which is sufficiently distant from the grid to allow transverse averaging. Figures 4.16 (a) and (b) show the invariants of the spectral aRST computed for bands of wavenumbers, with the central wavenumber κ_b. The cut-off wavenumber κ_c is indicated by the black vertical dash-dotted line.

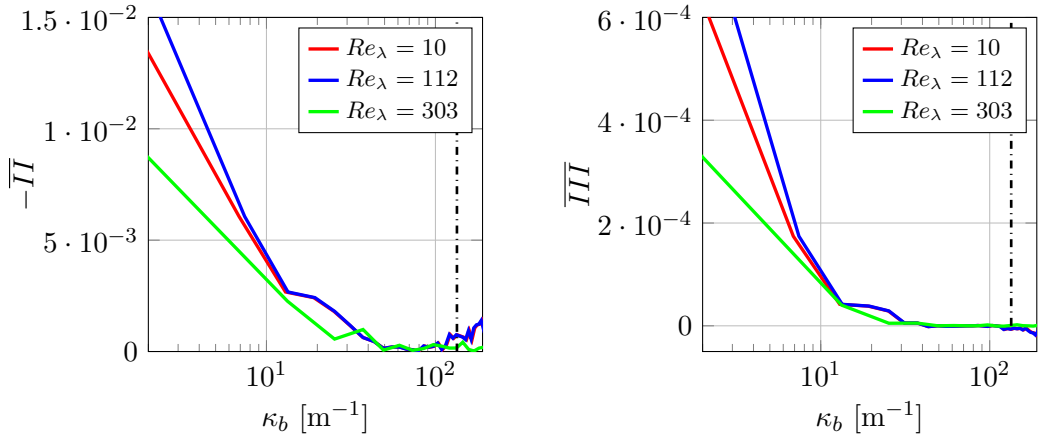

(a) Second invariant of the spectral aRST. (b) Second invariant of the spectral aRST.

Figure 4.16: Transversally averaged invariants of the spectral aRST as a function of Reynolds number at $x/G_p = 30$. Vertical dash dotted line indicates mesh cut-off wavenumber.

It is immediately apparent that the anisotropy of the very lowest wavenumber bands is decreased as the Reynolds number increases. However, the invariants of the wavenumber bands converge rapidly with increasing wavenumber, with only minimal differences beyond $\kappa_b = 10$ m^{-1}. Thus, the increased isotropy is restricted to the largest scales only and has only a limited impact on the overall anisotropy of the flow. Furthermore, it is noted that the vast majority of the anisotropy as quantified by the spectral invariants is contained in motions of scales significantly larger than κ_c.
The present results are in agreement with the experimental investigations of Comte-Bellot and Corrsin [26], Schedvin, Stegen and Gibson [214], as well as Kurian and Fransson [215], who reported a trend of increasing isotropy in the flow as the Reynolds number is increased. However, in all of the experimental studies, the trend was found to be small, which is consistent with the present results.

4.4.2 The turbulent decay in a restricted domain

Due to the presence of both anisotropic and inhomogeneous as well as isotropic and homogeneous turbulence in the presented turbulence development case, it is possible to investigate when and where isotropic relations often used when analysing turbulent flow hold, and how they are influenced by Reynolds number. A quantity which is often difficult to compute is the dissipation, and the related Taylor length scale λ [61; 214]. Assuming homogeneity and isotropy, the dissipation ε can be computed for decaying grid turbulence, i.e. with no production, as [16]:

$$\frac{\mathrm{d}k}{\mathrm{d}t} = -\varepsilon, \tag{4.5}$$

which in turn is related with the Taylor length scale by,

$$\varepsilon = 15\nu\overline{u^2}/\lambda^2. \tag{4.6}$$

Since Eqn. (4.6) relies on both large- and small scale isotropy [50], it is not expected to obtain a good fit in regions where the anisotropy is high. It is thus necessary to validate whether the values for λ are correct. To this end, the methodology proposed by George [49] is used. He argued that the two-point statistics collapse when plotted in Taylor variables. This has been shown to be an appropriate scaling for data from many different investigations, such as the experiments of Comte-Bellot and Corrsin [219], Warhaft and Lumley [220], and most recently Antonia *et al.* [221], Kang *et al.* [181], as well as Seoud and Vassilicos [50]. It is therefore investigated whether this scaling holds true in this case as well, and if so at which point the flow obtains the so-called equilibrium similarity state.

An interesting observation was made by Seoud and Vassilicos [50], who pointed out that small-scale isotropy may be sufficient for $\varepsilon \approx C_0\nu\langle u\rangle/\lambda^2$, with the constant C_0 not necessarily equal to 15. As C_0 is unknown for the current flow, however, no correction for the anisotropy could be made, and the analysis is restricted to regions of the flow where the turbulence anisotropy is limited.

One of the most common scalings for the axial energy spectra is Kolmogorov's universal scaling. Figure 4.17 shows the energy spectra for the axial component for the three simulations at Reynolds numbers of $Re_\lambda = 10$, $Re_\lambda = 112$, $Re_\lambda = 303$, scaled with the Kolmogorov length η_K for a distance of $x/G_p = 40$ from the grid.

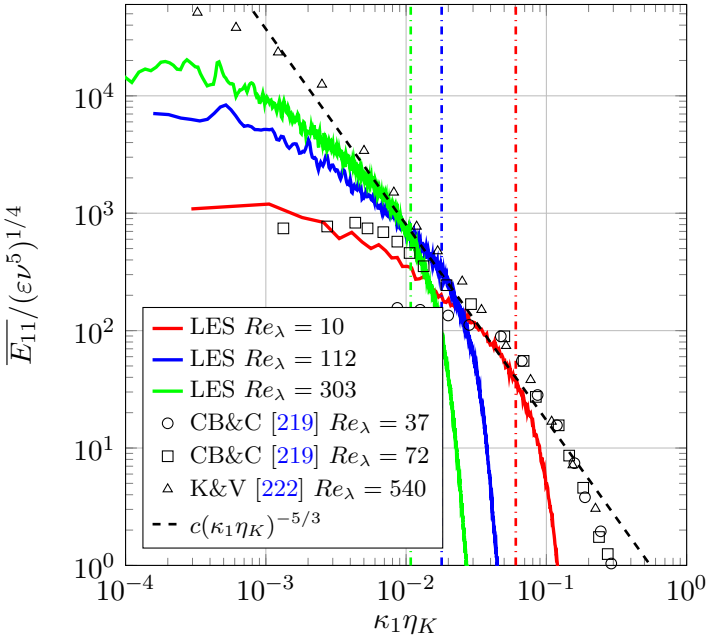

Figure 4.17: Axial energy spectra as a function of Reynolds number at $x/G_p = 40$ in Kolmogorov scaling. Vertical dash-dotted lines indicate $\kappa_c\eta_k$ for the various Reynolds numbers.

In order to provide some qualitative comparison to experiment, the values for the spectra at various values of Re_λ from experiments of Comte-Bellot and Corrsin [219] and Kistler and Vrebalovich [222] are included as well. A dashed line indicates the slope of the power law decay proportional to $\kappa^{-5/3}$, which is associated with the universal equilibrium range. Vertical dash-dotted lines indicate $\kappa_c\eta_k$ for the various Reynolds numbers, with colours corresponding to colour of the energy spectrum of the respective Reynolds number.
From Figure 4.17 it is apparent that the large differences are present between the energy spectra obtained for an experiment of one value of Re_λ, and the energy spectra from a LES with a comparable Re_λ. While the spectra from the LES at $Re_\lambda = 10$ should, in Kolmogorov scaling, be below the experimental spectra obtained by Comte-Bellot and Corrsin for at a $Re_\lambda = 37$, it exceeds the experimental values by up to one order of magnitude. This is caused by the significantly higher dissipation present in the current simulations. Following Eqn. (2.14), this leads to a decreasing Kolmogorov scale, which due to the relationship [16]:

$$\lambda = \sqrt{10}\eta_K^{2/3}L^{1/3}, \tag{4.7}$$

with $L = k^{3/2}/\varepsilon$ equivalent to a length scale representing the large scales, results in decreasing value of the Taylor length scale, and therefore too low a value for Re_λ.
Considering the context of the mesh cut-off wavenumbers κ_c as well as the $\kappa^{-5/3}$ decay law of the energy cascade, it is observed that the spectra at all simulated Reynolds numbers exhibit a slope equivalent to the $\kappa^{-5/3}$ decay law at wavenumbers $\kappa_1\eta_K \approx \kappa_c$. However, the spectra drop off quickly thereafter, indicating excessive dissipation errors. It is concluded that while the beginning of the universal equilibrium range is captured, as is best practice when conducting LES, for applications where the accurate representation of the universal equilibrium range is of larger importance than the present case, more accurate numerical schemes and higher grid resolutions are recommended.
According to George [223], an appropriate scale for the collapse of the energy spectra is the Taylor length scale λ. Since the accurate determination of λ according to either Eqn. (4.6) or Eqn. (4.7) requires the isotropy of the flow, collapse of the spectra is a good test of the isotropy of the flow. Figures 4.18 (a) and (b) show the axial energy spectra for the mid and the low Reynolds cases, respectively, for distances $x/G_p \geq 16$. The mesh cut-off wavenumber κ_c, indicated by the vertical dashed line, is scaled using the value of λ at $x/G_p = 14$, which represents the conservative case as λ increases with x/G_p.
With the exception of the lowest wavenumbers, it is found that the collapse of the spectra is acceptable for both Reynolds numbers at distances $x/G_p \geq 25$. The observation that the largest scales seem to reduce in energy content at large distances serve as further indication that the integral length scales are not sufficiently well resolved [223]. However, in the intermediate region $25 \leq x/G_p < 50$, George's [49] equilibrium similarity hypothesis is well satisfied, showing that this state is relatively quickly obtained by the flow, and that the computation of ε and λ using isotropic assumptions is possible.

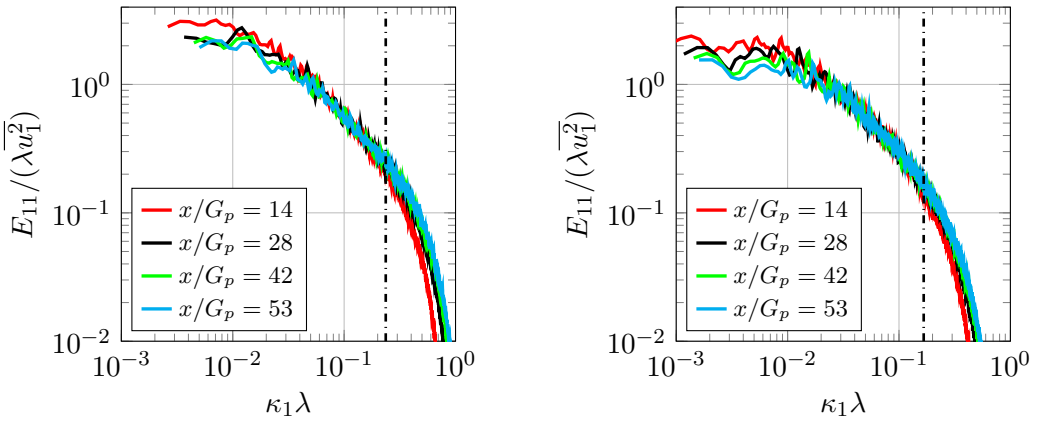

(a) $Re_\lambda = 112$. (b) $Re_\lambda = 303$.

Figure 4.18: One dimensional axial energy spectrum in Taylor coordinates. Dash dotted line indicates κ_c

As discussed in Section 2.2, the convergence of the turbulence decay towards a constant value of the decay exponent n is a common property of decaying turbulence. It is closely related to the condition that λ^2 is linearly dependent on time and inversely on n [224]. To investigate when this condition is met in the present simulations, λ^2 is plotted in Figure 4.19 (a) for the three Reynolds numbers simulated. From this, n is computed following the unambiguous method suggested by George *et al.* [225]:

$$\frac{1}{\nu}\frac{\mathrm{d}\lambda^2}{\mathrm{d}t} = -\frac{10}{n}. \tag{4.8}$$

Figure 4.19 (b) shows the resulting development of the decay coefficient. For reference, a range of ±5% around $n = -1.4$ is indicated by dotted lines. Since the high anisotropy in the close-grid distances invalidates the use of Eqn. (4.6) for the computation of the Taylor length scale, they are omitted.

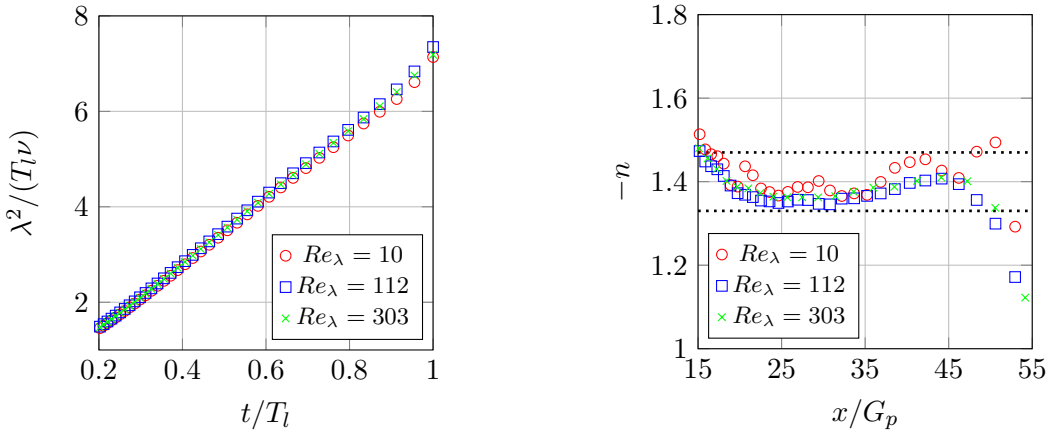

(a) λ as a function of Reynolds number. (b) n as a function of Reynolds number.

Figure 4.19: Development of Taylor length scale λ and the turbulence decay exponent n.

In Figure 4.19 (a), the throughflow time $T_l = l/U_0$, where l is the extent of the computational domain, is used to normalize the curves to facilitate comparison. In this scaling, the values of λ collapse for all Reynolds numbers. An approximate linear relationship is present in all cases, although some variation is present especially at large times.
The conclusions made about the development of λ directly translate to n, shown in Figure 4.19 (b). Although there is some scatter in the results, the values are within $\pm 5\%$ of $-n = 1.4$ between $15 < x/G_p < 45$. The agreement in terms of n between the different Reynolds number cases is considerable, in particular for $Re_\lambda = 10$ and $Re_\lambda = 112$, and qualitative trends are similar up to $x/G_p = 45$. These results are expected, considering the well-known dissipation anomaly, which is central to all turbulence theories, phenomenology and modelling [50]. The dissipation anomaly states that although the kinetic energy dissipation is caused by viscous forces, the kinetic energy dissipation rate has consistently been observed to remain constant with increasing Reynolds number [50], which is generally understood to represent the ratio of inertial to viscous forces. While the dissipation anomaly would be partially enforced in this simulation by the sub-grid model used, which acts as a Smagorinsky-like model for freely decaying turbulence [155], the resolved dissipation is under no such constraints, allowing the present case to be used for the investigation of the dissipation anomaly for the special case of flows where isotropy of the small scales is enforced, but large scale isotropy is not.
Qualitatively, in Figure 4.19 (b) an area of relatively constant values of n is observed between $20 < x/G_p \leq 35$, not unlike the one found in the experiments of Lavoie, Djenidi and Antonia [24], but larger in magnitude. Considering the choice of the sub-grid scale model, as well as the isotropic mesh of the presented cases, it is concluded that the variation in dissipation is a result of a change in the resolved dissipation ε_r alone. As such, it is hypothesized that the increased values of n at $x/G_p < 25$ are caused by the significant anisotropy present near the grid, which has been shown to impact dissipation significantly by Lavoie, Djenidi and Antonia [24]. The marked decrease of the decay coefficient $x/G_p > 45$ is argued to be due to the growing influence of the limited size of the numerical domain, since the spectrum progressively shifts to lower frequencies and larger scales, while the size of the domain remains constant. While, as discussed in Appendix B, the grid resolution as well as the numerical schemes with their associated dissipative and dispersive errors can be expected to have a considerable influence on the development of the turbulence, their influence is considered to be uniform across the whole domain, since a homogeneous mesh was used. As such, a rapid change in the qualitative development of n is considered not be related to the refinement of the domain. Conversely, a number of authors [24; 25; 49; 226; 227] have shown that the energy content at low wavenumbers has a significant influence on the value of n, and thus, it is concluded that the decay coefficients computed downstream of $x/G_p > 45$ do not represent freely decaying homogeneous and isotropic turbulence any more. This argument is supported by the plot of the non-dimensional rate of return to isotropy,

defined as:

$$\rho^* = \frac{k/(\,\mathrm{d}k/\,\mathrm{d}t)}{II/(\,\mathrm{d}II/\,\mathrm{d}t)}, \tag{4.9}$$

which is shown in Figure 4.20.

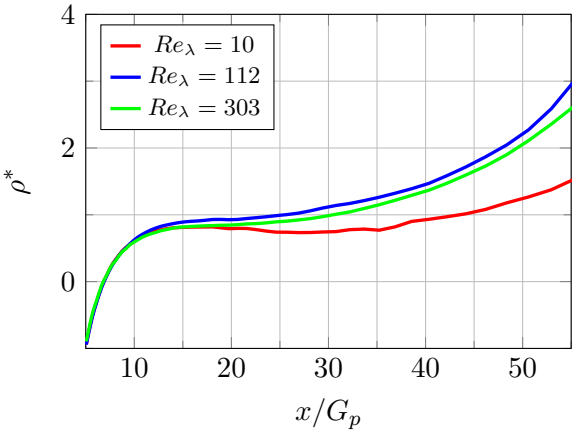

Figure 4.20: Dimensionless return to isotropy as a function of Reynolds number.

While prior investigations such as the DNS conducted by Zusi and Perot [43] has shown an asymptotic development of the ρ^*, the simulations show a clearly diverging behaviour, which is especially pronounced past $x/G_p > 35$. It is hypothesized that the largest scales in the axial direction, which would, in the case of a free-stream, continue to grow, are at this point restricted by the domain, while the transverse scales are still growing. Thus, the rate of return accelerates.

4.5 Summary

This Chapter has used the turbulence creation method proposed by Blackmore [13] to investigate the processes responsible for the creation of anisotropy encountered in typical flows behind a grid-like obstacle. This was accomplished by conducting LES at three different Reynolds numbers, assuming an incompressible flow, and by keeping the case setup constant. The case with the lowest Reynolds number, being comparable with Reynolds numbers often achieved in experiment, was used to demonstrate the applicability of the inlet-grid turbulence creation method for the reproduction of turbulent flows produced by grids. By doing so, it was aimed to establish that the turbulent flow in the interaction problems discussed in Chapters 5 and 6 is close to those typically used in experiments.

Additionally, in order to improve the understanding of the creation and development processes of the anisotropy, an investigation of the near-grid region was performed. For the purpose of quantifying the anisotropy of the energy carrying scales, the method of computing a spectral anisotropic Reynolds-stress tensor was introduced.

By comparing the spectra and invariants of the three cases, indications of the effect of

the Reynolds number on the energy carrying scales were obtained. Finally, the simulations allowed the investigation of the effect of domain restriction on the decay and return to isotropy of the turbulent flow. The main conclusions drawn from this Chapter are:

- The inlet-grid turbulence creation method, combined with the simulation method of LES, can produce turbulence which is in terms of the required parameters of energy spectra, Reynolds-stresses and invariants representative of that produced by many grid-like turbulence generators. The anisotropy common to grid turbulence [26] was found to be predominantly exhibited by the large scales, and as such is associated with wavenumbers significantly below the grid cut-off wavenumber established in Appendix B. Thus, dissipation and dispersion errors can be considered negligible for the scales of interest. Near-grid development of the energy carrying scales exhibit behaviours found in the literature. Therefore, the method can be used for the investigation of the anisotropy of the energy carrying scales, and for the production of turbulence for more complex turbulence interaction problems, such as discussed in Chapters 5 and 6.

- By relating the 1D-energy spectra for axial and transverse components to the states of the invariants in the AIM, it is qualitatively shown that the complex development of the anisotropy of the energy carrying scales close the grid is caused fundamentally by a change in dominance of energy from scales associated with the wake oscillation to scales of the order of the integral length scale. It is noted that in the present results, the wake oscillation frequency coincides with the mesh cut-off frequency, and the dispersive error of the employed numerical schemes may contribute to the rapid diffusion of the energy at this peak. Further mesh refinement studies are recommended to assess the influence of the dispersive error.

- The method of computing a spectral anisotropic Reynolds-stress tensor and its invariants can be used to quantitatively assess the anisotropy of the energy carrying scales to a high resolution and provides more information on the development of the flow than the often used ratio of the axial to transverse normal Reynolds-stress, or the ratio of the axial and transverse integral length scales.

- A comparison of the anisotropy obtained from two simulations conducted at higher Reynolds number to the low Reynolds number case was presented and showed that while a small trend towards reduced anisotropy with increased Reynolds number exists, the underlying flow phenomena are qualitatively very similar. Thus, the findings concerning the complex return to isotropy of the energy carrying scales are also applicable to flows at higher Reynolds number.

- An investigation of the energy spectra as well as the Taylor length scales and related decay coefficients has been presented. Indications have been found that

scalings commonly used for the description of turbulence are applicable to the flow, but that the simulation domain is too small to support the growth of the largest scales up to the outlet. Further investigation suggests that this has implications on both the return to isotropy as well as the rate of decay. However, further simulations at additional Reynolds numbers and with larger numerical domains are recommended to support these conclusions.

Thus, this Chapter has established the inlet-grid turbulence creation method as a valuable tool for the study of turbulent flows. A deeper insight into the complex development of the anisotropy close to the grid has been gained, allowing to relate the energy spectra to the invariants of the AIM. A novel methodology to quantify the anisotropy of the energy carrying scales has been presented.

Chapter 5

The interaction of infinite aerofoils with simulated grid turbulence

In previous chapters, the methodology chosen to investigate the interaction of turbulence with the leading edges of aerofoils has been presented. The link between the simpler turbulence development problem, used in Chapter 4 to study the generation and development of turbulence by the inlet-grid turbulence creation method, to more complex problems such as the case of turbulence interacting with an aerofoil, discussed in this Chapter, was established in Chapter 3.
For the purpose of demonstrating the capability of a LES solving the full, compressible Navier-Stokes equations on an unstructured mesh to be used for the investigation of turbulence interaction with the leading edge, and the associated noise production, the inlet-grid turbulence creation method is applied produce a turbulent flow in which an infinite aerofoil is immersed. The case of an infinite aerofoil interacting with turbulence is a well-known problem in the field of aeroacoustics, and a large database of experimental, numerical and analytical results exists. Thus, it is ideally suited for the evaluation of the capability of LES of reproducing the acoustic emissions of an aerofoil in a turbulent flow. The main aims of this chapter are:

- To demonstrate the application of the inlet-grid turbulence creation method to the benchmark problem of an unloaded, thick, infinite aerofoil, using a compressible LES on an unstructured mesh.
- To investigate the interaction of evolving turbulence with a leading edge, which is crucial to noise production.

- To evaluate the capability of this method to reproduce experimental values obtained in the well-documented measurement campaign of Paterson and Amiet [97] for validation purposes.
- To assess the fidelity of this method of predicting known effects such as the decrease of noise levels due to thickness, the non-compactness effects present at higher frequencies as well as the effects or lack thereof of applying an angle of attack to the aerofoil.
- To establish a baseline for the investigation of the finite aerofoil.

The Chapter is structured as follows. Section 5.1 provides a discussion of the effects of the unstructured meshing approach on the numerical results, supported by the analysis on the linear wave advection properties of the used numerical schemes conducted in Appendix B. In Section 5.2, comparison with the experimental data of Paterson and Amiet [97] for a comparable case is conducted to establish the current setup as being representative of the problem of an isolated aerofoil interacting with a turbulent flow. The development of the turbulence near the leading edge, as well as the aerofoil surface pressures, are discussed in Section 5.3. The noise emission predictions for the case of a thick, unloaded aerofoil computed with and without the assumption of compressibility, as well as for an aerofoil at a small angle of attack, are compared in Section 5.4. Finally, the findings of the Chapter are summarized in Section 5.5.

5.1 LES on unstructured meshes

The application of the LES method to unstructured meshes is problematic, as the underlying mesh generation algorithms of many grid generators make control of the mesh quality difficult. While this is by design, since the main strength of unstructured meshing is the reduction of mesh generation times and complexity, the very strict requirements of LES for meshes lead to unstructured meshes often being unsuitable. The main reason for this is that in the formulation of LES the integral and the derivative operators are commuted, and the terms depending on the filter size are neglected when the conservation equations are filtered. Thus, a non-uniform mesh introduces an error when used for LES. While it was found by van der Bos and Geurts [228] that the error becomes small if the change in the filter is slow and its skew is limited, LES are still vulnerable to mesh anomalies which lead to considerable numerical problems, such as un-physical oscillations of the flow quantities. This section introduces the domain setup for the turbulence interaction case of an infinite aerofoil, and discusses simulation results for the more problematic areas of the domain, i.e. leading and trailing edge of the aerofoil, as well as the associated derefinement zones.

5.1.1 Numerical setup of the turbulence interaction case

Since placing the inlet grid turbulence creator at distances commonly used distant from the aerofoil would lead to a prohibitive cell count, and even more problematic to a very small turbulence intensity, the alternative approach of the U-shaped domain shown in Figure 5.1 was adapted. The distance of the inlet to the aerofoil, equivalent to $16G_p$, was then chosen based on a prior parameter study, which returned the appropriate distance and inlet flow velocities in order to facilitate qualitative comparisons with the experimental results of Paterson and Amiet [97].

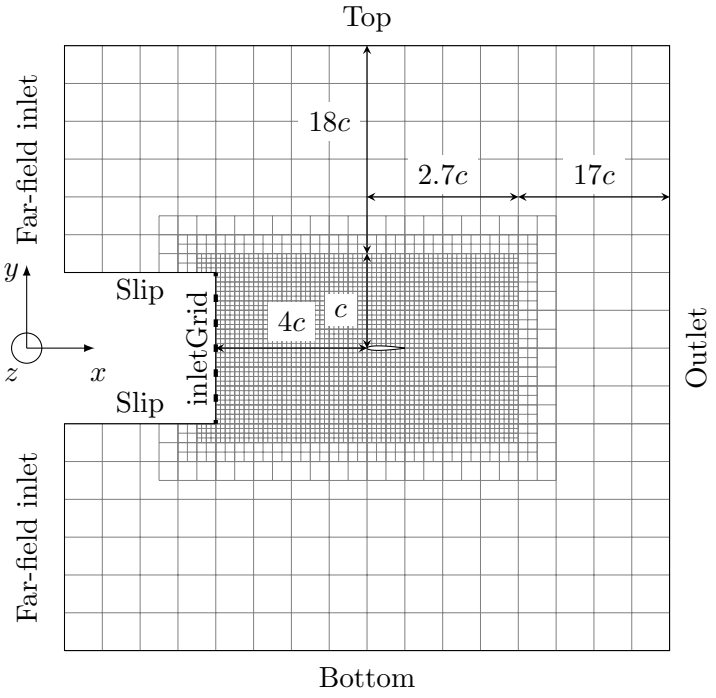

Figure 5.1: Domain setup of background case (without aerofoil) and interaction case (with aerofoil). Thick dashes illustrate position and approximate size of grid "bars". The origin of the coordinate system coincides with the aerofoil leading edge. The illustration is not to scale.

In order to minimize, if not eliminate, reflections of acoustics waves from the boundaries, two measures were taken. By significantly coarsening the mesh outside the turbulent domain, cell count could be minimized and outgoing and returning waves would dampened by numerical dissipation. Additionally, the non-reflective boundary condition *waveTransmissive*, provided in the OpenFOAM package, was set for the pressure. This boundary condition represents a simplified implementation of the non-reflective scheme based on eigenvalue analysis developed by Poinsot and Lele [229], and is discussed in more detail in Appendix C.2. Table 5.1 summarizes the boundary conditions chosen.

Patch	Variable	Type	Definition
Wall	U	Dirichlet	$\mathbf{U} = (0, 0, 0)$
	p	Neumann	$\mathrm{d}p/\,\mathrm{d}x = 0$
Inlet	U	Dirichlet	$U_1 = \dot{m}/(A_p\rho_0), U_2 = U_3 = 0$
	p	Neumann	$\mathrm{d}p/\,\mathrm{d}x = 0$
Far-field inlet	U	Dirichlet	$U_1 = \dot{m}/(A_p\rho_0), U_2 = U_3 = 0$
	p	Neumann	$\mathrm{d}p/\,\mathrm{d}x = 0$
Slip-wall	U	Dirichlet	$\mathbf{U} = (U_1, U_2, 0)$
	p	Neumann	$\mathrm{d}p/\,\mathrm{d}x = 0$
Outlet	U	Mixed	Eqn. (3.17)
	p	Mixed	$\mathrm{D}p/\mathrm{D}t \approx 0$, See Appendix C.2, [229]
Top, Bottom	U	Neumann	$\mathrm{d}U/\,\mathrm{d}x = 0$
	p	Mixed	$\mathrm{D}p/\mathrm{D}t \approx 0$, See Appendix C.2, [229]
Front, back	U, p	Periodic	1:1 field mapping to opposite boundary

Table 5.1: Boundary conditions for the simulation of the turbulence interaction with an infinite aerofoil.

Grid resolution in the turbulent domain is the same as in the simple turbulence development case. This grid resolution was maintained up to a distance of $3c$ downstream of the aerofoil. The extent of the finely resolved volume in the y direction is one chord length relative to each side of the aerofoil, which corresponds to the height of the grid inlet with an additional small buffer to accommodate a likely turbulent shear layer. In the remaining domain, the cell sizes were chosen to be much larger with $\Delta_c = G_p = 0.06$ m. Grid transition between this coarse domain and the finely resolved region of the turbulent flow behind the grid was handled by 4 refinement steps of 10 cell layers each. Except for the grid inlet, the other far-field boundaries are set at $20c$ from the prospective aerofoil position on all sides. The aerofoil span was set to $3G_p$. The total cell count for this case was 22.3×10^6, consisting of 97% hexahedral cells, and 1.4% prisms, 0.6% pyramids and 0.03% tetrahedral cells. A more detailed description of the mesh generation procedure and chosen refinement parameters is given in Appendix C.1.

The solver *rhoPimpleFoam*, implemented in OpenFOAM v3.0, was used, which conducts pressure-velocity coupling using the merged PISO [201] and SIMPLE [202] algorithms.

5.1.2 Analysis of leading edge and trailing edge flow

Figures 5.2 (a) - (d) illustrate the distribution of the CFL number, as well as of the DES switch parameter, which controls the use of the RANS or LES model, at leading and trailing edge of the aerofoil.

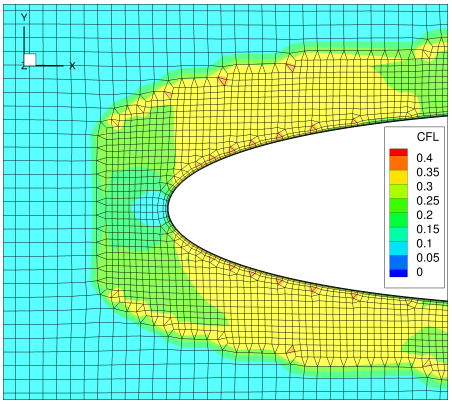

(a) CFL at leading edge.

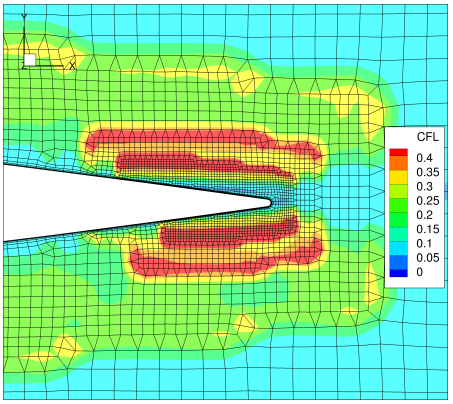

(b) CFL at trailing edge.

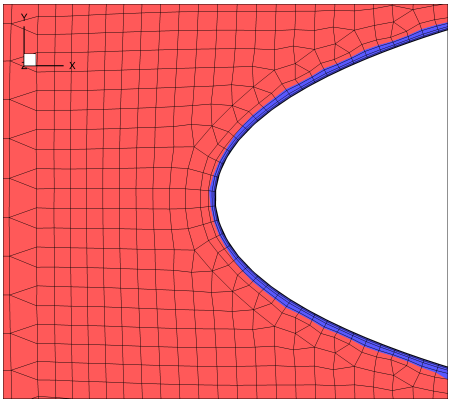

(c) DES mode at leading edge.

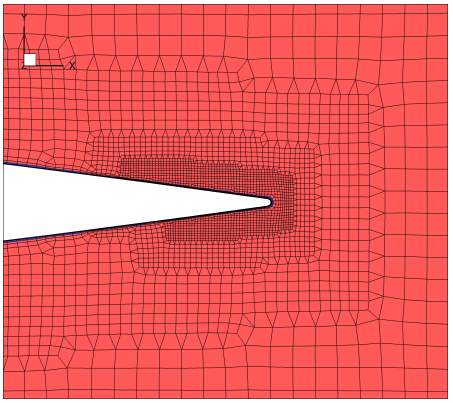

(d) DES mode at trailing edge.

Figure 5.2: CFL number distributions and DES modes, with red being LES volumes and blue being DES volumes in the aerofoil vicinity.

As mentioned previously in Section 3.2.1, a CFL number of below 0.5 was used, based on the investigation of the wave propagation properties documented in Section B, in order to keep temporal numerical dissipation low and to increase stability of the simulations. It is apparent from Figures 5.2 (a) and (b), that the maximum values of the CFL number are concentrated in tetrahedral cells in the layers that are refined, or where curvature needs to be resolved. During this research, numerous situations occurred where numerical oscillations would be produced by these cells, which also exhibit the largest values of skewness and non-orthogonality, the latter being defined as the angular deviation of the line connecting two cell centres from the normal vector of the face. It is therefore of utmost importance that conditions should be chosen for meshes incorporating these cells which increase the numerical stability in these critical areas, whilst maintaining an acceptable accuracy, such as a low time step, combined with an appropriate number of

non-orthogonality corrector steps.

The maximum values of the CFL number were obtained in the highly refined areas in the vicinity of the trailing edge, as shown in Figure 5.2 (b). The high level of refinement was chosen to be able to capture a blunt trailing edge. While capturing the trailing edge noise is not the focus of the current research, and a sharp trailing edge could have been chosen to alleviate computational cost, the intention of investigating a finite aerofoil with a round tip necessitated the choice of a meshing approach capable of resolving small radii. Due to this consideration, and to facilitate a more direct comparison of the LES results for an infinite aerofoil and a finite aerofoil, a blunt trailing edge was used in the present simulations. Due to the refinement necessary to capture the trailing edge radius, very small cells are created, reducing the typical non-dimensional time step achieved to $\Delta_t U_0/t_a = 6.7 \times 10^{-3}$.

In the boundary layer, $y^+ < 0.5$ was not exceeded, while the non-dimensional viscous lengths in the streamwise and spanwise directions were below $x^+ = z^+ < 40$. Figures 5.2 (c) and (d) illustrate that prism cells in the immediate vicinity of the grid are being handled by the RANS mode of the DES, while the vast majority of the domain is being handled by the LES mode of the DES. This is desirable, as it reduces the impact of the turbulence modelling inherent of the RANS mode to a minimum.

It is important to note that the realistic growth of the boundary layer, and in particular its laminar or turbulent nature, are issues which are neither expected to be accurately modelled by this approach, nor considered to be of large importance to the core object of the research, which is the prediction of leading edge turbulent interaction noise. As shown by Gill *et al.* [121], the influence of the boundary layer on the leading edge interaction noise is negligible. While aerofoils at low Reynolds number have been observed to exhibit noise generation at the trailing edge, due to the interaction of boundary layer instability waves with the trailing edge singularity and a subsequent feedback loop due to the produced acoustic waves [230], the present case is investigated at a chord-based Reynolds number of $\mathrm{Re_c} = 1.03 \times 10^6$, well above the regime where such noise generation is typically observed for unloaded aerofoils [231]. Consequently, as discussed previously in Section 2.4, the leading edge is the dominant noise source, and contributions of the boundary layer fluctuations become only significant at relatively high frequencies, as shown by Chaitanya *et al.* [94]. Thus, analysis of the boundary layer is omitted.

As shown by Figures 5.2 (a) - (d), while the mesh is, for the most part, of high quality in terms of skewness, orthogonality and aspect ratio of most cells, the transition from one refinement zone to another is associated with a very strong growth ratio of 2. This is significantly above commonly used meshing practices for LES, and its effect on the turbulent quantities must therefore be investigated. Figures 5.3 (a) - (d) show the contours of the axial Reynolds stress u_{11} as defined by Eqn. (2.20), as well as the root mean square values of the unsteady pressure, p_{RMS}, for the vicinity of leading and trailing edge.

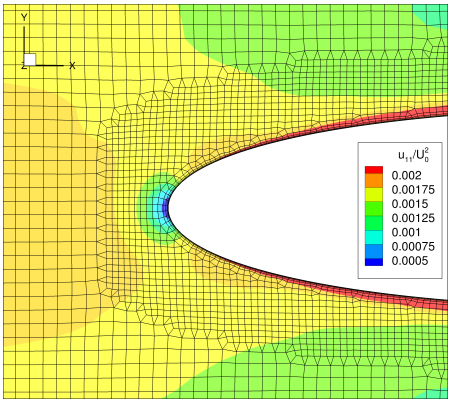

(a) Axial stresses at leading edge.

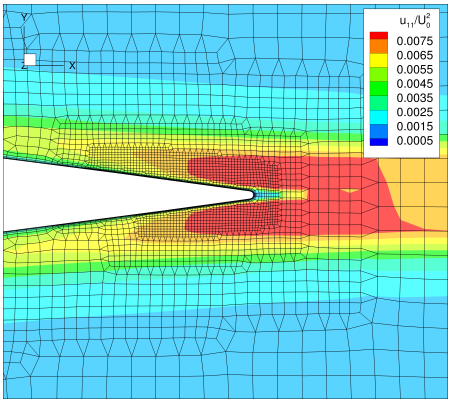

(b) Axial stresses at trailing edge.

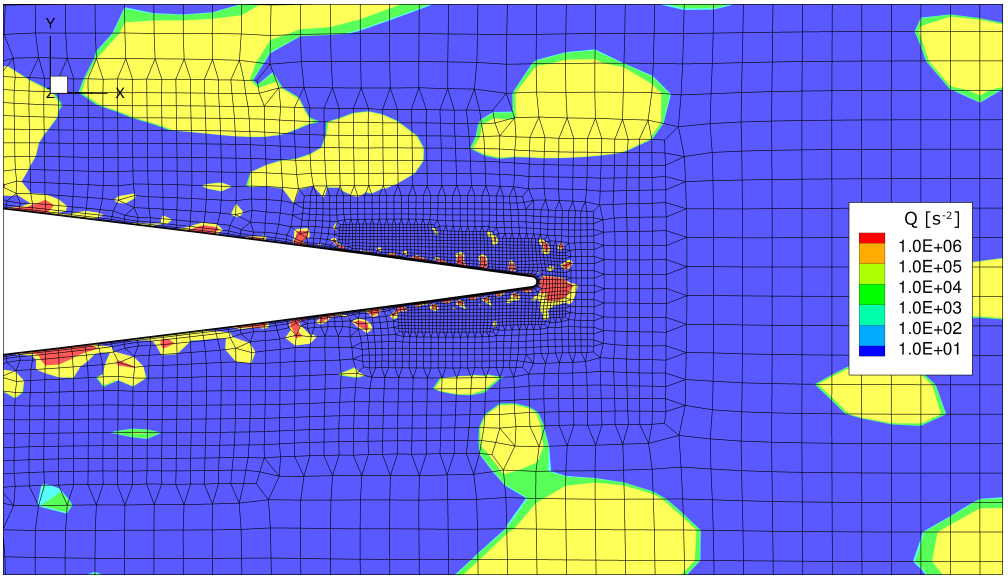

(c) Turbulent structures visualized by Q-criterion at trailing edge.

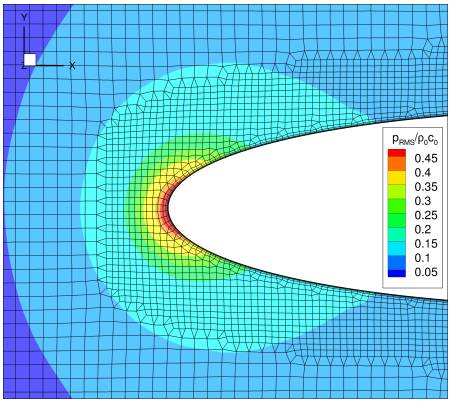

(d) p_{RMS} at leading edge.

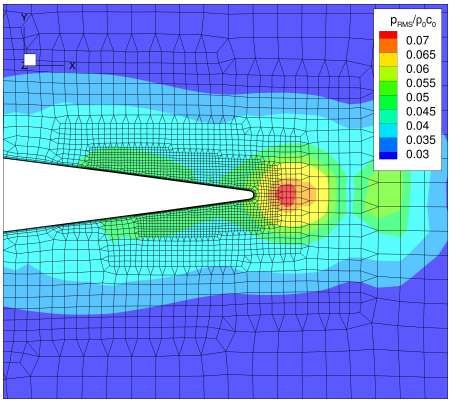

(e) p_{RMS} at trailing edge.

Figure 5.3: Turbulent quantities in the aerofoil vicinity.

From Figure 5.3 (a), no obvious influence of mesh density or cell growth rate on the contours of the values of u_{11} is observed. The results appear qualitatively very similar to

those obtained by Gea-Aguilera [103], who used structured meshes capable of supporting very small growth ratios. Equivalent to the present results, Gea-Aguilera reported a rapid decrease of u_{11} in the immediate vicinity of the leading edge, which was related to the reduction of mean flow axial velocity due to flow stagnation, and the resulting restriction of the velocity fluctuations in this direction. On the top and bottom of the aerofoil, a widening area of increasing values of u_{11} indicate a growing boundary layer. At larger distances from the symmetry plane, steadily decreasing values of u_{11} in the direction of the flow are observed. This is caused by two effects. Firstly, the turbulent decay due to dissipation reduces the magnitude of u_{11}. Secondly, the potential effect of the aerofoil imposes a mean strain on the flow, which acts in a manner similar to a contraction in a wind tunnel, and leads to a decrease of u_{11}, as observed in several experiments [26; 232].

At the trailing edge, shown in Figure 5.3 (b), the effects of mesh inhomogeneity are significantly more pronounced. The axial turbulent stresses grow rapidly, before dropping off significantly as the refinement is reduced. These increased stresses are caused by the increased wavenumber range of the resolved fluctuations in the finer mesh, as illustrated in Figure 5.3 (c) by the presence of very small turbulent structures in the vicinity of the trailing edge, which are smaller than the cell size of the outer turbulent domain. As the grid is derefined, these fluctuations are no longer resolved, and are dissipated quickly.

In order to investigate the impact of this forced dissipation of small-scale eddies due to grid derefinement at the trailing edge, the root mean square of the fluctuating pressure is shown in Figures 5.3 (d) and (e). As shown in Figure 5.3 (a), the increase of p_{RMS} close to the leading aerofoil is significant, as is expected. Similarly to the development of the axial stresses upstream the leading edge, no clear influence of the mesh refinement is observed.

Figure 5.3 (d), showing the distribution of p_{RMS} in the vicinity of the leading edge, illustrates how the rapid derefinement of the mesh leads to a significant rise in local unsteady pressure fluctuations. It is apparent that the forced dissipation of the small eddies within the boundary layer, resolved by the fine mesh at the trailing edge, shown in Figure 5.3 (c), will constitute an un-physical noise source. However, the p_{RMS} at the trailing edge is observed to be more than 6 times less than the value at the leading edge. Thus, it is expected that the influence of this noise source on the leading edge noise, which is the primary interest of this investigation, is negligible. This is further investigated in Section 5.3.2.

A source of error which cannot completely be excluded with the current methodology are spurious reflections of acoustic waves at the mesh derefinement interfaces such as present at the trailing edge of the aerofoil as shown in Figure 5.3 (e). As these would likely lead to similar effects as the non-compactness effects discussed in Section 2.4.2.1, mesh parameter studies are recommended using a structured mesh to assess whether they are dominant component in the present setup. However, considering the assessment of the presence of spurious reflections caused by the derefinement zones on top and

bottom of the aerofoil outside the turbulent jet, documented in Appendix D.1, which showed no obvious reflection of acoustic waves, it is not considered likely that significant reflections at the mesh derefinement interfaces take place.

5.2 Homogeneity and spectra of the turbulent background flow

In order to ensure realistic flow conditions for the case of an isolated aerofoil, appropriate boundary conditions must be chosen accordingly. In Section 3.3, the streamwise homogeneity of the flow was investigated with the setup as shown in Figure 5.1, and it was established that the turbulent domain exhibits a homogeneous core region extending up to one grid period from the plane of symmetry, as shown Figures 3.10 (a) and (b). In this section, the analysis is extended to include the spanwise homogeneity, as well as the energy spectra at this point, which are compared against those of the investigation of Paterson and Amiet [97]. All results discussed in the following are obtained from the background simulation, i.e. the simulation of the turbulence interaction setup, but with the aerofoil removed.

While the inlet grid turbulence creation proposed by Blackmore [13] is flexible and easy to implement, the method is limited in its capability to produce turbulence of exact *a priori* parameters. While a preliminary parameter study was conducted to determine the grid geometry and aerofoil placement settings most likely to reproduce the conditions in experiment, some deviations could not be avoided. The turbulence of the validation case varies from the flow as measured by Paterson and Amiet as shown by Table 5.2.

Flow quantity	Infinite aerofoil	Experiment [97]
U_0	67.2 m/s	60 m/s
$\sqrt{u_{11}}/U_0$	3.91%	4.36%
$\sqrt{u_{22}}/U_0$	3.85%	3.92%
I_{11}	3.64 cm	3.01 cm
I_{22}	1.11 cm	2.48 cm

Table 5.2: Flow parameters of infinite aerofoil simulation versus experiment of Paterson and Amiet [97].

With the exception of the integral length scales I_{11} and I_{22}, as defined by Eqn. (2.10), the deviations are relatively small, making a qualitative comparison to experiment possible. It should be noted that due to the considerable computational expense associated with performing the turbulence interaction simulation, there is an uncertainty

of up to 20% associated with the values of I_{11} and I_{22} following the discussion documented in Section 3.2.2, since the simulation could only be performed for a physical time sufficient for the convergence of the aeroacoustic quantities which were of primary interest. In order to account for the difference in mean flow velocity U_0, a dipole correction of $60\log_{10}(U_{\text{LES}}/U_{\text{Exp.}})$ is applied to acoustical results, following the arguments of Hersh [96].

5.2.1 Turbulence and mean flow homogeneity

The homogeneity of the turbulent flow in the yz plane, i.e. normal to the streamwise direction, is investigated for the position $x/G_p = 0$ in Figures 5.4 (a) - (e).

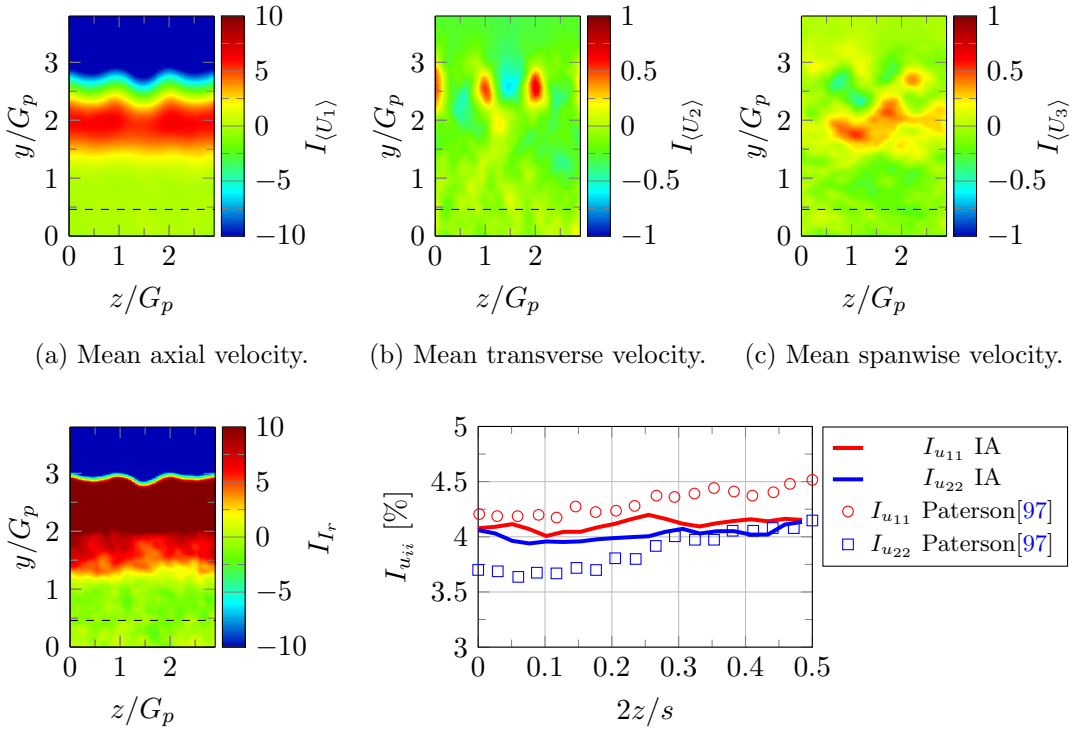

(a) Mean axial velocity. (b) Mean transverse velocity. (c) Mean spanwise velocity.

(d) Turbulence intensity. (e) Turbulence intensity along Infinite Aerofoil (IA) leading edge position. s is aerofoil span.

Figure 5.4: Flow inhomogeneity in the yz plane as quantified by I_ϕ. Dashed lines indicate thickness of aerofoil in subsequent interaction case.

In order to provide context in terms of the aerofoil dimensions in the interaction case, dashed lines indicate the maximum thickness of the NACA 0012 aerofoil used. The inhomogeneity parameter I_ϕ proposed by Ertunc *et al.* [56], as defined in Eqn. (3.23), is computed relative to the spanwise mean $\overline{\phi}$ at $y/G_p = 0$, and is in the case of the transverse mean velocities computed relative to the axial mean velocity.

As illustrated by Figure 5.4 (a), the mean axial velocity in the yz plane exhibits its largest inhomogeneity relative to the velocity in the centre in the shear layer, which extends between $1.5 < y/G_p \leq 2.8$. This is also the case of the transverse and the

spanwise mean velocities, however the inhomogeneities are less systematic and an order of magnitude smaller. In the centre of the turbulent flow, the inhomogeneity parameter is very low for all mean flow components. Since the peak values of all I_ϕ in the core region, i.e. for $y/G_p < 1$, appear random, they are considered not to be caused by the grid, and are likely to disappear when more data is used for averaging.
Figure 5.4 (d) shows in terms of the turbulence intensity $I_r = \sqrt{(2k/3)/U_0}$, a reasonably homogeneous state is obtained below $y/G_p = 1$, with turbulence intensity values within 0.5% of 4%.
Figure 5.4 (e) shows the spanwise variation of the axial and the transverse turbulence intensity components $I_{u_{11}}$ and $I_{u_{22}}$, respectively, which are computed by substituting u_{11} or u_{22} for k. In order to provide context, the level of homogeneity reported in the experiment by Paterson and Amiet [97] is superimposed in Figure 5.4 (e). While the comparison can only be qualitative, due to the difference in mean flow velocity of 10% as well as differences in the setup and geometry, e.g. no end-plates in the simulation, Figure 5.4 (e) shows that the homogeneity in terms of $I_{u_{11}}$ and $I_{u_{22}}$ of the LES is consistent with the experimental values. Furthermore, as no end plate is present in the LES, the increasing turbulence intensity levels with increasing $z/(2d)$ observed in the experiment is absent from the simulation.
An additional observation from Figure 5.4 (e) is the relatively high degree of isotropy exhibited in the simulation, when compared to the values measured by Paterson and Amiet. While the spanwise average of the experimental data yields a value of the anisotropy parameter of $\overline{\gamma_{12}} = 1.1$, a value of $\overline{\gamma_{12}} = 1.02$ is obtained for the LES. While the inlet-grid generation method has been shown in Section 4.1.2 to exhibit a considerable anisotropy for positions of $x/G_p < 20$ downstream of the grid, the use of blended upwind-biased schemes required for stability leads to a considerable reduction of the anisotropy, as shown in Section 3.2.4. An assessment of the effect of this mismatch in terms of anisotropy is conducted in Sections 5.2.2 and 5.4.

5.2.2 Validation of turbulence statistics

As documented in Section 3.3.2, the normal components of the RST as well as the correlations functions A_{ii} of the turbulence development case, discussed in Chapter 4 and the turbulence interaction case, discussed in the present Chapter, collapse in the centre of the turbulent flow for distances $x/G_p > 10$. Consequently, parameter studies based on the turbulence development setup can be used to establish suitable grid parameters to produce turbulence of similar statistics as those of prior experiments for validation purposes. In the present section, quantitative comparison of the simulated turbulent flow in the domain illustrated by Figure 5.1 with the experiments of Paterson and Amiet is conducted by comparing the correlations for the axial and transverse components, A_{11} and A_{22}, in Figures 5.5 (a) and (b). In order to account for the difference in integral length scale, the axial distance was normalized by κ_e as defined in Eqn. (2.17).

The value used for the integral length scale is given by Table 5.2. Additionally, the correlation model by Liepmann as given by Paterson and Amiet [97] was included to provide information as to how accurately the experiment and the simulation meet the criterion of isotropic turbulence, which is assumed in many analytical models. For the axial component, Liepmanns correlation was computed as,

$$A_{11}(r) = e^{-\kappa_e r/0.75}, \tag{5.1}$$

while for the transverse component,

$$A_{22}(r) = \left(1 - \frac{\kappa_e r}{1.5}\right) \cdot e^{-\kappa_e r/0.75}, \tag{5.2}$$

was used. In the experiments of Paterson and Amiet [97], the correlations were computed with the aerofoil removed, at a position equal to the centre of the aerofoil chord and span. However, they note that prior experiments had shown little dependency of the turbulent quantities on the streamwise position for distances shorter than the aerofoil chord. Due to this insensitivity, the correlations and spectra presented here are computed with data extracted at the intended position of the leading edge in the subsequent turbulence interaction simulations.

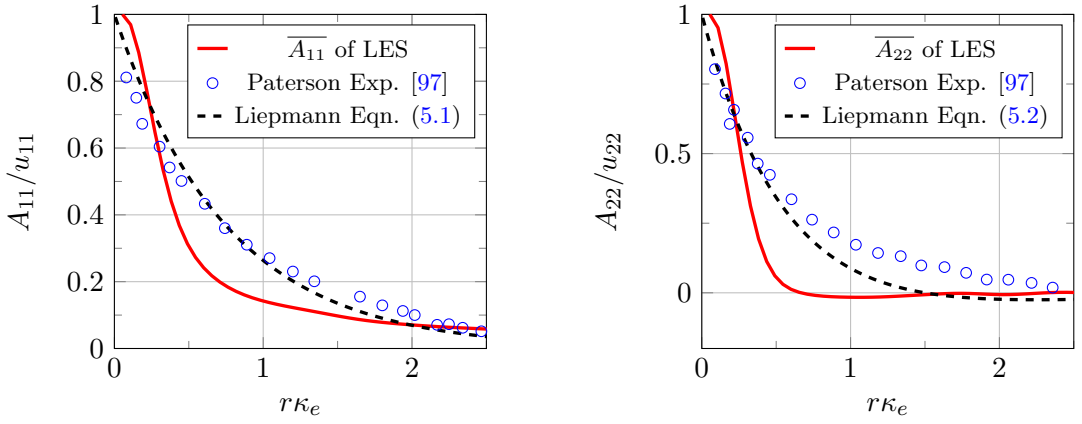

(a) Axial autocorrelation A_{11}.

(b) Transverse correlation A_{22}.

Figure 5.5: Comparison of correlation functions from LES (solid) with Experiment [97] (symbols) and Liepmann model Eqn. (5.1) and Eqn. (5.2) (dashed).

For the axial autocorrelation function A_{11}, shown in Figure 5.5, a reasonably good fit is obtained for $r/\kappa_e < 0.4$ and $r/\kappa_e > 2$. However, the correlation decays faster than either the model or the values obtained in the experiment. In case of the transverse correlation A_{22}, shown in Figure 5.5 (b), it is apparent that the correlations based on the simulation data do not agree with both the correlations obtained from the experiment as well as the analytical model. The values of correlation obtained from the LES decay too rapidly, whereas the values measured in experiment show higher flow correlation for $r/\kappa_e \geq 0.5$. In order to investigate the effects of this under-prediction on the 1D energy spectra, Figures 5.6 (a) and (b) compare $\overline{E_{11}}$ and $\overline{E_{22}}$ at the position of the leading edge, against

the results of Paterson and Amiet [97]. To facilitate comparison, the spectra were normalized by the value of the von Kármán 1D model spectrum, as defined in Eqn. (2.16), at $\kappa_x = 0$, and the wavenumber has been normalized by the factor of $3/(8\pi\kappa_e)$. The cut-off wavenumber κ_c, using a criterion of 25 PPW as established in Appendix B , is indicated by the vertical dash dotted line.

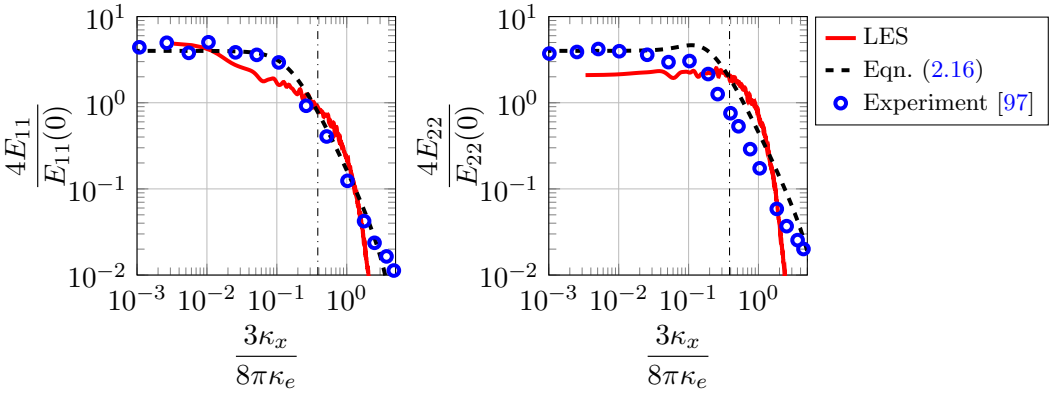

(a) Normalized axial energy spectrum.

(b) Normalized transverse energy spectrum.

Figure 5.6: Comparison of normalized spectrum from LES (solid) against model Eqn. (2.16) (dashed) and experimental data of Paterson and Amiet [97]. κ_c indicated by dash dotted line.

It is observed that the cut-off wavenumber, normalized by κ_e, appears to coincide with the first intersection of the model spectra of von Kármán and the spectra as obtained from LES. However, considering the uncertainty associated with the I_{11}, as discussed earlier in this Section in reference to Section 3.2.2, this is not considered meaningful, as the earlier investigation of the effect of using a central versus an upwind biased scheme for the convective term, documented in Section 3.2.4 illustrated that κ_c is more closely associated with the second intersection of the model spectra with the LES spectra, as shown in Figures 3.6 (a) and (b). Therefore, the scaling using κ_e is considered to be misleading for quantitative purposes, but may still be used for qualitative comparison of the experimental spectra to the spectra from LES. Considering the rapid loss of correlation observed in Figure 5.5 (a), as well as the energy deficit mid-wavenumber range $0.02 < 3\kappa_x/(8\pi\kappa_e) \leq 0.03$, it is concluded that the intermediate length scales are under-predicted in terms of correlation and energy content. However, as the predictions of leading edge noise is primarily dependent on the transverse energy spectrum, a further investigation of these discrepancies is omitted here.

In case of the transverse energy spectrum, shown in Figure 5.6 (b), deviations from the analytical spectrum are observed both in regards of the experimental spectrum, as well as the spectrum obtained from the LES. While Paterson and Amiet [97] provide no explanation for the deviation from the analytical spectrum, it is reasonable to relate the difference to the level of anisotropy present in the experimental flow. The transverse

spectrum from the LES is observed to deviate from both the experimental and the analytical. While the energy at wavenumbers $3\kappa_x/(8\pi\kappa_e) \leq 0.2$ is reduced, for wavenumbers $3\kappa_x/(8\pi\kappa_e) \geq 0.2$ a larger energy content is exhibited relative to both the analytical and the experimental spectrum.
As such, the shape of the axial and the transverse energy spectra explains the mismatch between the anisotropy parameter γ_{12}, which indicates an almost isotropic flow, and the ratio of the integral length scales I_{11}/I_{22}, which according to the values given in Table 5.2 indicates a strongly anisotropic flow. When integrating over the energy spectra, the lack of energy in the mid-wavenumber range of E_{11}, combined with the excess of energy in the high wavenumber range of E_{22} will lead to a value of γ_{12} close to isotropy. However, since the integral length scales of the axial and transverse components are primarily determined by the energy content of the lowest wavenumbers, a state of strong anisotropy will be observed such as presented in Table 5.2.
Since the transverse energy spectrum is primarily responsible for the acoustic emissions, a more in-depth investigation of the consequences of the observed deviation from the isotropic spectrum is conducted in Section 5.4.

5.3 Leading edge interaction physics and aerofoil on-surface pressures

The qualitative investigation on the effect of conducting LES on unstructured meshes, documented in Section 5.1, has given a first insight into the flow phenomena in the vicinity of the leading edge. To analyse the noise production processes, the region immediately upstream of the leading edge is investigated in this section more in detail. As pointed out by Roger and Moreau [12], broadband leading edge noise is fundamentally produced by the rapid modification of turbulent structures by the interaction with a solid surface. This section will investigate the turbulence distortion in the leading edge region. Additionally, the resulting on-surface pressure spectra are presented and compared to experiment.

5.3.1 Turbulence interaction with leading edge

Figures 5.7 (a) and (b) illustrate the distribution of the root mean square values of the unsteady pressure in the immediate vicinity of the leading edge, as well as of the distribution of the unsteady pressure at one arbitrary moment in time, respectively. In order to provide context on the aerodynamic environment of the aerofoil, Figure 5.7 (b) provides a larger view of the simulated domain, including the transition shear layer of the turbulent flow to the steady far-field.
The analysis of p_{RMS} at the leading edge in Figure 5.7 shows that the contour lines centre around the stagnation point of the leading edge. They are found to be almost

circular, whereas the simulations of Gill [7] and Gea-Aguilera [103] predict contours of p_{RMS} to attain a dipole-like distribution, with maxima on each side of the stagnation point. Amiet's theory, however, assumes the maximum p_{RMS} at the leading edge of the flat plate [15]. It should be noted that the studies of Gill and Gea-Aguilera were conducted using an LEE methodology, where the linearisation of the equations allows to decouple vortical, acoustic and entropy waves and therefore allows to introduce turbulent flows which consist solely of vortical perturbations transported in a frozen manner by the mean flow. Consequently, such turbulent flows would not exhibit density or pressure fluctuations in the linearised Euler equations.

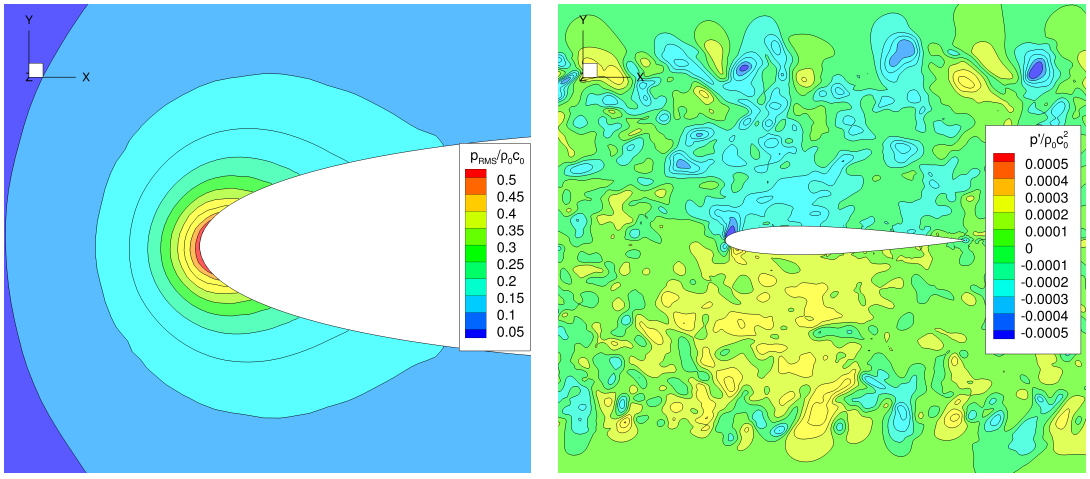

(a) $p_{RMS}/\rho_0 c_0$ at the leading edge. (b) $p'/\rho_0 c_0^2$ in the vicinity of the aerofoil.

Figure 5.7: Unsteady pressure mean and instantaneous distributions.

The turbulent flow simulated here is not divergence free and does contain, as shown in Figure 5.7 (b), considerable hydrodynamic pressure fluctuations. These will contribute to the p_{RMS} at every point in the flow, leading to p_{RMS} no longer being representative of the acoustic fluctuations only. As such, the instantaneous pressure distribution, shown in Figure 5.7 (b), does not permit to identify acoustic fluctuations unambiguously. At best, the influence of an acoustic wave can be observed in an area where the hydrodynamic pressure fluctuations are decreased or lowered relative to the remainder of the turbulent flow, as shown in Figure 5.7 (b) by the light blue area and the yellow area on top and bottom of the aerofoil, respectively.

An investigation of the influence of domain setup and mesh refinement on the results of Figures 5.7 (a) and (b) was conducted and is documented in Appendices D.1 and D.2, respectively.

In order to assess the effect of the presence of the aerofoil on the mean flow velocity and the turbulent stresses, the development of $\langle U_1 \rangle$ as well as of u_{11}, u_{22} and u_{33} upstream the leading edge is shown in Figure 5.8. The distance to leading edge is given in terms of the coordinate r/r_{LE}, where r_{LE} is the leading edge radius, defined for NACA 4-digit aerofoils as $r_{LE}/c = 1.1019(t_a/c)^2$, with t_a being the aerofoil thickness.

As Figure 5.8 (a) shows, the development of the mean axial velocity collapses well with

the experimental values. This is an expected result, as this development is due to the potential effect of the aerofoil, which is determined by the mean flow, and therefore deviations arise due to differences in boundary conditions only. The present results indicate that the numerical domain setup as illustrated by Figure 5.1 is appropriate to investigate the problem of an isolated, infinite aerofoil. The only observable deviation occurs in the region closest to the leading edge, where Santana *et al.* [101] report $\langle U_1 \rangle$ to align more closely to the values of the potential solution of a cylinder than for an aerofoil, in agreement with theoretical arguments of Mish and Devenport [233].

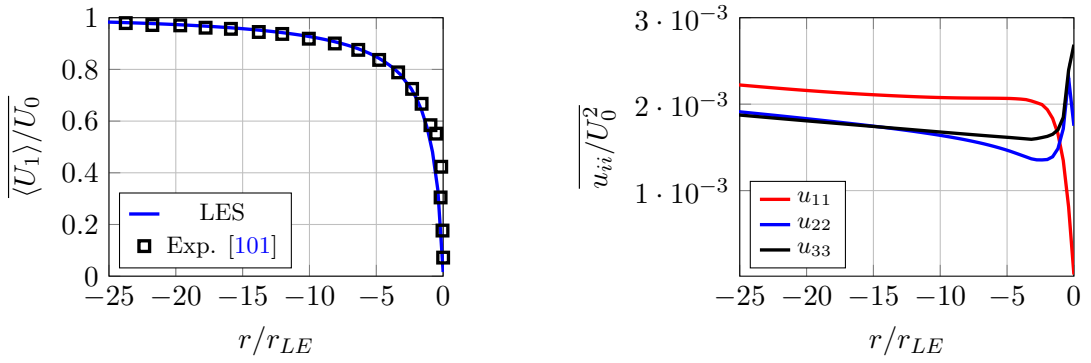

(a) Mean axial velocity.

(b) Normal RST components.

Figure 5.8: Development of the velocity quantities towards the leading edge.

In terms of the development of the normal RST components, shown in Figure 5.8 (b), a considerable difference is observed in the development of the streamwise turbulent stress compared to the transverse components. While the former monotonically decays towards the leading edge, the two latter components exhibit a considerable increase in the immediate vicinity of the leading edge. This is in disagreement with the PIV measurements of Santana *et al.* [101], who reported an increase of all three stresses. However, the CAA studies of Gill *et al.* [121], Hainaut *et al.* [102] and Gea-Aguilera [103], reported a development of the turbulent stresses equivalent to the present results. It is noted that theoretical considerations of Hunt [115], based on the rapid distortion theory, predict an increase of u_{11} with decreasing distance to the leading edge. While no increase of u_{11} can be observed in the present simulation, for $-15 \leq r/r_{LE} = -3$ the axial stress is observed to remain approximately constant. It is conceivable that the theoretical increase of u_{11} according to Hunt is just sufficient in this case to cancel the decrease of axial turbulent stress due to dissipation. Furthermore, as Hunt computed closed form solutions only for asymptotic cases, i.e. for eddies much smaller and much larger than the body size, it is considered likely that the present simulations, which would not be able to capture the largest and smallest scales, are not able to completely reproduce these effects. However, since the axial energy spectrum is for the leading edge noise production of reduced importance [15], this is considered acceptable.
An investigation of the effects of mesh dependency on the results illustrated by Figures 5.8 (a) and (b) was conducted and is documented in Appendix D.2.

The development of the one-dimensional energy spectra is shown in Figures 5.9 (a), (c) and (e) in absolute terms, and in (b), (d) and (f) relative to their value at $x/r_{LE} = -21$.

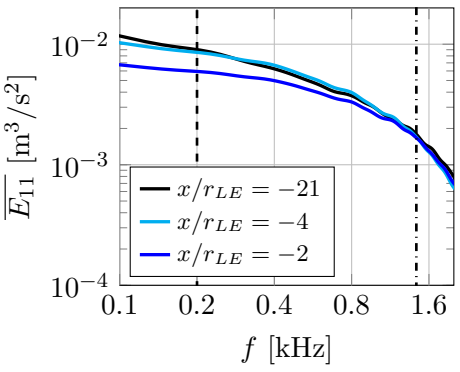

(a) Absolute axial energy spectra.

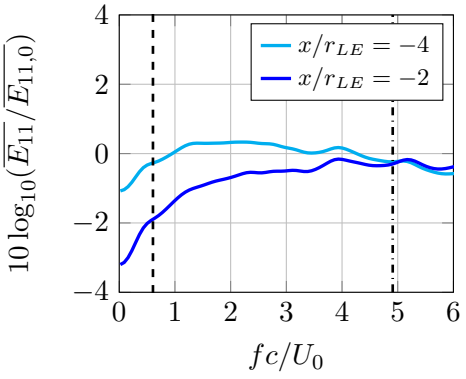

(b) Axial energy spectra relative to $x/r_{LE} = -21$.

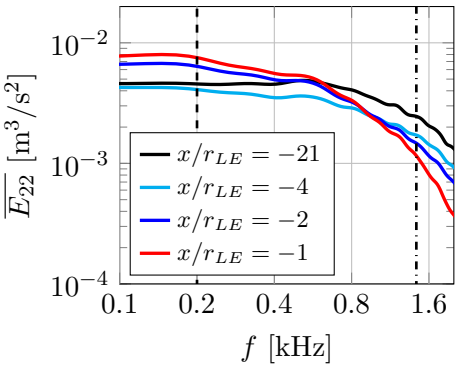

(c) Absolute transverse energy spectra.

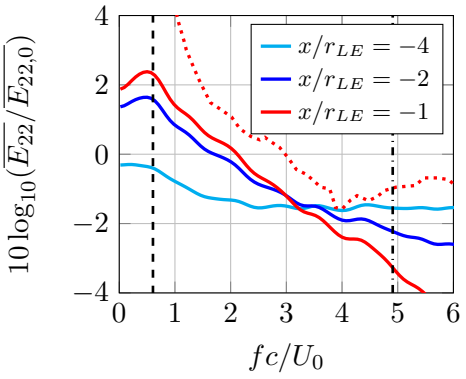

(d) Transverse energy spectra relative to $x/r_{LE} = -21$.

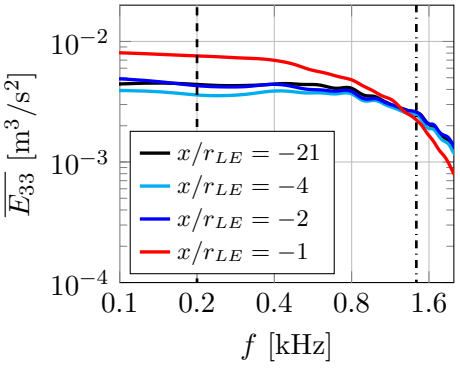

(e) Absolute spanwise energy spectra.

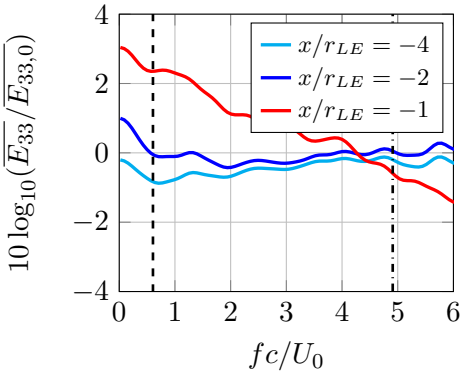

(f) Spanwise energy spectra relative to $x/r_{LE} = -21$.

Figure 5.9: Development of the one-dimensional energy spectrum towards the leading edge. Dashed line indicates applicability of frozen turbulence hypothesis. Dash dotted lines indicates mesh cut-off frequency for vortical waves. Dotted red line in (d) illustrates results of Gea-Aguilera [103] for $x/r_{LE} = 1.26$ upstream a NACA0012 at a mean flow velocity of $M_0 = 0.3$.

It is noted that at this point the mean axial velocity is still slightly nonuniform, as potential effects decay proportionally to $1/\sqrt{r}$. However, experimental results [101] as well as numerical parameter studies [103] indicate in agreement with the analysis shown in Figure 5.8 (b) that the RST and the energy spectra at $x/r_{LE} = -21$ can be considered representative of the undisturbed turbulent flow, and that the distortion of the turbulence due to the presence of the leading edge happens at distances of the order of the leading edge radius.

Due to mean velocity gradients, the assumption of frozen turbulence is not applicable to the whole spectrum. Consequently, the criterion for frozen turbulence developed by Lumley [20], defined by Eqn. (2.6) is indicated by the vertical dashed line. It is evaluated for the gradient closest to the leading edge, which returns the most conservative estimate for the applicability of the frozen turbulence assumption. In addition, the mesh cut-off frequency for vortical waves of $f_{cv} = 1429$ Hz, using the criterion of 25 points per wavelength as established in Appendix B , is indicated by the dash dotted line.

As the axial energy spectra at $x/r_{LE} = -1$ is considerably reduced, it has been omitted in Figures 5.9 (a) and (b). The analysis for positions $x/r_{LE} = -4$ and $x/r_{LE} = -2$ confirms the earlier observation that a small increase of the axial energy spectrum is present, although the effect is very limited. Further investigations with more accurate numerical schemes are recommended to confirm this observation. It is noted that although at $x/r_{LE} = -2$, E_{11} is consistently below the energy spectrum of the reference position $x/r_{LE} = -21$, the decrease is not uniform, and the spectra shows little decreased energy for frequencies towards $fc/U_0 \approx 5$. It is conceivable that idealized frozen turbulence, which does not evolve and dissipate energy, would show a positive energy content for those frequencies in alignment with the theoretical considerations of Hunt [115]. However, the results of CAA simulations using frozen turbulence as conducted by Gea-Aguilera [103] agree qualitatively with the essentially energy decrease across all frequencies, as in Figures 5.9 (a) and (b). As in the present results, the frequencies for which the energy decrease is minimal are at or above the cut-off frequency determined for the current mesh, a more refined domain is recommended establish the development of the axial energy spectra towards the leading edge at higher frequencies. However, since the effects of the axial energy spectra on the turbulence interaction noise are small, such investigation was not conducted in the course of this research.

The development of the energy spectra of the transverse component is investigated in Figures 5.9 (b) and (c). From an aeroacoustic perspective, the development of E_{22} has been related to the thickness effects exhibited by aerofoils of finite thickness [98; 101], which lead to the reduction of leading edge noise emissions at high frequency. Chaitanya *et al.* showed experimentally [94] that this will result in the trailing edge noise of the aerofoil becoming dominant at lower frequencies than in the case of thin aerofoils. In their investigations, they found the limiting frequency for the dominance of trailing edge noise to be at $ft_a/U_0 \approx 1$, which is for the present case $f_{TE} = 2.4$ kHz, and as such is beyond the mesh cut-off frequency for vortical waves and consequently omitted from

the analysis above.

It is apparent from Figure 5.9 (c) that the development of E_{22} is complex, and dependent on frequency as predicted by Hunt [115], and subsequently shown by Hainaut *et al.* [102] and Gea-Aguilera [103]. When comparing the present results with the results of the latter of the two authors, illustrated by the red dotted line in Figure 5.9 (d) an acceptable qualitative agreement is found, as E_{22} increases for low frequencies and decreases for high frequencies. While there are significant quantitative differences, they are primarily related to differences in analysis positions. A further discussion of the thickness effects is documented in Section 5.4. Since the spanwise velocity fluctuations do not have any impact on the noise emissions of an aerofoil [15], little investigation has been conducted into their behavior at the leading edge. However, as this research investigates a finite aerofoil which does exhibit a singularity in the spanwise direction, the energy spectra are discussed here to establish a baseline for the comparisons with the finite aerofoil case, presented in Chapter 6. As shown in Figure 5.9 (e), the transverse fluctuations increase almost across the entire frequency range as the leading edge is approached. Since the leading edge represents a constant geometry for the entire length of the spanwise correlation length, and therefore impacts all scales equally, this is expected. Only for the position closest to the leading edge does the energy content at the high frequencies become significantly less than at the free stream reference point, which may be caused by the impact of viscosity. Still, as shown in Figure 5.9 (f), significantly more energy is contained in the spanwise energy spectra than in the transverse or axial energy spectra.

5.3.2 Aerofoil surface pressures

For the purpose of validation of the boundary conditions as well as the consequences of the inhomogeneity of the mean flow, the time averaged pressure coefficient $\langle c_p \rangle = (\langle p \rangle - p_0)/(0.5\rho_0 U_0^2)$ is compared to a validation case provided by the NASA Langley Research Center in Figure 5.10 (a). The experimental data was presented by Gregory and O'Reilly [234] at a Reynolds number of $\mathrm{Re} = 2.88 \times 10^6$. Considering the smaller chord-based Reynolds number of the aerofoil interaction case of $\mathrm{Re} = 1.04 \times 10^6$, some minor differences are to be expected, but are expected to be small enough for the purpose of the validation of the steady aerodynamics.

As expected, some minor differences in the magnitude of the time averaged pressure coefficient can be observed in Figure 5.10 (a), but the shape of the $\langle c_p \rangle$ distribution is well predicted. It is concluded that the potential effects of the aerofoil are captured, which are a product of the steady aerodynamics, and are thus independent from the turbulent fluctuations resolved by the LES. As such, the good reproduction of the $\langle c_p \rangle$ distribution indicates that the complex boundary conditions illustrated by Figure 5.1 are appropriate for the investigation of an isolated aerofoil in a turbulent flow.

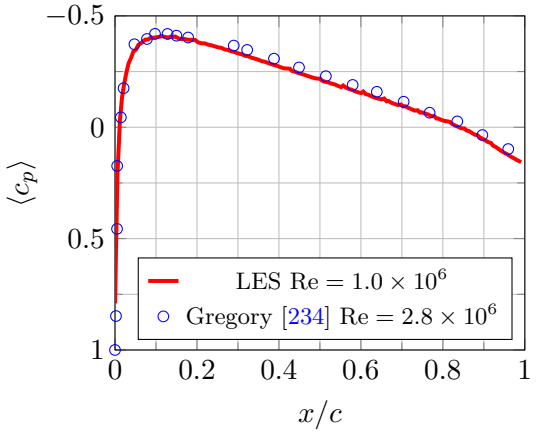

(a) $\langle c_p \rangle$ compared to experimental data of Gregory and O'Reilly [234].

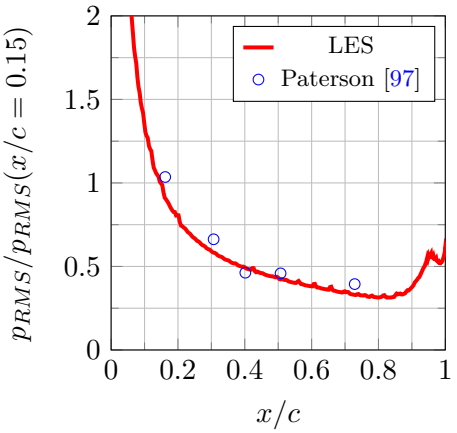

(b) Root mean square of fluctuating pressure on the aerofoil surface of LES compared to experimental data of Paterson and Amiet [97].

Figure 5.10: Validation of mean and unsteady surface pressure distributions.

The experimental values for the root mean square of the fluctuating pressure as measured by Paterson and Amiet [97] are compared with those obtained from the present LES in Figure 5.10 (b). While values for p_{RMS} relative to $x/c = 0.15$ are available only for four other measurement positions, the good agreement between the experimental values of and the values obtained from LES indicates that the important trend of increasing pressure fluctuation magnitudes towards the leading edge is captured by the LES. A second smaller increase of p_{rms} is observed towards the trailing edge, which may be associated with the boundary layer interactions with the trailing edge. However, due to lack of experimental data, no validation is possible at this point. Future investigations, potentially utilizing the aerofoil test rig designed and manufactured in the course of this research and documented in Appendix A, are suggested to determine whether this secondary peak is physical. However, as the peak is significantly below the peak associated with the leading edge noise, its contribution to the total noise emissions is considered negligible.

In order to further validate the unsteady pressure on the aerofoil surface, surface pressure Sound Power Level (SPL) spectra have been computed at three points and are compared to the corresponding experimental data of Paterson and Amiet [97] in Figure 5.11. The SPL is computed according to

$$\mathrm{SPL}(f) = 10 \log_{10} \left(\frac{S_{pp}(f)}{p_{\mathrm{ref}}^2 \cdot 1\mathrm{Hz}} \right) \tag{5.3}$$

with $S_{pp}(f)$ as the power spectral density on the aerofoil and $p_{\mathrm{ref}} = 2 \times 10^{-5}$ Pa as the acoustic reference pressure. The results from the LES were corrected for the variations in span and velocity between the LES and experiment by applying a scaling factor of $20 \log_{10}(s_{\mathrm{LES}}/s_{\mathrm{Exp.}})$ for the span differences and $60 \log_{10}(U_{\mathrm{LES}}/U_{\mathrm{Exp.}})$.

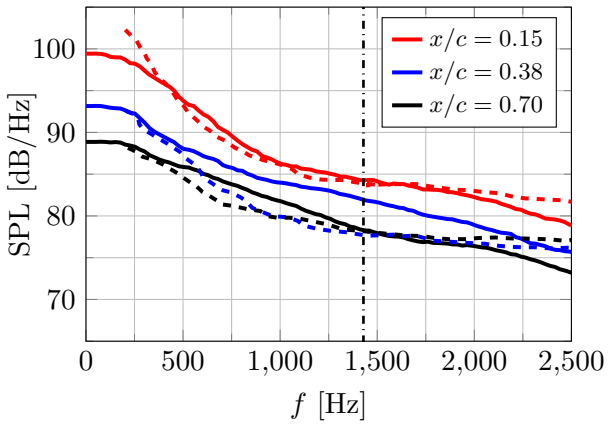

Figure 5.11: Surface pressure spectra computed for LES (solid) compared to experimental results of Paterson and Amiet [97] (dashed) at three chordwise positions. LES spectra were corrected for span and velocity differences. Mesh cut-off frequency for vortical waves indicated by dash dotted line.

When comparing the spectra of the unsteady surface pressure, larger discrepancies are identified. The best agreement in terms of overall spectral shape occurs at the position closest to the leading edge, $x/c = 0.15$, in a frequency range of $400 \leq f < 2000$ Hz, as shown by the red lines in Figure 5.11. The mismatch at high frequencies is expected, as the cut-off frequency of the mesh, as shown by Figures 4.4 (a) and (b) is at 2500 Hz. However, for positions further downstream, at $x/c = 0.38$ and $x/c = 0.70$, little agreement is observed. Except for a frequency range of $250 \leq f < 500$ Hz, both amplitudes as well as trends show large deviations. A potential cause for these discrepancies are the hydrodynamic fluctuations associated with the eddies contained in the boundary layer, which was also recognized by Paterson and Amiet [97], as they state that it is difficult to separate pressure fluctuations associated with lift and those associated with the turbulent boundary layer on the surface of the aerofoil. Since the pressure fluctuations due to the turbulent boundary layer are not explicitly resolved by the current methodology, which uses a RANS for the near wall regions, a discrepancy between the surface pressure spectra and the experimental results cannot be avoided. However, as the influence of the boundary layer was shown to be negligible for the purpose of the investigation of leading edge noise by Gill *et al.* [121], this discrepancy from experimental results is considered acceptable, as the investigation of leading edge noise is the primary object of this study. In order to assess the influence of the pressure fluctuations at the trailing edge, caused by the rapid diffusion of the small boundary layer eddies by the derefinement of the trailing edge mesh, the surface pressure spectra along chord are shown in Figure 5.12.

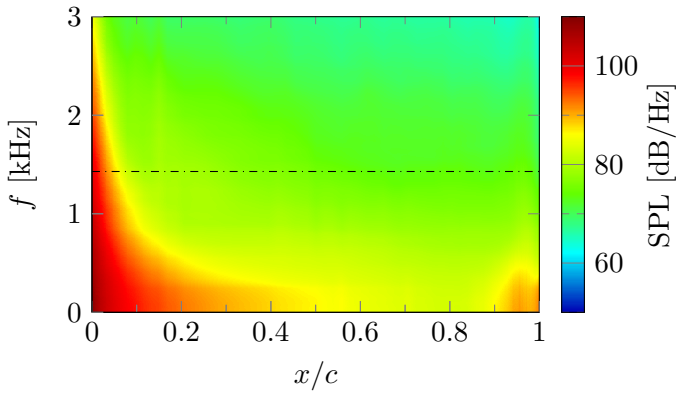

Figure 5.12: Surface pressure spectra along chord at mid span.

From Figure 5.12 it is apparent that the pressure fluctuations are largest at the leading edge over the entire frequency range investigated. While the hydrodynamic pressure of the turbulent eddies is contained in these fluctuations, this is considered a strong indication that the leading edge is the dominant source of noise, and that the un-physical pressure fluctuations at the trailing edge can be considered a negligible factor in terms of the total aerofoil noise emissions.

5.4 Noise prediction results

Having compared the properties of the simulated turbulent flow to that of the experiments of Paterson and Amiet [97], the effect of the observed deviations is assessed in terms of the leading edge noise emissions from the aerofoil. Noise emissions to the far-field are computed using the methodology described in Section 3.1.3. A free-field Green's function is used, under the assumption of a uniform mean flow equal to the axial mean flow velocity in the turbulent domain.

5.4.1 Results of the thick and unloaded aerofoil

For the purpose of comparing the results from LES to the analytical method developed by Amiet [15], the formulation for an observer in polar coordinates as given by Eqn. (2.33) was used. The values used for U_0, I_{11} and $\sqrt{u_{11}}/U_0$ to evaluate Eqn. (2.33) were extracted from the background flow, i.e. without the aerofoil, and correspond to the values given in Table 5.2. The implementation of the analytical solution of Amiet [15] includes both the low and high frequency aerofoil response functions as given by Eqn. (2.35) and Eqn. (2.36), thereby including the effects of non-compactness. At the frequency where the switch occurs, i.e. 400 Hz, a small discontinuity is observed. However, this is considered minor for the purposes of this comparison.
Figures 5.13 (a) and (b) show the SPL spectra at two downstream observer angles,

i.e. $\theta = 30°$ and $\theta = 60°$, while (c) shows the SPL spectra at the overhead position $\theta = 90°$. In order to allow comparison to the experimental measurements of Paterson and Amiet [97], scaling factors of $20\log_{10}(s_{\text{LES}}/s_{\text{Exp.}})$ for the span differences and $60\log_{10}(U_{\text{LES}}/U_{\text{Exp.}})$ for the mean flow differences are applied to the experimental values, as the leading edge noise source is considered a dipole following the arguments of Hersh and Meecham [96]. For additional context, vertical lines have been added where the thin dash-dotted lines illustrate the highpass cut-off frequency due to the finite signal length f_{cT}, which is chosen conservatively as 40 Hz to eliminate potential aliasing. Furthermore, thin dash-dotted lines indicates the mesh cut-off frequency for vortical waves f_{cv}, the thin dotted lines illustrate the frequency f_{TE} where experiments have found trailing edge noise to be dominant, and a thick dashed blue line indicates the frequency of the dip in the spectra associated with non-compactness effects, $f_{c,0}$, as defined by Eqn. (2.46). It is noted that while the mesh cut-off frequency is relevant in this analysis in so far that the vortical waves, which act as the underlying cause of the noise generation, are rapidly diminishing in energy content past f_{cv}, the acoustic waves which are produced by them are not subject to the same cut-off frequency, due to the significantly higher propagation speed and consequently increased number of points per wavelength compared to vortical waves, as discussed in Appendix B.

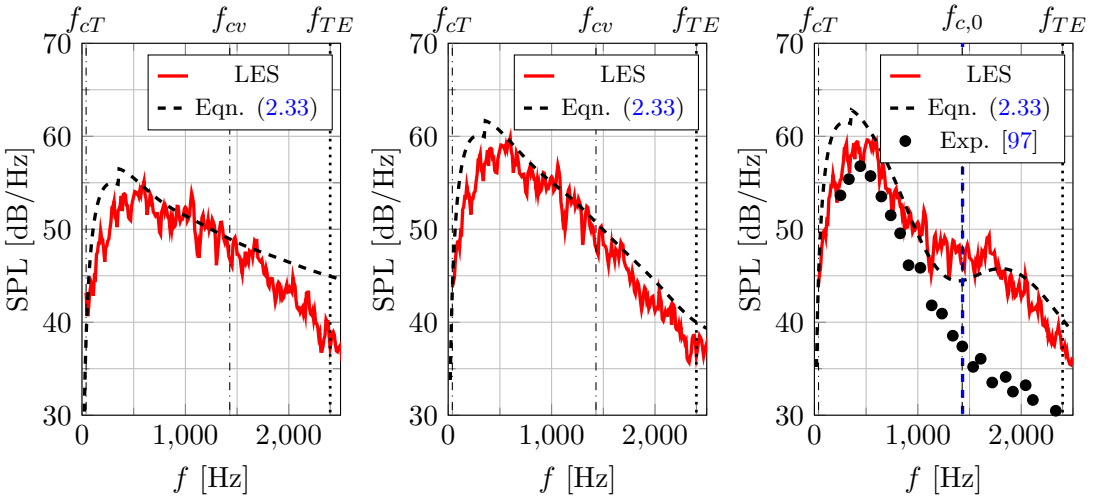

(a) $\theta = 30°$. (b) $\theta = 60°$. (c) $\theta = 90°$.

Figure 5.13: Far-field noise at downstream and overhead observer angles with LES (red, solid), analytical Eqn.(2.33) (black, dashed), experimental values of Paterson and Amiet [97] (black, symbols).

For the downstream observer angles at $\theta = 30°$ and $\theta = 60°$, it is observed from Figures 5.13 (a) and (b) that the agreement with the analytical spectrum of Amiet is within 2 dB over most of the frequency range investigated, with the exception of frequencies in excess of 2000 Hz for the observer position at $\theta = 30°$. At the overhead position, shown in Figure 5.13 (c), indications of a dip in the spectra associated with non-compactness at $f_{c,0}$ are observed, although it is not as pronounced as in the analytical solution.

Furthermore, there are indications that the LES tends to under-predict the peak SPL at $f \approx 400$ Hz more significantly as the observer angle is increased.
The noise emission results for the upstream observer angles are shown in Figures 5.14 (a) and (b) for $\theta = 120°$ and $\theta = 150°$, respectively.

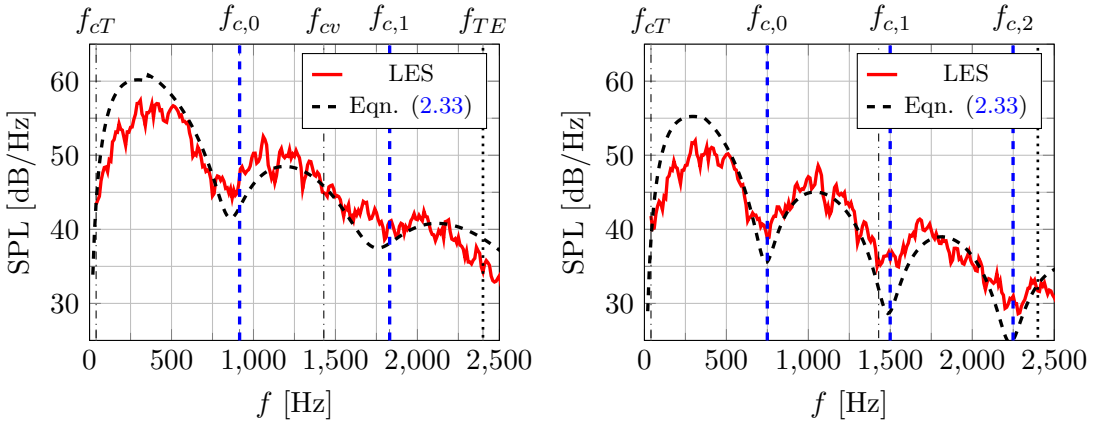

(a) $\theta = 120°$.

(b) $\theta = 150°$.

Figure 5.14: Far-field noise at upstream observer angles with LES (solid), analytical Eqn. (2.33) (dashed).

Qualitatively, it is apparent from Figure 5.14 (a) and (b) that the dips in the spectra of both the LES as well as the analytical model of Amiet [15] align well with the frequencies given by Eqn. (2.46). Quantitatively, it is also observed that the trend of the first SPL peak to be underestimated is continued at the upstream observer angles, with a discrepancy of approximately 4 and 5 dB at $f = 250$ Hz.
Considering the highpass cut-off frequency f_{cT}, the mesh cut-off frequency f_{cv} and the frequency f_{TE} typically associated in experiment [94] with dominant trailing edge noise contributions, it is concluded from the results shown in Figures 5.13 and 5.14 that the frequency range $f_{cT} \geq f < f_{cv}$ is meaningful for physical interpretation and comparison to literature. While, as discussed in Appendix B, the mesh is suitably refined for the propagation of acoustic waves at frequencies considerably larger than f_{cv}, as the underlying source mechanism cannot be considered physical, since the energy spectrum dropoff is too steep, the corresponding acoustic emissions are also not considered for discussion. Furthermore, while the trailing edge noise has been found not to be dominant up to frequencies of the order of $ft_a/U_0 \approx 1$ [94], the trailing edge noise can be expected to contribute increasingly to the total noise emissions even before f_{TE} is attained.
When restricting the analysis to the frequency range below 1500 Hz, two conclusions are drawn from Figures 5.13 and 5.14.
Firstly, it is observed that while the frequency $f_{c,0}$ of the first dip associated with the non-compactness effect is for downstream and overhead observer angles at frequencies beyond the validity of the present LES, $f_{c,0}$ is well within the resolved frequencies for upstream observer positions. As such, the current results emphasise the necessity of including non-compactness effects to compute the SPL spectra for upstream observers.

However, as SPL spectra were reported only by Paterson and Amiet [97] only for the overhead position, comparison is limited to a qualitative assessment of the directivity patterns in Figures 5.16 (a) - (c). Further validation of the present results is recommended, potentially using the experimental setup developed and constructed in the course of this research project and documented in Appendix A.

Secondly, it is apparent from Figure 5.13 (c) that the noise emissions obtained from the LES are much closer to those expected from a flat plate, rather than those measured by Paterson and Amiet [97]. While the agreement is acceptable at frequencies below 1000 Hz, the simulation predicts noise levels up to 10 dB higher than measured in experiment for the higher frequencies. The overall good agreement with the analytical solution at other observer angles is considered further indication that the noise results from the LES for the thick aerofoil are close to those of an ideal flat plate in isotropic turbulence. This is despite the fact that the aerofoil simulated is considerably thicker than a flat plate, and that the earlier investigation of the energy spectra, documented by Figures 5.6 (a) and (b), has shown significant deviations from the isotropic model.

For the investigation of this mismatch, an approach is required to more accurately represent the anisotropic energy spectra exhibited by the simulated turbulence. One such model was proposed by Kerschen and Gliebe [128], and subsequently used in studies by Posson *et al.* [130] and Karve *et al.* [235]. While it has been shown to be effective for these purposes, attempts to use it to model the spectra exhibited by the simulated turbulent flow here failed, in particular when computation of the noise emissions is attempted. This is due to the formulation of the model, which results in the transverse velocity spectra $\phi_{22}(\kappa_1, \kappa_3 = 0)$ becoming independent of u_{22} [103; 236]. Parameter studies indicate that the model appears to require the ratios of u_{22}/u_{11} and I_{22}/I_{11} to be quite similar, although this is not explicitly stated by Kerschen and Gliebe [128]. When the model was used in combination with the analytical method of Amiet, considerable under-predictions occurred, which could be traced to a significantly reduced transverse energy content. It is hypothesized that this is related to the derivation of the Kerschen and Gliebe spectrum from the modified Liepmann spectrum [35; 235], which is, like the von Kármán spectrum, fairly rigid in its modelling of the energy containing range. As such, it is unable to yield a good fit to the energy spectra of the current case, where the anisotropy is primarily contained in the largest scales. While this observation deserves further investigation, additional analysis is outside the scope of this work.

Instead of using the axisymmetric spectrum of Kerschen and Gliebe, an alternative approach was chosen. According to Amiet [15], the velocity spectrum primarily responsible for the noise emissions of the infinite aerofoil is the transverse velocity spectrum. Consequently, the anisotropic transverse velocity spectrum obtained from the simulation is represented in the analytical solution by a fit of the von Kármán spectrum to the result of this quantity from the LES. While this will lead to a considerable under-representation of the axial energy spectrum, for the purpose of computing the noise emissions of a flat

plate immersed in such an anisotropic flow, this approach is valid for a first-order estimation of the effects of the anisotropy as observed in the simulation.
A least-squares fit of the von Kármán isotropic spectra to the transverse energy spectra as obtained from the LES returned values of 1.8 cm and 2.73 m/s for the input parameters I_{11} and $\sqrt{u_{11}}$, respectively. The resulting transverse energy spectra are shown in Figure 5.15 (a).

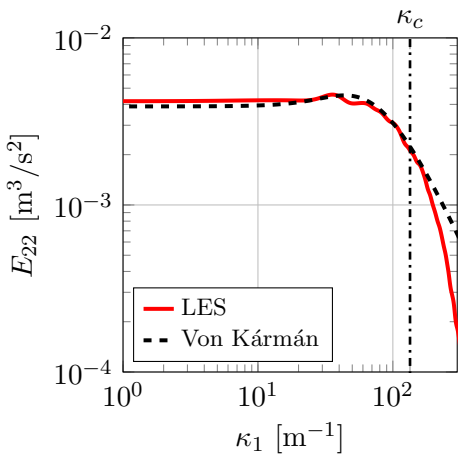

(a) Least squares fit of von Kármán transverse spectrum to transverse spectrum from the turbulence interaction simulation background flow.

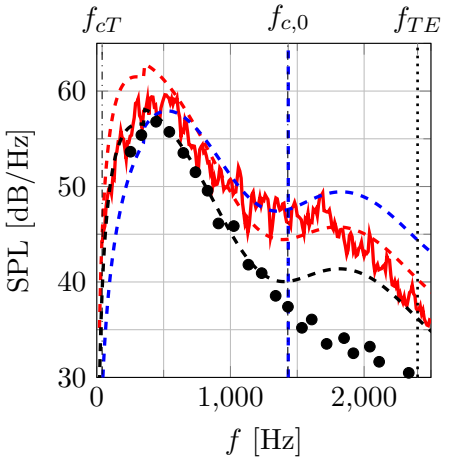

(b) Comparison of noise emissions. Dashed lines: analytical solution [15] computed with isotropic spectrum (red), anisotropic approximation (blue) and input parameters of Paterson [97] (black), respectively. Solid line: LES. Symbols: Measurements of Paterson [97].

Figure 5.15: Impact of turbulence anisotropy on noise emissions for an observer at the overhead position $\theta = 90°$.

When the fitted model spectrum is used in conjunction with the Amiet's analytical noise prediction method [15], a result is obtained as shown by the dashed blue line in Figure 5.15 (b). The prediction as obtained from the LES collapses well over the entire range where also a collapse between the experimental measurements and the corresponding analytical result is observed. At frequencies $f > 1250$ Hz, the results obtained from the LES start to consistently predict lower SPL than the analytical solution, similarly to the experimental values which also show lower SPL than the analytical model at frequencies in excess of 1250 Hz. This result increases the confidence that the thickness effect, i.e. the reduction of noise emissions at high frequencies, is present in the LES, and that the deviation from experiment is primarily associated with the difference of the transverse energy spectrum of the turbulent flow present in the simulation and in the experiment. The effect of redistribution of energy by the change of the ratio of the axial to transverse integral length scale I_{11}/I_{22} is retained, as also shown by Gea-Aguilera [103].
In order to investigate the noise emissions for the remaining observer angles, the spectra were integrated over 1/3rd octave narrowbands and normalized by the bandwidth. The resulting directivities are shown in Figures 5.16 (a) to (d) for bands centred at 400, 800,

1200 and 1600 Hz. Solid lines represent results obtained from the LES, with the line width chosen to reflect a 95% confidence interval, based on the variance $\pm + 0.25$ dB observed in the convergence study documented in Section 3.2.2. Dashed lines illustrate the analytical predictions with the isotropic model spectrum of von Kármán using I_{11} and $\sqrt{u_{22}}$ as input parameters, and dotted lines illustrate the effect of using the von Kármán model spectra, fitted to the transverse spectrum of the simulated flow, for the analytical solution. For the purpose of comparison against experiment, the measured directivity results of Paterson and Amiet [97] are illustrated by black symbols. As the measured data is not 1/3rd octave narrowband integrated and normalized, an arbitrary scaling factor has been applied to facilitate qualitative comparison.

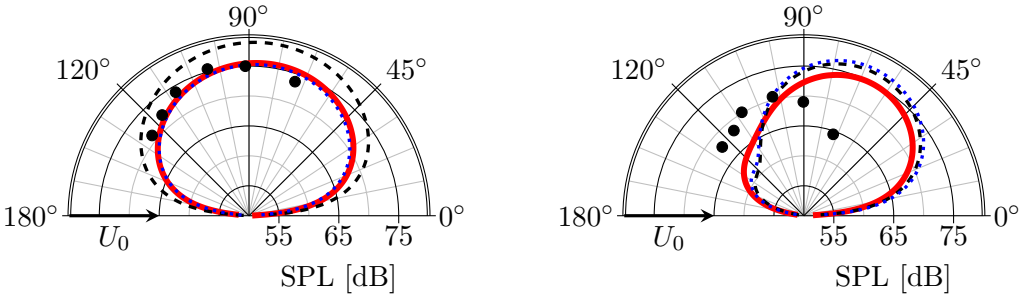

(a) $f = 400$ Hz.

(b) $f = 800$ Hz.

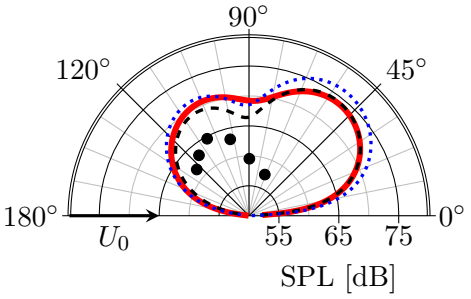

(c) $f = 1200$ Hz.

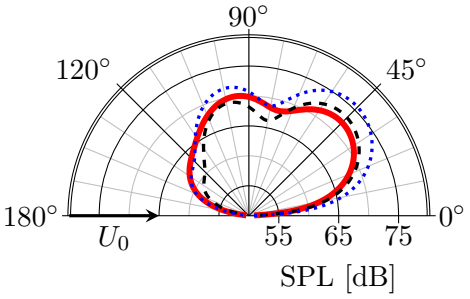

(d) $f = 1600$ Hz.

Figure 5.16: Directivity plots with LES (solid, line width representative of 95% confidence interval due to finite signal length), analytical Eqn. (2.33): isotropic (dashed), anisotropic approximation (dotted). Experimental values of Paterson and Amiet [97] (symbols), scaled with arbitrary constant factor.

As Figure 5.16 (a) shows, the results obtained from the LES for 400 Hz match the analytical solution with the anisotropic approximation as input, while the analytical solution for isotropic flow is approximately 5 dB higher for all observer angles. This is interpreted to be caused by the transverse energy spectra of the LES exhibiting considerably less energy at these frequencies than the isotropic case. Consequently, the noise is reduced, a conclusion which is supported by the fact that the analytical solution with the von Kármán model fitted to the E_{22} matches much better. It is observed from the qualitative comparison to the measured values from the experiment of Paterson and Amiet [97] that the directivity pattern is reasonably well reproduced.

At larger frequencies, shown in Figures 5.16 (b) - (d), the differences increase, although the noise in the spectra and the only approximate fit of the anisotropic transverse spectrum make conclusions on the cause for the differences difficult. Nevertheless, the deviations from the directivities as computed by the model are within 5 dB, and the directivity patterns are reasonably well matched, although the match is slightly better on the upstream than on the downstream side. This is likely attributable to the effect of thickness, as Gea-Aguilera [103] reported a more pronounced reduction of noise emissions for downstream observer angles.

Considering the directivity pattern as indicated from the experimental measurements of Paterson and Amiet [97], it is observed from Figure 5.16 (b) that the upstream directivity lobe is present more prominently at a frequency of 800 Hz than either the data from LES or the analytical model would indicate. By 1200 Hz, shown in Figure 5.16 (c), the downstream lobe has almost completely vanished, which is in line with observations of Gea-Aguilera [103] regarding the stronger thickness effect for downstream observer angles. Taking into account the arbitrary constant scaling factor, it is concluded that there is a qualitative agreement between LES, experiment and analytic model of Amiet [15] regarding the shapes of the upstream lobe at both 800 and 1200 Hz, which is considered as indication that the non-compactness effect, which contributes to the shape of the lobe, is captured by the LES. It is further concluded that the noise reduction by the aerofoil thickness is not captured sufficiently, which predominantly affects higher frequency and downstream noise emissions.

In order to quantify the noise emission reductions attributable to the aerofoil thickness in more detail, the sound power level was computed following the definition given by Blandeau and Joseph [237]:

$$\mathrm{PWL}(f) = 10\log_{10}\left(\frac{4\Pi(\omega)\delta\omega}{\mathcal{P}_{ref}}\right), \tag{5.4}$$

with a reference power of $\mathcal{P}_{ref} = 1 \times 10^{-12}$ W, $\delta\omega$ being the bandwidth, and

$$\Pi(\omega) = \frac{2\pi r_0^2}{\rho_0 c_0}\int_0^{\pi} S_{pp}(r_0, \theta, \omega)\sin(\theta)\,\mathrm{d}\theta, \tag{5.5}$$

which assumes that the effects of mean flow convection on noise emissions are negligible. A more direct comparison to the results of Chaitanya *et al.* [94], who conducted an extensive parameter study on the effects of aerofoil geometry on the interaction noise, is facilitated by plotting the PWL over the dimensionless frequency ft_a/U_0. The comparison is conducted in Figure 5.17 using the analytical results with the model spectrum of von Kármán fitted to the transverse energy spectrum, as this has been shown to be more representative of the noise emissions produced by the simulated flow. In addition, the reduction in interaction noise due to aerofoil thickness as postulated by the theory of Gershfeld [114],

$$\Delta\mathrm{PWL}(f) = 10\log_{10}\left(e^{\pi\frac{ft_a}{U_0}}\right), \tag{5.6}$$

is computed by subtracting $\Delta\text{PWL}(f)$ from the analytical result. The reduction measured by Chaitanya *et al.* [94], for a NACA 0012, at a mean flow velocity of $U_0 = 60$ m/s and a turbulence intensity of 2.5%, is also shown by subtraction from the analytical result.

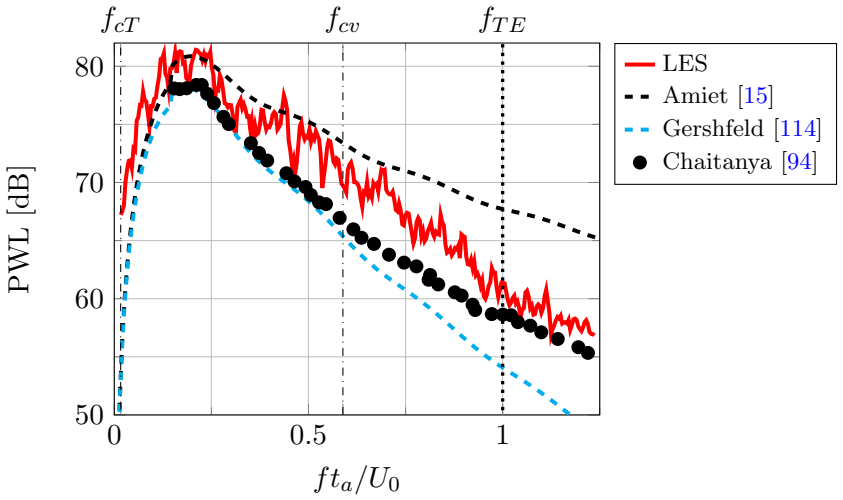

Figure 5.17: Evaluation of power level spectra. Dotted line indicates values for which the self-noise has been shown to be dominant [94].

When compared to the experimental results of Chaitanya *et al.* [94] for the noise reductions, it is apparent that while the noise reductions attributable to thickness do exist, they are not as large as those observed in experiment. While Chaitanya *et al.* obtain reductions in excess of 5 dB for $ft_a/U_0 > 0.4$ close to those computed using Gershfeld's correction, the LES results do show reductions of 5 dB only for $ft_a/U_0 > 0.75$. Additional studies are recommended to identify whether this result is due to the LES method, or whether it is caused by the particular shape of the energy spectrum discussed in Section 5.2.2. Qualitatively, however, the reduction is reasonably close in shape to Amiet's spectrum with Gershfeld's correction. It can be concluded that the self-noise of the simulated aerofoil is negligible compared to that of the experimental case, which is expected considering the chosen meshing and simulation method.

5.4.2 Comparison with incompressible case

In order to support the earlier identification of compressible effects, such as the non-compactness effects, the problem of the infinite aerofoil interacting with turbulence was investigated using an incompressible solver. All numerical parameters were kept the same, and data was acquired for the same amount of time, 0.5s of physical time. The distribution of pressure coefficient and mean square unsteady pressure values along the chord are shown in Figure 5.18 (a) and (b).

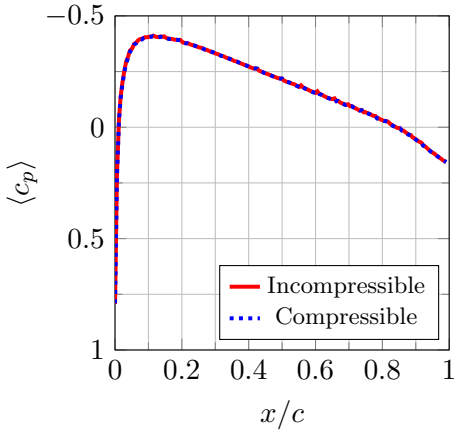

(a) Time averaged c_p.

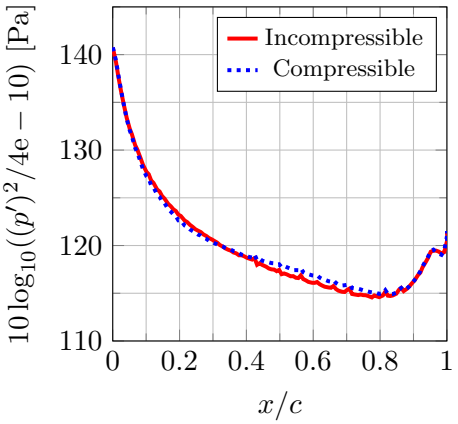

(b) Mean squared unsteady pressure on aerofoil surface.

Figure 5.18: Mean and unsteady surface pressure distributions.

As expected due to the low Mach number of the investigated case, the values of the time-averaged pressure coefficient $\langle c_p \rangle$ for the incompressible and the compressible simulation essentially collapse in Figure 5.18. Only small differences exist regarding the distribution of the mean square unsteady pressure values, which are exhibited primarily on chordwise values of $0.4 < x/c \leq 0.8$. However, as these discrepancies are very small relative to the pressure fluctuations at the leading edge, any impact on the radiated noise is expected to be negligible.

An increase of the mean squared pressure on the aerofoil surface is observed for chord positions at $x/c > 0.9$. This increase is related to the refinement of the mesh close to the trailing edge, and the small scale eddies resolved in this region. While this represents a source of error, the pressure fluctuations are 20 dB below the fluctuations at the leading edge, and can therefore be considered negligible.

Close examination of the distribution of p^2 yields a pattern of regular, albeit small discontinuities for values of $0.4 < x/c < 0.9$. The cause of these discontinuities is investigated in Figure 5.19.

It is apparent that the discontinuities are associated with the presence of tetrahedral cells in the unstructured mesh, which are required by the mesh to adapt to the aerofoil curvature, which at this point is slightly diverging from the prevalent direction of the grid lines. Considering this behaviour, the boundary layer at this point must be considered un-physical, and thus the current methodology is not suitable for the investigation of trailing edge noise, which is primarily caused by the interaction of boundary layer turbulence with the singularity of the trailing edge. However, since the focus of this research is the investigation of leading edge noise, this un-physical behaviour is considered negligible, as the resulting fluctuations are more than two orders of magnitude smaller than the pressure fluctuations on the leading edge.

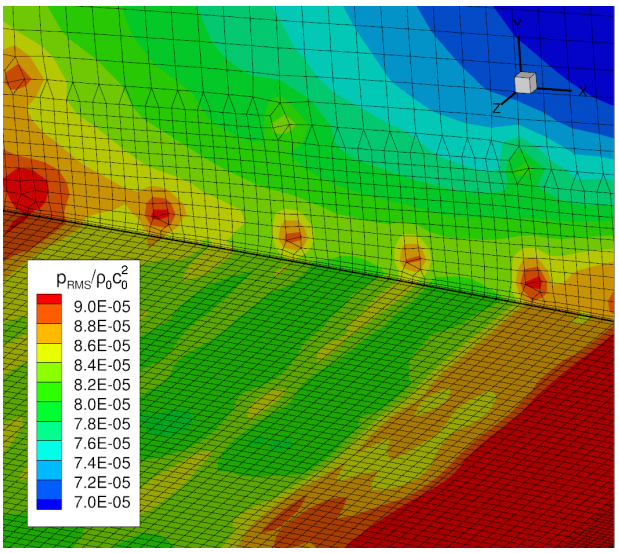

Figure 5.19: Dimensionless unsteady pressure RMS values on the late suction side of the unloaded, thick aerofoil.

As discussed in Section 5.3.2, the turbulence produced by the inlet-grid turbulence creation method is not divergence free, and thus contains hydrodynamic pressure fluctuations. A method to identify the dominant type of pressure fluctuations, as used extensively by Mish [238], are the cross-correlations of the fluctuating pressure on the aerofoil surface. The pressure cross-correlation is defined as

$$R_{pp}(x_0, x_1, \tau) = \frac{\langle p'(x_0, t)p'(x_1, t+\tau)\rangle}{\langle p'(x_0, t)p'(x_1, t)\rangle} \tag{5.7}$$

where x_0,x_1 are two points on the aerofoil surface. For a statistically stationary flow, R_{pp} becomes independent of t, and is therefore a function of the delay time τ only for any two values of x_0 and x_1. The pressure cross-correlations were computed for the compressible and the incompressible LES and are shown in Figures 5.20 (a) and (b), respectively, for a value of $x_0/c = 0.01$. This value was chosen to allow qualitative comparison with the experimental results of Mish [238]. In order to facilitate the interpretation of the correlation lobes, a dashed line indicates time delays representative of the convective transport of an eddy from x_0 to x_1, i.e. $(x_0 - x_1)/U_0$, whereas a solid line illustrates the time delay associated with the inviscid response of the aerofoil, i.e. the time $(x_0 - x_1)/c_0$.

It is apparent that the inviscid response of the aerofoil dominates the cross-correlations in both simulations. In addition, while the main lobe of R_{pp} in the case of the compressible simulation is aligned with the line of the time delay associated with the speed of sound, the main lobe of the incompressible case is not. Instead, the lobe of the incompressible simulation indicates an infinite speed of sound, which is to be expected from an incompressible simulation. As such, the response of the aerofoil becomes un-physical at high frequency.

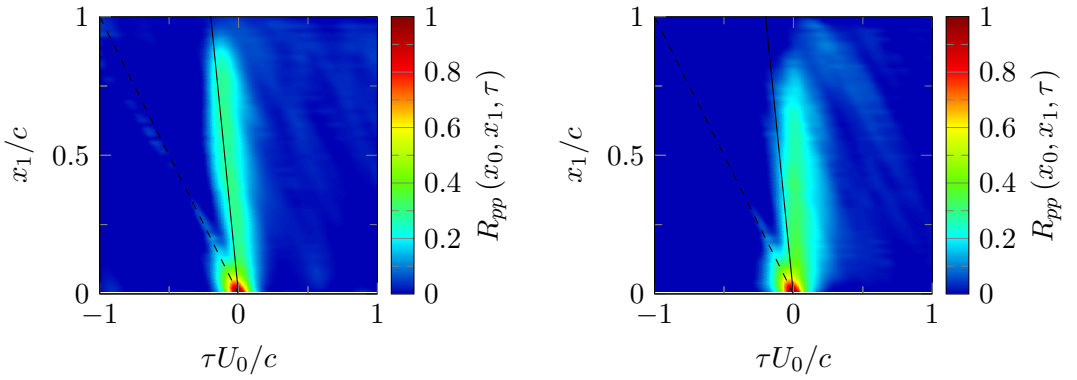

(a) Compressible flow simulation.

(b) Incompressible flow simulation.

Figure 5.20: Unsteady pressure cross-correlation for $x_0 = 0.01x/c$. Dashed line indicates correlations due to eddy convection with mean flow, solid line indicates correlation due to inviscid aerofoil response.

The effect of this un-physical aerofoil response on the far-field noise radiation is investigated in Figures 5.21 (a) and (b) for the downstream as well as the overhead observer positions at $\theta = 60°$ and $\theta = 90°$. For additional context, vertical lines have been added where the thin dash-dotted lines illustrate the highpass cut-off frequency due to the finite signal length f_{cT} as well as the mesh cut-off frequency for vortical waves f_{cv}, and thin dotted lines illustrate the frequency f_{TE} where experiments have found trailing edge noise to be dominant [94].

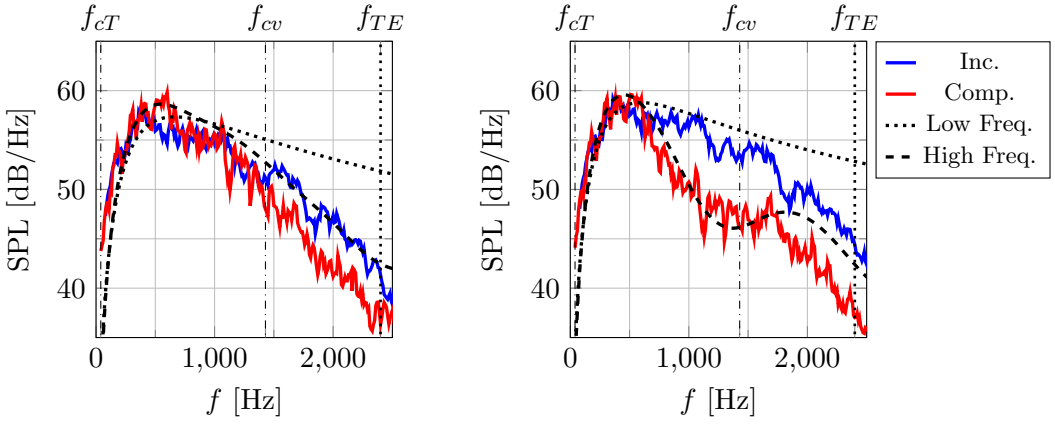

(a) $\theta = 60°$.

(b) $\theta = 90°$.

Figure 5.21: Far-field noise results at downstream and overhead observer angles with incompressible LES (Inc., blue), compressible LES (Comp., red), Amiet's model Eqn. (2.33) with low frequency response function Eqn. (2.35) (Low Freq., dotted, black) and high frequency response function Eqn. (2.36) (High Freq., dashed, black.)

From Figure 5.21 (a) it is observed that the noise predictions from the four different solutions collapse to within 2.5 dB below a frequency of 1000 Hz, but diverge increasingly for higher frequencies. Conversely, from Figure 5.21 (b) it is observed more clearly that the prediction from the incompressible LES tends to coincide with the prediction of Amiet's model Eqn. (2.33) using the low frequency response function Eqn. (2.35), whereas the prediction from the compressible LES tends to coincide with the results of the analytical model using the high frequency response function (2.36).
For the overhead observer position, this is found to be the case even for frequencies which are beyond the mesh cut-off frequency for vortical waves, f_{cv}, which is expected as the dissipative and dispersive errors for acoustic waves at this frequency are much lower than for vortical waves, as discussed in Appendix B. Consequently, non-compactness effects can be expected to be exhibited by the compressible LES, as acoustic waves are propagated on the numerical mesh in the vicinity of the aerofoil virtually unchanged. However, for the purpose of assessing the capability of a compressible LES on an unstructured grid to replicate non-compactness effects, only the frequency range $f_{min} < f \leq f_{cv}$ is considered, ruling out effects due to un-physical source mechanisms.
Figures 5.22 (a) and (b) show the SPL for the upstream observer positions $\theta = 120°$ and $\theta = 150°$ where the frequencies associated with the non-compactness dips as defined by Eqn. (2.46) are within the trust region of the simulation results, as established in Section 5.4.1.

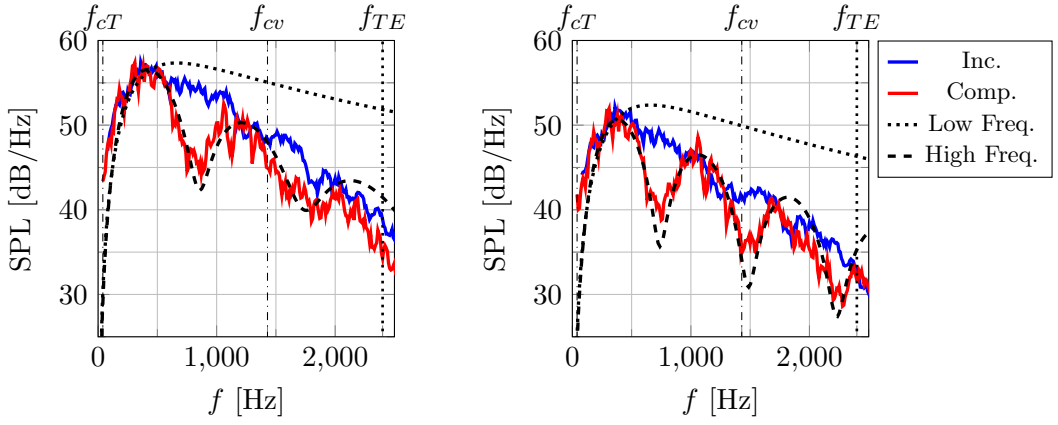

(a) $\theta = 120°$. (b) $\theta = 150°$.

Figure 5.22: Far-field noise results at upstream observer angles with incompressible LES (Inc.), compressible LES (Comp.), Amiet Eqn. (2.33) with low frequency response function Eqn. (2.35) (Low Freq., dotted) and high frequency response function Eqn. (2.36) (High Freq., dashed).

From Figures 5.22 (a) and (b) it is apparent that the non-compactness effect dips as exhibited by the Amiet' model Eqn. (2.33) with the high frequency response function as defined by Eqn. (2.36) are well replicated in the LES noise results of a compressible flow. Conversely, the noise results as obtained from the LES of an incompressible flow do not exhibit the dips associated with non-compactness, which is expected as the

physical mechanism responsible for them is absent in the incompressible simulation. Qualitatively, the SPL spectrum as obtained from the LES of an incompressible flow is similar to the spectra of the analytical model using the low frequency response function as defined by Eqn. (2.35), although the spectra diverge with increasing frequency and observer angle. As both the assumption of incompressibility as well as the use of the low frequency response function in Amiet's analytical model [15] is not appropriate in the high frequency regime, discussion of this discrepancy is omitted.
Considering the qualitative agreement of the shape of the upstream lobe with experiment, as shown in Figures 5.16 (a) - (c), the quantitative agreement of the local minima in the SPL spectra in terms of frequency with those present in the analytical solution using high frequency response function Eqn. (2.36), the disappearance of these minima in the SPL spectra upon introduction of the assumption of incompressibility and the resulting un-physical response of the aerofoil as shown in Figure 5.20 (b), as well as the absence of potential numerical reflections of acoustic waves from the derefinement zones as discussed in Appendix D.1, it is concluded that the compressible LES of an infinite aerofoil on an unstructured mesh is capable of capturing the non-compactness effects of an aerofoil.

5.4.3 The noise emissions of a thick, loaded aerofoil

As it is intended to incorporate the aerodynamic and aeroacoustic effects of a tip vortex in the investigation of the finite aerofoil in a turbulent flow, the finite aerofoil has to be loaded, as a symmetrical, unloaded aerofoil will not develop a tip vortex. For the purpose of establishing a baseline for comparisons, a compressible simulation of the turbulence leading edge interaction problem for a thick, loading aerofoil was conducted, and is presented here. As the chosen angle of attack is still relatively small, the deviation towards models assuming unloaded aerofoils such as Amiet's analytical method is expected to be minor, in particular in the light of recent investigations showing that the effect is weak in a majority of cases [12]. However, other investigations have shown significant effects of the angle of attack when the turbulence is anisotropic [100; 113].
For the investigation of angle of attack effects, an infinite NACA 0012 aerofoil was immersed in a turbulent flow at an angle of attack of $\alpha = 3°$. Since time averaged pressure coefficients and mean square unsteady pressures, as well as the correlations do not deviate significantly from the changes which can be expected to be associated with a change in angle of attack, only the end result of noise emissions is shown here, as the noise emission spectra and directivities are the quantities most of interest in this investigation. Figure 5.23 (a) - (c) show the noise emission spectra for an observer at the downstream and overhead positions $\theta = 30, 60, 90°$ as computed using a compressible LES.

As expected for an aerofoil with a relatively small angle of attack of $\alpha = 3°$ [100], the noise emission spectra do not significantly deviate from those obtained for $\alpha = 0°$,

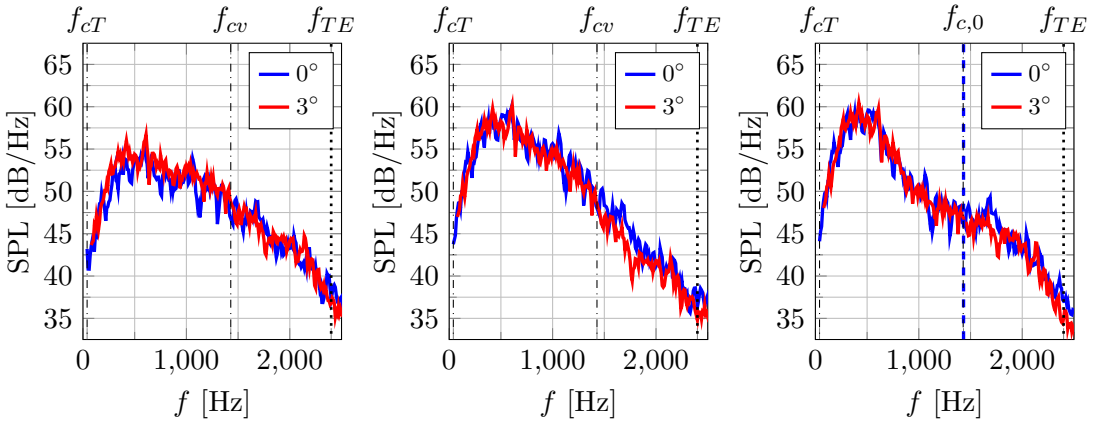

(a) $\theta = 30°$. (b) $\theta = 60°$. (c) $\theta = 90°$.

Figure 5.23: LES far-field noise results at downstream and overhead observer angles for aerofoil at an angle of attack of 0°, 3°.

with the differences largely within the noise of the spectra. The downstream observer positions $\theta = 120°$ and 150° are shown in Figures 5.24 (a) and (b).

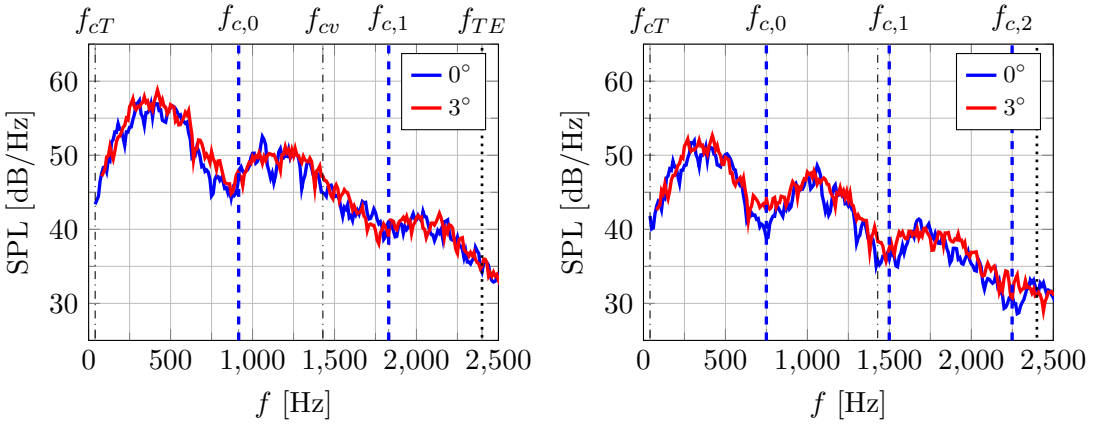

(a) $\theta = 120°$. (b) $\theta = 150°$.

Figure 5.24: LES far-field noise results at upstream observer angles for aerofoil at an angle of attack of 0°, 3°.

Again the effects of the angle of attack on the far-field noise results are small, and almost entirely within the noise of the spectra. However, there are indications of meaningful differences for the upstream observer angles at the frequency of the first non-compactness dip $f_{c,0}$.

A more meaningful insight into the effect of the angle of attack on noise emission of an aerofoil can be gained when the directivities are examined. Here, a notable asymmetry can be expected from the aerofoil at 3 degrees of attack, while the aerofoil at zero angles of attack should exhibited a perfectly symmetrical directivity pattern. The noise spectra were computed for 360 degrees at one degree intervals and are shown in Figure 5.25 (a) - (d) for 1/3rd octave bands centred at 400, 800, 1200 and 1600 Hz, with the line widths

chosen to reflect a conservatively estimated LES uncertainty ±0.5 dB, based on the convergence study documented in Section 3.2.2.

The differences in terms of the directivity patterns are, as expected, small, and do exceed the 95% confidence interval of ±0.5 dB only for some observer angles above 400 Hz. Qualitatively, they are in agreement with the findings of Gea-Aguilera [103], who found that small angles of attack result in a shift of the directivity pattern, with an increase of the noise levels below the aerofoil, and a decrease of the noise level above the aerofoil. Therefore, the methodology presented here can be expected to deliver reliable noise predictions of thick, loaded aerofoils in turbulent flows.

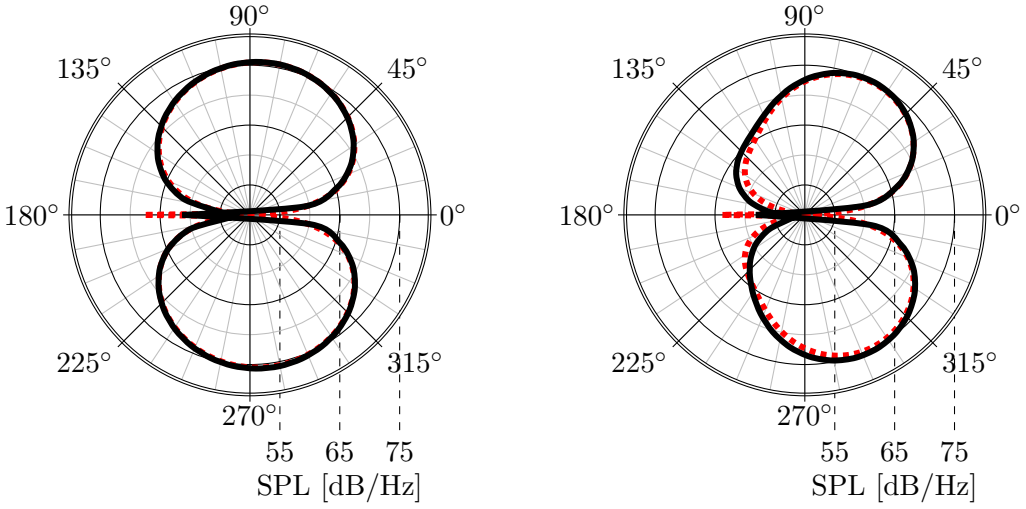

(a) $f = 400$ Hz.

(b) $f = 800$ Hz.

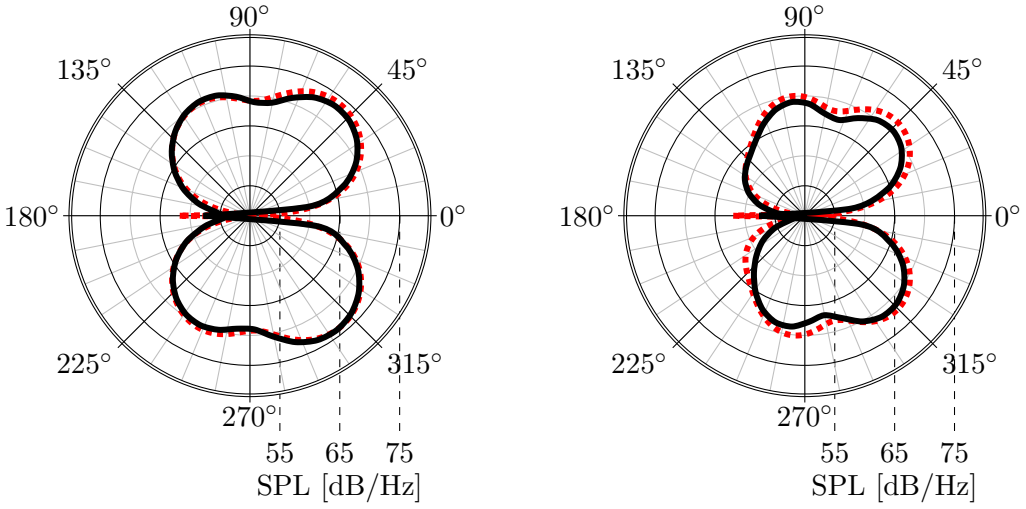

(c) $f = 1200$ Hz.

(d) $f = 1600$ Hz.

Figure 5.25: Directivity plots of the infinite aerofoil at $\alpha = 0°$ (dotted) and at $\alpha = 3°$ (solid). Line widths representative of 95% confidence interval due to finite signal length.

5.5 Summary

This chapter presented the application of the turbulence creation method proposed by Blackmore [13] for the case of a leading edge interaction problem. For this purpose, a simulation setup suitable for both reproducing the aerodynamics of an isolated aerofoil as well as the investigation of its aeroacoustic properties was developed. Geometric and flow parameters were chosen in such a way that comparison to the experiments of Paterson and Amiet [97] was facilitated. Aerodynamic properties of the flow were assessed against those of the experiments. Leading edge turbulence interaction was analysed and compared against literature. Noise emissions were computed by extracting the surface pressure signals on the aerofoil, and using an Ffowcs-Williams and Hawkings [118] solver to compute the far-field noise levels. A comparison was conducted against both the experimental values, as well as to the analytical solution for the noise results of an unloaded, infinite flat plate given by Amiet [15]. Thickness effects were assessed using the correction factors proposed by Gershfeld, as well as the experimental results of Chaitanya *et al.* [94]. Additional simulations of an incompressible comparison case, as well as of an aerofoil at a small angle of attack were presented. The main conclusions from this chapter are:

- When applied to an aeroacoustic investigation, the inlet grid turbulence creation method is found to create turbulence which is qualitatively comparable to the turbulence created by grids in experiment while also not introducing spurious noise sources, as shown in Appendix D.1. However, similar to the use of grids in experimental campaigns, the exact replication of flow conditions using the inlet-grid turbulence creation method proves difficult. While initial parameter studies allowed matching to the experimental values of Paterson and Amiet [97] to some degree, significant deviations remain, in particular in terms of the energy spectra of the transverse component E_{22}, which primarily determines noise emissions.

- The LES on an unstructured mesh is capable of capturing the turbulence interaction with the leading edge qualitatively correctly, allowing to investigate such phenomena to a high level of detail.

- The anisotropic energy spectra produced by the inlet-grid turbulence creation method lead to significant differences of the resulting noise emissions from the analytical predictions using Amiet's flat plate theory [15], which assume an isotropic flow. When an energy spectrum fitted to the transverse spectrum from the simulation is used as an input for Amiet's theory, the fit with the noise emissions from the simulation is considerably improved, allowing a better determination of the thickness effects. It is concluded that using a model spectrum for the representation of the energy spectrum in the non-universal energy-carrying range may lead

to considerable under or over prediction of noise emissions if analytical methods are used.

- Comparison of the incompressible case to the compressible simulation shows that pressure fluctuations associated with the inviscid response of the aerofoil dominate over the hydrodynamic pressure fluctuations associated with the turbulent flow. It is concluded that the unstructured, compressible LES is applicable for the investigation of non-compactness effects on acoustic emissions of complex geometries.
- Directivity patterns obtained for the unloaded aerofoil are in reasonable qualitative agreement with analytical results, and the direction of the poles is well predicted. Results for the loaded aerofoil show the expected shift in the directivities. As such, a baseline for the investigation of a finite, thick aerofoil in Chapter 6 was established.

Thus, this Chapter has established the inlet-grid turbulence creation method as a tool suitable for the generation of turbulent flows to study turbulence interaction noise. Furthermore, the use of a compressible LES on an unstructured mesh for the investigation of leading edge turbulence interaction noise has been assessed and partially validated for the first time, allowing geometries that are more complex than the infinite aerofoil to be studied in the future.

Chapter 6

Finite aerofoils in simulated grid turbulence

The inlet-grid turbulence creation method, proposed by Blackmore [13], has been shown in Chapter 4 to be capable of producing turbulence of realistic spectra and development. This method was then applied in Chapter 5 to the classical turbulence leading edge interaction problem of an aerofoil, immersed in a turbulent flow. It was shown that the turbulence distortion at the leading edge, and the resulting noise emissions including thickness and non-compactness effects, can be predicted using a compressible LES on an unstructured mesh.
In the present chapter, the inlet-grid turbulence creation method is applied to the problem of the noise emissions of a finite, thick, loaded aerofoil. The main aims of this chapter are:

- To demonstrate the application of the inlet-grid turbulence creation method to a problem of considerable complexity, which is difficult to investigate with or outside the capabilities of commonly used analytical or numerical tools.
- To conduct an aerodynamic analysis to verify that all the phenomena of importance, such as leading edge turbulence interaction, as well as tip vortex formation and interaction with surrounding turbulence, are reproduced.
- To investigate the effects of the presence of the leading edge tip singularity, as well as of the tip vortex on far-field noise levels and directivities.

The chapter is structured as follows. In Section 6.1, the setup of the numerical simulation is presented, and the changes which had to be made when adapting the infinite aerofoil problem setup to that of a finite aerofoil are discussed. As the aerodynamics of a finite, loaded aerofoil immersed in a turbulent flow are of a considerable complexity, an

investigation with a focus on the distortion of the turbulence at the leading edge, as well as the interaction of the tip vortex with the turbulent flow, is conducted in Section 6.2. Subsequently, in Section 6.3, the aeroacoustic results of the finite aerofoil simulation are given. Finally, the chapter is summarized in Section 6.4.

6.1 Simulation setup of the finite aerofoil problem

In order to minimise the differences of the finite aerofoil setup with that of the infinite aerofoil to facilitate comparison, the case setup was chosen to be as similar as possible and is illustrated in 6.1.

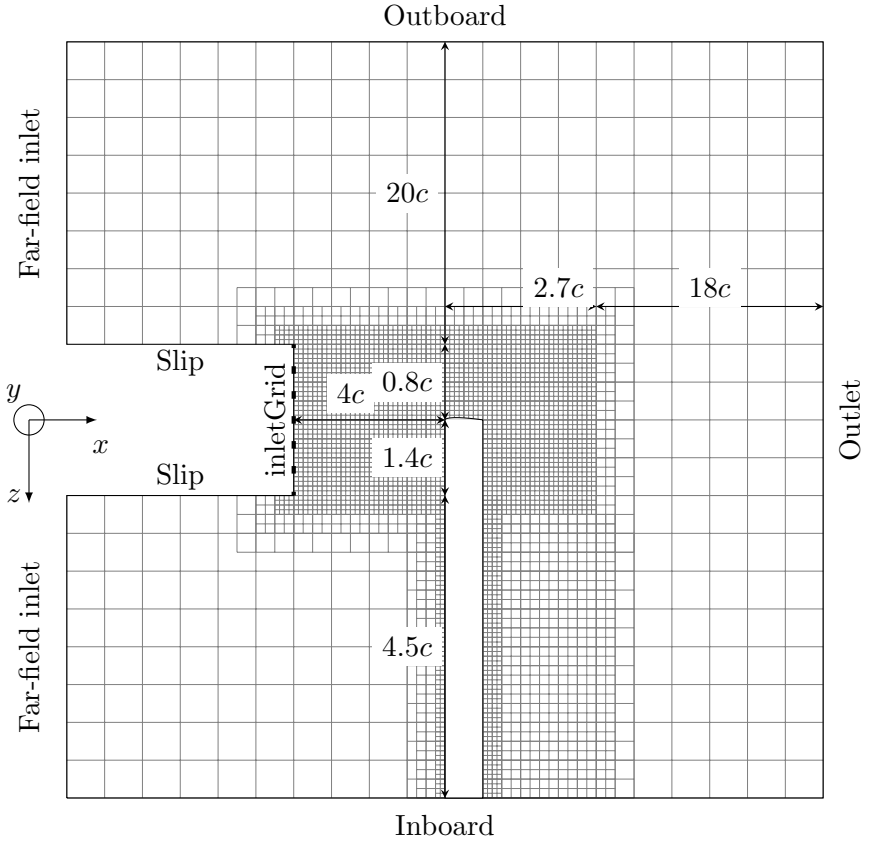

Figure 6.1: Domain setup of finite aerofoil interaction simulation. Thick dashes illustrate position and approximate size of grid bars. The origin of the coordinate system coincides with aerofoil leading edge at the tip. Illustration is not to scale.

In the xy plane, i.e. normal to the aerofoil span, domain geometry and boundary conditions are exactly the same as those illustrated in Figure 5.1 for the infinite aerofoil case. The aerofoil was placed at the same distance to the inlet grid, equivalent to $16G_p$, as for the infinite aerofoil interaction studies discussed in Chapter 5, to facilitate comparison. The mesh was created following the same unstructured meshing approach as in the case of the infinite aerofoil. More information on this approach is given in Appendix C.1.

However, due to the presence of the aerofoil tip, the boundary conditions in the spanwise direction had to be adapted. In case of the free-field direction of the span, i.e. outboard with $z < 0$, the domain was extended by adding a sufficiently large turbulent flow domain to obtain a homogeneous turbulent flow region for the expected extent of the tip vortex. Beyond the turbulent domain, the domain was extended for 20 chord lengths. An assessment of potential non-uniform grid reflections has been conducted and is documented in Appendix D.1, finding that grid reflections can be expected to be negligible. The same far-field boundary conditions were applied as for the "Top" and "Bottom" patches of the infinite aerofoil interaction simulation, given in Table 5.1. The boundary conditions chosen for the finite aerofoil case are given in Table 6.1.

Patch	Variable	Type	Definition
Wall	U	Dirichlet	$\mathbf{U}(x_0) = (0, 0, 0)$
	p	Neumann	$\mathrm{d}p/\,\mathrm{d}x = 0$
Inlet	U	Dirichlet	$U_1 = \dot{m}/(A_p\rho_0), U_2 = U_3 = 0$
	p	Neumann	$\mathrm{d}p/\,\mathrm{d}x = 0$
Far-field inlet	U	Dirichlet	$U_1 = \dot{m}/(A_p\rho_0), U_2 = U_3 = 0$
	p	Neumann	$\mathrm{d}p/\,\mathrm{d}x = 0$
Slip wall	U	Dirichlet	$\mathbf{U} = (U_1, U_2, 0)$
	p	Neumann	$\mathrm{d}p/\,\mathrm{d}x = 0$
Outlet	U	Mixed	Eqn. (3.17)
	p	Mixed	$\mathrm{D}p/\mathrm{D}t \approx 0$, See Appendix C.2, [229]
Outboard	U	Neumann	$\mathrm{d}U/\,\mathrm{d}x = 0$
	p	Mixed	$\mathrm{D}p/\mathrm{D}t \approx 0$, See Appendix C.2, [229]
Inboard	U	Dirichlet	$\mathbf{U} = (U_1, U_2, 0)$
	p	Mixed	$\mathrm{D}p/\mathrm{D}t \approx 0$, See Appendix C.2, [229]
Front, back	U	Neumann	$\mathrm{d}U/\,\mathrm{d}x = 0$
	p	Mixed	$\mathrm{D}p/\mathrm{D}t \approx 0$, See Appendix C.2, [229]

Table 6.1: Boundary conditions of finite aerofoil interaction simulation.

For the inboard plane of the finite aerofoil, i.e. $z > 0$, several options were considered. The most computationally inexpensive option would be to keep the boundary coinciding with the edge of the inlet grid turbulence generator patch. However, such a boundary would be required to be able to accommodate the turbulent fluctuations in a physical manner. As there is no corresponding boundary on the other side of the domain any

more, the periodic boundary condition used in the previous infinite aerofoil simulations, presented in Chapter 5, cannot be applied. A symmetry boundary condition on this patch, while able to support the turbulent fluctuations, would impose an non-physical symmetry on the turbulence at this boundary, and furthermore act as a mirror for the acoustical emissions of the aerofoil. Finally, applying a slip wall boundary condition for the velocity, coupled with the non-reflective *waveTransmissive* boundary condition was not considered applicable for a boundary immersed in the turbulent flow as the interaction of turbulent fluctuations with suppressed spanwise velocity component at the intersection of the aerofoil with the boundary would constitute an unknown source of error. The most physically realistic, yet numerically expensive approach would be to use a wall boundary condition, which is what would be present in experimental conditions. Due to the high numerical cost, but also because of the unknown effect of wall reflections, this approach was not considered.

With these considerations, it was decided to extend the aerofoil out of the turbulent domain and apply a slip wall boundary condition for the velocity, and the *waveTransmissive* boundary condition of Poinsot and Lele [229] for the pressure on the inboard boundary. The aerofoil was extruded for a length of $4.5c$, to allow incorporation of a large derefined volume between the turbulent domain containing the aerofoil tip, and the inboard plane boundary condition. This supports the reduction of acoustic reflections from the inboard plane boundary condition by dissipating the acoustic waves. Additionally, the considerable span of the aerofoil supports the physical applicability of the slip wall velocity boundary condition, as the aerodynamics of the aerofoil can be considered to be two-dimensional at such distances to the tip [135], and therefore the velocity component normal to the inboard plane is minimized.

In order to produce a tip vortex, the aerofoil is set at an angle of attack of $\alpha = 3°$. As mentioned above, care was taken to isolate the tip from both the effects of the shear layer between the potential far-field flow, and the interaction effects of this shear layer with the aerofoil itself. As the analysis conducted in Section 5.2.1 has shown that the turbulent flow is, at least in terms of the mean flow velocities, reasonably homogeneous up to distances of one grid period from the centre of the jet, the tip of the aerofoil at $x, y, z = 0$ is separated to the edges of the turbulent flow by at least three grid periods in the transverse directions and the outboard direction, and by more than $5G_p$ in the inboard direction. Since it was expected that the shear layer would cause strong interactions with the aerofoil, the edge of the shear layer is at this point 3 grid periods distant from the tip of the aerofoil in the spanwise direction.

In order to minimize the effect of the other end of the aerofoil, which does not end in a tip, the aerofoil was extended by $4.5c$ before it meets the far-field boundary, where a slip boundary condition for the velocity combined with a wave transmissive condition for the pressure is applied. As the flow over the distance of $4c$ starting from the inboard boundary conditions is steady, no significant leading edge noise is produced. Refinement over the section of the aerofoil outside the turbulent domain is kept at a minimum to reduce

computational expense. The mesh is only refined enough to allow sufficient geometry resolution, as well as adequate aerodynamic behaviour. Assessment of the aerodynamics of the aerofoil sections in the steady domain as well as their influence on the sections within the turbulent jet, which are the main focus of this Chapter, is documented in Appendices E.2 and E.3.

Since keeping refinement levels in the vicinity of the aerofoil the same as in the case of the infinite aerofoil was found to lead to an excessive number of cells, the mesh around the aerofoil had to be slightly derefined when compared to the infinite aerofoil cases. Figures 6.2 (a) and (b) highlights the major mesh differences, the effects of which are investigated in Sections 6.2 and 6.3.1.

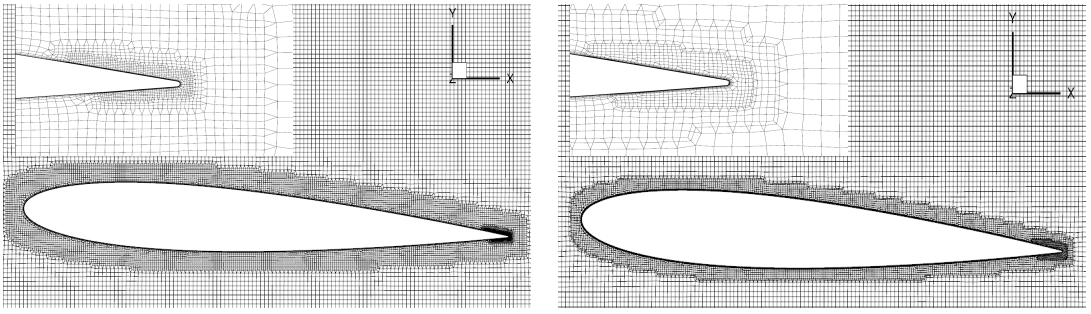

(a) Infinite aerofoil. (b) Finite aerofoil.

Figure 6.2: Mesh normal to span. Details in upper left show trailing edge mesh.

In terms of the meshing parameters discussed in Appendix C.1, the change in refinement in the aerofoil vicinity consistent in reducing the number of the diffusion level during mesh generation from 4 to 2. This resulted in the number of cell layers around the aerofoil, which are of the refinement level on the aerofoil surface, to drop from 10 to 5. Besides this decrease in the extent of the more finely resolved mesh around the aerofoil, the mesh is equivalent to that used for the turbulence interaction cases discussed in Chapter 5, with $y^+ < 0.5$ not exceeded within the boundary layer mesh, while the non-dimensional viscous lengths in the streamwise and spanwise directions were below $x^+ = z^+ < 40$. A mesh sensitivity study with all refinement levels reduced by one was conducted, and is documented in Appendix D.2. Considering that the interaction of the turbulence with the leading edge of the aerofoil was still reproduced reasonably well, it is expected that the reduction in refined layers around the aerofoil has a negligible impact.

Figure 6.3 illustrates the mesh at the trailing edge of the tip of the aerofoil, where the round tip narrows to the trailing edge radius, motivating the choice of a meshing methodology capable of capturing blunt trailing edges.

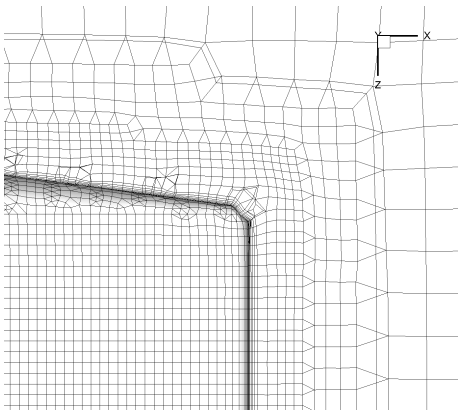

Figure 6.3: Trailing edge discretisation at the tip of the finite aerofoil.

It is observed that the mesh generation algorithm led to a small deformation of the trailing edge geometry at the tip, as the trailing edge radius is on the order of $\Delta_c \approx 1$ for the finite aerofoil. While a higher mesh refinement may be able to better resolve the small radii at this position, it was found to be impractical to refine the mesh sufficiently while maintaining acceptable computational cost. The final mesh consisted of 79×10^6 cells, consisting of 96.8% hexahedral, 2.3% prism, 0.1% pyramidal and 0.001% tetrahedral cells.

The solver *rhoPimpleFoam*, implemented in OpenFOAM v3.0, was used, which conducts pressure-velocity coupling using the merged PISO [201] and SIMPLE [202] algorithms. A slight reduction in the time step was necessary compared to the time step used for the simulation of the infinite aerofoil discussed in Chapter 5 since the finite aerofoil was found to be setup is associated with a higher mean flow velocity. Thus, the time step achieved was $\Delta_t U_0/c = 3.1 \cdot 10^{-4}$. On the computer cluster IRIDIS 5, using 520 processors, an average of 10 s of computational time was required for one time step. This resulted in a computational time of approximately 11.5 days per $tU_0/c = 31$ simulated physical non-dimensional time, not accounting for queuing time.

6.2 Aerodynamic analysis of a finite aerofoil in a turbulent flow

While there have been simulations investigating formation and development of the tip vortex of a finite aerofoil in steady flow conditions [131; 132; 133; 239], as discussed in Section 2.5, no numerical study of the problem of a finite aerofoil immersed in a turbulent flow has been conducted to date. As such, no numerical data for comparison exists both in terms of the aerodynamics and the aeroacoustics. While it is generally assumed in analytical and numerical models of leading edge noise that the interaction of turbulent eddies with the leading edge is independent of spanwise geometry, if the geometry of the leading edge is constant within the spanwise correlation length [165],

few investigations have been conducted to validate this assumption, in particular for thick, loaded aerofoils. Some authors investigated the influence of spanwise variation of turbulent inflow conditions [124; 240], but due to the considerable meshing complexity of an aerofoil tip, no numerical investigations have investigated the turbulence interaction with the tip of an aerofoil. This section presents an investigation of the leading edge interaction of turbulence with a finite aerofoil, and the comparison to a comparable infinite aerofoil problem, i.e. an infinite aerofoil at the same angle of attack.
A second topic of interest from both an aerodynamic as well as an aeroacoustic perspective is the tip vortex, in particular its formation and its impact on the aeroacoustics. As discussed in Section 2.5, several experimental investigations [137; 138; 139; 140] have focussed on the behaviour of a tip vortex in a turbulent flow. This section will present results from the first LES to investigate the formation of a tip vortex in a homogeneous turbulent flow and compare the findings to experimental measurements.

6.2.1 Homogeneity of the turbulent flow

As discussed in Section 6.1, the domain had to be adapted considerably to accommodate the finite aerofoil problem. This resulted in a deviation of the mean flow parameters of the turbulent flow from the turbulent flow in the infinite aerofoil problem. The parameters are compared in Table 6.2, for a position $x/c = -1$.

Flow quantity	Infinite aerofoil	Finite aerofoil
U_0	67.2 m/s	71.2 m/s
Re_c	1.03×10^6	1.09×10^6
$\sqrt{u_{11}}/U_0$	3.91%	4.98%
$\sqrt{u_{22}}/U_0$	3.85%	4.80%
I_{11}	3.64 cm	3.01 cm
I_{22}	1.11 cm	0.46 cm

Table 6.2: Flow parameters of infinite aerofoil simulation versus finite aerofoil simulation.

As discussed in Section 5.2, while a parameter study with the simple turbulence development setup shown in Figure 3.1 can be used to establish suitable grid parameters for a turbulent flow of the desired flow quantity values to some degree, a more complex domain setup will lead to unavoidable discrepancies from the targeted flow values. With the current setup for the finite aerofoil, a turbulent flow is retained which exhibits a slightly increased mean flow velocity, and slightly decreased turbulent stresses. This is considered to be due to the addition of two shear layers in the spanwise direction, and

the related change in the mean flow development in the domain. The quantity most effected by the change in boundary conditions is the integral length scale. Considering the parameter studies of Honnery *et al.* [241], this is reasonable, as the largest scales are inherently more strongly affected by the boundary conditions than any other scale.
Prior to the investigation of leading edge turbulence interaction or of the turbulent tip vortex, the homogeneity of the turbulent flow is assessed. In order to evaluate the homogeneity of the turbulence, the mean velocities and Reynolds stress components were computed for a plane one chord length upstream of the leading edge. At this point, the potential effects of the aerofoil are expected to be minimal, considering the discussion of Section 5.3.1. The extents of the plane in y and z direction were chosen to include parts of the shear layer, in order to provide information of the size of the area of homogeneous flow.
Figures 6.4 (a) - (c) show the homogeneity of the mean velocities $\langle U_i \rangle$. The inhomogeneity parameter I_ϕ, defined in Eqn. (3.23), is computed for all components relative to the value of the mean axial velocity at $y = 0$, $z = 0$. Dashed lines indicate the outlines of the aerofoil.

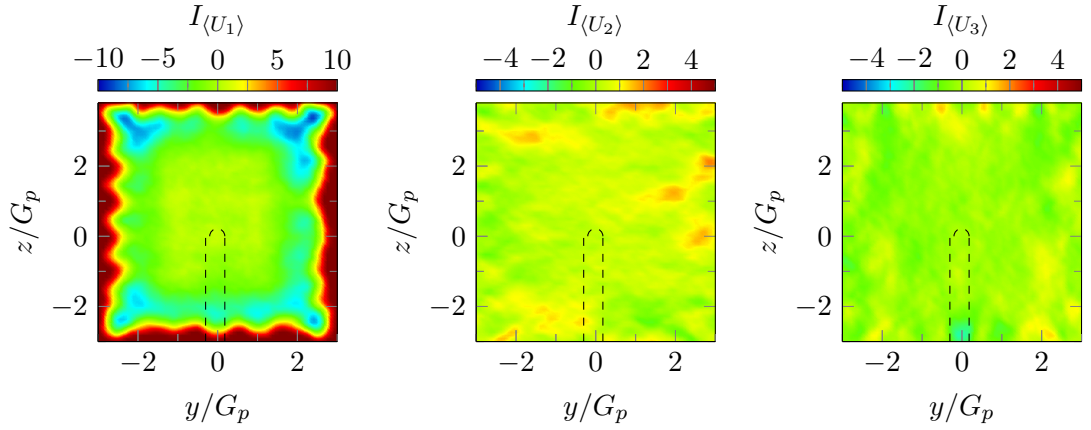

(a) Axial velocity. (b) Transverse velocity. (c) Spanwise velocity.

Figure 6.4: Homogeneities of the mean velocities one chord length upstream the leading edge.

It is found that the setup as used for the simulation results in a fairly homogeneous flow in terms of the mean velocities in a large area in the centre of the grid. The transverse mean velocities in particular are highly homogeneous, with deviations in the centre of the grid largely within 1% of $\langle U_1 \rangle$. Except for the shear layer areas in the distribution of $\langle U_1 \rangle$, no patterns attributable to either aerofoil or grid are visible in the distribution of the mean velocity inhomogeneities in the vicinity of the aerofoil. It is noted that the extent of the domain shown in Figures 6.4 (a) - (c) is wholly contained within the finely refined turbulent flow domain, which also contains the shear layer areas in a manner analogous to the turbulence interaction case investigated in Chapter 5. As such, the investigation of the potential influence of the mesh derefinement zones in Appendix D.1 is applicable, where it was shown that the shear layer is solely due to the mean flow

gradient between the turbulent jet flow and the steady far-field, and that no numerical grid reflections can be identified.
Figures 6.5 (a) - (c) show the distribution of the normal RST components in the same plane. The quantities were normalized relative to their value at $y = 0$, $z = 0$.

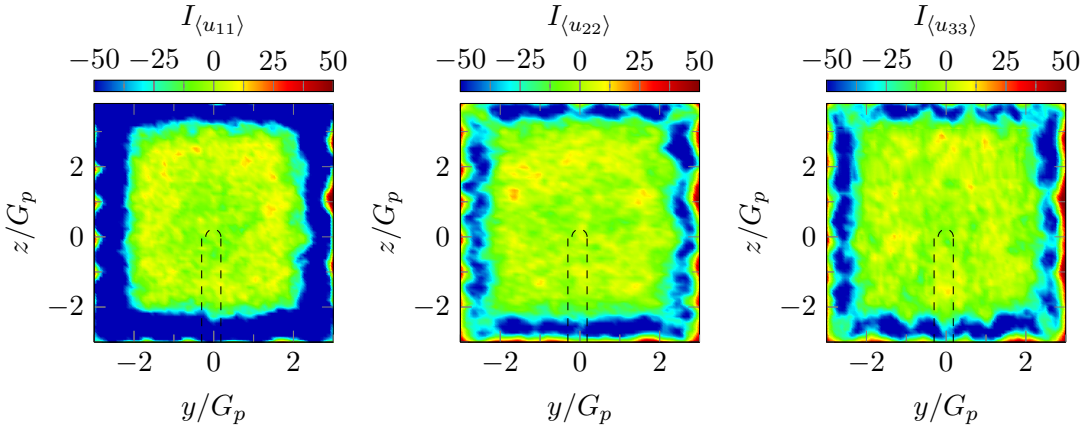

(a) Axial RST component. (b) Transverse RST component. (c) Spanwise RST component.

Figure 6.5: Homogeneities of RST components one chord length upstream the leading edge.

It is apparent that the inhomogeneities of the turbulent stresses are, for the most part, within 10% of the value at $y = 0$, $z = 0$. It is concluded that the aerofoil is immersed in largely homogeneous turbulence up to a position of $z/G_p = 2.5$. Thus, for the purpose of simulating the tip of an aerofoil in a homogeneous turbulent flow, the setup used in this simulation is appropriate.

6.2.2 Leading edge turbulence interaction

Having established the homogeneity of the turbulent flow, the interaction of the turbulence with the leading edge is investigated. As discussed previously for the case of an infinite aerofoil in Section 5.3.1, before the turbulence directly interacts with the leading edge, it passes through a region of rapidly changing mean flow conditions, which are caused by the potential effect of the aerofoil.
In order to investigate the effect of the finiteness of the aerofoil geometry on the mean flow velocities, Figure 6.6 (a) - (c) show the development of the mean flow components $\langle U_i \rangle$ in the $y = 0$ plane upstream the leading edge. Since the angle of attack of the aerofoil is small, the stagnation point does not shift significantly from the $y = 0$ plane. In order to facilitate analysis of the rapidly changing mean flow conditions, a logarithmic scale is chosen for the streamwise direction. Dashed lines indicate the position $x/r_{LE} = 1$.

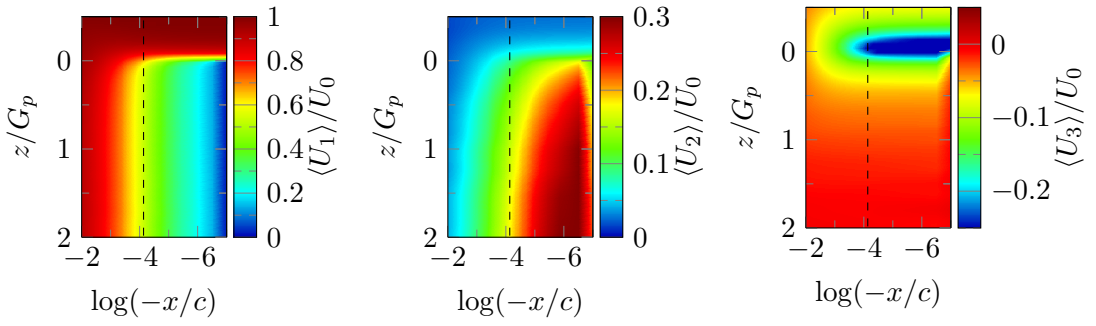

(a) Axial velocity. (b) Transverse velocity. (c) Spanwise velocity.

Figure 6.6: Mean velocity components in the $y = 0$ plane upstream the leading edge. Dashed lines indicate the position $x/r_{LE} = 1$.

It is immediately apparent that the finiteness of the aerofoil varies in its effect on the mean flow velocities. As shown by Figure 6.6 (a), the axial velocity $\langle U_1\rangle$ decreases towards the leading edge in a manner independent of the spanwise coordinate, decreasing close to zero at the last point just off the aerofoil surface. $\langle U_2\rangle$, shown in Figure 6.6 (b) displays a strong dependence on the spanwise coordinate, which is caused by the aerofoil loading, which approaches that of an infinite aerofoil as the distance to the tip is increased. Finally, $\langle U_3\rangle$, shown in Figure 6.6 (c), is close to 0 at almost all points, with the exception of the tip, where the potential effects of the flow around the tip result in a non-zero value. Both $\langle U_2\rangle$ and $\langle U_3\rangle$ exhibit decreasing values at the positions closest to the leading edge, indicating that the last coordinate shown in Figures 6.6 (a) - (c) is contained within the boundary layer. It is concluded that in terms of mean velocity gradients, the effect of the tip extends at least up to $z/G_p = 1$ for this geometry at this angle of attack.

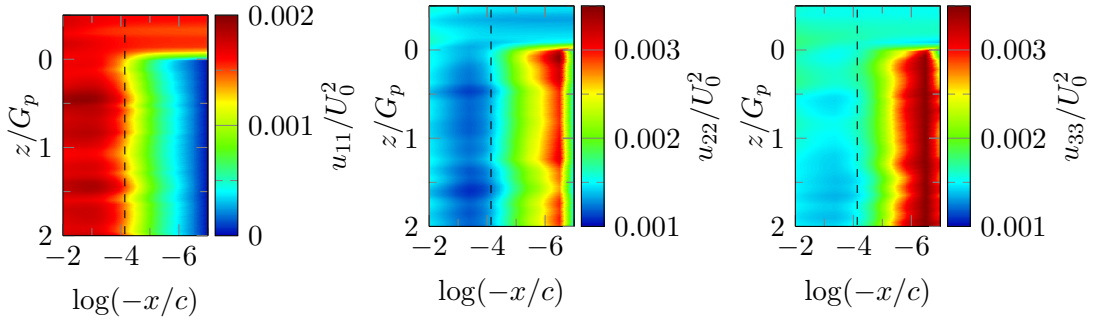

(a) Axial RST component. (b) Transverse RST component. (c) Spanwise RST component.

Figure 6.7: Normal stress components in the $y = 0$ plane upstream the leading edge. Dashed lines indicate the position $x/r_{LE} = 1$.

In order to investigate the effects of the mean velocity gradients on the turbulent stresses, the normal Reynolds stresses on the plane $y = 0$ are shown in Figures 6.7 (a) - (c). As discussed in Section 5.3.1, the majority of the deformation of the turbulent structures happens at distances of the order of the leading edge radius. Thus, a dashed line indicates

the position $x/r_{LE} = 1$ in all plots. Due to the discretization of the aerofoil curvature, the cells closest to the leading edge were found to have a positive x-coordinate, their x-coordinates were set to an arbitrarily small negative value to allow inclusion in the figures below.

Although significant inhomogeneities persist in all normal turbulent stresses, it is apparent that the influence of the tip is much more restricted than in case of the mean flow velocities. Visible variations are only observed for $0 < z/G_p \leq 0.5$. The effect appears to be more pronounced in the axial and transverse component, whereas only a very limited effect can be detected in the spanwise component. The distribution of the turbulent stresses is qualitatively similar to that of the mean axial velocity, as shown in Figure 6.6 (a). As the strongest gradients in the plane $y = 0$ are exhibited by $\langle U_1 \rangle$, it is hypothesized that the development of the Reynolds stresses is largely determined by $\mathrm{d}\langle U_1 \rangle / \mathrm{d}x$.

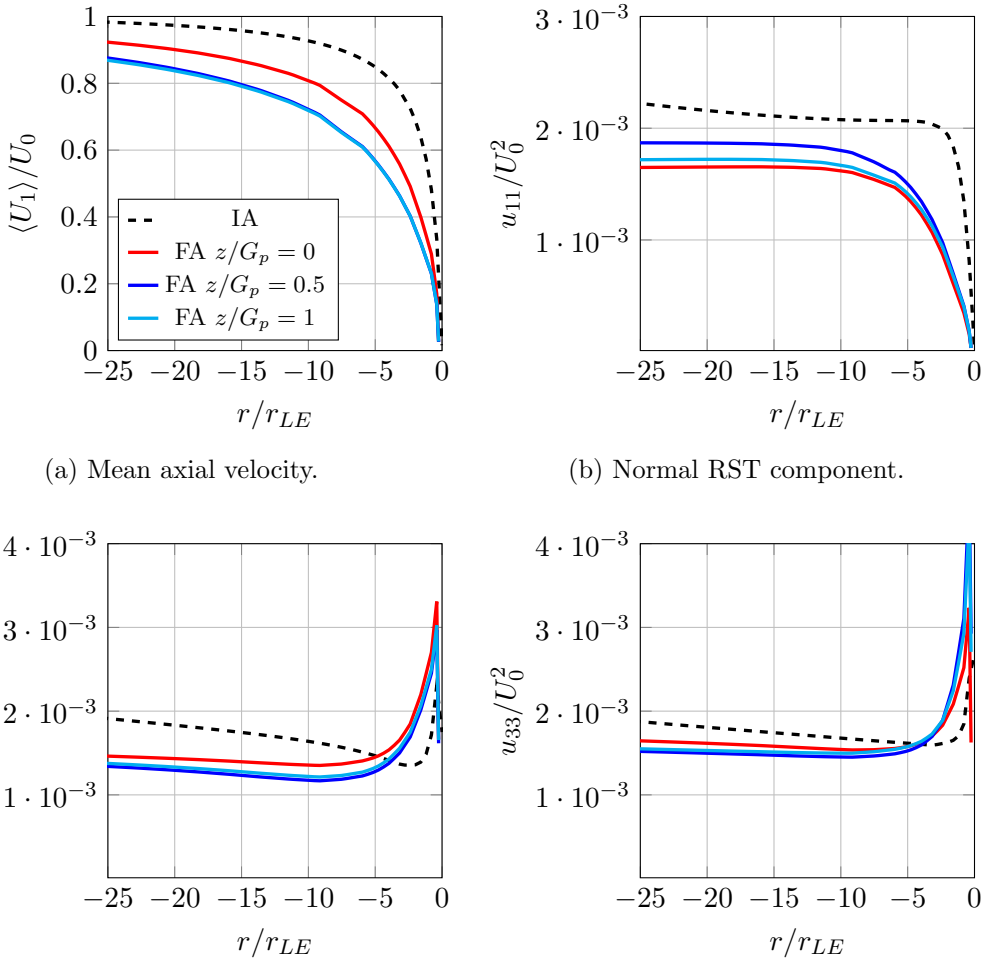

(a) Mean axial velocity.

(b) Normal RST component.

(c) Transverse RST component.

(d) Spanwise RST component.

Figure 6.8: Development of the velocity quantities towards the leading edge. Infinite Aerofoil (IA): dashed, Finite Aerofoil (FA): solid.

In order to investigate quantitatively at which point the mean flow quantities upstream of the finite aerofoil are developing in a manner equivalent to the infinite aerofoil, the axial mean velocity as well as the turbulent stresses are compared in Figures 6.8 (a) - (d). Dashed lines illustrate the development of the respective quantities for the infinite aerofoil, while solid lines indicate the development of the quantities for the finite aerofoil. From Figure 6.8 (a) it is apparent that there is a considerable quantitative deviation of the mean axial velocity $\langle U_1 \rangle$ from the values obtained in the case of the infinite aerofoil at all investigated spanwise locations. As all these locations are quite close to the tip, it is expected that the aerodynamics are still significantly affected by three-dimensional effects due to the tip vortex, as shown in Figures 6.6 (a) to (c). However, it is difficult to assess how large these effects are, as there is a lack of experimental data on mean flow gradients upstream of finite aerofoils. In order to provide some context on the validity of the presented results, a comparison of the surface pressure coefficient along several sections on the wing to the measurements of McAlister and Takahashi [135] is provided in Appendix E. The comparison indicates that the lift is quantitatively under-predicted in the current setup, which will influence the mean flow gradients upstream of the aerofoil.

The effect of the reduced mean flow gradient upstream of the aerofoil on the development of the turbulent stresses is illustrated in Figures 6.8 (b) to (d). The diminished velocity gradients are shown to lead to a more gradual distortion of the turbulent eddies prior to the region of strongest turbulence distortion, which is, in agreement with the experimental findings of Santana [101], restricted to a region of the order of the leading edge radius.

In order to investigate the distortion of the energy spectra in this region, Figures 6.9 (a) - (i) illustrate the development of the one-dimensional energy spectra E_{ii}, relative to the respective values of the energy spectra at the position $x/r_{LE} = -21$, at three positions $z/G_p = 0,\ 0.5$ and 1. Since, unlike in the case of the infinite aerofoil, no spanwise averaging could be conducted in the case of the finite aerofoil, more noise is present in the spectra. As such, any fluctuations below 0.5 dB/Hz are not considered meaningful. Dash dotted lines indicate the mesh cut-off frequency for vortical waves f_{cv}.

Considering the relative energy spectra of the axial component, shown in Figures 6.9 (a) - (c), it is observed that there is little difference between the tip position at $z/G_p = 0$ and the two positions further inboard. This is expected, as the geometry can be considered to be constant in terms of its effect on correlation length scales in the axial direction, as all axial scales are equally affected by the presence of a upstream body in the flow. Minor differences are hypothesised to be caused by inhomogeneities in the flow, which are not eliminated in this case due to the lack of spanwise averaging, as well as due to minor differences in terms of the mean flow gradient distribution as shown in Figure 6.7 (a).

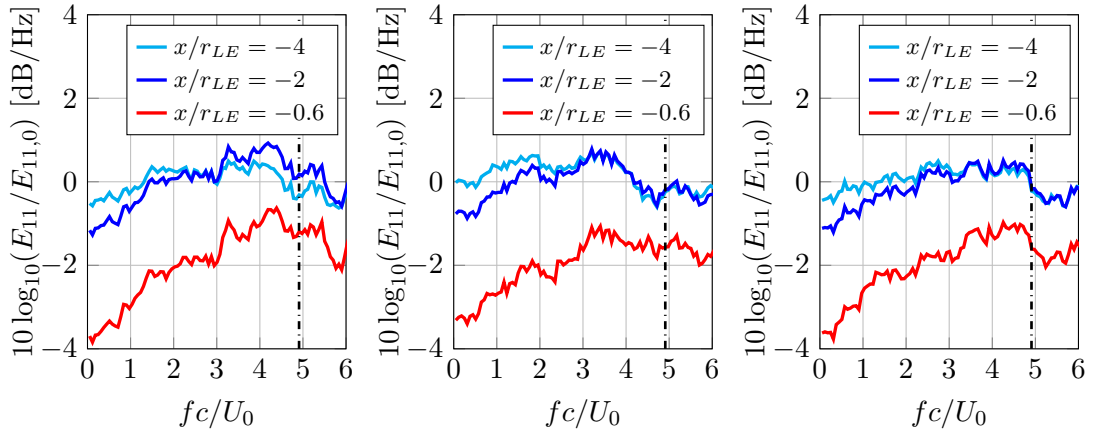

(a) Relative E_{11} at $z/G_p = 0$. (b) Relative E_{11} at $z/G_p = 0.5$. (c) Relative E_{11} at $z/G_p = 1$.

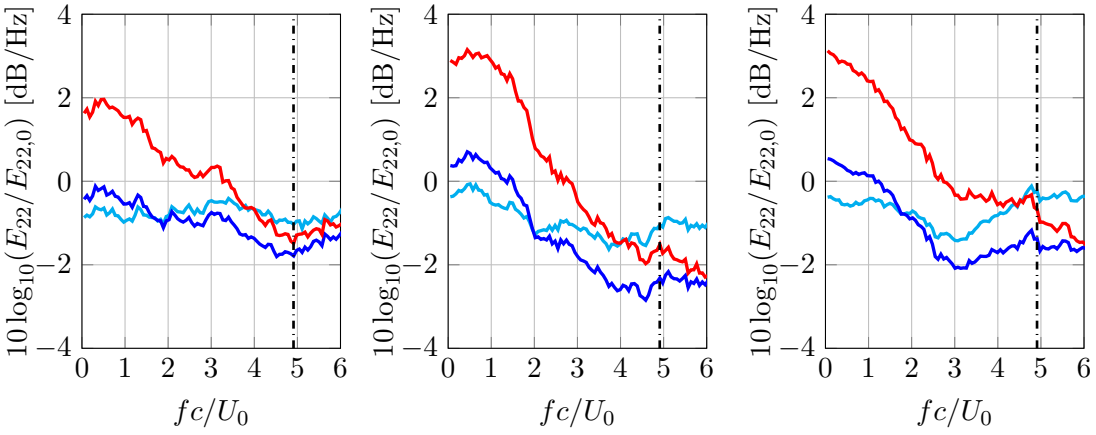

(d) Relative E_{22} at $z/G_p = 0$. (e) Relative E_{22} at $z/G_p = 0.5$. (f) Relative E_{22} at $z/G_p = 1$.

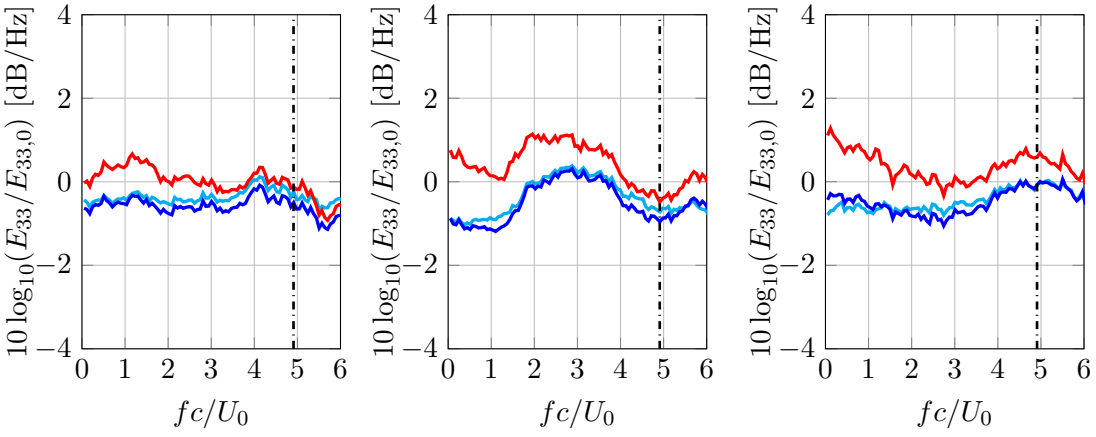

(g) Relative E_{33} at $z/G_p = 0$. (h) Relative E_{33} at $z/G_p = 0.5$. (i) Relative E_{33} at $z/G_p = 1$.

Figure 6.9: Development of the one-dimensional energy spectra, normalised by their values at $x/r_{LE} = -21$, towards the leading edge at $x/G_p = 0$ at three positions along the span. Dash dotted line indicates mesh cut-off frequency for vortical waves.

The development of the relative energy spectra of the transverse component, shown in Figures 6.9 (d) - (f), exhibits the largest change in the spanwise direction. This change is particularly prominent at low frequencies, i.e. $fc/U_0 < 2$ which are representative of the largest fluctuating motions. It is hypothesised that at these scales, the change in aerofoil geometry with span is having an effect on the turbulence distortion, although this appears to be limited to the tip-most sections. However, due to the significant noise present in the spectra related to the limited sampling time, further studies are recommended to ascertain this observation.
Finally, the development of the relative energy spectra of the spanwise component, shown in Figures 6.9 (g) - (i) is observed to show indications of larger distortion of the turbulent eddies as the distance to the tip is increased. However, the fluctuations likely associated with noise as well as flow inhomogeneities are also observed to be relatively large. Further investigations, potentially placing the aerofoil at larger distances to the turbulent grid, or using longer sampling times to improve convergence of the spectra, is recommended to facilitate more detailed and conclusive analysis.

6.2.3 Tip vortex analysis

A loaded finite aerofoil produces a tip vortex, which is due to pressure gradient of suction and pressure side. As the present simulation setup not only incorporates a finite, loaded aerofoil, but also a free-stream turbulent flow, it is suited to the investigation of the tip vortex formation processes in a turbulent flow, and its initial development. An experimental investigation very close to the current setup was conducted by Bailey [140]. His experimental setup consisted in a NACA 0012 finite aerofoil, immersed in grid turbulence at a maximum flow speed of 30 m/s. The produced turbulence was, with a ratio of $\gamma_{12} = 1.2$, similarly anisotropic to the turbulence obtained in the current simulations.
In Figure 6.10, the tip vortex and its surrounding turbulence is visualized by means of the Q-criterion at two values. In order to aid the reader, Figures 6.10 (a) and (b) illustrate the location of the detail plots in Figures 6.10 (c) and (d), respectively. As visualizing all of the surrounding turbulence would lead to the tip vortex becoming completely concealed, the turbulent flow is visualized for a small volume containing the tip vortex only and its immediate vicinity. Additionally, the iso-surfaces indicating the lower of the two Q-criterion values are set to be semi-transparent to facilitate identification of the tip vortex.
It is apparent from Figure 6.10 (a) that in the immediate vicinity of the wing up to a distance of a few chord lengths, the tip vortex tube is clearly separated from the surrounding turbulence, as there is a considerable gap between the tip vortex tube and its surrounding turbulence. As such, using the Q-criterion, no visible merging of the external eddy structures with the tip vortex tubes is observed in the vicinity of the aerofoil.

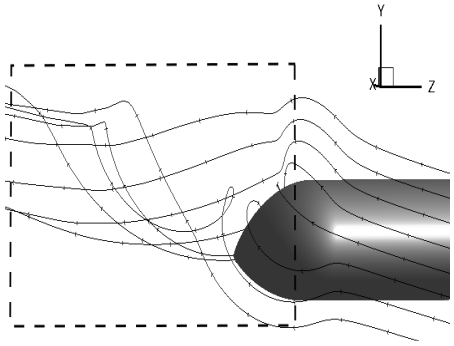

(a) Viewpoint orientation Figure (c).

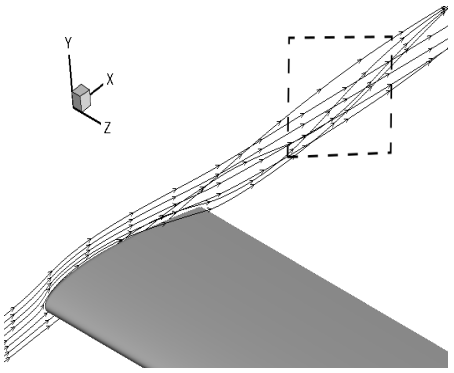

(b) Viewpoint orientation Figure (d).

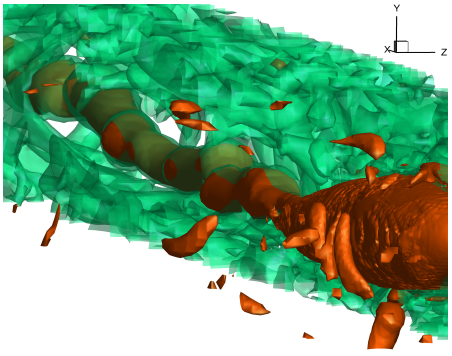

(c) Tip vortex production.

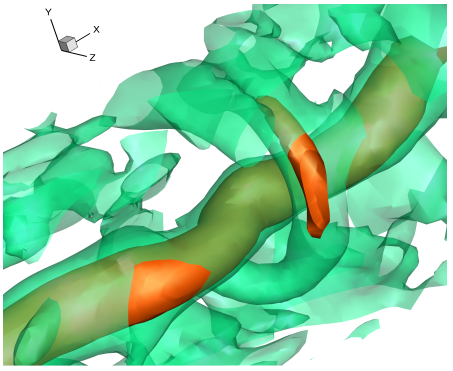

(d) Free-stream vortex wrapping process.

Figure 6.10: Tip vortex - free-stream turbulence interaction. Iso-surfaces of Q-criterion at two values, orange being the higher level, green the lower.

As shown by Figure 6.10 (b), the warping effect which isolated vortex tubes have been reported to have [157; 163] is developing rapidly, considering the mean streamwise flow velocity of $U_0 = 70$ m/s and the fact that examples of eddies deformed in this manner can be found at positions not far downstream of the aerofoil.

The vortex tube, far from having smooth curvature, is in the presence of free-stream turbulence characterized by several kinks, i.e. abrupt changes in trajectory. Figure 6.11 illustrates one example of such a kink. In order to enhance the clarity of the plot, the iso-surfaces corresponding to the tip vortex have been highlighted by thick black lines. Additionally, an eddy structure apparently connected to this kink has been highlighted with an orange dotted line.

Figure 6.11 illustrates the strong curvature which is associated with the kinks of the vortex tube. It is reasonable to assume that these kinks are highly unsteady and are strongly associated with the phenomenon of vortex wandering. The presence of an eddy structure fitting exactly into this kink strongly suggests a coupling of the free-stream turbulence and the generation of kinks in the tip vortex tube.

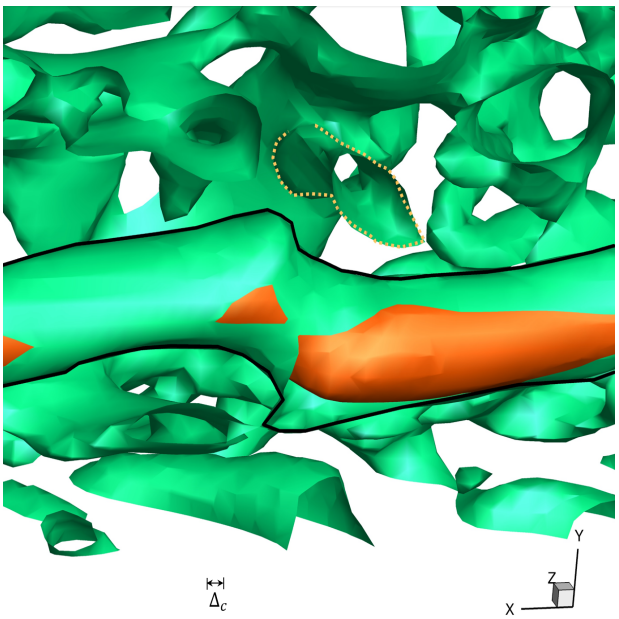

Figure 6.11: Tip vortex kink generation, illustrated by Q-criterion iso-surfaces. Vortex tube highlighted with black lines. Free-stream eddy lying within kink highlighted by orange dotted line. Mesh cell length scale illustrated for reference.

In their experimental investigation of the interaction of tip vortices with surrounding turbulence, Bailey and Tavoularis [242] observed an increase of the vortex wandering amplitude as a the turbulence intensity is increased, and suggested that the wandering is due to transport of the vortex by the free-stream eddies. The present results support this conclusion, and illustrate that the transport may be highly localized depending on the size of the free-stream eddy.

As pointed out by Devenport *et al.* [136], the wandering of the vortex can have considerable effects on the mean flow quantities. Given sufficient wandering, the velocity field will attain a Gaussian form, resulting in a misleading representation of the vortex as a q-vortex, or Batchelor vortex [148]. Considering the strongly turbulent flow present in the current simulations, it is expected that the vortex wandering is significant.

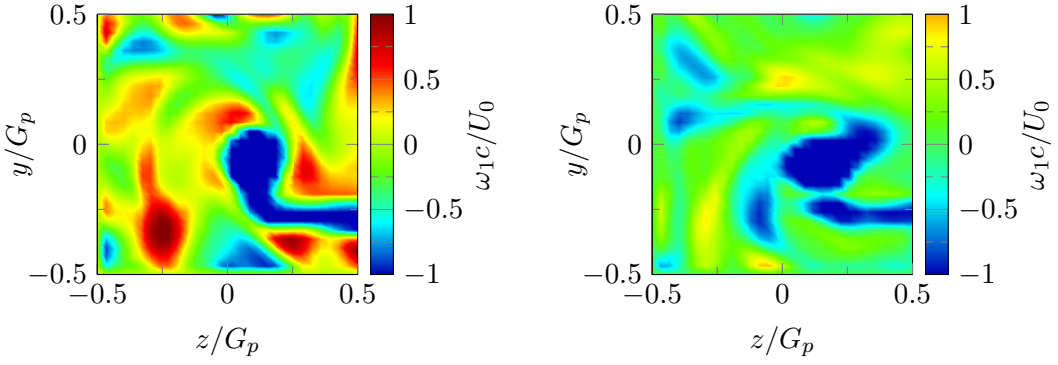

(a) ω_1 at t_1. (b) ω_1 at t_2.

Figure 6.12: Instantaneous axial vorticity for two arbitrary instants in time.

For the purpose of illustrating the tip vortex in its turbulent environment, the axial vorticity ω_1 at two arbitrary instances in time, t_1 and t_2, is shown in a plane at $x/c = 1.5$, normal to the streamwise direction, in Figures 6.12 (a) and (b).
It is immediately apparent from Figures 6.12 (a) and (b) that the tip vortex is characterised by very large negative values of ω_1 relative to the surrounding turbulence. This observation was used to develop a simple algorithm to compute mean flow quantities in the frame of reference of the moving vortex. By determining the maximum value of ω_1 in the $y-z$-plane at each time step, a time history of the vortex positions was obtained. It was then assumed that the surrounding turbulence in the vicinity of the vortex, which is in the process of wrapping around the central vortex tube, is moving with the vortex core. As the sampled plane consisted of a discrete grid of points, the spatial shift of the vortex core from one time step to the next was equal to an integer number of points in the two lateral directions. By applying this shift to the grid points, a time history of the velocity signal in the frame of reference of the moving vortex was reconstructed. Thus, the effects of the vortex wandering on the computation of the mean flow quantities is taken into account by a deterministic algorithm. While this algorithm becomes less applicable with increasing distance from the vortex core, where the flow will not follow the vortex wandering, it is expected to provide reasonable results of the vortex structure and its interaction with the nearest eddies.
For the three sampled planes at $x/c = 1.5$, 2 and 2.5, Figures 6.13 (a), (c) and (e) show the histogram of the vortex positions obtained for 0.5 s simulated physical time, where the discrete points of the sampled grid are used as bins, and the number of points n_p in the most populated bin, $n_{p,\max}$, is used to normalize the distribution. The distribution of the mean circumferential velocity $\langle U_\theta \rangle$, as computed with the algorithm described above in the frame of reference of the moving vortex, normalized by the far-field velocity U_0, for the three planes is shown in Figures 6.13 (b), (d) and (f). Since the application of spatial shifts necessary for the computation of the averaged quantities is associated with a reduction of the area for which information is available, the plots of $\langle U_\theta \rangle$ are slightly shifted relative to the plots of instantaneous quantities.
It is apparent from Figures 6.13 (a), (c) and (e) that the distribution of vortex core positions quickly spreads with downstream distance, which is in agreement with the results of Devenport *et al.* [136]. In all cases the distribution is approximately Gaussian in shape, in agreement with the experimental results of Heyes, Jones and Smith [243]. However, with increasing axial distance, the distribution becomes contaminated by the numerical error. This is related to the limited physical time simulated, which appears to be insufficiently long to produce a completely converged histogram at all vortex positions, including those of low probability. A slight movement of the distributions in the positive z direction is observed, which is a well-known behaviour of wing-tip vortices after formation [140].

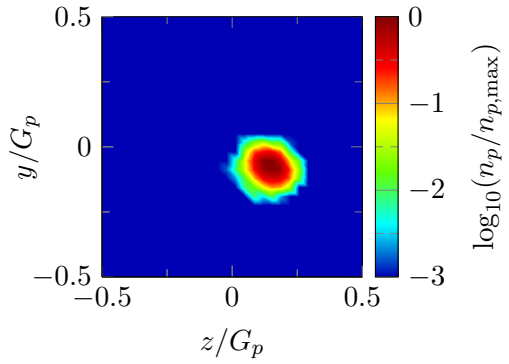

(a) Histogram of vortex positions at $x/c = 1.5$.

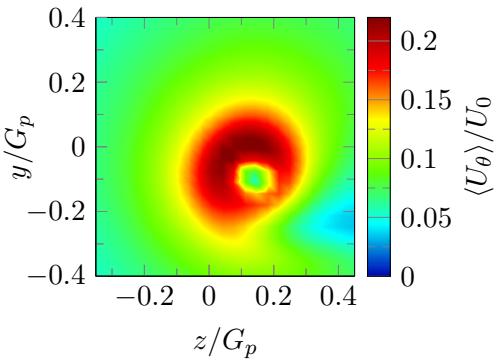

(b) $\langle U_\theta \rangle$ at $x/c = 1.5$.

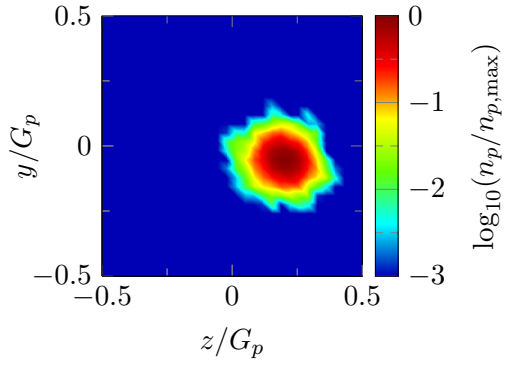

(c) Histogram of vortex positions at $x/c = 2$.

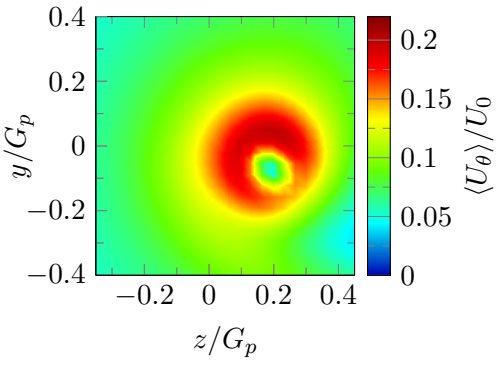

(d) $\langle U_\theta \rangle$ at $x/c = 2$.

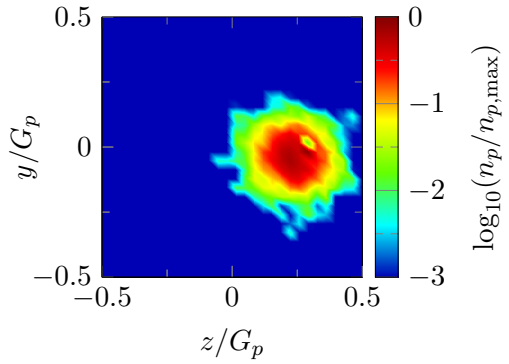

(e) Histogram of vortex positions at $x/c = 2.5$.

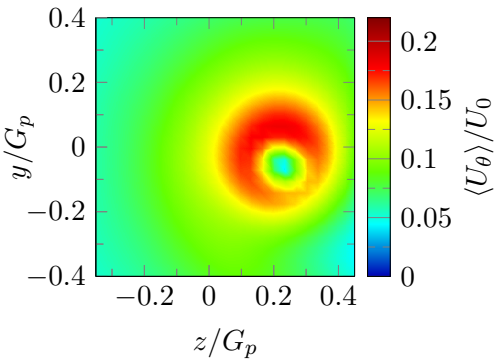

(f) $\langle U_\theta \rangle$ at $x/c = 2.5$.

Figure 6.13: Spatial histograms of vortex core positions and tangential velocity distributions at three positions downstream the trailing edge.

As shown by the contour plots of the absolute perpendicular velocity $\langle U_\theta \rangle$ in Figures 6.13 (b), (d) and (f), the averaging method chosen is capable of neutralising the effects of vortex wandering to a large extent, and allows the structure of the vortex to be investigated in detail. The viscous core of the vortex, characterized by decreasing values of $\langle U_\theta \rangle$, similar to solid body rotation, can be identified in all investigated planes. As such, the vortex structure resembles the well-known model of Lamb-Oseen, as shown in Figure 2.6. The contour plots of $\langle U_\theta \rangle$ indicate that the vortex does not become axisymmetric within the distance investigated, although a trend towards axisymmetry can be

observed. The apparent "C"-shape present at all planes is in agreement with the results of the experimental study of Bailey [140], who found a similar appearance of the iso-lines of the circumferential velocity in the vicinity of the wing. He related this phenomenon to the effect of the spanwise velocity induced over the pressure and suction side of the wing. A quantitative way to investigate the vortex wandering was proposed by Bailey *et al.* [244]. Taking y_v and z_v as the time-dependent deviations of the vortex centre from its mean position in a plane, the wandering frequencies and wavelengths can be examined by means of power spectral densities. Figure 6.14 (a) and (b) illustrate the vortex wandering power spectral densities at two positions downstream the trailing edge, at $x/c = 1.5$ and $x/c = 2.5$. Non-dimensionalisation is done following Bailey *et al.* with the vortex radius r^*, i.e. the distance from vortex centre and the point of maximum U_θ, and the far-field velocity U_0.

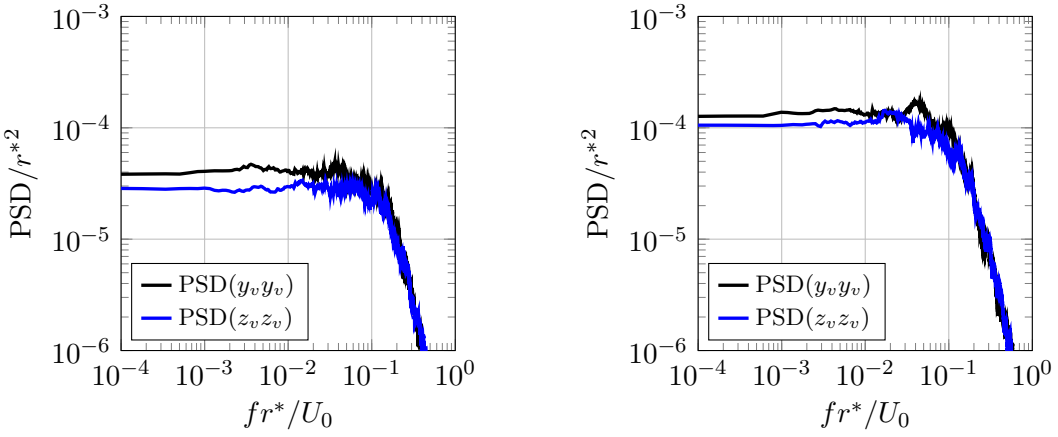

(a) $x/c = 1.5$. (b) $x/c = 2.5$.

Figure 6.14: Power spectral densities of the vortex wandering components y_v and z_v on two positions downstream the aerofoil.

The spectra at both positions are qualitatively similar to each other, and resemble the spectra obtained by Bailey *et al.* [244] for the experimental setup with a small grid, which produced a flow of low turbulence intensity compared to a comparable setup with a larger grid. The frequency plateau until a certain value of fr^*/U_0, after which a monotonic decay sets in. Quantitatively, the spectra obtained are considerably lower than those obtained by Bailey *et al.* by approximately an order of magnitude. This may be related to the position of the probe planes being closer to the trailing edge. Comparing Figures 6.14 (a) and (b) it is apparent that the spectra at the more downstream is higher by approximately a factor of 2. Considering that the first spectra of Bailey *et al.* was measured at $x/c = 3.75$, it is not inconceivable that approximately the same magnitude of vortex wandering would be obtained.

Unlike the results of Bailey *et al.* [244], the vortex wandering is found to be slightly asymmetric, with fluctuations in the y direction having a slightly larger magnitude than in z direction. However, as shown by Figure 6.14 (b), the two frequency spectra exhibit a converging behaviour, indicating that this is a phenomenon restricted to the early

formation of the vortex. It should furthermore be noted that considerable differences are present between the experiment by Bailey *et al.* and the present simulations, which were primarily aimed at the investigation of leading edge interaction noise. As such, neither turbulence intensity, nor mean flow velocity or integral length scale of the turbulence are equal to those of the experiment of Bailey *et al.* [244], in addition to the present use of a round tip in contrast to the use of a blunt tip by Bailey *et al.* Furthermore, as Holzäpfel pointed out [157], LES methods have their shortcomings when modelling vortex core evolution, since the development of turbulence in this region of very high vorticity flows is often not appropriately modelled by the subgrid model. As such, this setup represents a suitable test case to validate the modelling of the vortex core evolution by the subgrid scale model. However, such an investigation is beyond the scope of the current work. The good match of spectral shape demonstrates that the developed method of accounting for the effects of vortex wandering is appropriate.

Having established the validity of the developed averaging method, the mean absolute axial velocity U_1, as well as the axial turbulent stress u_{11}, is investigated in Figure 6.15 (a) - (f).

It is immediately apparent from Figures 6.15 (a), (c) and (e) that the tip vortex core is associated with a significant mean axial velocity deficit. While vortex cores with a jet-like axial velocity profile have been reported [154], the experiments of Anderson and Lawton [149] showed that for small angles of attack, which are associated with relative low circulation strength, an axial velocity deficit across the vortex develops. The results presented here agree with this finding, as the chosen angle of attack of 3 degrees is lower than the lowest investigated in their study.

While the axial velocity exhibits a large degree of symmetry, the contour plots of the axial turbulent stress, shown in Figures 6.15, illustrate a considerable asymmetry, which, however, diminishes with downstream distance. The "C" shaped region of elevated values of u_{11} is hypothesized to be produced by external turbulence structures which are in the process of wrapping themselves around the vortex. In prior studies of the interactions between vortex tubes and homogeneous turbulence, such a behaviour has not been reported [150; 163]. This is likely because all of these studies investigated the problem of a vortex tube immersed in homogeneous turbulence, and no simulation of a body in the flow producing the vortex was attempted. Such a body would introduce an asymmetry to the problem, which is hypothesized to be the cause by the preferential wrapping of the turbulent structures. A DNS of a vortex pair in a constantly sheared and turbulent environment was conducted by Holzäpfel *et al.* [157], however no quantification of the axial turbulent stresses was reported. Although there have been numerous LES investigating the formation and development of the tip vortex, the majority have been conducted in steady flows [131; 132; 133; 239], and where profiles for the u_{11} have been reported, they did not exhibit the present "C" shaped region. A LES with evidence of vortex wandering was recently presented by Boudet *et al.* [245] for the case of a fan tip-clearance flow, however, no contours of u_{11} were reported.

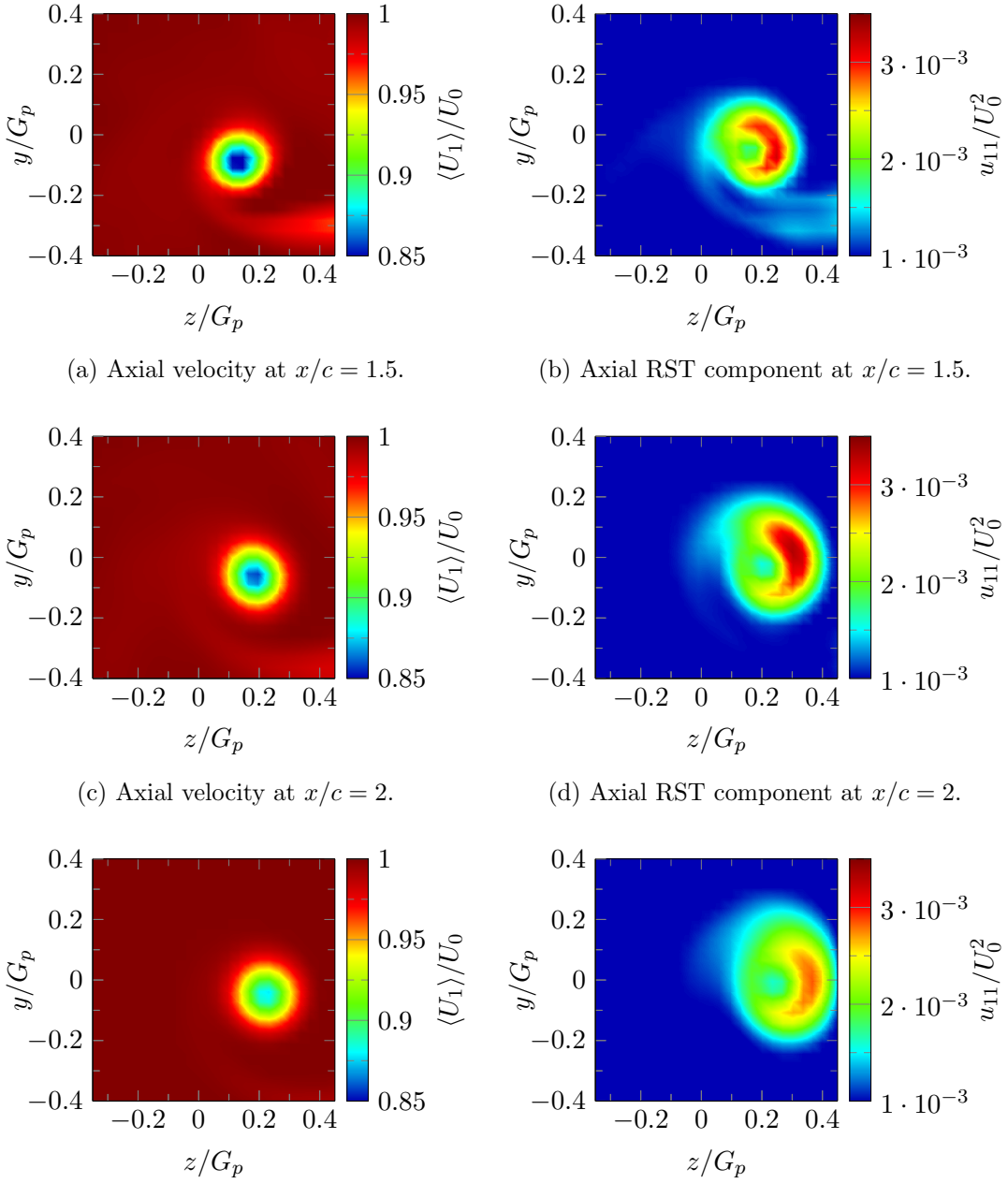

(a) Axial velocity at $x/c = 1.5$.

(b) Axial RST component at $x/c = 1.5$.

(c) Axial velocity at $x/c = 2$.

(d) Axial RST component at $x/c = 2$.

(e) Axial velocity at $x/c = 2.5$.

(f) Axial RST component at $x/c = 2.5$.

Figure 6.15: First and second moments of the axial velocity averaged in the frame of reference of the vortex core.

It is noted that in the experimental measurements of Chow *et al.* [246] of a NACA 0012 aerofoil at an angle of attack of 10° under steady inflow conditions, a "C" shaped region was reported to be present very close to the point of vortex formation, but disappeared relatively quickly with downstream distance, which may be related to the larger angle of attack compared to the present case, as well as the fact that the turbulence originated in the shear layer where the vortex forms from the aerofoil surface. In the present case, while some turbulence is associated with the shear layers from the aerofoil wake as evidenced by the light blue areas in Figure 6.15 (b), the contribution to the

axial turbulent stress from eddies in the process of wrapping around the tip vortex is considered to dominate, creating a "C" shaped region very similar to the experiment, but different in origin, and considerably longer persistent. This suggests that the presence of free-stream turbulence leads to an altered formation process of tip vortices as in the case of laminar inflow conditions. Further experimental studies, e.g. using the experiment rig presented in Appendix A are recommended to validate the present findings.
In order to further support the hypothesis that the dominating contribution to u_{11} is from eddies in the process of wrapping around the tip vortex, the movement of the turbulent eddies around the vortex tube is investigated by computing two-point spatial cross correlations of the axial unsteady velocity components in the frame of reference of the wandering vortex. Figure 6.16 (a) to (c) show the contour plots of the maxima of the correlation coefficient $R_{11}(x_0, x_1, \tau)$ for all positions $x_1 = (y, z)$ on the plane $x/c = 2$ when x_0 is fixed on the plane $x/c = 1.5$. The positions of x_0 are highlighted with a black x marker.

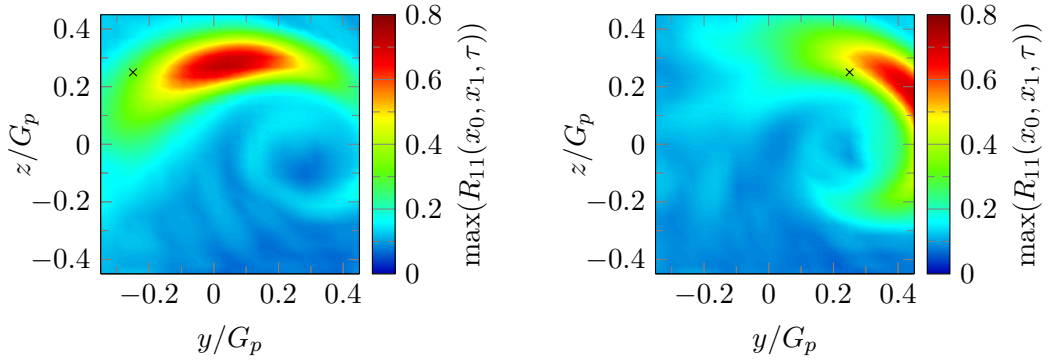

(a) $x_0 = (-0.25, 0.25)$.

(b) $x_0 = (0.25, 0.25)$.

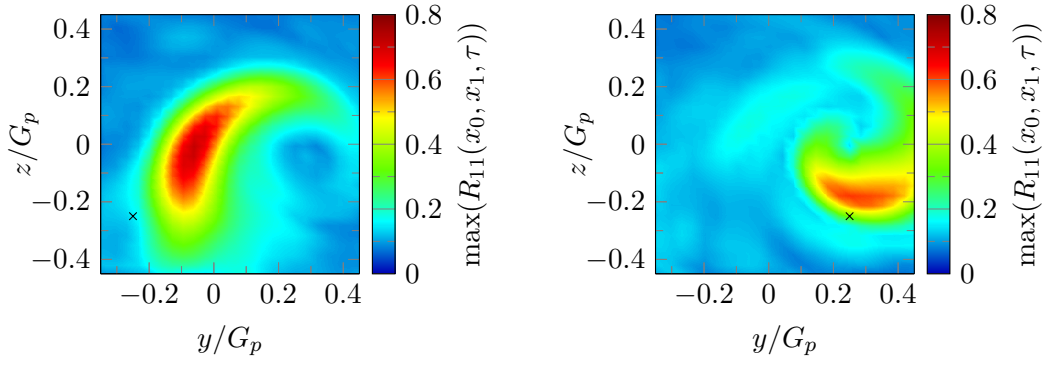

(c) $x_0 = (-0.25, -0.25)$.

(d) $x_0 = (0.25, -0.25)$.

Figure 6.16: Velocity cross correlations from fixed points x_0 in the plane $x/c = 1.5$ to any point x_1 in the plane $x/c = 2$.

It is immediately apparent that the vortex dominates the region of the flow investigated in Figures 6.16 (a) - (d), leading to considerable correlation even for points which are, when considering the distribution of the tangential velocities shown in Figures 6.13 (b), (d) and (f) well outside the area of strongest tangential velocities. The largest

displacement of the area of highest correlation is obtained for $x_0 = (-0.25, -0.25)$. This is caused by its position in the plane of the trailing edge, where the vortex roll-up occurs. In an analogue manner, the cross correlation of the velocity is computed for the planes $x/c = 1.5$ and $x/c = 2.5$ and shown in Figures 6.17 (a) - (d).

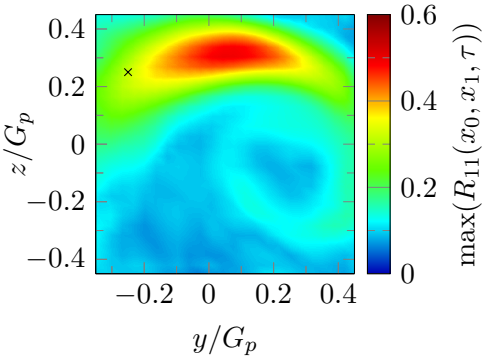

(a) $x_0 = (-0.25, 0.25)$.

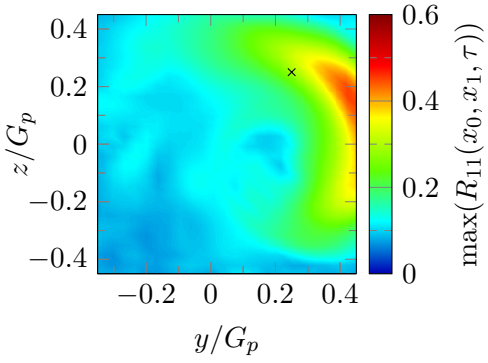

(b) $x_0 = (0.25, 0.25)$.

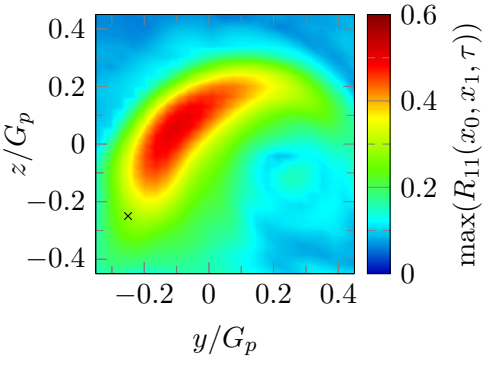

(c) $x_0 = (-0.25, -0.25)$.

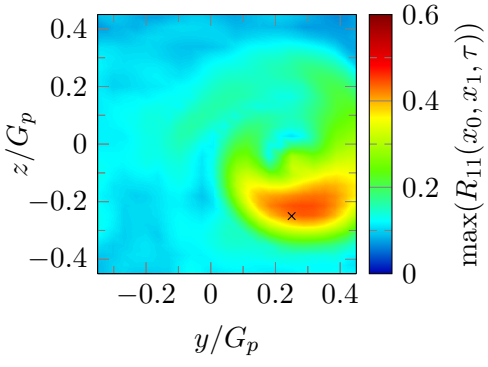

(d) $x_0 = (0.25, -0.25)$.

Figure 6.17: Velocity cross correlations from fixed points x_0 in the plane $x/c = 1.5$ to any point x_1 in the plane $x/c = 2.5$.

As expected considering the more downstream position of the second plane, Figures 6.17 (a) - (d) show significantly reduced maxima of correlation, and a general spreading of the correlated areas.

In order to obtain a qualitative view of the development of the correlation maxima for all possible positions x_0, the procedure applied for Figures 6.16 and 6.17 is now applied for all positions x_0 on the plane $x/c = 1.5$. For each point x_0, the cross-correlation distributions to any point in the plane $x/c = 2.5$, as shown in Figures 6.16 and 6.17 is computed. Then, the maximum value contained in the two-dimensional cross-correlation distribution is determined and assigned to the grid point representing x_0. The result of this algorithm is shown in Figure 6.18.

The maximum values of the cross-correlation in the vortex-relative frame of reference, shown in Figure 6.18 support the earlier hypothesis that for the early tip vortex formation downstream an aerofoil, the eddy wrapping process is asymmetric. Furthermore, a relatively sharp distinction can be made between eddies which have finished the wrapping

process, located in a region outlined by the dotted line, and those which are only in the process of wrapping, located in a region outlined by the dashed line. While the former retain a considerable amount of correlation, the warping of the turbulent structures of the latter region during the process of wrapping leads to a significant decrease in correlation. The area of very low correlation values at $0 < y/G_p \leq 0.4$ and $z/G_p > 0.4$ is caused by the turbulent structures which are convected outside the area of measurement.

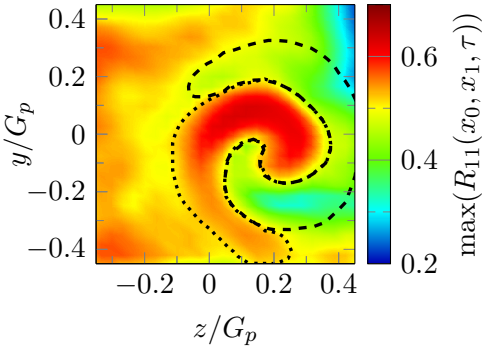

Figure 6.18: Maximum cross correlation value of each point x_0 in plane $x/c = 1.5$ to any point x_1 contained in plane $x/c = 2.5c$.

Finally, the vectors between two points of maximum correlation on the planes $x/c = 1.5$ and $x/c = 2$ are investigated in Figures 6.19 (a) and (b). While in Figure 6.19 (a), the grid points are associated with the magnitude r_{cc} of the vector between x_0 and its corresponding maximum correlation on the downstream plane, Figure 6.19 (b) illustrates the direction of this vector by means of the angle Θ_{cc} between the vector and the positive spanwise direction z. In order to facilitate comparison with the areas of high and low flow velocity cross-correlation identified in Figure 6.18, dashed and dotted lines indicate their respective extents.

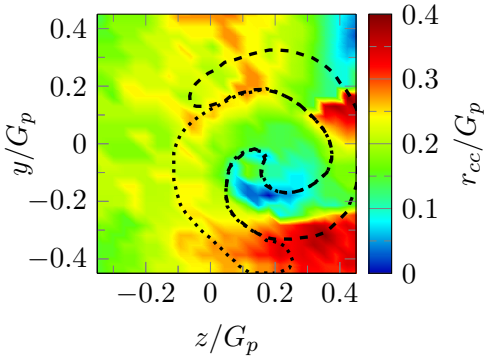

(a) Distance between (y_0, z_0) and peak value of cross correlation.

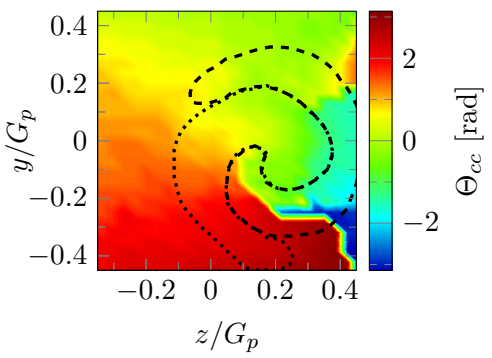

(b) Angle between correlation displacement vector and positive spanwise direction.

Figure 6.19: Measures of turbulence movement from planes $x/c = 1.5$ to $x/c = 2$ in the vortex-core relative coordinate system.

It is apparent from Figure 6.19 (a) that the cross-correlation vector magnitude, r_{cc} in particular exhibits a considerable amount of noise. Additionally, some local peaks in vector magnitude exist, such as at $y/G_p \approx 0.1$, $z/G_p \approx 0.4$, which are due to the turbulent structures being convected outside the sample plane, and thus the algorithm is no longer able to determine the correct point of maximum correlation on the downstream plane.

Nevertheless, it is observed that the area of lowest r_{cc} at $y/G_p \approx -0.2$, $z/G_p \approx 0.2$ is associated with an area of low flow correlation. It is noted that while the magnitude of the vector is not large at this point, the streamline curvature may be considerable, which will act to impede radial motions and increase turbulence decay, leading to relaminarization [136; 151; 152]. The vortex core represents the most challenging region for LES, as noted by Holzäpfel [157], which is why a complete reproduction of experimental results is not expected. In particular the complete relaminarization would not be reproduced by the present methodology.

Considering the areas of high correlation, it is observed that a lower r_{cc} is associated with a higher correlation value, indicating that the strongest deformation takes place during the early wrapping process. Furthermore, it is apparent from Figure 6.19 (a) that turbulent structures entering the $x/c = 1.5$ plane in the lower half of the lower right quadrant, i.e. at $z/G_p > 0.2$, $y/G_p < -0.2$, are susceptible to the largest rotation around the vortex. Figure 6.19 (b) confirms that this movement is directed clockwise around the vortex core, which is as expected in the direction of vortex rotation. The sharp gradients in Figure 6.19 (b) are caused by the singularity in the *atan2* function used for post processing.

From the qualitative analysis of the interaction of the tip vortex with the surrounding turbulence, it is concluded that the main phenomena, such as the wandering of the vortex as well as the wrapping of eddies around the vortex, appear to be captured, although further quantitative comparison with experimental or numerical studies is recommended in order to validate the findings. This may be accomplished using the experimental rig documented in Appendix A. However, for the purposes of this study, which was focused on the noise emissions of finite aerofoils immersed in turbulent flow, the validation of the long-term development of the tip vortex and surrounding turbulence is out of scope, as the leading edge noise is expected to be dominant [12]. The influence of the tip vortex on the noise emissions is further investigated in Section 6.3.

As such, this investigation serves to illustrate the potential of the current methodology to be used to assess interaction effects between tip vortex and the external turbulence and highlights a promising application case for the future development and validation of advanced sub-grid scale models capable of reproducing initial vortex formation and wrapping processes of the surrounding turbulence.

6.3 Aeroacoustic analysis

Having discussed the aerodynamic phenomena associated with the interaction of a finite aerofoil with a turbulent flow, the aeroacoustics of this case are analysed. As this is the first time the case of a finite aerofoil interacting with turbulence is investigated with a focus on the aeroacoustics, experimental validation of the results is difficult due to the lack of comparable cases in the literature.
First, surface pressure spectra are discussed and compared with those of an infinite aerofoil at an angle of attack. Surface pressure cross-correlations are computed to identify the inviscid response of the aerofoil. Subsequently, the far-field noise radiation is computed, using the same hybrid approach as applied in Chapter 5, discussed in Section 3.1.3. In order to eliminate potential contributions of the sections of the aerofoil exposed to steady flow and to facilitate identifying the contributions of the tip-most sections to the far-field nose, a blanking step was used in which the fluctuating pressure signals of selected sections would be set to zero. In doing so it was assumed that correlation of the fluctuating pressure on the blanked sections and those where the pressure signal is retained is negligible. This assumption was further investigated as documented in Appendix E.2, where it was found that the pressure fluctuations, present in case of the steady sections of the aerofoil only on the late suction side, are not correlated to a significant degree to the pressure fluctuations of the sections of the aerofoil which are exposed to the turbulent flow, which are the prime interest of this study.
Finally, the noise directivities in case of the finite aerofoil are presented both in the span-normal as well as in the streamwise-normal plane, as this case allows to investigate the noise emissions for out-of-plane observers.

6.3.1 Surface pressure spectra

Following the approach taken in Section 6.2.2, the development of mean pressure quantities is investigated in the plane normal to the transverse direction. Figure 6.20 (a) shows the distribution of the dimensionless pressure coefficient $\langle c_p \rangle$ upstream the aerofoil, while Figure 6.20 (b) illustrates the development of the RMS of the pressure fluctuations, p_{RMS}, divided by the mean density ρ_0 and the speed of sound c_0 squared. In order to emphasize the development towards the leading edge, a logarithmic scale is used for the streamwise coordinate x.
It is apparent from Figure 6.20 (a) that $\langle c_p \rangle$ exhibits a dependency from the spanwise coordinate only very close to the aerofoil tip. Considering the earlier analysis of the development of the mean velocities, shown in Figures 6.6 (a) - (c), this is expected, as the streamline curvature, which is proportional to the pressure gradient, is largely determined by the gradient of the axial velocity, as it exhibits the largest gradients. Since the axial velocity is developing independent of the spanwise coordinate up to a distance very close to the tip, it follows that the mean pressure exhibits the same behaviour.

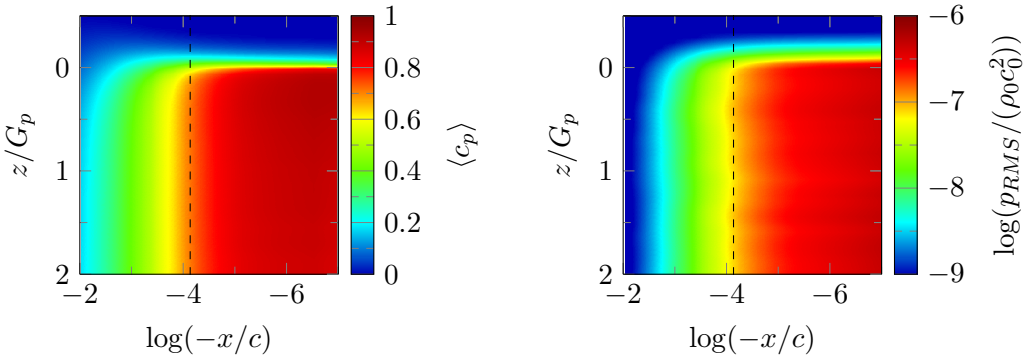

(a) Time averaged pressure coefficient.

(b) Non-dimensional root mean square of unsteady pressure.

Figure 6.20: Pressure contour plots upstream of finite aerofoil leading edge. Dashed lines indicate the position $x/r_{LE} = 1$.

Similarly, p_{RMS} mirrors the contour of the axial turbulent stress u_{11}, shown in Figure 6.7 (a). The only material difference between the contours of $\langle c_p \rangle$ and p_{RMS} is the slightly larger zone of increased values of p_{RMS} beyond the aerofoil tip, which is due to the circulation around the tip inducing a slight acceleration of the flow in the transverse direction, which lowers the mean pressure.

On surface pressure contour plots for $\langle c_p \rangle$ and p_{RMS} on the suction side of the aerofoil are shown in Figures 6.21 (a) and (b), respectively, for values of the spanwise coordinate between $0 \leq z/G_p < 2$, i.e. excluding the rounded tip.

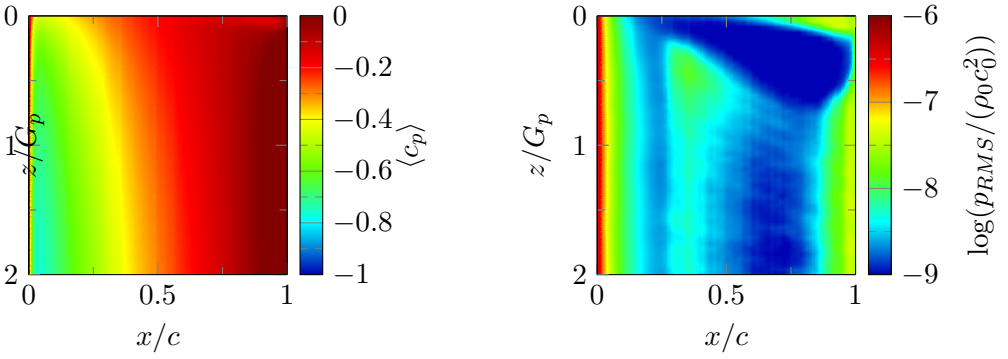

(a) Time averaged pressure coefficient.

(b) Non-dimensional root mean square of unsteady pressure.

Figure 6.21: Pressure contour plots on the suction side of the finite aerofoil.

Figure 6.21 (a) exhibits the well-known distribution of the mean pressure coefficient $\langle c_p \rangle$ for finite aerofoils, with the pressure distribution converging towards the two-dimensional distribution as the distance to the tip grows.

Although the distribution of the non-dimensional root mean square of fluctuating pressure shows the expected peak at the leading edge, an unexpected increase of p_{RMS} on the early suction side needs to be investigated. In order to assess this phenomenon in more

detail, Figure 6.22 shows the values of the non-dimensionalised p_{RMS} on a slice normal to the spanwise direction at position $z/G_p = 0.5$, as well as on the aerofoil surface.

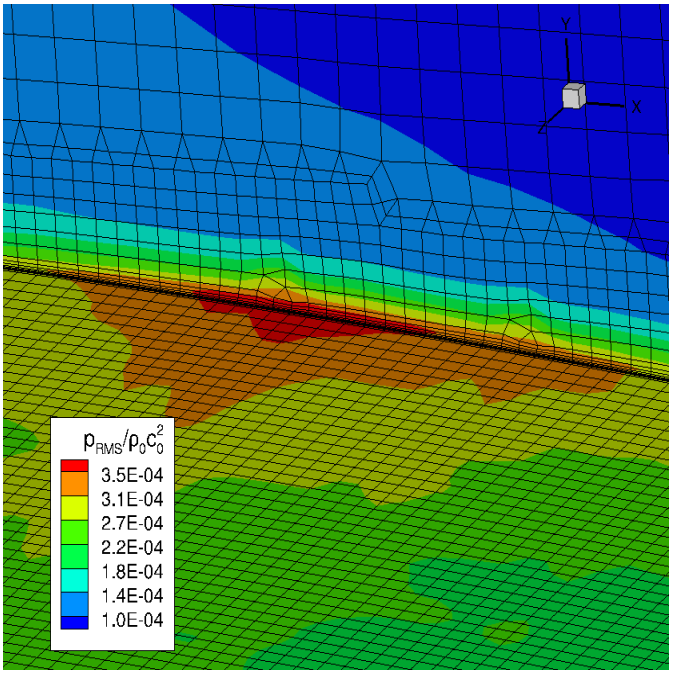

Figure 6.22: Area of high fluctuating unsteady pressure on early suction side. Slice at position $z/G_p = 0.5$.

It is apparent that the increased regions of p_{RMS} are associated with small inhomogeneities in the mesh, in particular the tetrahedral cells close to the surface. This is similar to the small peaks in p_{RMS} observed in case of the infinite aerofoil, shown in Figures 5.18 (b) and 5.19. However, in the case of the finite aerofoil, the magnitude of these fluctuations is far greater than in case of the infinite aerofoil, but crucially is a much smaller contribution to the far-field noise emissions compared to the leading edge noise, as Figure 6.21 (b) indicates. At this point, it is not entirely clear what is the cause of this. Two possible causes are the slightly higher mean flow velocity of the finite aerofoil simulation, as well as the smaller extent of the refined region in the near-field of the aerofoil. Further investigation of the effects of this phenomenon on the inviscid response of the aerofoil, which is the primary object of this research project, is conducted in Section 6.3.2. For the purpose of assessing the effect of these non-physical fluctuations on the surface pressure spectra, Figure 6.23 (a) and (b) show the surface pressure spectra for the infinite aerofoil at an angle of attack of 3 degrees, as well as for the finite aerofoil, respectively. A spanwise position of $z/G_p = 0.5$ is chosen, as this was observed in Figure 6.21 (b) to be the point where the peaks of p_{RMS} on the early suction side had the largest magnitude. A dash-dotted line indicates the mesh cut-off frequency for the propagation of vortical waves, f_{cv}.

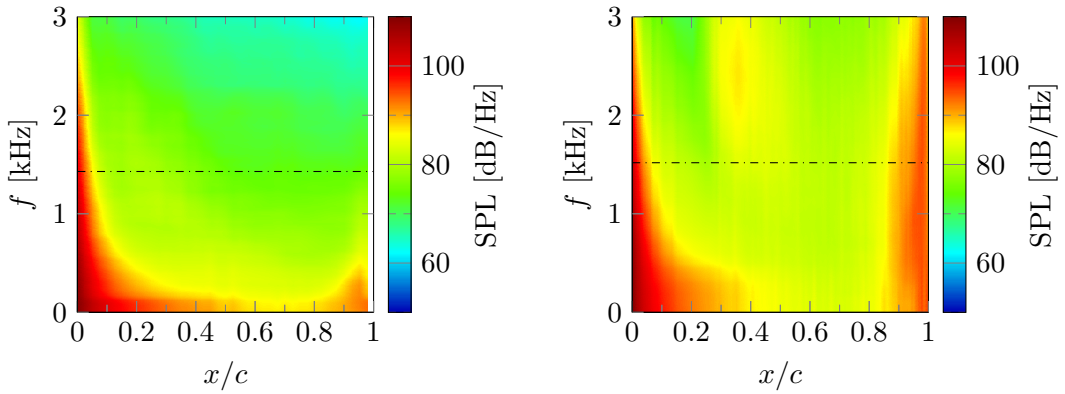

(a) Infinite aerofoil at $\alpha = 3°$.

(b) Finite aerofoil at $\alpha = 3°$.

Figure 6.23: Surface pressure spectra along chord, $z/G_p = 0.5$.

Figure 6.23 (a), illustrating the infinite aerofoil case, shows the expected result of the highest SPL at the leading edge over the entire width of the spectrum investigated, and is in reasonable agreement with results obtained for thick aerofoils such as by Gea-Aguilera [103]. While the spectra of the finite aerofoil, shown in Figure 6.23 (b), show similarly SPL at the leading edge, the surface spectra deviate from the infinite case in two aspects. The regions of elevated p_{RMC} at chordwise positions between $0.3 < x/c \leq 0.5$ appear associated with a broadband hump at frequencies larger than 1000 Hz. It is hypothesised that the broadband hump is associated with the areas of high fluctuating unsteady pressure shown in Figure 6.22, where tetrahedronal cells appear to lead to a numerical tripping of the flow. However, the SPL at the leading edge for these frequencies are considerably higher than between $0.3 < x/c \leq 0.5$.

Secondly, a considerably higher SPL is also observed for the finite aerofoil at the trailing edge over the entire frequency range. Since, at frequencies up to 1500 Hz, surface SPL are in excess of 10 dB higher at the leading edge than at the trailing edge, it is expected that leading edge noise will still dominate at low frequency, and thus the present results can be used to study leading edge interaction noise. However, for frequencies $f > 1500$ Hz, the increased noise emissions from the trailing edge are expected to become a dominating factor.

The analysis of the surface pressure spectra of the finite aerofoil would be incomplete without an investigation of the spanwise variation of these statistics. This not only provides indication of the extent of the tip vortex effects on the unsteady aerodynamics, but also allows conclusions about the spanwise uniformity of the flow to be drawn. Figures 6.24 (a) and (b) shows the power spectral density of the surface pressure at the positions $x/c = 0.01$ and $x/c = 0.7$. It is emphasized that the scaling of the two graphs is not identical, which is due to the larger variation of spectral levels over frequency of positions closer to the leading edge compared to those closer to the trailing edge. It is furthermore noted the spanwise extent shown is well within the finely resolved turbulent domain, and the mesh coarsening in the spanwise direction is initiated only

at $z/G_p = 5.34$, as discussed in Section 6.1. For reference, a dash-dotted line indicates the mesh cut-off frequency for the propagation of vortical waves, f_{cv}.

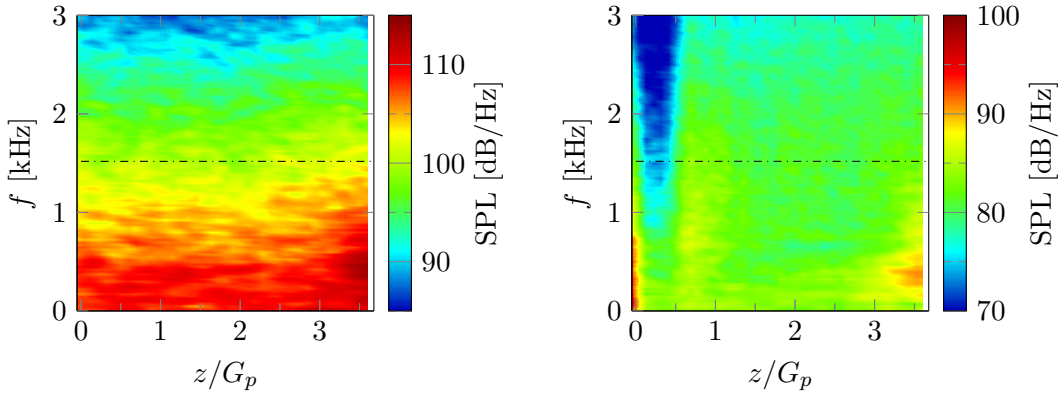

(a) $x/c = 0.01$. (b) $x/c = 0.7$.

Figure 6.24: Surface pressure spectra along span.

As Figure 6.24 (a) shows for positions close to the leading edge, the spectra of the unsteady surface pressure are approximately uniform over the spanwise coordinate z. Only at positions $z/G_p > 3$ are small increases of the spectral levels observable, which are related to the shear layer between turbulent grid jet flow and the laminar far-field. Further investigation of the unsteady surface pressure is documented in Appendix E.2, where analysis of the span-wise cross-correlation of the unsteady pressure indicates that the shear layer is associated with a minor increase in correlation extent.

It is concluded that the part of the aerofoil immersed in the turbulent flow is subjected to homogeneous turbulence up to $z/G_p = 3$. It is also noted that the SPL is consistently in excess of 100 dB for frequencies $f > 1500$ Hz, further indicating that the leading edge noise contributes dominantly to the far-field noise relative to the trailing edge pressure fluctuations observed in Figure 6.23 (b).

For a position closer to the trailing edge, shown in Figure 6.24 (b), the tip vortex is shown to have the effect of significantly decreasing the SPL for frequencies $f > 1000$ Hz. A possible explanation for this phenomenon is that the vortex formation process has the effect of stretching the turbulent structures in the spanwise direction, which increases the wavelengths, and therefore leads to a shift of the energy spectrum towards lower frequencies. Additionally, the tip vortex may spatially transport the turbulent structures along the span. This may lead to regions on the aerofoil surface which are subject to to additional pressure fluctuations. An indication of this effect is observed in Figure 6.24 (b) for the spanwise positions $0.5 < z/G_p \leq 1$, where, for frequencies $f < 2000$ Hz, SPL levels are increased relative to other sections. This effect has not been reported previously, as experiments of finite aerofoils have so far been restricted to the investigation of the tip vortex, and no numerical or analytical investigations of the effects of tip vortices in turbulent flows on the aerofoil surface pressure spectra have been reported. Taking into account the mesh dependency study documented in

Appendix D.2 the present simulation is considered suitably refined for the frequencies where this effect is observable. However, as the mesh dependency study was focused on the interaction of the turbulence with the leading edge, which is the main focus of the present research, and the tip vortex introduces considerable rotation to the flow at the point assessed in Figure 6.24 (b), further studies are recommended to investigate this finding, and establish mesh and methodology independence of this phenomenon. An experimental test setup suitable for the investigation of this phenomenon was designed and constructed during the course of this research, and is documented in Appendix A.

6.3.2 Investigation of the inviscid response of the finite aerofoil

A possible interpretation of the regions of elevated p_{RMS} is that at these positions, a numerically induced tripping of the flow takes place. From an aeroacoustic perspective, this additionally produced turbulence may then lead to a loss correlation of the acoustic waves. While the analysis of the surface pressure spectra is beneficial as it allows a frequency-resolved insight into unsteady surface pressure, the lack of phase information prohibits distinction between hydrodynamic pressure fluctuations and fluctuations associated with acoustic waves.

In order to investigate the effects of the regions of increased p_{RMS} on the early suction side on the far-field noise emissions, the cross-correlations of the unsteady surface pressure were computed in a manner analogue to the analysis conducted in Section 5.4.2. Comparison is conducted in Figures 6.25 (a) - (d) with the surface pressure cross-correlations of the infinite aerofoil case at $\alpha = 3°$, setting $x_0/c = 0.01$ for both cases.

As the comparison of the cross-correlations of the infinite to the finite aerofoil shows, significant differences are present. The R_{pp} of the infinite aerofoil relative to $x_0/c = 0$, displayed in Figure 6.25 (a), shows a correlation pattern with two dominant lobes aligned with the two characteristic correlation delays for the eddy transport and the inviscid aerofoil response, as expected considering the results for the infinite aerofoil at zero angle of attack, shown in Figure 5.20 (a). However, the cross-correlation values for the finite aerofoil, shown in Figure 6.25 (b), exhibit considerably decreased R_{pp} values for values $x_1/c > 0.3$. It is apparent that the pressure fluctuations, first observed in the increased p_{RMS} values of Figure 6.21 (b), lead to a loss of correlation. However, it is noted that some correlation to the leading edge fluctuations remains in the pressure signal, even at positions $x_1/c > 0.3$, and can be observed to persist for the same distance as the R_{pp} of the infinite aerofoil case. Thus, it is expected that while non-compactness effects are diminished, they will be still reproduced to some degree in the present simulation.

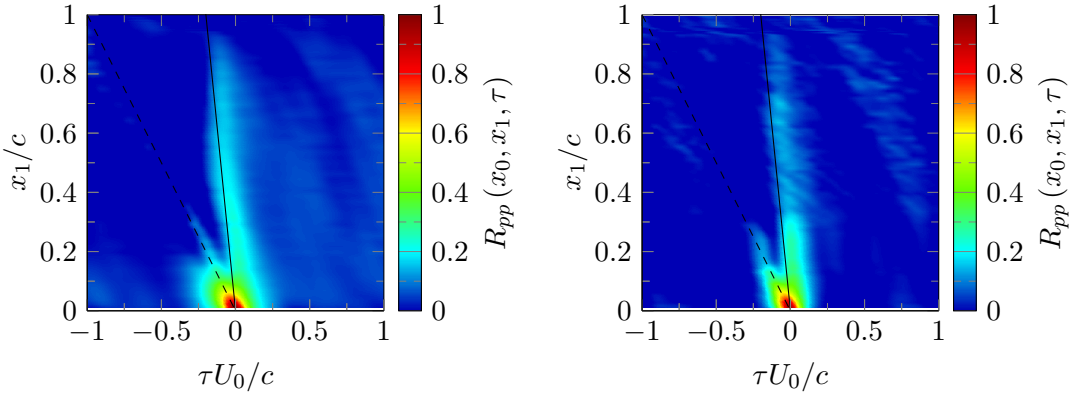

(a) Infinite aerofoil, $x_0 = 0.01c$.

(b) Finite aerofoil, $x_0 = 0.01c$.

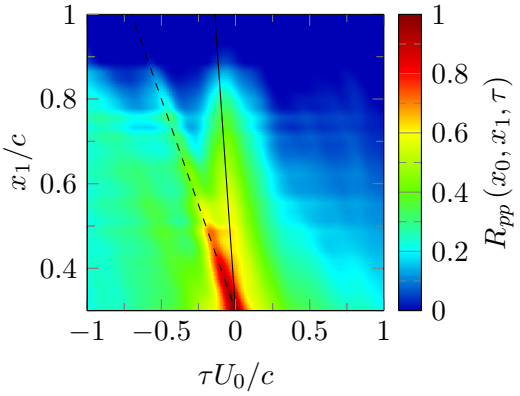

(c) Infinite aerofoil, $x_0 = 0.3c$.

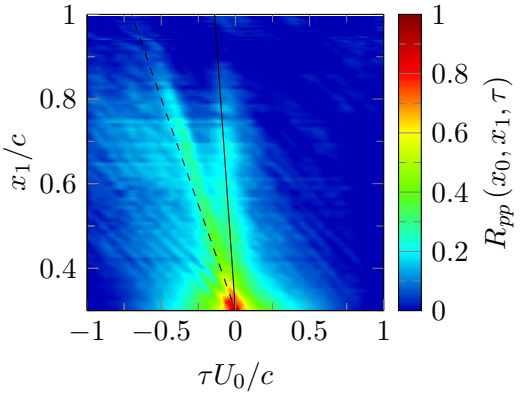

(d) Finite aerofoil, $x_0 = 0.3c$.

Figure 6.25: Comparison of the surface pressure cross correlations of the loaded infinite aerofoil at mid span to the loaded finite aerofoil at the spanwise coordinate $z/G_p = 1.5$. Propagation speed equivalent to convection velocity (dashed line), propagation speed equivalent to speed of sound (solid line).

When the cross-correlations relative to the position $x_0 = 0.3c$, shown in Figures 6.25 (c) and (d), is conducted, it is observed that downstream this position, in case of the Finite aerofoil, correlations are dominated by small scale periodic eddies, which are convected at a speed lower than U_0. It is apparent that these small eddies are wholly immersed in the boundary layer, where convection speeds may be significantly reduced compared to U_0. Correlation of pressure values due to larger eddies convected at U_0, as well as due to the inviscid response of the aerofoil is still present to a small amount, but both lobes do not dominate, with the inviscid response being the slightly smaller of the two effects. This is in stark contrast to the cross-correlation of the infinite aerofoil at this point, which shows overall very high values of correlation due to the presence of eddies of all sizes being convected at a range of speeds by the boundary layer. However, the two main lobes of the inviscid response of the aerofoil and the convection speed U_0 clearly dominate.

For the purpose of investigating a possible spanwise dependency of R_{pp} in the case of a finite aerofoil, R_{pp} is computed by setting $x_0/c = 0.01$ and $x_1/c = 0.7$ and extracting the

pressure signal at various positions along the aerofoil span. The result is shown in Figure 6.26. Time shifts corresponding to the transport of hydrodynamic pressure fluctuations, as well as to the propagation time of acoustic waves from x_0 to x_1 are shown by the dashed and solid lines, respectively.

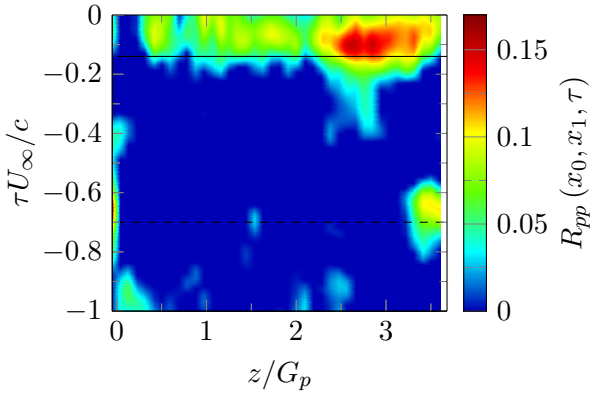

Figure 6.26: Surface pressure cross-correlations for $x_0 = 0.01c$, $x_1 = 0.7c$ along span.

As expected from the discussion of the pressure cross-correlations at one spanwise position, shown in Figure 6.25 (b), correlation attributable to transport of hydrodynamic pressure fluctuations has essentially vanished at this point. However, there is still some correlation at time-shifts equal to the time necessary for acoustic waves to cover this distance. The cross-correlation attributable to acoustic pressure fluctuations is smallest at spanwise positions $z/G_p < 0.5$. Considering the surface SPL shown in Figures 6.24 (a) and (b), this observation is related to the influence of the tip vortex. discussed in Section 5.4.2, the non-compactness effects are associated with the pressure cross-correlation for time shifts equal to the time period of acoustic propagation between two points. Therefore, the present results are considered to indicate that one of the main effects of the finite aerofoil on the far-field noise emissions may be the reduction of non-compactness effects due to the decorrelating effect of the tip vortex at positions closest to the tip. It should be noted that the present setup features an angle of attack of only $\alpha = 3°$, and thus a relatively weak tip vortex. It is conceivable that a larger angle of attack, which is associated with a stronger tip vortex, would result to a larger decorrelated region at the trailing edge, and thus to stronger effects on the far-field noise.

At positions further inboard, i.e. $0.5 \geq z/G_p < 2.5$, larger levels of R_{pp} are observed, which remain constant within the level of convergence of this quantity in this region. It is concluded that non-compactness effects are present for these sections to the same degree as for the infinite aerofoil case, provided that effects such as the earlier discussed pressure fluctuations on the early suction side are negligible.

Finally, at positions $z/G_p \geq 2.5$, R_{pp} is observed to increase significantly. As these positions are affected by the shear layer of the turbulent domain, this is considered to be a product of the current setup rather than an inherent property of the finite aerofoil

turbulence interaction problem. Since that the mesh coarsening in the spanwise direction is initiated only at $z/G_p = 5.34$, and the investigation of conceivable non-uniform grid reflections, documented in Appendix D.1 did not find such reflections taking place, influences of mesh inhomogeneity in the spanwise direction are considered negligible. Nevertheless, in order to facilitate assessment of the noise emissions of the finite aerofoil, this region of inhomogeneous turbulence will be omitted in the subsequent far-field noise investigation.

6.3.3 Far-field radiation

From the analysis in Sections 6.3.1 and 6.3.2 it is apparent that compared to the infinite aerofoil, the finite aerofoil simulation exhibits two phenomena, namely pressure fluctuations on the early suction side as well as increased SPL levels at the trailing edge, which prevent accurate results at high frequency. However, the lower frequencies, where the leading edge noise has been shown to be dominant [94; 97] are less affected by these phenomena.

Due to the considerable computational expense of the finite aerofoil case, it was found necessary to reduce the sampling of the surface pressure data for a physical time of $tU_0/c = 77.4$ only. The effect of this reduced sampling time is investigated in Section 3.2.2 for the infinite aerofoil case, and it is found that the OASPL does not deviate more than 0.25 dB from its final result for a given observer angle once data has been sampled for more than $tU_0/c = 46.4$ of physical time.

In order to investigate the noise emissions of the finite aerofoil in detail, use is made of the method of value blanking on the aerofoil surface. Blanking is achieved by setting pressure fluctuations on all faces of the surface of the aerofoil with a spanwise coordinate higher than a threshold z_b to zero. This not only allows spurious noise sources, which are only present in the simulation because of modelling necessity, to be eliminated, but also to quantify the effect of various source zones on the aerofoil. All spectra are scaled with a correction factor of $20\log_{10}(s_1/s_2)$, where s_1, s_2 are the active spans, i.e. the spanwise extents for which surface pressure fluctuations are sampled for the computation of the far-field noise, to account for the changes in effective span due to value blanking.

Far-field radiation spectra were computed using the methodology outlined in Section 3.1.3. In order to eliminate the noise production caused by the interaction of the turbulent shear layer with the aerofoil, z_b is set to $3G_p$. A constant correction factor of $60\log_{10}(U_{IA}/U_{FA})$ was applied to take the slightly increased mean axial velocity of the finite aerofoil case, relative to the infinite aerofoil simulations, into account. Using the values for the mean streamwise velocities given in Table 6.2, this correction amounts to -1.7 dB.

Figures 6.27 (a) and (b) show the far-field noise prediction results from the finite aerofoil immersed in a turbulent flow in the context of an infinite aerofoil at the same angle of attack, i.e. 3° for the downstream observer position at $\theta = 60°$ as well as for the overhead position at $\theta = 90°$. Dash-dotted black lines indicate the highpass cutoff frequency due to the finite signal f_{cT} and the mesh cutoff frequency for vortical waves f_{cv}. Considering the analysis of the surface pressure fluctuations in Section 6.3.1, only a frequency range between $f_{cT} = 80$ Hz and $f_{TE} = 1500$ Hz is assessed for the finite aerofoil, as beyond f_{TE} the excessive levels of pressure fluctuations close to the trailing edge, i.e. at $x/c > 0.8$, are expected to be dominant. In order to illustrate the frequencies associated with the dips attributable to the non-compactness effect, thick dashed blue lines indicate the frequencies $f_{c,i}$ as defined by Eqn. (2.46).

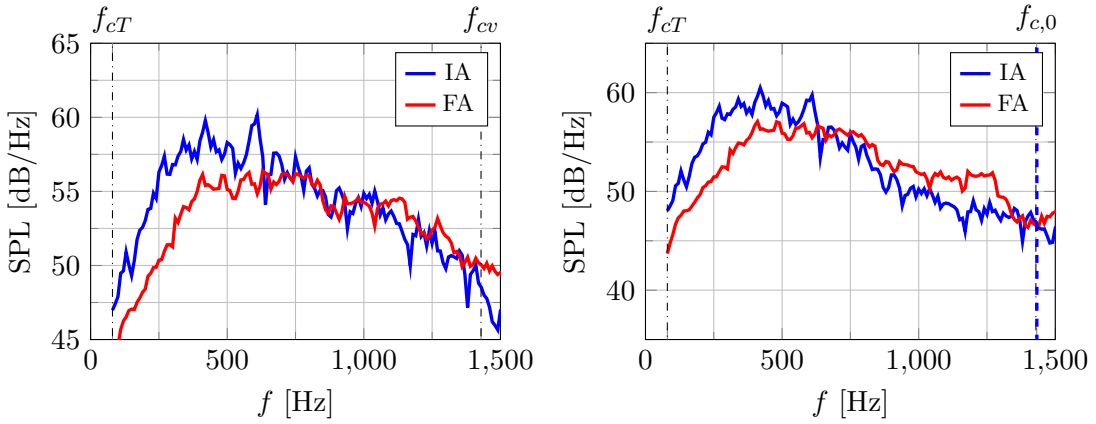

(a) $\theta = 60°$. (b) $\theta = 90°$.

Figure 6.27: Far-field noise results at downstream and overhead observer angles of loaded Infinite Aerofoil (IA), loaded Finite Aerofoil (FA).

From Figures 6.27 (a) and (b) it is apparent that the far-field spectra obtained for the finite aerofoil simulation for the downstream and overhead observer angles deviate significantly from those of the infinite aerofoil. While the maximum SPL level of the infinite aerofoil is not obtained for the observer angles investigated, the agreement of the slope of the spectra is better for an observer at $\theta = 60°$ than at $\theta = 90°$. A potential explanation for this observation is the effect of the tip vortex on the non-compactness effects, which are more prominent for overhead and upstream observer angles than for downstream observer angles, as illustrated in Section 5.4.2.

In order to assess the presence of the non-compactness effects in more detail, Figures 6.28 (a) and (b) show the far-field noise prediction results for the finite aerofoil relative to those of the infinite aerofoil at the upstream observer angles $\theta = 120°$ and $\theta = 150°$.

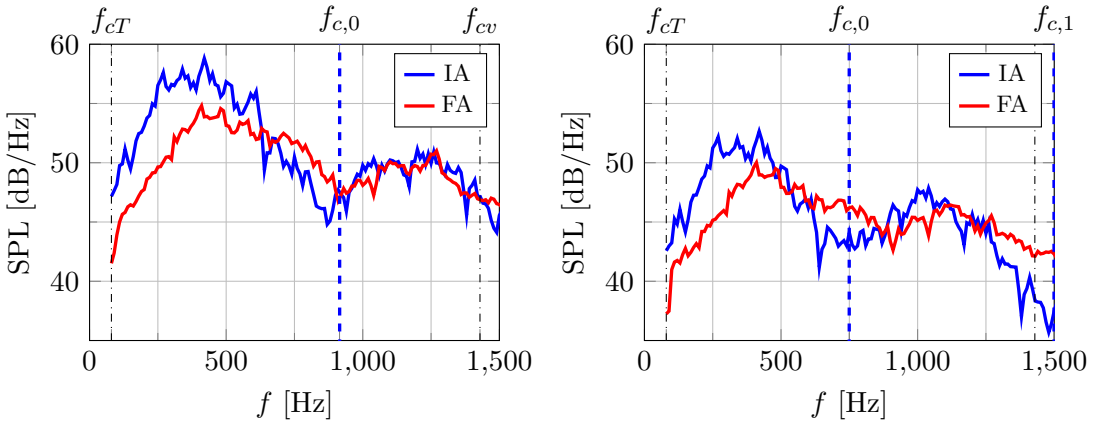

(a) $\theta = 120°$. (b) $\theta = 150°$.

Figure 6.28: Far-field noise results at upstream observer angles of loaded Infinite Aerofoil (IA), loaded Finite Aerofoil (FA).

Considering the upstream observer position at $\theta = 120°$, shown in Figure 6.28 (a), a relatively pronounced non-compactness dip is observed at $f_{c,0}$, which indicates that at observer angles where the dip frequencies are shifted towards lower values, the non-compactness effects in the form of the typical dips manifest for the finite aerofoil as well. However, the dip is less well established in case of the finite aerofoil than for the infinite aerofoil. This may be due to the pressure fluctuations at the trailing edge creating a higher noise floor than in the case of the infinite aerofoil simulations, but may also be due to the effects of the tip vortex, which was observed to affect the surface pressure fluctuations towards the trailing edge as shown in Figure 6.24 (b).

For the upstream observer position at $\theta = 150°$, shown in Figure 6.28 (b), it is observed that the dip associated with non-compactness effects does not coincide with the frequency $f_{c,0}$ at this angle. While this may also be due to an unknown effect of the tip vortex, the exact cause for this is not known, as there is no available reference data from comparable numerical or experimental investigations of finite aerofoils interacting with turbulent flows. A potential influence of the change in meshing methodology, i.e. the reduction of boundary layer mesh thickness, on the non-compactness effects is considered small, as the discretisation of the acoustic waves in the chordwise direction is unchanged between the infinite and finite aerofoil interaction cases. As the wave propagation study, documented in Appendix B has shown negligible dissipative and dispersive errors of acoustic waves for the frequencies investigated in Figures 6.27 and 6.28, the influence of these numerical errors on the present results is considered negligible. Nevertheless, further numerical and experimental studies are recommended to establish mesh independence of the present results, in particular at higher frequencies, and determine the influence of the non-physical pressure fluctuations near the trailing edge on the non-compactness effects.

Finally, at all observer angles shown in Figures 6.27 and 6.28, it is observed that at low frequency, noise emission results from the LES for the finite aerofoil are 2-5 dB less

than the results for an equivalent span of the infinite aerofoil, depending on observer position. Due to the dominance of the pressure fluctuations at the leading edge at low frequencies, i.e. up to 1000 Hz, the SPL levels at these frequencies are considered to be more meaningful than the results for frequencies $f > 1400$. Considering the analysis conducted in Section 6.2.2, a possible cause for this decrease is the reduced distortion of the turbulence prior to interaction with the leading edge. However, further investigation is required to confirm this hypothesis.

Other possible causes include a reduced response of the aerofoil to turbulent gusts due to the presence of the tip, and additional spanwise coherence of the noise emissions present in the infinite aerofoil due to the spanwise periodical boundary conditions. Regarding the former, when taking the earlier analysis of the leading edge pressure spectra, shown in Figure 6.24 (a), into account, it is considered unlikely that a decreasing response of the aerofoil to turbulent gusts with decreasing distance to the tip is taking place, with the associated noise reductions.

To investigate the latter hypothesis, the cross-correlation of the unsteady pressure at the leading edge is shown in Figure 6.29 at mid span for the infinite aerofoil simulation, and for several positions along the leading edge of the finite aerofoil.

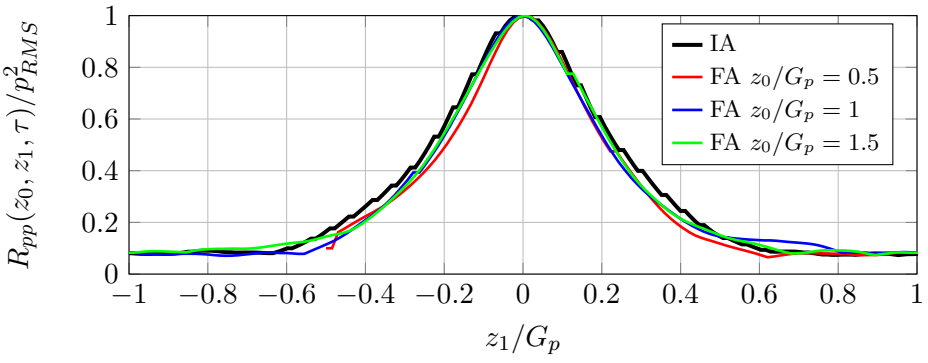

Figure 6.29: Cross-correlation of pressure fluctuations on the leading edge in the spanwise direction for the Infinite Aerofoil (IA) and the Finite Aerofoil (FA).

As shown in Figure 6.29, the cross-correlation of the pressure fluctuations is virtually identical for infinite and finite aerofoil. It is concluded that any differences between the finite and the infinite aerofoil in terms of the spanwise coherence of the gusts are within the statistical averaging uncertainty, and are considered negligible.

In order to investigate the effects of the tip vortex on the far-field noise emissions, Figure 6.30 compares the noise predictions for an observer angle of $\theta = 120°$ at a spanwise observer position of $z/G_p = 1.5$, with various amounts of value blanking. It is assumed in this analysis that the spanwise correlation of pressure fluctuations between areas which are blanked and those which are not is small. While this has been shown in Appendix E.2 to be a justified assumption for the correlation of the pressure fluctuations on sections within and outside of the turbulent flow, it is anticipated considering Figure 6.29 that some amount of spanwise R_{pp} is present between adjacent sections where the distance of the respective section centre is $z/G_p \leq 0.4$. Therefore, for a first-order estimation of

the contribution of different sections of the aerofoil in the turbulent flow to the far-field noise emissions, it is assumed that although such correlation may be present, the far-field noise emissions are predominantly due to flow interaction local to the section. Further investigation using numerical or experimental studies is recommended to validate this assumption.

In Figure 6.30, the observer angle was chosen to facilitate identification of non-compactness effects. As the observer position does not correspond to the mid plane for all investigated sections, an investigation on the effect of an out-of-plane is conducted in Section 6.3.4.

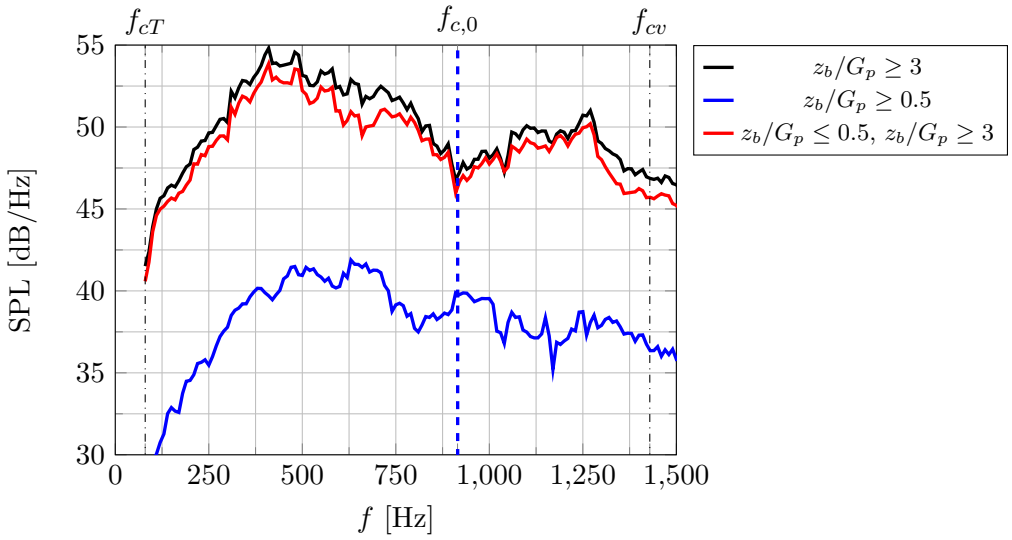

Figure 6.30: Far-field noise at $\theta = 120°$ with $z_b/G_p \geq 3$, impact of tip blanking. Span correction factor only applied for dashed curve.

For $z_b/G_p \geq 3$, a baseline prediction is obtained, which includes the noise produced by the aerofoil immersed in the homogeneous region of the turbulent flow, but excludes the effects of the shear layer, as well as potential trailing edge noise of the part of the aerofoil outside of the turbulent domain. Conversely, for $z_b/G_p \geq 0.5$, far-field noise emissions for the tip most sections only are retained, which are defined as those sections with a considerable influence from the tip vortex considering Figure 6.26. Finally, if value blanking for regions $z_b/G_p \leq 0.5$ and $z_b/G_p \geq 3$, is applied, noise emission results are obtained for the sections of the finite aerofoil interacting with homogeneous turbulence only, and the tip as well as shear layer effects on noise are omitted. In order to illustrate the relative magnitude of the contribution of the various sections to the overall noise emissions, the span correction factor of $20\log_{10}(s_1/s_2)$ is not applied to the prediction results.

As discussed in Section 6.3.1, at frequencies $f > 1500$ Hz, the trailing edge becomes a dominating source of noise in the present simulation. Since the investigation of trailing edge noise is not the focus of this thesis, discussion of these frequencies is omitted.

It is apparent from Figure 6.30 that the spectra of the finite aerofoil with and without

additional tip blanking almost collapse, even if no correction is applied. This is related to the very low SPL level of the tip section alone, indicated by the blue line, which are less than 42 dB across the entire frequency range investigated. As such, it is found that for the current the tip-most sections contribute very little to the SPL in the far-field. This is expected, as the tip-most sections have a very limited spanwise extent.
Furthermore, it is observed that the spectral shape of the tip section noise emissions do not exhibit any clear non-compactness effects. Taking into account the lack of chordwise pressure cross-correlation for these sections, as shown by Figure 6.26, this is considered an indication that the presence of the tip vortex in this section leads to a reduction of non-compactness effects. This effect has not been reported to date. While the influence of dissipative and dispersive error on the acoustic waves investigated here can be considered negligible, as discussed in Appendix B, further numerical and experimental studies are recommended to demonstrate mesh independence and validate this finding.

6.3.4 Directivity analysis

In order to assess the impacts of the presence of a tip on the aerofoil on the directivities, Figures 6.31 (a) - (d) show the SPL for observers in the xy plane, i.e. normal to the spanwise direction. Line widths are chosen to reflect a conservatively estimated LES uncertainty ± 0.5 dB, based on the convergence study documented in Section 3.2.2.
Considering the lowest frequency $f = 400$ Hz, Figure 6.31 (a) shows quantitatively that the reduced SPL first observed in Figures 6.27 and 6.28 are more pronounced for observer angles approaching 90 and 270 degrees. Qualitatively, the good agreement in terms of directivity shapes indicates that finite aerofoils emit noise at these frequencies in a manner equivalent to infinite aerofoils.
A larger mismatch in terms of directivity shape is observed at 800 Hz, as shown by Figure 6.31 (b). Considering the investigation of the effects of tip blanking, shown in Figure 6.30, it is concluded that the reduction of non-compactness effects due to the tip vortex leads to a more dipole-like directivity pattern, even for higher frequencies where the lobes caused by non-compactness effects are typically present for infinite aerofoils.
While the excessive levels of pressure fluctuations near the trailing edge, discussed in Section 6.3.1, are considered to only dominate for $f > 1500$ Hz, it is anticipated that directivity results at frequencies $f > 1000$ Hz are also contaminated to some degree, e.g. by a higher noise floor reducing the magnitude of the dips associated with the non-compactness effects. Conversely, as discussed in Section 6.3.3, the dissipative and dispersive errors for acoustic waves are considered negligible, as the discretisation in the chordwise direction remains unchanged for the finite aerofoil interaction case compared to the infinite aerofoil interaction case, for which the dissipative and the dispersive error were shown small for acoustic waves in Appendix B.

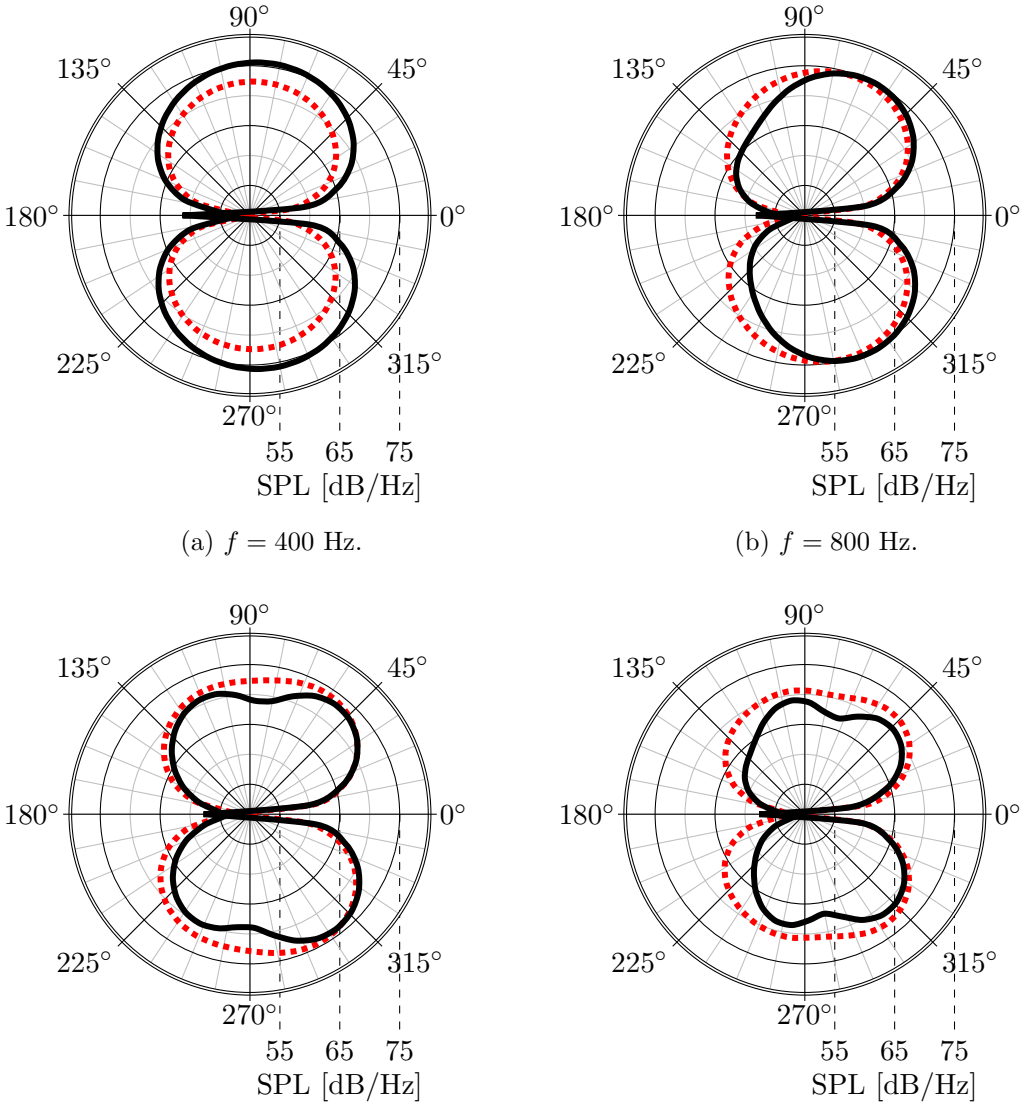

(a) $f = 400$ Hz. (b) $f = 800$ Hz.

(c) $f = 1200$ Hz. (d) $f = 1600$ Hz.

Figure 6.31: Directivity plots with finite aerofoil (dotted), infinite aerofoil (solid). Line widths representative of LES uncertainty.

However, the influence of the numerical error manifesting in excessive levels of surface pressure fluctuations at $x/c > 0.8$ on the directivity results cannot be considered small and as such, the results for frequencies higher than 1000 Hz, shown in Figures 6.31 (c) and (d) for $f = 1200$ Hz and $f = 1600$ Hz respectively, must be considered compromised, and are shown here for the purpose of completeness. Indications of a multi-lobed pattern attributable with non-compactness effects are observed. However, due to the presence of numerical error, further investigations are recommended to determine the directivity patterns of finite aerofoils at frequencies in excess of 1000 Hz.

Finally, the case of a finite aerofoil allows the directivity pattern in the yz plane, i.e. normal to the streamwise direction, to be investigated. For this purpose, observer positions are defined as shown in Figure 6.32.

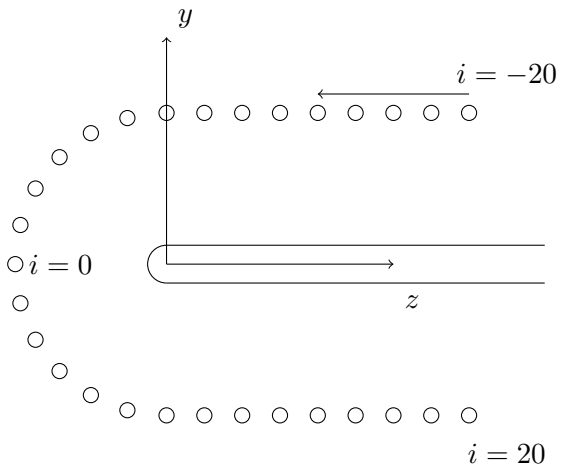

Figure 6.32: Illustration of observer positions (circles) in yz plane. Aerofoil outlines indicated by black lines. Not all observer positions shown.

In total, there are 41 observers, of which not all are shown in Figure 6.32. The yz plane investigated is aligned with the coordinate system origin, i.e. the leading edge of the round tip. For the purpose of symmetry, observer position 0 coincides with the xz plane. Figures 6.33 (a) and (b) illustrate the SPL per frequency and observer position, for the case of value blanking past $z_b/G_p = 3$ and for $z_b/G_p \leq 0$, $z_b/G_p \geq 3$ in (a) and (b), respectively.

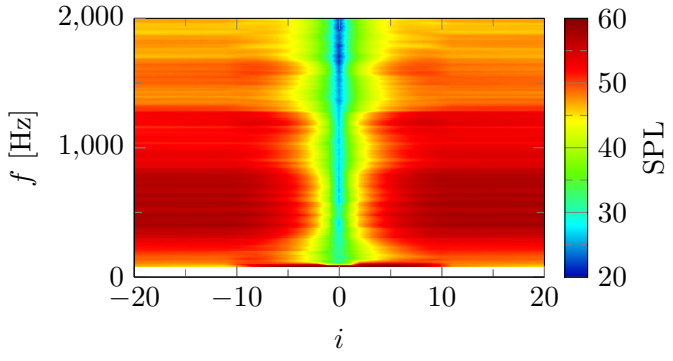

(a) $z_b/G_p \geq 3$.

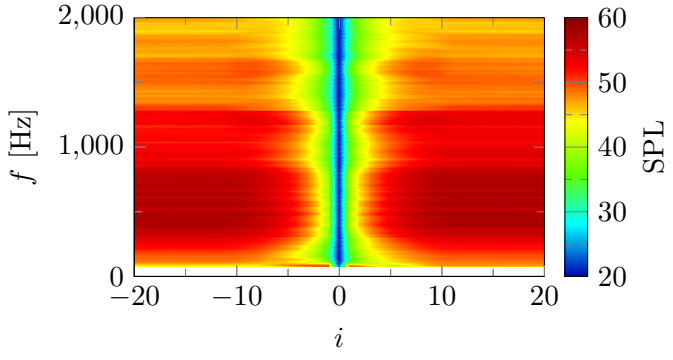

(b) $z_b/G_p \leq 0$, $z_b/G_p \geq 3$.

Figure 6.33: SPL levels in the yz plane.

As shown by Figures 6.33 (a) and (b), a two-lobed directivity pattern exists in the yz plane. SPL level remain constant across all frequencies until an observer index of $i = \pm 5$, which corresponds to an angle of ± 50 degrees relative to the xz plane. For even smaller observer angles, the noise radiation from the tip itself becomes dominant, as is apparent when comparing Figure 6.33 (a) to (b). It is expected that these noise emissions would be highly dependent on the tip shape, with the round tip representing a relatively low noise configuration, due to the lack of sharp angles and the associated eddy shedding.

6.4 Summary

This chapter presented the application of the turbulence creation method proposed by Blackmore [13] to the problem of thick, loaded, finite aerofoil. For this purpose, the infinite aerofoil setup was suitably altered for the simulation of a finite aerofoil. This involved an expansion of the turbulent domain, to ensure that a sufficiently wide span of the aerofoil is immersed in homogeneous turbulence. Thus, simulation runtime is increased considerably. Due to change in boundary conditions, it was observed that mean flow statistics, such as axial flow velocity and turbulence intensities deviated from those of the infinite aerofoil simulations. However, these mismatches are not considered to impact the main conclusions.
As the two main phenomena of interest are the interaction of turbulence with the leading edge of a finite aerofoil, as well as the formation and behaviour of the tip vortex in simulated turbulence, and its contribution to noise emissions, a main focus was put on conducting qualitative comparison to similar experimental and numerical studies. While the turbulence interaction at the leading edge was compared with the results of the infinite aerofoil simulation, documented in Chapter 5, the tip vortex aerodynamics were compared qualitatively against literature.
Aeroacoustic results were computed in a manner analogous to the one used in Chapter 5, i.e. by extracting the surface pressure signals on the aerofoil and using an Ffowcs-Williams and Hawkings [118] solver to compute the far-field noise levels. The main conclusions from this chapter are:

- In this initial study, the interaction of turbulence with the leading edge is found to exhibit a constant behaviour up to distances very close to the tip position, i.e. of the order of one tenth of the aerofoil chord. As such, the development of the turbulent stresses is largely representative of the axial velocity gradient, which is the largest of the mean velocity gradients and is primarily caused by flow stagnation.

- The tip vortex is found to exhibit a considerable amount of wandering, which is in line with experiments investigating tip vortices interacting with turbulence. Using a correction algorithm to obtain averaged flow quantities in the frame of reference

of the wandering vortex, the vortex core is shown to be considerably asymmetric, with a development towards symmetry at larger downstream distances. Indications are observed that the wrapping of the vortex structures is asymmetric close to the wing and may contribute to the asymmetry of the vortex core.

- Closer investigation of the surface pressure fluctuations reveals two regions, where the aerodynamics of the finite aerofoil unexpectedly deviate from those of an infinite aerofoil. Firstly, a process creating turbulence on the early suction side is observed, which is traced to tetrahedral cells in the prism layers of the aerofoil wall mesh. Secondly, pressure fluctuations associated with the mesh refinement near the trailing edge, which were found to be minor in case of the infinite aerofoil setup, are found to be significantly increased in case of the finite aerofoil. The effects of these, likely un-physical, phenomena are assessed, and it is found for the present case study, for frequencies below 1500 Hz, the leading edge dominates as a noise source, illustrating the potential of the current methodology to be used as a tool to investigate the leading edge noise production of complex geometries.

- Aerodynamic and aeroacoustic investigation indicate that for the frequency range where the dissipative and dispersive errors for acoustic waves are small, and where the influence of the un-physical surface pressure fluctuations are limited, the main effect of the finiteness of the aerofoil is the reduction of the non-compactness effects of the aerofoil sections in the region of influence of the tip vortex. In the present simulation, the tip vortex is found to significantly suppress pressure fluctuations on the suction side, in particular in the vicinity of the trailing edge for $x/c > 0.7$, which is related to a loss of correlation between acoustic waves emitted from the leading edge and scattered from the trailing edge at this position. While the effect is found to be relatively minor for the current case of a finite aerofoil at a low angle of attack, larger angle of attacks are hypothesised to lead to a more pronounced effect of the tip vortex on the far-field noise emissions. Further investigations are recommended to better quantify these observations. An experimental setup suitable for the validation of the present results was designed and constructed during this research project, and is documented in Appendix A.

- Investigation of the noise directivity in the stream-normal plane indicates that noise levels are constant up to an angle more than $\pm 50°$ relative to the streamwise-spanwise plane. A local minimum is observed for observers in the streamwise-spanwise plane. Due to lack of suitable data in the literature for the purpose of comparison, the use of the experimental setup documented in Appendix A is recommended to further validate this finding.

Thus, this Chapter has presented the use of a LES methodology for the investigation of the aerodynamics and aeroacoustics of a finite aerofoil immersed in a turbulent flow. As the application of LES to the case of a finite aerofoil with upstream homogeneous

turbulence is novel, comparison is limited to qualitative assessment of the results against literature, but the presented findings indicate promising avenues for future research.

Chapter 7

Conclusions and future work

In this chapter, the conclusions of this thesis are given. Additionally, recommendations for future work are presented.

7.1 Thesis summary

The turbulence interaction with leading edges is an important source of noise in many applications, for example for outlet guide vanes of bypass ducts, for fan blades interacting with ingested boundary layers, and for the downstream row of a counter rotating open rotor. As shown in the literature review in Chapter 2, the noise produced by a translating, infinite aerofoil in a turbulent flow is well understood, and numerical as well as analytical tools exist for its prediction. However, the leading edge noise production of complex geometries, such as finite aerofoils, have so far not been extensively investigated. For analytical models, the aerodynamics of the aerofoil tip represents a formidable challenge, due to the difficulty of modelling the effect of the tip vortex. For numerical prediction methods, such as CAA, the difficulty in generating meshes of sufficiently high quality for the utilized high-order schemes has been found to be prohibitive up to this point. While hybrid methods, which use a CFD solver to compute the near-field unsteady aerodynamics, and an acoustic analogy in a post-processing step to compute the far-field noise radiation have shown promise [124; 125], to date, none have been applied to the problem of a finite aerofoil interacting with turbulence.
As discussed in Section 2.5, LES has been recognised as a suitable tool for the investigation of finite aerofoils due to its superior ability to reproduce the formation and development of the tip vortex when compared to RANS, while still maintaining acceptable computational cost. Since the focus of the studies to date has been to reproduce tip vortex formation as measured in experiment, and not the investigation of finite aerofoil aeroacoustics, published results are available only for finite aerofoils in steady conditions [131; 132; 133; 239]. Conversely, a number of experimental studies have assessed finite

aerofoils in turbulent flows, but have not reported acoustic results.
This thesis investigated the ability of LES, coupled with a suitable turbulence generation tool, to be used for the aerodynamic and aeroacoustic study of turbulent flows, and in particular their interaction with complex geometries. An assessment of the state of the art of common turbulence generation approaches led to the selection of the inlet grid turbulence generation method proposed by Blackmore *et al.* [13].
The inlet grid turbulence generation method is investigated in Chapter 4 to assess its capability to reproduce the turbulent flows produced by grid turbulence generators qualitatively, and to study the development of turbulence anisotropy close to the grid. The inlet-grid turbulence generation method is then applied in Chapter 5 to the problem of the turbulence interaction of an infinite aerofoil, in order to conduct quantitative comparisons against the analytic model of Amiet [15], as well as qualitative comparison against experiment, thereby evaluating the use of a compressible LES on unstructured meshes for the study of the interaction of evolving turbulence with leading edges, and the prediction of leading edge noise. Finally, in Chapter 6, the developed methodology is used in an initial case study of the aerodynamics and aeracoustics of the complex geometry of a finite aerofoil. The conclusions of these chapters are summarized in the sections below.

7.1.1 The inlet grid turbulence creation method for LES

In Chapter 4, the method of creating grid turbulence for LES first proposed by Blackmore [13] is investigated. While commonly used synthetic turbulence generators are superior in terms of allowing to precisely control the operational conditions, the inlet grid turbulence creation method was chosen as it produces homogeneous turbulence from transitioning steady flow conditions, which is considered to be a suitable approach to avoid the introduction of spurious noise for the benefit of conducting aeroacoustic investigations [66]. Furthermore, it does not require any modification to the underlying code. Although it does not allow to set turbulence parameters *a priori*, as the user only chooses the dimensions of the grid as well as inlet mass flow, it produces energy spectra very close to those encountered in experiment. Finally, the method can be used to investigate the physics of evolving turbulence.
Expanding on the work of Blackmore [13], the anisotropy of the turbulence is investigated in more detail, with a focus on the processes responsible for the development of the anisotropy of the energy carrying scales. For this purpose, the method of computing invariants of the Reynolds stress tensor to quantify the anisotropy was combined with spectral analysis, thereby allowing the distribution of the anisotropy over the energy carrying scales to be investigated. Additionally, in order to investigate the effect of the Reynolds number on the anisotropy of the energy carrying scales, two simulations at higher Reynolds numbers were conducted. The main conclusions of this chapter are:

- When comparing the axial and transverse one-dimensional energy spectra against the von Kármán model for isotropic turbulence, a good fit is obtained up to the mesh cutoff frequency for E_{11}, which appears to include the begin of the inertial subrange, although a more refined mesh is found to be required to unequivocally capture the typical $-\frac{5}{3}$ power law of this range. A considerable amount of anisotropy is observed in case of E_{22}, with the majority of the anisotropy present in the largest scales, in agreement with experiments. As the wavenumbers containing the anisotropic motions are considerably above the mesh cutoff wavenumber determined in Appendix B, the influence of dissipative and dispersive error on the present results is considered negligible.

- An investigation of the turbulence anisotropy in the vicinity of the grid shows similar behaviour to comparable simulations in the literature. Using the one-dimensional energy spectra for axial and transverse components, it is shown qualitatively that an apparent early isotropic state close to the grid is caused by a change in the dominance from the energy contained in transverse, periodic motions, which are related to the grid bar wake oscillations, to energy contained in large scale, axial motions of the order of the integral length scales. It is noted that while the dissipative error of the employed numerical schemes is very small, the dispersive error may contribute to the rapid reduction of coherent motions associated with the grid bar wake oscillation frequency close to the grid. However, the interaction between adjacent wakes is expected to produce a similar effect.

- For energy spectra deviating significantly from model spectra, as is the case in this application, it is shown that the method of computing a spectral anisotropic Reynolds stress tensor can provide quantitative information on the anisotropy of the various energy carrying scales. This measure is more appropriate than the often used ratio of the axial to transverse normal Reynolds stresses, or the ratio of the axial and transverse integral length scales.

- The comparison of two simulations at higher Reynolds number to the baseline reveals little effect of the Reynolds number on the anisotropy of the flow. It is concluded that the findings concerning the non-monotonic development of the anisotropy in the flow are also applicable to flows at higher Reynolds number, provided the influence of the dispersive error on the observed mechanisms is small.

- Long term development of the flow shows that scalings commonly used for the description of turbulence are applicable. However, it is found that the simulation domain is too small to support the growth of the largest scales up to the outlet. Indications are observed that the turbulent decay as well as the return to isotropy is affected by the restriction of the largest scales. As the investigation of the turbulence interaction noise is conducted at a position considerably upstream of this point, the effect of the restriction of the growth of the largest scales is considered to be negligible.

7.1.2 The interaction of infinite aerofoils with simulated grid turbulence

Having assessed the inlet grid turbulence generation method in a simple setup aimed at the investigation of the produced grid turbulence, a comparative study for the use of this method for the more complex problem of turbulence interaction noise is conducted in Chapter 5. For this purpose, a thick, symmetrical, unloaded aerofoil is immersed in the turbulent flow, which represents a well-known benchmark problem in the field of leading edge interaction noise. In order to allow qualitative comparison of the simulation results against experimental data, flow parameters were chosen to be representative of the experiment of Paterson and Amiet [97]. After assessing mean flow quantities as well as the development of the turbulence upstream the leading edge, results for the acoustic emissions are computed using a hybrid approach. The surface pressure on the aerofoil is sampled, and the far-field noise radiation is calculated by means of a Ffowcs-Williams and Hawkings [118] solver. The main conclusions of this chapter are:

- Since the inlet-grid turbulence generation method does not allow to specify the exact turbulence parameters *a priori*, the exact flow parameters of the experiment of Paterson and Amiet [97] could not be reproduced. While the axial energy spectrum of the turbulence has been found to collapse well with the experimentally measured values, the transverse energy spectrum was found to show considerable deviations, a finding similar to the conclusions of Chapter 4. As the transverse energy spectra is predominantly responsible for the noise emissions, it was concluded that the noise predictions obtained from the LES will deviate from the experimental values.

- As expected, the mismatch of the transverse energy spectrum of the simulated flow in regards to the experimental flow conditions is found to lead to a deviation from the acoustic results of the experiment. However, a good fit is obtained to the analytical solution of Amiet [15], which can be adjusted for any given turbulence spectrum. The fit is improved considerably when the turbulence model spectrum used in the analytical model is adjusted to reproduce the exact transverse energy spectrum in the simulation, i.e. when the anisotropy of the simulated turbulence is taken into account.

- It is thus shown that a compressible large eddy simulation can be used to investigate the noise emissions of an infinite aerofoil interacting with evolving turbulence, and is able to reproduce non-compactness effects as defined in Section 2.4.2.1 and the resulting directivity patterns. Furthermore, a parameter study with an aerofoil at an angle of attack of 3 degrees is presented, which exhibits the expected shift in directivity pattern.

7.1.3 Finite aerofoils in simulated grid turbulence

Having established the capability of the methodology to be used for the investigation of turbulence leading edge interaction problems, the first use of a large eddy simulation for the study of a loaded, finite aerofoil immersed in a turbulent flow is presented in Chapter 6. The simulation of the finite aerofoil necessitates a modification of the previously used numerical domain, which is associated with a considerable increase in computational cost. After the homogeneity of the turbulent flow is established, the development of flow statistics upstream of the leading edge, and in particular close to the aerofoil tip, is investigated. As the tip vortex is a phenomenon of considerable importance, its development in the turbulent flow is assessed by making use of an algorithmic approach to compute flow quantities in the frame of reference of the wandering vortex. Finally, the noise emissions of the finite aerofoil are computed using the same hybrid approach as for the infinite aerofoil, and the results are compared to the infinite aerofoil baseline. The main conclusions of this chapter are:

- The present results indicate that for finite aerofoils at low angles of attack, tip effects on the turbulence interaction are limited to the immediate vicinity of the tip, and the interaction of the turbulence with the leading edge is largely constant in the spanwise dimension.
- In the present case study, the tip vortex is subject to a considerable amount of wandering. When this is taken into account by the use of a correction algorithm, it is found that the vortex exhibits a strong asymmetry, in particular close to the trailing edge. The wrapping of free-stream eddies around the tip vortex is found to be similarly asymmetric and may contribute to the asymmetry of the vortex core.
- An investigation of the surface pressure fluctuations on the simulated geometry revealed areas of increased mean square unsteady pressure, which must be considered non-physical as they align with mesh features. While such areas have been found to exist to a very limited extend in the infinite aerofoil cases discussed in Chapter 5, the finite aerofoil simulation exhibits considerably stronger fluctuations on the suction side, in particular in the vicinity of the trailing edge, for $x/c > 0.9$. When these non-physical noise sources were taken into account, it was found that for frequencies up to 1500 Hz, for which the dissipative and dispersive errors of vortical and acoustic waves can be considered small, the leading edge still dominates as a source of noise in the present simulation.
- The present results indicate that on the aerofoil sections closest to the tip, the tip vortex has the effect of suppressing pressure fluctuations within the resolved frequency range for vortical waves considerably. A possible hypothesis is that the turbulent fluctuations are stretched by the tip vortex, and the energy is shifted

towards lower wavenumbers. Analysis of the surface pressure cross correlations in the present case study showed that for time shifts associated with the inviscid response of the aerofoil, the sections influenced by the tip vortex exhibit a considerable decrease in correlation. Subsequent aeroacoustic post processing indicated a reduced influence of the non-compactness of the aerofoil on the far-field noise results within the resolved frequency range where the leading edge noise dominates. As such, the current results suggest that the tip vortex increases far-field SPL for the tip most sections due to its decorrelating effect. While this effect of the tip vortex is found to be small in the present results, as it is limited to the immediate vicinity of the tip, it is hypothesised that finite aerofoils at a larger angles of attack, which are associated with a stronger tip vortex, would exhibit a stronger influence of the tip vortex on the far-field noise emissions.

7.2 Suggested future work

This thesis has demonstrated the capability of the large eddy simulation technique to be used for investigations of turbulence, illustrated its applicability for the analysis of turbulence interaction noise of infinite aerofoils, and presented its first use for the analysis of the case of a finite aerofoil immersed in a turbulent flow. The method may be beneficial for the future design of low-noise applications. However, experiments are still required to validate the simulations, in particular the results regarding the effect of the tip vortex. An experimental setup designed for such investigations has already been designed but could unfortunately not used in time to support the findings of this thesis. The test rig and its design methodology are described in Appendix A, and future work will consist of using it to corroborate the findings of this thesis. In addition, mesh refinement studies are recommended to assess mesh dependency of the present results.
As shown in Chapter 4, the inlet grid turbulence creation method allows the development of turbulent flows to be investigated to a considerable level of detail. A topic of potential future research interest is the investigation of the return to isotropy of the largest scales, and the associated development of the resolved dissipation. First results regarding this problem have been presented in Section 4.4.2, illustrating the capability of this approach to investigate these fundamental problems. While DNS is commonly used to investigate these phenomena due to its capability to resolve fluctuations up to the Kolmogorov scales, the present methodology allows flows at a higher Reynolds numbers to be studied, due to the reduced computational cost of LES, and under the assumption of a partially isotropic dissipation tensor.
A shortcoming of the simulations are the un-physical pressure fluctuations identified in Chapters 5 and, to a larger extent, in Chapter 6. It is strongly recommended for future simulations to utilize mesh generators capable of producing higher quality prism layers close to surfaces. By doing so, the valid frequency range of this hybrid approach can

be extended to higher frequencies and may be able to capture the contribution of the trailing edge to the far-field noise into consideration as well.

An investigation out of scope for this research project, but potentially of large interest to the scientific community, is the comparison of the present methodology which features evolving turbulence, with CAA methods, which feature mainly frozen turbulence. For an isolated aerofoil, the time scales are too small for the evolution of the turbulence to have a large effect. This is evidenced by the excellent agreement between CAA methods for infinite aerofoils and experiments. However, for multi-stage interaction problems, the effect of evolving turbulence may be relevant.

Due to its suitability for aeroacoustic investigations, the simulation technique presented in this thesis may be used for research into novel design strategies for the geometry of the wing tip. Recent studies have shown the beneficial effect of serrated leading edges to reduce leading edge noise emissions, and it is conceivable that an optimised wing-tip shape would also be capable of reducing noise emissions, while retaining aerodynamic performance. Although the method is too expensive to be used in an optimisation loop, upon further validation of the results presented in Chapter 6, it can serve as a validation tool for fast semi-empirical or wholly analytical prediction tools suitable for optimisation algorithms in the future.

An application of considerable interest may be the investigation of the physics of tip vortex formation in a turbulent flow. While numerous experimental studies exist for comparable setups, most numerical investigations have so far focussed on direct numerical simulations of isolated or twin vortices in homogeneous turbulent flows. The presented methodology can be used to gain insights into more applied problems, and support in improving turbulence modelling of strongly rotational flows.

Appendix A

The design and manufacturing of a finite aerofoil test rig

A.1 Experiment strategy

After having established suitable locations for the instrumentations, it is necessary to ensure that data recorded by the pressure tappings can be unambiguously related to specific flow phenomena. Even though the static aerofoil is a relatively simple case, there are still a number of complexities involved which need to be investigated before the full case is realized. Thus, an experimental strategy was developed to solve the problem in a stepwise fashion, which allows to gain information about each feature of the experiment as it is added. The steps are, in detail:

1. Infinite wing design: Being one of the most common test rig configuration for aerofoils, this setup will serve as baseline for future tests. Furthermore, it will be used a platform to validate unsteady simulations for the prediction of aeroacoustics conducted in parallel to the experimental work. These simulations will be based on both the turbulence creation approach explored in chapter 4. Self noise levels can be measured, and leading edge noise emissions can be evaluated when additional turbulence grids are installed.

2. Infinite wing design, wall reflection setup: By adding a plate parallel to the aerofoil, flush to the nozzle lip, it will not only be possible to investigate reflection effects, which are important for an analytical code developed at the ANTC [247], but also to evaluate the effect of constraining the sides of the jet on the mean flow at the aerofoil location. It will also give valuable information about the characteristics of the corner flow at the locations where two perpendicular plates meet, as well as allow to investigate the need for boundary layer separation devices at the sides of a future enclosed test section. Another interesting variant of this setup is to

allow for variation of distance of the lower plate to the aerofoil, thereby testing a possible boundary layer separation mechanism, and measuring the noise radiation from the leading edge of the plate.

3. Infinite wing design, fully enclosed setup: By adding a Kevlar panel on top, flush to the nozzle lip, to the previous setup, the aerofoil can be fully enclosed in a semi-open test section, where any shear layers at the streamwise position of the aerofoil are eliminated. This allows for a test of the Kevlar panel as an acoustically transparent wall, and to measure the deflection of the Kevlar cloth due to the flow.

4. Closed wind tunnel setup: The installation of additional panels to fully enclose the flow between nozzle and collector will render the open jet wind tunnel facility closed. Such a system will require an additional set of calibrations and measurements before it can be used for experimental purposes.

5. Closed wind tunnel setup, boundary layer creation: The creation of a turbulent boundary in experiment presents a challenging problem on its own. Thus, experiments need to be conducted to establish the most suitable method to create boundary layers of the required thickness.

6. Closed wind tunnel setup, infinite wing setup: Using the infinite wing setup in a closed wind tunnel will allow to investigate the flow when a device of considerable blocking factor is introduced to the tunnel. Additionally, acoustical data can be generated for comparison with the later case of a finite aerofoil, which features a tip.

7. Closed wind tunnel setup, finite wing setup: Finally, the finite wing setup is investigated with full information about all side effects. Thus, the effect of the finite span can be unambiguously investigated. By using different grids and boundary layer depths, the effect of isotropic and anisotropic turbulence on noise generation can be experimentally clearly identified.

A.2 Infinite wing design

The infinite wing design presents the basis for the experimentation strategy outlined above. It has to be designed with the final setup in mind to enhance re-usability, and yet still be simple in geometry and manufacturing to decrease costs. The complete design, with the context of the wind tunnel nozzle, is shown in figure A.1. Visible components are numbered. The design presented in figure A.1 is near finalized, and has been developed in close collaboration with advisers from the R.J. Mitchells Wind tunnel, University of Southampton, as well as Scale Engineering, the selected manufacturing company.

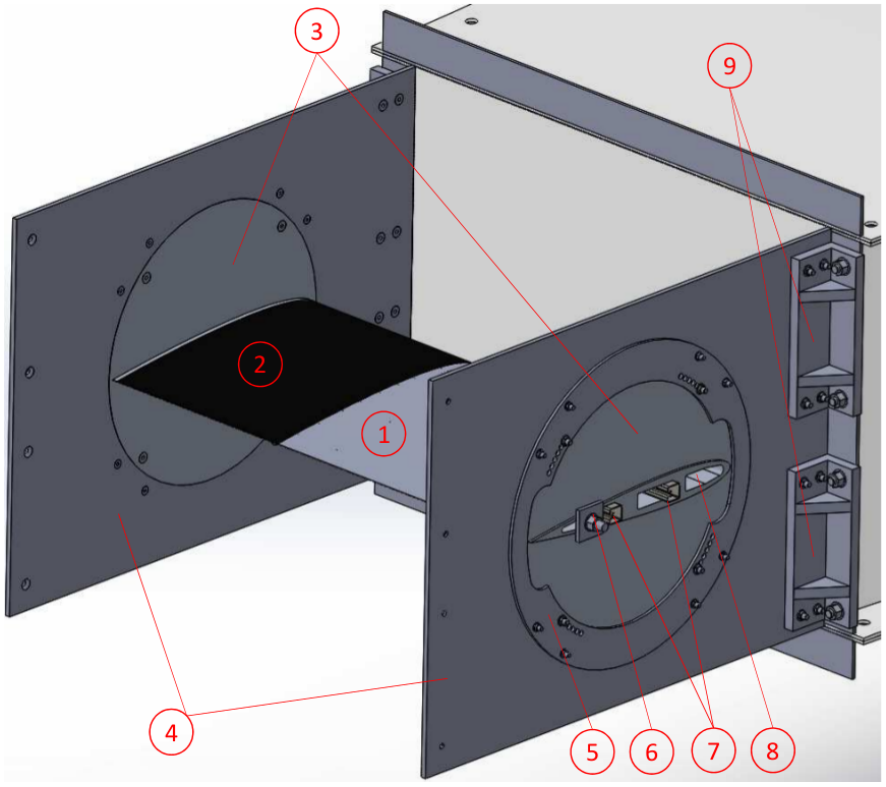

Figure A.1: Design overview for 2D infinite wing design.

The components shown are:

1. **Test aerofoil**: The test aerofoil is a NACA 0012 aerofoil of a span of 0.6m and a chord of 0.5m, with pressure tappings at three spanwise locations. It will be discussed in more detail in section A.2.1.

2. **Dummy aerofoil**: The second aerofoil section, here shown in black, is also of a NACA 0012 profile, but lacks instrumentation. It will only be used to serve as connecting element between instrumented aerofoil and opposing wall.

3. **Wall disk**: The aerofoil is connected to either side to two wall disks, which allow angle of attack variation.

4. **End plate**: The end plates are rectangular aluminium plates of a height of 0.75m and a length of 1m. These dimensions were chosen to allow mounting both at the sides of the nozzle as well as along the bottom or top. They are flush mounted to the lip of the nozzle, keeping flow disturbance at minimum.

5. **Degree strip**: A gap less connection between wall disk and end plate is provided by using circular aluminium disks. Angle of attack variation is possible by using one of 6 mounting holes, which allows the aerofoil to be mounted at angles ranging from 0 to 18 degrees, with 3 degree increments.

6. **Stiffening rod**: To provide additional safety against spanwise failure, a stiffening rod with threads on both ends will be used to tighten two square aluminium plates against the ribs.

7. **Struts**: Additional spanwise stiffness will be provided by addition of two off-the-shelf struts in test and dummy aerofoil, each.

8. **Bottom rib**: The bottom rib is designed to be mounted by means of stitch soldering to the wall disk, providing ample stiffness against bending moments, while avoiding warping of the wall disks through excessive heat. Additionally, it provides spanwise stiffness to the wing by protruding 75mm into the aerofoil.

9. **L-profile fixture**: Two off-the-shelf cast iron L-profiles on either side will provide ample support for the end plates. They are discussed in more detail in section A.2.3.

All screws on the flow side of the plates are designed to be countersunk, so as to minimize flow disturbance.
Not shown in figure A.1 are devices for turbulence generation, such as a grid at the nozzle outlet. This is due to the fact that it is at this point not wholly clear how the turbulence should be created, as it will also depend on ambient turbulence levels, noise production by the grid, and required streamwise development lengths. It is expected, however, that the mounting of a turbulence grid should be relatively straightforward.

A.2.1 Aerofoil design

The aerofoil is the most critical of all the rig components, and has to be designed with care. Not only does it have to withstand the considerable forces of the wind tunnel, it also has to be manufactured to a great accuracy in order to accurately represent the geometry used in simulations. Furthermore, it has to provide sufficient space for instrumentation, and allow easy access for installation and maintenance of sensors.
Figure A.2 shows the test aerofoil design with attached wall disk. The suction side surface is displayed in a transparent blue colour, to allow insight into the inner structure of the wing. Yellow dashed lines show the location of the pressure tappings on the suction side, which are continued on the pressure side.

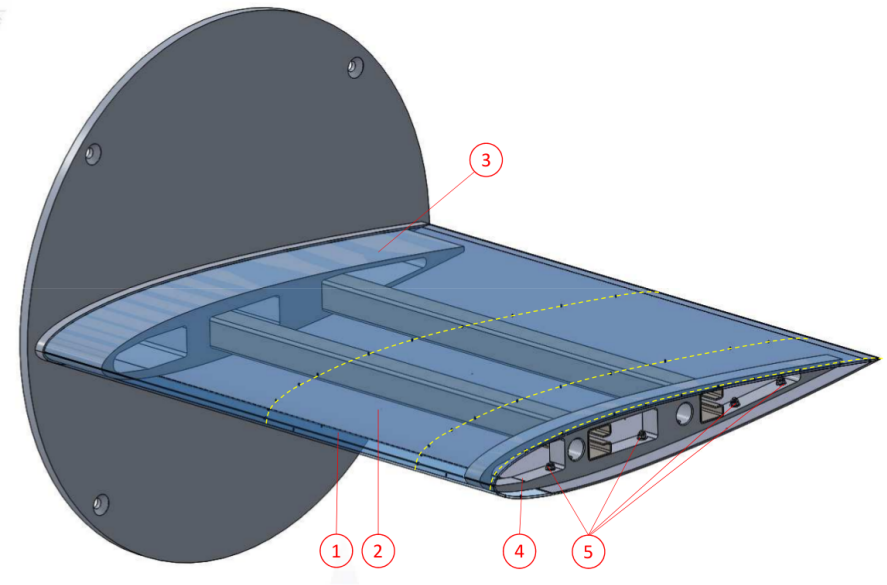

Figure A.2: Design overview for test aerofoil.

The components numbered are:

1. **Suction side surface**: The suction side surface is to be made of carbon composite, and permanently glued to the bottom and top rib, shown here as components three and four, respectively.

2. **Pressure side surface**: Also to be made from carbon composite, the pressure side surface is designed to be detachable to allow easy access for installation and maintenance of the pressure taps. In order to create a smooth surface, the pressure side surface will be slid into the suction side surface, with the latter overlapping the former by 20mm.

3. **Bottom rib**: The bottom rib is stitch welded on the outside of the wall disk, which is not shown here, and provides a large bonding surface to the suction side surface, preventing detachment due to the forces at large angles of attack. It is to be water jet cut, with pockets for struts and cables, as well as holes for the fixtures for attachment of the pressure side.

4. **Top rib**: The top rib is recessed by 20mm from the end of the wing to provide space for the pressure taps. Beside the pockets for struts and cables, as well as the holes for the pressure side fixtures, it contains two holes providing attachment points for the dummy aerofoil, or for future tips.

5. **M6 countersunk screwed connections**: Four such connections on each rib provide stable connection of the pressure side surface component to the ribs. Additional safety against the nuts becoming loose through vibration is obtained by using spring washers.

Following previously conducted steady simulations,, the pressure tap locations are chosen at 0.3 m, 0.5 m and 0.59 m respectively, as measured from the wall disk. When the wing is operated in the finite wing configuration, this would translate to the one at 0.3 m being subjected to the mean flow, the one at 0.5 m measuring the outer boundary layer while the row of pressure taps at 0.59 m would be able to record the effects of the tip vortex on surface pressure. Each of the locations contains 16 taps. Their chordwise locations were chosen based on the result of an optimization algorithm, documented in Section A.2.2.
The dummy aerofoil is essentially identical in design to the test wing, with the differences of having no pressure tappings and no detachable pressure surface.

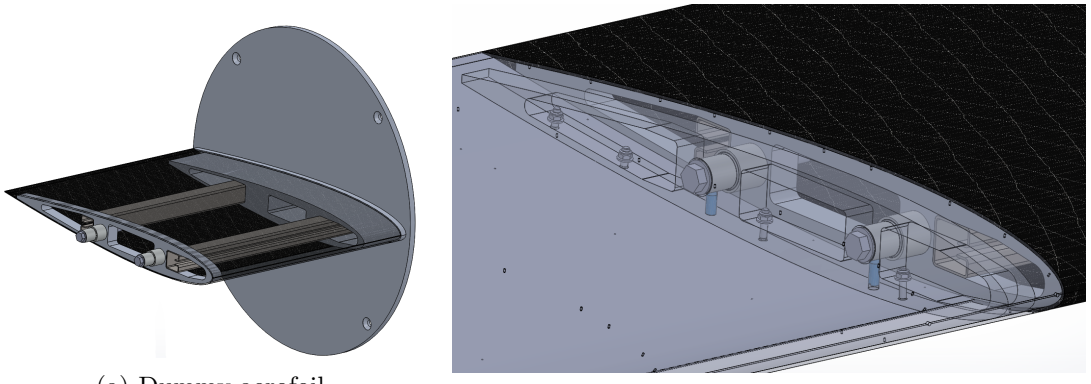

(a) Dummy aerofoil.

(b) Grub screws.

Figure A.3: Dummy aerofoil and aerofoil connection details.

Figure A.3 a) shows the design overview of the dummy aerofoil. The design for the bottom rib is reused to reduce production costs. Again, two struts provide additional spanwise stiffness. As there is no need to access instrumentation in the leading edge of the aerofoil, the front strut is relocated towards the leading edge. At the top rib, two thick bolts are fixed, which are essential to mounting dummy aerofoil to test aerofoil. Figure A.3 b) illustrates how the connection is made. The test aerofoil suction side surface, as well as the top rib, has been made transparent, and the struts are omitted for greater image clarity. The bolts are slid into their corresponding holes in the top rib of the test aerofoil, and fixated by means of two grub screws, which are shown in a light blue colour. The screws are designed to be sunk completely in their threaded holes. Any remaining surface imperfection is to be smoothed over by means of tape. This is essential, as these holes are close to the tip of the aerofoil when the rig is operated in the finite aerofoil setup. Since one of the main research interests is the flow phenomena of tip vortices, the surface must be kept as smooth as possible.

A.2.2 Tapping location optimization procedure

Since the number of pressure tappings has to be limited to a manageable amount of channels, information of the surface pressure acquired from the experiment is limited to

a number of positions on the aerofoil. In order to compute the pressure distributions, it is ideal when these positions are chosen in such a way that they measure the pressure finely spaced where large gradients exist, and coarsely spaced where the pressure is largely constant. Prior experiments [99; 135] have often chosen to cluster the sensors close to the leading edge, where stagnation point and suction peak are expected, and spread sensor placement further apart towards the trailing edge. Furthermore, these experiments often also worked with a larger number of sensors. However, as detailed surface pressure data from a number of numerical simulations run for the experiment design is available in this case, it is possible to determine these positions with high accuracy prior to experiment.

The method developed for the optimization of the tapping locations follows the consideration that the error when computing the lift coefficient c_l should be minimal. A straightforward algorithm for computing c_l from a set of discrete data points is using the trapezoidal rule for numerical integration:

$$\int_{x_a}^{x_b} p(x)\,\mathrm{d}x \approx (x_b - x_a)\left[\frac{p(x_a) + p(x_b)}{2}\right], \tag{A.1}$$

where x_a and x_b are positions on the aerofoil surface, and $p(x)$ is the surface pressure as a function of position. As the lift of a given section of the aerofoil can be calculated with high accuracy using the information from the simulations, a cost function is now defined:

$$F = \sum_{n=1}^{n_{taps}} \sqrt{(c_{l_{num}}(n) - c_{l_{disc}}(n))^2}, \tag{A.2}$$

where $c_{l_{num}}(n)$ is the accurate lift for a segment n of the surface between two positions $p(x_a), p(x_b)$, computed from the pressure information extracted from the numerical simulation, and $c_{l_{disc}}(n)$ is the lift for this segment computed using only the pressure information from the two points to either side of the segment, thereby mimicking the condition in experiment. The pressure data was extracted from a simulation of a finite aerofoil an emulated boundary layer at 6° angle of attack.

Using this cost function, the optimization loop shown in figure A.4 can be set up.

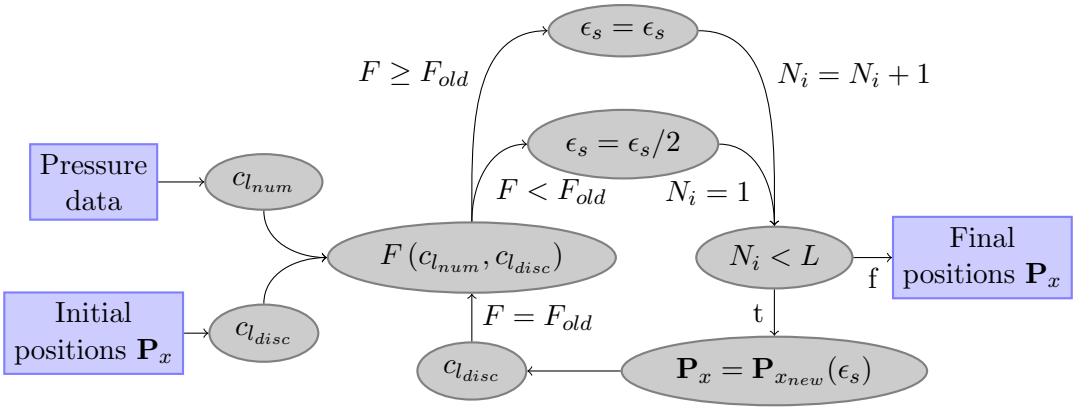

Figure A.4: Simplified optimization loop diagram.

In order to reduce the complexity of the diagram, the loop over all segments n of the aerofoil surface is omitted. Blue boxes symbolize input and output, while grey ellipses represent computational steps. The optimization takes as input the pressure data of an aerofoil section, as well as an initial vector $\mathbf{P}_x$ of probe positions. These may be equally spaced, or already pre-arranged by the user. The algorithm then computes the initial lift coefficients $c_{l_{num}}$ and $c_{l_{disc}}$ for each segment. The results are subsequently fed into the optimization loop, which evaluates the error for each element and sums them to obtain the absolute value of the cost function. The value of the cost function is then compared against an initial value for the cost function, which can be set to a high value for the first iteration. In subsequent iterations, if the cost function value is higher than the value of the previous iteration, the step size ϵ_s, which determines how far the positions of the pressure taps can be moved by the improvement algorithm, is kept constant. In this case, the iteration counter N_i is increased. If the cost function value is lower, ϵ_s is halved, and N_i reset. The next step consists in comparing the iteration counter against a limit L, which is set by the user. If $N_i < L$ is false, the loop is exited and the final positions are obtained. If $N_i < L$ is true, the vector of the probe locations $\mathbf{P}_x$ is updated with the improvement algorithm. It narrows the distance between pressure taps, thereby decreasing the error of the segment. During this procedure, priority is given to segments with the largest errors, and the position of each tap can only be moved once in each iteration. The value of the cost function for the old $\mathbf{P}_x$ is stored to F_{old}, and the new value $c_{l_{disc}}$ is computed with the updated $\mathbf{P}_x$. The cost function is then recalculated, and the cycle begins from anew.

There are a number of constraints put on the placement of the pressure taps. As the suction side is the more aerodynamically important side of the aerofoil, it was decided to place 10 pressure taps there, and only 6 on the pressure side. An additional, fixed, probe location is the leading edge, where it is intended to install a pressure transducer capable of recording high frequency pressure changes for aeroacoustic analysis. Furthermore, a hard-coded limit was put on the probe locations in terms of their minimal proximity to the trailing edge, since the thickness of the aerofoil does not permit for instrumentation beyond a certain chordwise position.

The optimized probe locations are shown in figure A.5. Previously conducted experiments showed that the shapes of the pressure distribution of sections $z = 0.3$ m and $z = 0.5$ m are largely the same. Thus, only the optimization results for sections $z = 0.3$ m and $z = 0.595$ m are discussed here.

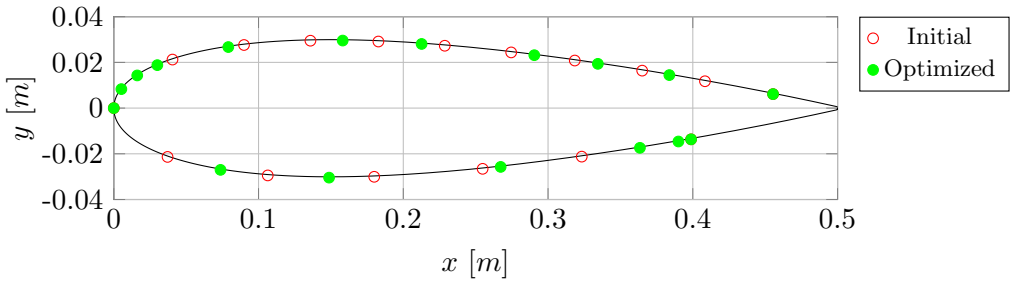

(a) $z = 0.3$m.

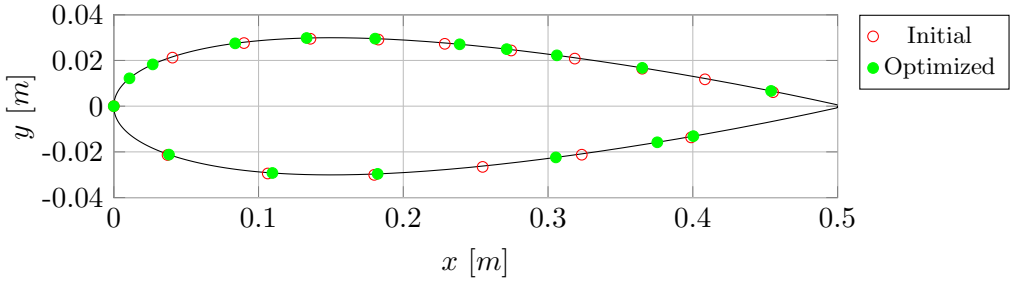

(b) $z = 0.595$.

Figure A.5: Optimized probe locations at two positions along the span.

When comparing figure A.5 a) with b), it is apparent that the optimization procedure led to a higher clustering of the pressure taps close to the leading edge in case of the free-stream section $z = 0.3$ m compared to the tip section $z = 0.595$ m. Considering the high pressure gradients which can be expected in free-stream conditions at this position, this is a desired outcome. The more spread out positions of the pressure taps in the tip section will also allow to measure tip vortex behaviour in greater detail.
The optimization of the positions of the pressure taps on the pressure side did not work as expected. Qualitatively, a trend can be observed where the probe locations are shifted downstream, as opposed to being clustered towards the leading edge. It is not entirely clear why this is the case. However, due to the low aerodynamic importance of the pressure side, it was decided to accept this optimization outcome and to arbitrarily place one of the probe locations half way between the optimized, first location on the pressure side, and the leading edge itself, in order to obtain a better information on the pressure gradient there.

A.2.3 Fixture apparatus

The Boldrewood anechoic wind tunnel facility is designed to provide a high quality anechoic environment. All walls are covered in foam cones, while the floor is covered by a steel wire mesh above a soft and sound absorbing surface. Thus, only limited fixture points are provided, which are designated for use by the traverse system as well as the

data acquisition systems. It is therefore necessary to mount the test rig solely to the nozzle. Until such time that the completely closed test section is assembled, all forces need to be managed by the connection to the nozzle alone, necessitating very sturdy connections.

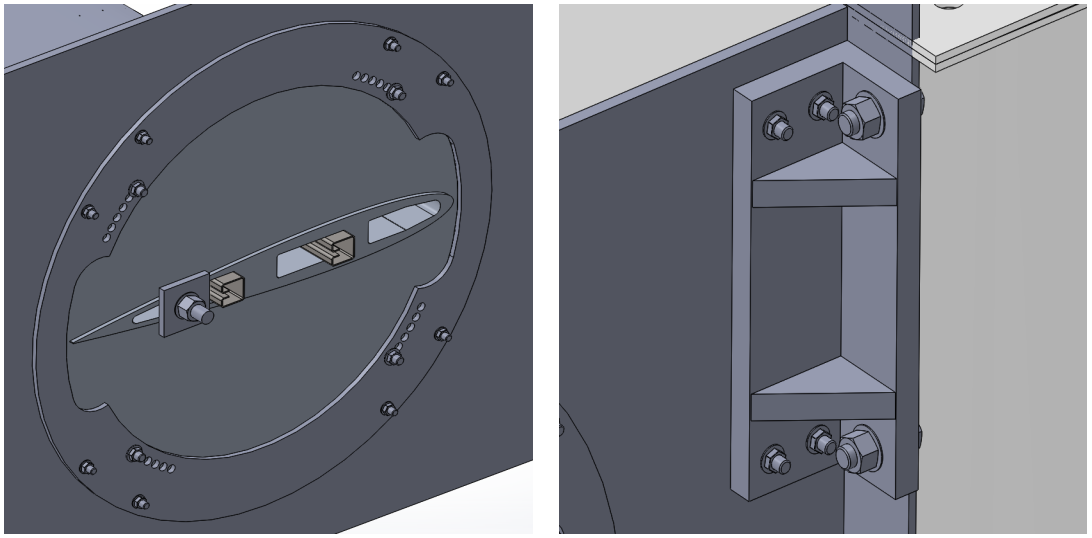

(a) Degree strip detail. (b) L-profile detail.

Figure A.6: Fixture details.

The fixtures are shown in more detail in figures A.6 a) and b). The degree strip, shown in figure A.6 a), provides four mounting points to the wall disk via four M10 bolts and is itself mounted to the side plate by means of eight M8 bolts. By sealing the gap between wall disk and side plate, any leakage of flow is eliminated and possible whistling effects are kept at a minimum. Although altering the angle of attack requires first the removal and then reassembly of 8 screws, this is considered a acceptable trade-off for the increased sturdiness.

Figure A.6 b) shows the L-profile and its connection to the nozzle frame. To keep expenses low, the profile is chosen from the catalogue of cast-iron fixtures supplied by NORELEM. The only additional machining required is the drilling of the mounting holes. The element will be fixed by two M16 bolts to the nozzle frame, and will be providing mounting to the side plate by means of 4 M10 countersunk screws. This connection should be able to provide sufficient support to wall plate and aerofoil, even when a high angle of attack is chosen. On-site machining will be required to drill the mounting holes in the nozzle frame.

A.3 Application during validation of the Boldrewood anechoic wind tunnel

Most recently, the author was informed that the finite aerofoil test rig has been used to validate the Boldrewood anechoic wind tunnel facility. Figures A.7 (a) and (b) show the finite aerofoil aerofoil test rig in its configuration as infinite aerofoil mounted to the nozzle of the wind tunnel, within the anechoic chamber.

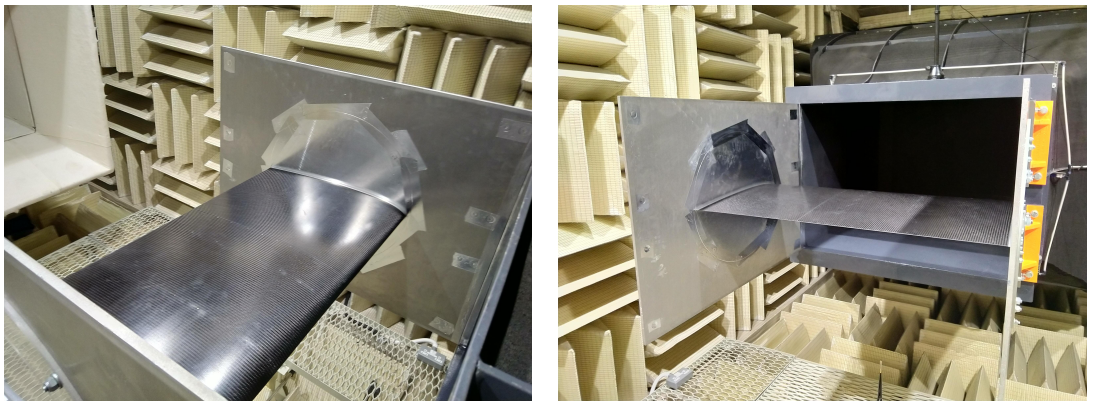

(a) Overhead view. (b) Upstream view.

Figure A.7: Mounted finite aerofoil test rig.

The author was informed that the finite aerofoil test rig performed very well for the purposes of wind tunnel validation, and funding is being pursued to allow to use the test rig for its intended purpose to further investigate the aeroacoustics of finite aerofoils interacting with turbulent flow.

Appendix B

Linear wave propagation analysis

While finite volume methods on unstructured grids are applicable to a wide of problems, they are often limited to a relatively low order of accuracy [248]. As such, this may lead to the introduction of an excessively large numerical error, which may lead to the results being invalid. This error may be associated with two main features of the unstructured meshing approach:

1. The use of relatively low order numerical schemes, which are able to handle the relatively poor mesh quality of unstructured meshes compared to structured meshes;
2. The use of mesh zones featuring rapid refinement and derefinement.

In regards to the first feature, as discussed in Section 3.2.4, due to the differences in terms of the requirements for the meshing methodology of the turbulence development problem compared to the turbulence interaction problem, and the associated mesh quality changes, it was not feasible to use the same numerical schemes for all simulations presented in this thesis. In order to support the analysis of the main body of this work, the effect on the dissipative and dispersive error associated with using either the second order upwind biased scheme, given by Eqn. (3.21), or the central scheme, given by Eqn. (3.20), for the convective term of Eqn. (3.2) are investigated in this section. By doing so, the cut-off wavenumbers of the utilised numerical schemes is established.
In regards to the second feature, the introduction of the aerofoil into the flow for the turbulence interaction cases was associated with the need for an additional refinement step to be able to properly resolve the aerofoil curvature, as discussed in Section 5.1.1 and documented further in Appendix C.1. While an assessment of the potential occurrence of spurious wave reflections at the interface of derefinement is discussed further in Appendix D.1, this section deals with the dissipation and dispersion errors associated with the propagation of a vortical wave through a refinement or derefinement interface.

B.1 Analysis methodology

In order to facilitate the analysis of dissipation and dispersion errors of the chosen numerical schemes on inhomogeneous meshes, a variant of the commonly used linear wave propagation analysis has been developed. The test domain, as well as its boundary conditions, is shown in Figure B.1.

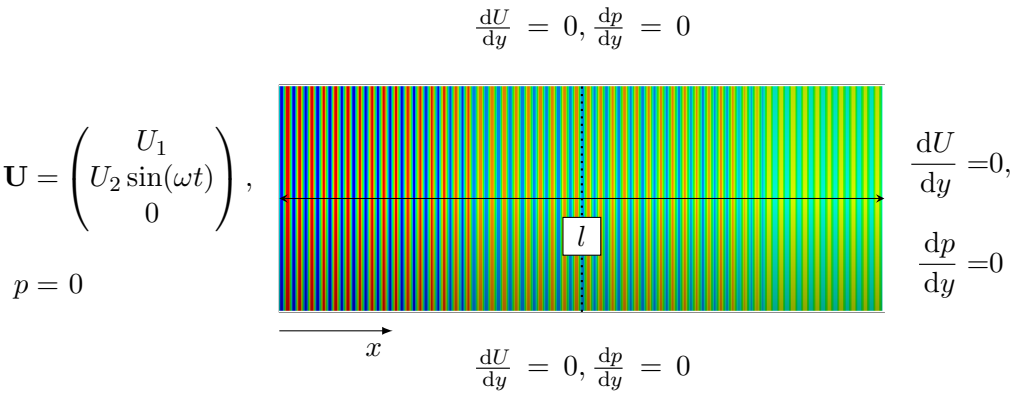

Figure B.1: Linear wave propagation analysis test case setup. Colours illustrate instantaneous vorticity wave contours. Dotted line indicates position of refinement or derefinement interface, if used.

For the inlet boundary condition, U_2 is chosen as an arbitrarily small constant fraction of U_1. In order to replicate the numerical setup used in the main body of the work as much as possible, the linear wave propagation tests were performed using the *pisoFoam* and the *rhoPimpleFoam* solvers for tests involving vortical waves and acoustic waves, respectively. The viscosity in the domain was set to zero to eliminate viscous diffusion. A cell size of $\Delta_x = 10^{-3}$ m was chosen. The transverse velocity is sampled at 7 positions along the centre line. All simulations were conducted using the second order implicit backward time scheme, as given by Eqn. (3.22).

A given numerical scheme may introduce two types of error to the result. These are dissipative and the dispersive errors. Following Anderson [248], who defines the dissipative error ε_{Diss} as the difference between the ratio of the magnitudes of a periodic signal at two successive time steps and unity, ε_{Diss} is defined for the present study over space in an analogous way as:

$$\varepsilon_{Diss} = \frac{|\mathbf{U}(x_{i+1})|}{|\mathbf{U}(x_i)|} - 1, \tag{B.1}$$

thereby quantifying the change of the wave magnitude as the wave is propagated through the domain. Similar definitions have been used by Hu *et al.* [249], Bogey and Bailey [250] as well as Najafi-Yazdi and Mongeau [251]. The dispersion error, which quantifies the property of the numerical solver to transport waves of different wavelengths at different velocities, is defined as:

$$\varepsilon_{Disp} = \frac{\omega/\kappa_1}{v_p(x_i)} - 1, \tag{B.2}$$

with

$$v_p(x_i) = \lambda_l \cdot \left(\frac{\omega}{2\pi} + \frac{2\pi\varphi_i}{x_i/U_1} \right), \tag{B.3}$$

where $\lambda_l = U_1/f$ is the wavelength and φ_i is the phase shift of the sinusoid at position x_i relative to the inlet boundary condition. The cut-off wavenumber κ_c is defined as:

$$\kappa_c = \frac{2\pi}{\text{PPW} \cdot \Delta_c}, \tag{B.4}$$

with Δ_c being the cell size, and PPW is the number of Points Per Wavelength, which has to be chosen such that ε_{Diss} and ε_{Disp} are within acceptable bounds. While for the assessment of low-dispersive and dissipative schemes for CAA purposes arbitrarily chosen accuracy limits ranging from $1 \times 10^{-}2$ [251] to $5 \times 10^{-}5$ [250] have been used for ε_{Diss} and ε_{Disp}, for the present, relatively low order, numerical schemes, a level of 0.05 for both types of numerical error can be considered sufficiently small[1].

The PPW criterion is related to the advection velocity and frequency of the transported wave by:

$$\text{PPW} = \frac{U_1}{f\Delta_x}, \tag{B.5}$$

allowing to study the PPW criterion on a fixed grid by varying either frequency or velocity. For the studies of the linear propagation of vortical waves, U_1 is kept at constant 60 m/s, corresponding approximately to the mean flow velocity U_0 used in Chapter 5 and Chapter 6.

The value of PPW required for the accurate propagation of waves in the domain depends on the numerical scheme employed. While high order schemes used for CAA are able to resolve waves with a minimum of 4 to 9 PPW [249; 250], more generally it is recommended to use 15 to 40 for acoustic purposes [252].

B.2 Spatial scheme errors

Figures B.2 (a) and (b) illustrate the spatially averaged error $\overline{\varepsilon_{Diss}}$ and $\overline{\varepsilon_{Disp}}$ for the streamwise wavenumbers $\kappa_1 = 104.72, 157.08, 209.44, 261.78, 314.16$ m^{-1}, which corresponds to 60, 40, 30, 24 and 20 points per vortical wavelength, respectively. To allow spatial averaging, a homogeneous mesh was used. The value of the time step is set to a CFL number of 0.2, which is assumed to be sufficiently low to minimize temporal integration errors, and furthermore corresponds to the typical CFL number in the vicinity of the aerofoil, as shown in Figures 5.2 (a) and (b).

It is apparent from Figure B.2 (a) that the dissipative error increases with increasing wavenumber if the upwind biased scheme is used for the convective term. Conversely, while the dissipative error is very small for all wavenumbers when the central scheme

[1] Internal Communication

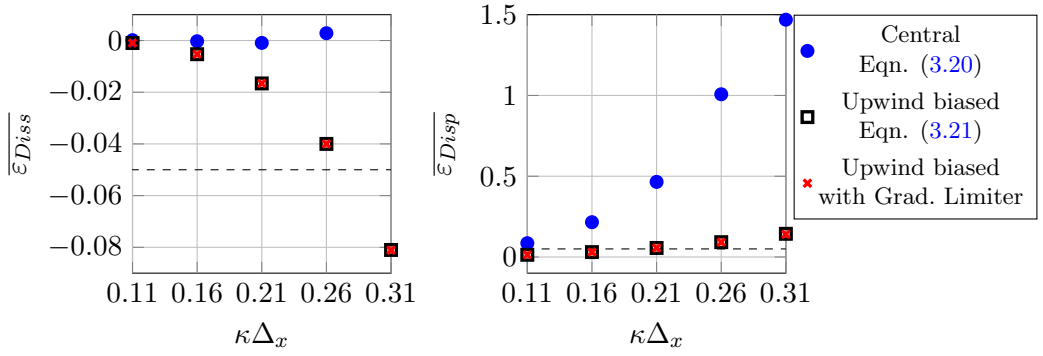

(a) Dissipative error.

(b) Dispersive error.

Figure B.2: Spatial dissipative and dispersive error as a function of wavenumber of the central scheme (blue circle), upwind biased scheme (black square), upwind biased scheme using a gradient limiter (red 'x') on a homogeneous mesh at a CFL number of 0.2. Dashed lines indicate the accuracy limit.

is used, the dispersive error increases rapidly with increasing wavenumber, as shown by Figure B.2 (b). This result is expected, as central space discretization schemes may exhibit severe spurious oscillations for advection dominated problems due to a lack of numerical dissipation [248], as indicated by $\overline{\varepsilon_{Diss}}$ of the central scheme being positive at some of the wavenumbers investigated in Figure B.2 (a). These spurious oscillations are particularly problematic in terms of the dispersive error introduced. It is concluded that in terms of the dispersive error, upwind biased schemes are superior, with the dispersive error not exceeding 0.2 for the wavenumbers investigated in this study.

Based on the results shown in Figure B.2 (a) and (b), it is concluded that at a CFL number of 0.2, a cut-off wavenumber of $\kappa_c = 251.33$ m^{-1} is associated with an acceptable level of ε_{Diss} and ε_{Disp} as the numerical errors are below the previously defined accuracy limit of 0.05. Consequently, it is concluded that a PPW value of 25 is adequate for the propagation of a vortical wave using the upwind biased scheme.

Finally, the use of a gradient limiter in the spatial discretisation schemes is not found to have a significant effect on either dissipative or dispersive error at the wavenumbers investigated and CFL number. It is concluded that the gradients in the present propagation tests are not exceeding the values set in the limiter function, and thus the results of the scheme with the gradient limiter function are identical to when no such function is used.

B.3 Temporal scheme errors

For the purpose of investigating the effect of the CFL number on the numerical accuracy, Figures B.3 (a) and (b) illustrate the results of a parameter study where the CFL number was varied between 0.1 and 1.0, and the inlet signal wavenumber was kept at $\kappa = 209.44$ m^{-1}, which corresponds to a PPW value of 30. In order to keep the points

per vortical wavelength constant, the CFL number was altered by changing the time step Δ_t.

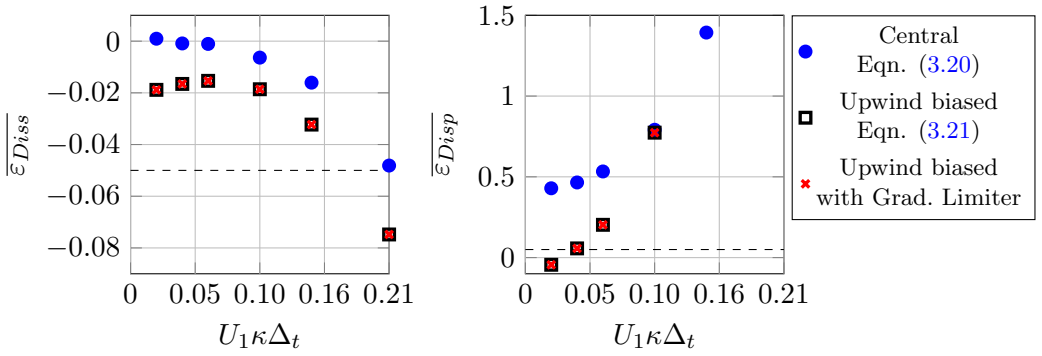

(a) Dissipative error.

(b) Dispersive error.

Figure B.3: Temporal dissipative and dispersive error as a function of Δ_t of the central scheme (blue circle), upwind biased scheme (black square), upwind biased scheme using a gradient limiter (red "x") at $\kappa = 209.44$ m^{-1}. Dashed lines indicate the accuracy limit.

Considering the dissipative error, shown in Figure B.3 (a), it is found that for a sinusoid of $\kappa = 209.44$ m^{-1}, i.e. with 30 points per wavelength, the dissipation error does not exceed -0.05 at CFL numbers of less than 1. Similarly to the results of the previous section it is found that, as expected, the central scheme is less dissipative than the upwind biased scheme.

Considering the dispersive error, shown in Figure B.3 (b), it is found that the upwind biased scheme exhibits lower dispersive error up to $U_1\kappa\Delta_t = 0.1$, which corresponds to CFL $= 0.5$, after which it performs worse than the central scheme. However, since ε_{Disp} is in excess of 0.5 even before this point, it is concluded that an excessive dispersive error must be anticipated if either of these spatial schemes is used in conjunction with the backward time scheme at CFL > 0.5.

In regards to the results discussed in Chapter 5, it is concluded from Figures B.3 (a) and (b) that for the CFL numbers encountered in the region of interest, i.e. in the vicinity of the aerofoil, ε_{Diss} and ε_{Disp} are relatively small when the upwind biased scheme is used to compute cell face fluxes.

Finally, the use of a gradient limiter in the spatial discretisation schemes is not found to have a significant effect on either dissipative or dispersive error at the CFL numbers investigated. It is concluded that the gradients in the present propagation tests are not exceeding the values set in the limiter function, and thus the results of the scheme with the gradient limiter function are identical to when no such function is used.

B.4 Refinement analysis

For a study of the effect of the refinement and derefinement interfaces on the dissipative and dispersive error, the cell size in streamwise direction is halved, i.e. from Δ_c to $\Delta_c/2$, or doubled, i.e. from $\Delta_c/2$ to Δ_c, respectively, in the middle of the domain as illustrated by the dotted line in Figure B.1. Figures B.4 (a) and (b) illustrate the mesh for a refinement and a derefinement interface, respectively.

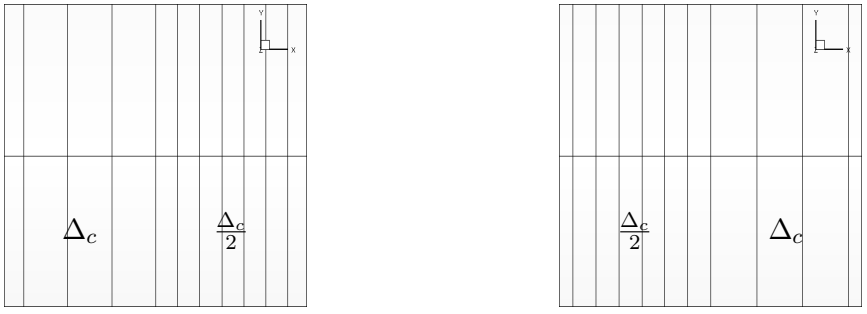

(a) Mesh refinement interface. (b) Mesh derefinement interface.

Figure B.4: Illustration of mesh refinement and derefinement interfaces.

As mesh refinement and derefinement interfaces were used only in conjunction with the upwind biased spatial scheme as defined by Eqn. (3.21), this scheme is also used to investigate the dissipation and dispersion error associated with these interfaces. In order to minimise ε_{Diss} and ε_{Disp} inherent to the upwind biased scheme, a conservative value of 40 PPW is used, which corresponds to a wavenumber of $\kappa_c = 157.08$ m^{-1}. The value of the time step is set to a CFL number of 0.2, based on Δ_c, in order to minimize temporal integration errors. The results for the dissipation and dispersion error across the interfaces illustrated in Figure B.4 are presented in Figures B.5 (a) and (b), respectively. It is noted that in regards to ε_{Diss} and ε_{Disp}, a refinement or derefinement step affects both the errors arising from the spatial as well as from the temporal schemes. While the time step is the same in the two cases, the local CFL number changes as it is dependent on the cell size.

Considering the dissipative error, shown in Figure B.5 (a) that upstream of the refinement step, the values of ε_{Diss} are in good agreement with those of ε_{Diss} for the upwind biased scheme on a homogeneous mesh. Further downstream, the effect of a sudden refinement step on ε_{Diss} is then observed to consist of a temporary positive value. This is due to the better downstream discretisation of the wave, which is better able to capture the extrema of the wave and hence the magnitude of the wave increases. However, at points further downstream, values of ε_{Diss} are obtained which are representative of homogeneous meshes of cell size $\Delta_c/2$. The opposite behaviour is observed for the case of a derefinement step. As such, the behaviour in both cases is as expected, as ε_{Diss} has been observed for the Upwind biased scheme in Sections B.2 and B.3 to be more dependent on the cell size than on the CFL number at the present low CFL numbers of

0.2 and 0.4 in the fine and coarse domain, respectively.
It is noted that the dissipative error, for this CFL number and PPW, does not exceed -0.01 for both refinement and derefinement steps, and is therefore considerably below the accuracy limit of -0.05. It is concluded that in terms of the dissipative error, the effect of the refinement and derefinement interfaces is limited to the immediate downstream vicinity of the interface.

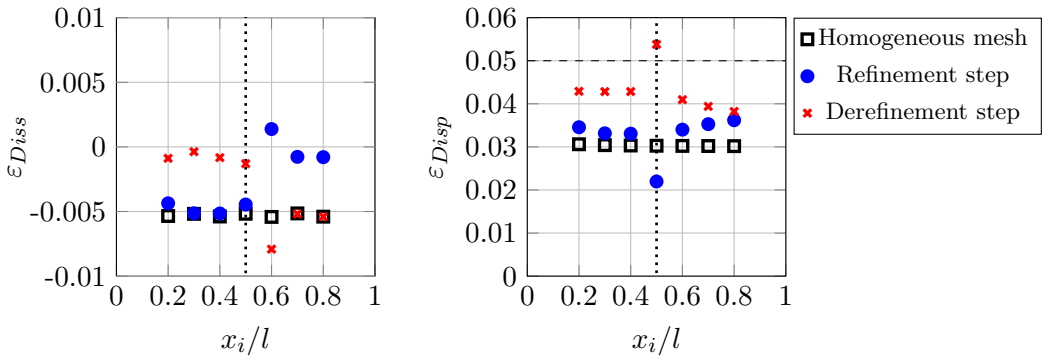

(a) Dissipative error.

(b) Dispersive error.

Figure B.5: Dissipative and dispersive error for a vortical wave across a refinement and derefinement interface using the upwind biased scheme Eqn. (3.21) at a CFL number of 0.2 and 40 PPW. Dashed lines indicate the accuracy limit, dotted lines indicate the position of the interface.

For the dispersive error, shown in Figure B.5 (b), it is observed that for both cases where the cell size is changed, ε_{Disp} is higher than for the homogeneous mesh case. In particular for the refined domains, this is attributed to the effect of the CFL number, as the spatial scheme used in conjunction with the backward temporal scheme was observed in Figure B.3 (b) to exhibit a significantly increasing ε_{Disp} with increasing CFL number, while ε_{Disp} was observed in Figure B.2 (b) to be not as strongly affected by the refinement level.
Downstream of the refinement or derefinement interface, ε_{Disp} is observed to follow an increasing and decreasing trend, respectively. It is conceivable that given sufficient development length, the value of ε_{Disp} would obtain a value representative of that of a homogeneous mesh. It is concluded that the effects of the refinement or derefinement step on the dispersive error are not limited to the vicinity of the interface, although the effects appear more prominent downstream than upstream. However, with the exception of the point immediately downstream of the derefinement interface, all dispersion errors are well below the accuracy limit of 0.05 for this wavenumber and CFL number.

B.5 Assessment of dissipative and dispersive error for acoustic waves

It is emphasised that the discussion above is applicable to the advection of vorticity waves, i.e. the turbulent eddies of the flow, which are being investigated predominantly in Chapter 4. Conversely, for the primary focus of this thesis, the generation and propagation of leading edge noise, the accurate advection of the acoustic waves is more relevant than the advection of the turbulent eddies, which are of secondary interest once the interaction with the leading edge has taken place, as the trailing edge noise generation has been found not to be affected by external turbulence [95]. Since acoustic waves propagate at $U_c = c_0 + U_1$, they are typically discretised in the numerical domain by a number of points per wavelengths of almost an order of magnitude higher than vorticity waves. Consequently, dissipative and dispersive errors are considerably reduced. For completeness, a study was conducted to investigate ε_{Diss} and ε_{Disp} for acoustic waves. This necessitated the use performing a compressible LES. Since the discussion of acoustic results are conducted predominantly in terms of frequency, specification of the pressure fluctuation is conducted via frequency.
Results for the dissipative error and the dispersive error of a propagating sinusoidal pressure fluctuation of 2000 Hz are shown in Figures B.6 (a) and (b), respectively. As the simulations in Chapters 5 and Chapter 6, where a potential numerical error in terms of the propagation of acoustic waves would affect the presented results, were conducted using the upwind biased scheme given by Eqn. (3.21) for the convective term, only results of the linear advection tests with the upwind biased schemes are shown.

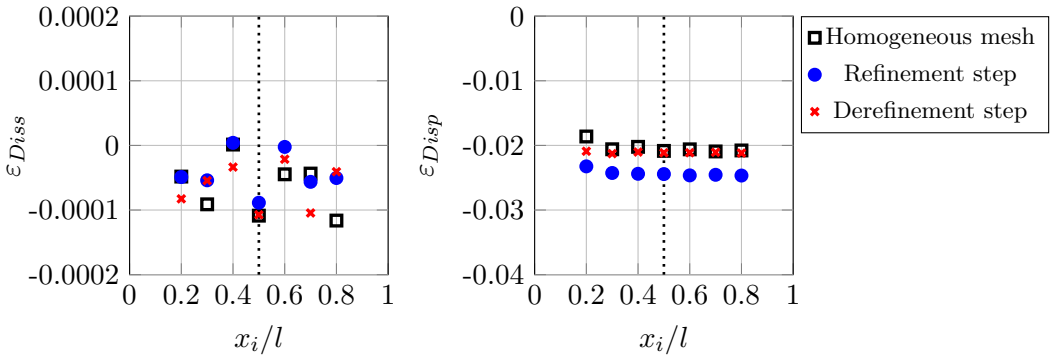

(a) Dissipative error.

(b) Dispersive error.

Figure B.6: Dissipative and dispersive error for an acoustic wave across a refinement and derefinement interface using the upwind biased scheme Eqn. (3.21) at a CFL number of 0.2 and 40 PPW. Dotted lines indicate the position of the interface.

It is apparent from Figure B.6 (a) that the high number of points per wavelength for an acoustic wave, in this case 203 points, contributes to very low dissipative errors, which are significantly below the threshold of 0.05. No consistent influence of the mesh

refinement step is observed within this case study for acoustic waves, as the variation of ε_{Diss} for the case with the refinement and derefinement steps is within the variation of ε_{Diss} of the case with a homogeneous mesh. As ε_{Diss} is, at all points, very small, further investigation is omitted.

As shown in Figure B.6 (b), the dispersive error is observed to develop similarly for the propagation of acoustic waves as for vortical waves in response to changes of the mesh, with the inhomogeneous meshes exhibiting higher absolute dispersive errors than the homogeneous mesh both upstream as well as downstream of the interface. However, in the case of acoustic waves, it is observed that the value of ε_{Disp} is affected globally, with no obvious difference between the upstream and downstream domains. As the differences in terms of ε_{Disp} for the homogeneous and inhomogeneous meshes are one order of magnitude below that of the accuracy limit of 0.05, it is concluded that impacts of the refinement and derefinement interfaces on the propagation of acoustic waves are negligible. It is concluded that using the upwind-biased spatial discretisation scheme for the convective term is adequate for the purpose of replicating the propagation of acoustic waves over distances not much larger than the aerofoil chord.

It is furthermore emphasised that in this work the acoustic waves were not propagated to the far-field. Instead, as discussed in Section 3.1.3, the acoustic analogy of Ffowcs-Williams and Hawkings [118] was used to determine the far-field acoustics from the on-surface pressure fluctuations induced by the impingements of the vortical disturbances on the leading edge. One area where the propagation of acoustic waves remains relevant are the non-compactness effects as discussed in Sections 2.4.2.1 and Section 5.4.2. Considering the very low magnitude of ε_{Diss} and ε_{Disp} for the frequencies of interest when an upwind biased scheme is used, it is concluded that the numerical errors are negligible in case of the aeroacoustic analysis conducted in Chapter 5 and Chapter 6.

Appendix C

Details of numerical methodology

C.1 Mesh generation methodology

In order to allow meshing of geometries more complex than the turbulence interaction case discussed in Chapters 3 and 4, an unstructured mesh generation approach was selected. To facilitate reproduction of the meshes used in Chapters 5 and 6, the process is described in the following.

The mesh generator used is part of the commercial package *HEXPRESS*^{TM}*/Hybrid* and generates unstructured, geometry fitted meshes based on a fractal approach. In a first step, the domain is discretized by hexahedral cells of size Δ_b. Subsequently, volumes and patches requested by the user to be of a higher refinement level are refined by subdividing the cells by a factor of two in all directions. The resulting cell size is computed as

$$\Delta_{n_r} = \Delta_b 0.5^{n_r}, \tag{C.1}$$

where n_r is the refinement level. The user may also specify a number of buffer layers between the refinement volume or patch and the surrounding domain, where the refinement level is kept constant. Once all patches and volumes have been refined, the generator moves points of cells which cross a patch onto the patch, and deletes cells outside the domain, i.e. those contained within an immersed geometry. Thus, a geometry-fitted mesh is obtained. Finally, the algorithm introduces prism layers onto immersed geometries to improve boundary layer refinement.

The general approach to generate the meshes used in Chapters 5 and 6 is the same, and is illustrated in Figures C.1 (a) and (b) for the far-field and the near-field domain, respectively.

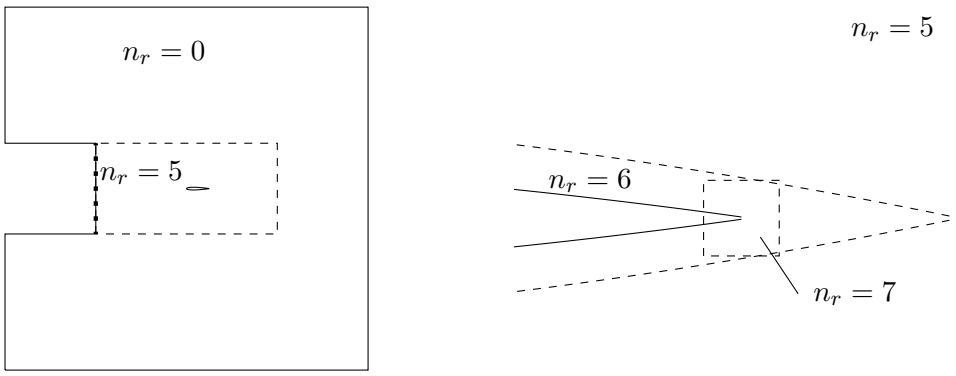

(a) Far-field domain.

(b) Trailing edge near-field domain.

Figure C.1: Setup of refinement zones.

The base grid cell size chosen for the domains used in Chapters 5 and 6 is $\Delta_b = G_p$, and is used in the buffer domain where the refinement level is $n_r = 0$, as illustrated in Figure C.1 (a). By setting $n_r = 5$ within the turbulence domain, which is indicated by the dashed lines in Figure C.1 (a), a discretization of 32 cells per grid period is achieved, satisfying the recommendations by Blackmore *et al.* [13] for the suitable resolution for the inlet grid turbulence creation method , and resulting in acceptable levels of dissipative and dispersive errors for the vortical waves in the energy carrying range as established in Section 4.1.3 and Appendix B.

In order to minimize interactions of the sides of the turbulent flow with the derefinement zones between turbulence domain and buffer domain, the derefinement zone outside the turbulence domain was extended by inserting 5 layers of cells for each refinement level before a derefinement step of a factor of 2 is performed. By doing so, a clear separation between derefinement zones and the sides of the turbulent jet was achieved, as shown in the investigation of the potential remaining interaction effects between the derefinement zone and the edges of the turbulent flow, documented in Appendix D.1.

In the near-field of the aerofoil, illustrated by Figure C.1 (b), an additional refinement step to a level of $n_r = 6$ is performed to achieve acceptable discretization of the curvature at the leading edge, which is of particular interest from an aeroacoustic perspective [94; 101]. This is also beneficial in terms of minimising dissipative and dispersive error of acoustic waves propagating from leading edge to trailing edge and vice-versa, which for the reproduction of the non-compactness effects. Between the aerofoil surface and near-field, a minimum of 10 cell layers were prescribed to achieve an acceptable thickness of this refined layer, while keeping computational expense acceptable. The number of these cell layers is, within the software *HEXPRESS*^{TM}*/Hybrid* governed by the so called diffusion level parameter, which determines to how many consecutive neighbours of a cell flagged for refinement the refinement level should be propagated. As noted in Chapter 6, this number had to be decreased from 4 to 2 in case of the finite aerofoil due to the added computational expense of a fully 3D geometry.

While the chosen meshing approach is versatile and has a rapid turnaround time compared to classical structured meshing approaches, it was found that the prism layer generation utilities on the surface of immersed geometries are lacking. While this is not a critical shortcoming for the present case, due to the negligible influence of the boundary layer on leading edge noise generation, it is suggested that a more advanced unstructured meshing methodology is used if a problem which is more dependent on the accurate capturing of the boundary layer is investigated. In the present investigation, the prism layer consisted of 10 cells inserted within a height of one cell at $n_r = 6$ and 7 for the main body of the aerofoil and the trailing edge, respectively.
Finally, a refinement level of $n_r = 7$ was selected for the trailing edge, in order to be able to discretize a blunt trailing edge.

C.2 Implementation of the non-reflective boundary condition *waveTransmissive* in OpenFOAM

In order to minimize reflections of waves from the boundaries of a numerical domain, non-reflective boundary conditions are required. A comprehensive investigation of this problem was conducted by Poinsot and Lele [229], who proposed an approach to compute characteristic boundary conditions for the numerical solution of the Navier-Stokes equations. The *waveTransmissive* boundary condition in OpenFOAM v3.0 is a simplified implementation of their approach, and aims to reducing reflections by solving:

$$\frac{\mathrm{D}\phi}{\mathrm{D}t} \approx \frac{\partial\phi}{\partial t} + w_p \nabla\phi = 0, \tag{C.2}$$

where $\mathrm{D}/\mathrm{D}t$ is the material derivative and w_p is the wave advection velocity, which is assumed to be normal to the boundary face. The wave advection velocity is then computed as:

$$w_p = \frac{\phi_p}{|S_f|} + \sqrt{\frac{\gamma}{\psi_p}}, \tag{C.3}$$

where ϕ_p is the patch face flux, S_f is the patch face area vector, γ is the ratio of specific heats, and ψ_p is the patch compressibility. Since waves may be incoming as well as outgoing, the advection velocity for waves coming into the domain is set to zero in a corrective step.
As pointed out by Poinsot and Lele [229], perfectly reflective boundary conditions may lead to an ill-posed problem, as the mean pressure is not imposed by any boundary. Consequently, they suggested to make use of partially non-reflective boundary conditions, where the static pressure is defined for a point far outside the domain, and is imposed to the simulated domain by an acceptably low level of reflection from the far-field boundaries.
In OpenFOAM v3.0, this behaviour is implemented by the use of a field relaxation

coefficient, defined as:

$$k_{rel} = \frac{w_p \Delta_t}{l_\infty}, \tag{C.4}$$

with l_∞ as the relaxation length scale. High values of l_∞ will lead to a less reflective boundary, and hence to a higher possible deviation of the boundary from the value of ϕ in the far-field, while low values of l_∞ will lead to more reflective boundary.
With this definition, the last unknown term in Eqn. (C.2) , the approximated partial derivative of the quantity ϕ in time on the boundary can then be computed using the second order accurate backward scheme Eqn. (3.22) as:

$$\frac{\partial \phi}{\partial t} = \frac{2\phi^{n-1} - 0.5\phi^{n-2} + k_{rel}\phi_\infty}{1.5 + k_{rel}}, \tag{C.5}$$

with ϕ_∞ being the value of the quantity ϕ in the far-field.

Appendix D

Mesh parameter studies

This appendix provides documentation of an assessment of the influence of the derefinement areas from the turbulence domain towards the buffer domain, as well as a limited mesh refinement study.

D.1 Elimination of the buffer domain for the turbulence interaction case

A potential concern of the domain setup used for the turbulence interaction case is the rapid derefinement from the turbulence domain towards the far-field buffer domain. It is conceivable that the derefinement zone may interfere with the turbulent shear layer between the steady far-field flow and the turbulent jet.

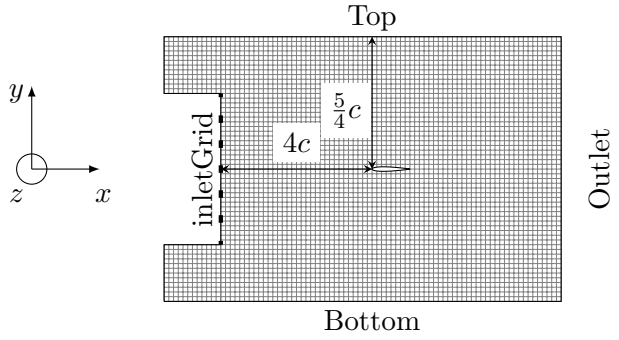

Figure D.1: Case setup of interaction case without buffer zones. Thick dashes illustrate position and approximate size of grid "bars". The origin of the coordinate system coincides with the aerofoil leading edge. Illustration is not to scale.

In order to address this concern, a dedicated turbulence interaction case was investigated, where the far-field buffer domain is eliminated in favour of a uniform mesh for the entire domain. This necessitated a significant reduction of the domain size, since the

computational cost of a finely resolved far-field domain would have been prohibitive. The resulting mesh is shown in Figure D.1.

To facilitate comparison, the boundary conditions for this case are analogous to those of the case with buffer zones and are given in Table 5.1. In order to investigate the potential influence of the grid derefinement on the turbulent jet, the resolved turbulent intensity I_r is shown for the interaction case with and without buffer domain in Figures D.2 (a) and (b), respectively. For reference, the zones of refinement are given by the black lines in Figure D.2 (a), with the highest refinement corresponding to the turbulent jet and the discretisation of the aerofoil geometry and boundary layer.

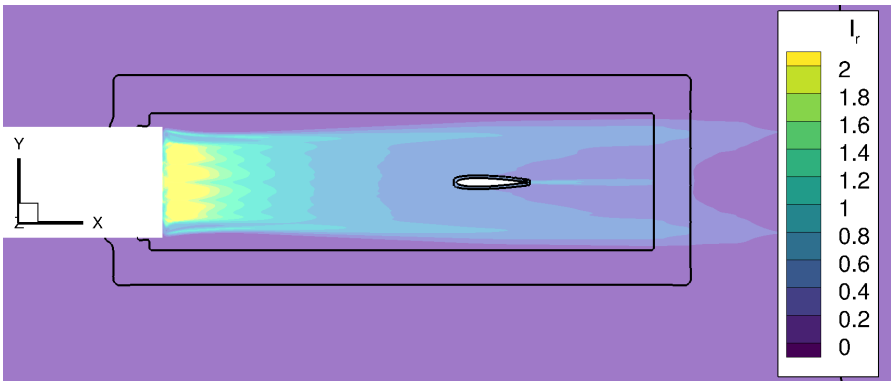

(a) Interaction case with buffer domain, i.e. mesh as shown in Figure 5.1. Lines indicate zones of refinement, with highest within the turbulent jet and close to the aerofoil.

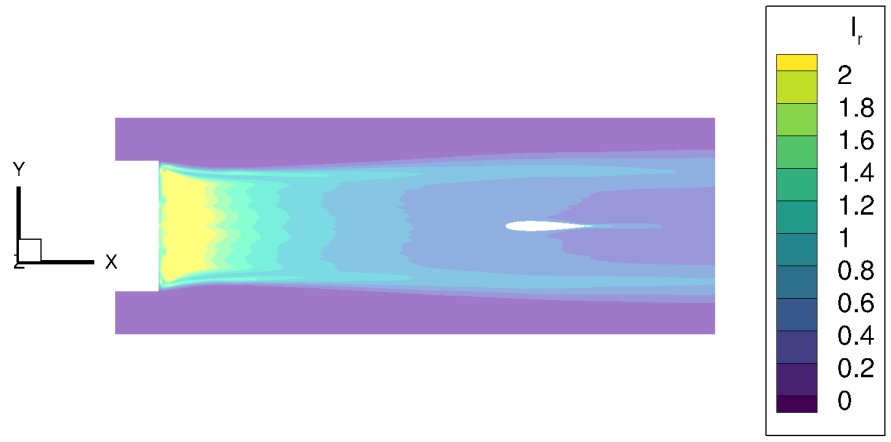

(b) Interaction case without buffer domain, and homogeneous mesh with the exception of the aerofoil near-field, i.e. mesh as shown in Figure D.1.

Figure D.2: Comparison of turbulence intensity of turbulence interaction case on domain with and without buffer domain.

By qualitative comparison of I_r, it is apparent that the presence of the derefinement zones does not have a significant effect on the development of the turbulent jet. This is related to the observation from Figure D.2 (a) that the turbulent jet does not pass through either of the derefinement zones in the transverse direction.

A qualitative comparison of the distribution of the root mean square of the fluctuating

pressure, p_{RMS} of the interaction cases with and without a buffer domain is shown in Figures D.3 (a) and (b).

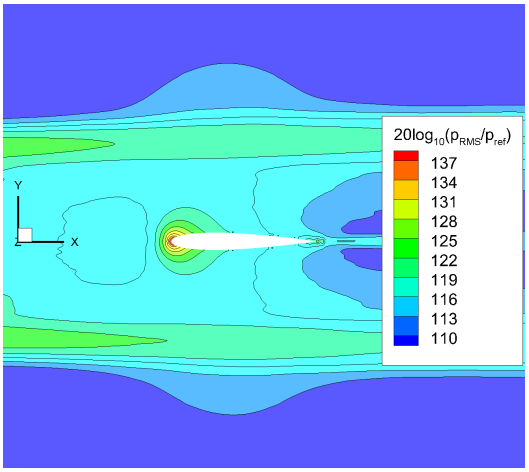

(a) Interaction case with buffer domain, i.e. mesh as shown in Figure 5.1.

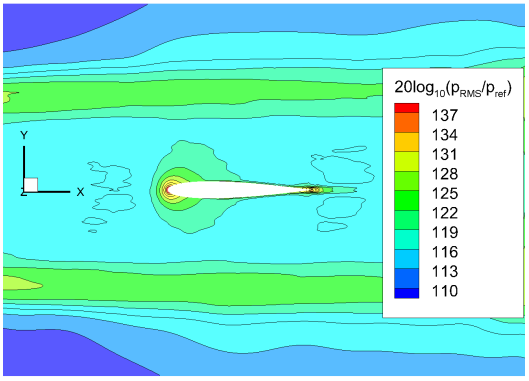

(b) Interaction case without buffer domain, i.e. mesh as shown in Figure D.1.

Figure D.3: Comparison of p_{RMS} of turbulence interaction case on domain with and without buffer domain.

The two cases are both found to exhibit areas of strong pressure fluctuations in the shear layer of the turbulent jet, which is expected considering the analysis of the turbulent intensity shown in Figures D.2 (a) and (b). There are indications that the pressure fluctuations are slightly stronger in the case without a buffer domain, which is related to the slightly elevated turbulent intensity of the interaction case without a buffer domain, as shown by the contours of I_r shown in Figure D.2 (b).

Furthermore, it is observed that only small areas of elevated pressure fluctuations are present in the case of the interaction case with a buffer domain outside the turbulent jet, which are constrained to the vicinity of the aerofoil. Conversely, in the case of the simulation without a buffer domain, the areas of elevated pressure fluctuations spread all the way to the boundary. This difference is attributed to the reduced dissipativeness of the finer mesh of the case without a buffer domain outside the the turbulent domain. Additionally, as discussed in Appendix C.2, the *waveTransmissive* boundary condition is not perfectly non-reflective, and as such, reflection of acoustic waves may contribute to the areas of elevated pressure fluctuations.

Finally, it is noted that the instantaneous pressure distribution on the surface of the aerofoil, as well as towards the trailing edge, exhibits significant fluctuations in the case of the domain without a buffer domain, as shown in Figure D.3 (b). As the near-wall discretisation of the two cases is identical, the cause of this phenomenon is unclear at this time. It is hypothesized that tetrahegonal cells near the wall introduce a significant sensitivity to the boundary conditions of the LES. Further investigation using different meshing strategies is advised to establish the cause of this phenomenon.

In order to investigate whether the derefinement zones have a detrimental effect on the propagation of the acoustic waves, in particular regarding potential reflection effects, the propagation of pressure waves in the near-field of the aerofoil is assessed. For this purpose, the pressure was recorded along the lines $l_1 = (-c \leq x > 0, y = 0, z = 1.5G_p)$ and $l_2 = (x = 0, 0 < y < c, z = 1.5G_p)$. These lines are considered to be representative of the acoustic wave propagation in the xz and yz planes, i.e. in the upstream and transverse directions, respectively.

To facilitate the distinction between hydrodynamic and acoustic pressure fluctuations, the cross-correlation R_{pp} of the fluctuating pressure at two points x_0, x_1, as defined in Eqn. (5.7), is computed. Figures D.4 (a) and (b) show R_{pp} for $x_0 = 0$, i.e. coinciding with the aerofoil leading edge, and $-c \leq x_1 > 0$, i.e. along line l_1. A dashed line indicates correlation associated with hydrodynamic pressure fluctuations transported downstream at the mean flow velocity U_0, whereas a solid line illustrates correlation associated with acoustic waves propagating upstream with $c_0 - U_0$.

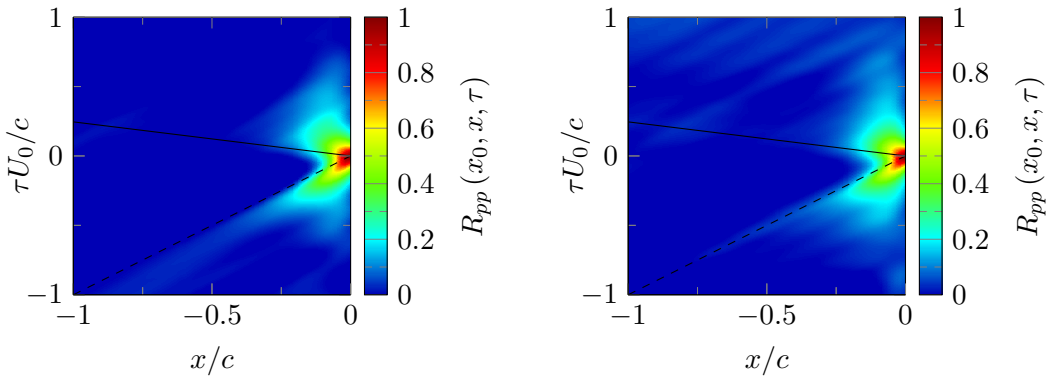

(a) Simulation with buffer domain.

(b) Simulation without buffer domain.

Figure D.4: Unsteady pressure cross-correlation for the near-field of the aerofoil. Dashed line indicates correlations due to eddy convection with mean flow, solid line indicates correlation due to inviscid aerofoil response.

In both simulations using domains with and without a buffer zone, a dominant lobe is associated with hydrodynamic pressure fluctuations, as expected. It is furthermore observed that the lobe associated with the propagation of acoustic waves upstream is relatively weak, which is related to the minimum of noise directivity in this direction, as discussed in Section 5.4. Since both simulations produce qualitatively similar results, it is concluded that the domain setup does not have a significant influence on the acoustic prediction in this direction.

A notable observation is that there is no lobe associated with a downstream propagation speed larger than U_0. It is concluded that if acoustic waves are produced by the inlet-grid turbulence generation method, then they have dissipated almost completely up to the position of the aerofoil. Consequently, errors associated with spurious noise created by the inlet-grid turbulence generation methods are considered negligible.

The cross-correlation of the fluctuating pressure in the transverse direction is shown in Figures D.5 (a) and (b). Since the focus is on potential un-physical reflections of acoustic waves from the derefinement interface between the turbulent domain and the coarser buffer domain, the point of reference for the R_{pp} is set as $y_0 = c$, and cross-correlations are computed for all points on l_2, i.e. $0 < y < c$. As the convection velocity of the turbulent flow, U_0, is normal to the line of investigation, the time delay is non-dimensionalised by the ratio of the speed of sound and the chord, c_0/c. Solid lines indicate correlation due to incoming and outgoing acoustic waves.

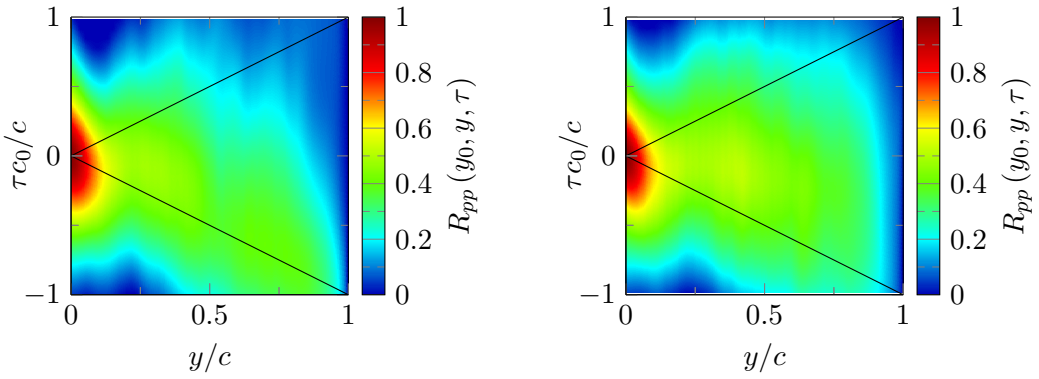

(a) Simulation with buffer domain.

(b) Simulation without buffer domain.

Figure D.5: Unsteady pressure cross-correlation for the near-field of the aerofoil. Solid line indicates correlation due to inviscid aerofoil response.

Unlike R_{pp} computed in the streamwise direction, shown in Figures D.4 (a) and (b), R_{pp} for the transverse direction exhibits a significant qualitative difference. The result for the simulation with a buffer domain, shown in Figure D.5 (a) exhibits one lobe associated with incoming acoustic waves, i.e. with negative time shifts, with a significant amount of correlation all along the line l_2, while correlation associated with outgoing waves, i.e. with positive time shifts is reduced relatively quickly. This indicates that the majority of acoustic waves is incoming, and reflections are minimal.
Conversely, the result for the domain without a buffer domain, shown in Figures D.5 (b) does not allow to make such a clear distinction, with the two lobes blending into each other. This indicates that there is a significant amount of reflection. It is concluded that the *waveTransmissive*, chosen to minimize reflections, is only partially able to do so, which is expected considering the discussion of the boundary condition documented in Appendix C.2. Consequently, for the accurate investigation of aeroacoustic phenomena, the combined use of buffer zones and the *waveTransmissive* boundary condition is recommended, and is therefore adapted for the investigations of Chapters 5 and 6.

D.2 Mesh refinement study

In order to investigate a potential dependency of the results presented in the main body of the thesis on the grid refinement, a limited mesh refinement study was conducted and is documented in this Section. While the refinement chosen in Chapters 5 and 6 is based on the best practices suggested by Blackmore *et al.* [13], and furthermore is computationally affordable, a further refinement would lead to computational costs exceeding one year of runtime for a single case. However, as pointed out by Georgiadis *et al.* [174], a derefined simulation may be instructive in determining whether the main fluid phenomena are captured appropriately in the baseline simulation, as a derefined case study which is incapable of even providing indications of an under-resolved simulation can be considered evidence that the baseline solution is not sufficiently resolved as well.
The derefined case study was conducted by following the meshing procedure as documented in Section C.1, with the sole difference that the refinement levels of the turbulence domain, the aerofoil as well as the trailing edge refinement zones were reduced by one level. The derefined case study will in the following be referred to as the derefined case, whereas the resolution used in the turbulence interaction cases investigated in Chapters 5 and 6 will be referred to as baseline case. Figures D.6 (a) and (b) illustrate the differences in terms of the generated mesh, as well as in terms of the contours of the root mean square of the fluctuating pressure p_{rms}.

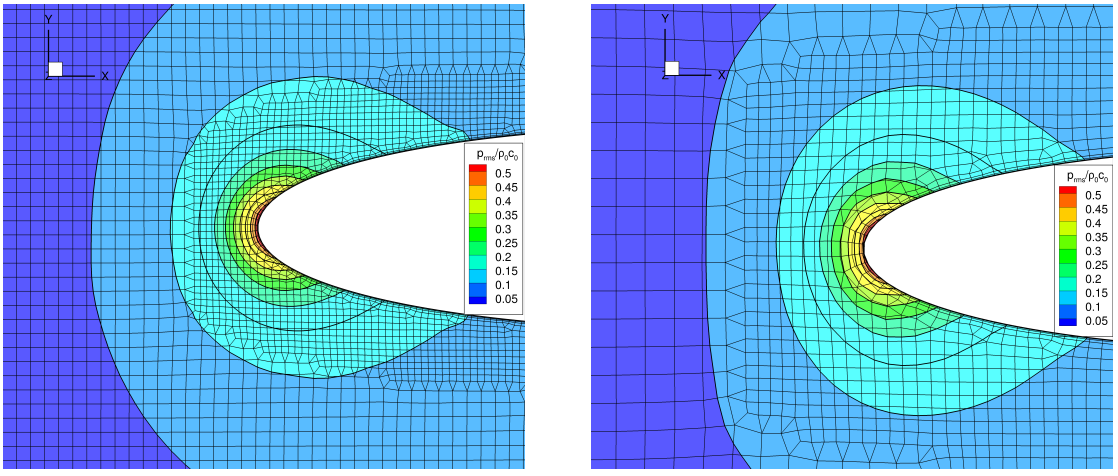

(a) Baseline case.

(b) Derefined case.

Figure D.6: Comparison of mesh and contours of non-dimensional root mean square of the fluctuating pressure at the leading edge for two mesh refinement cases.

It is apparent from the comparison of Figures D.6 (a) and (b) that while there are some differences, as expected considering the significantly higher refinement of the baseline case, the distributions of p_{rms} is qualitatively very similar between the two cases.
A qualitative comparison of the distribution of the non-dimensional instantaneous pressure $p'/\rho_0 c_0^2$ of the baseline and the derefined cases is shown in Figure D.7 (a) and (b).

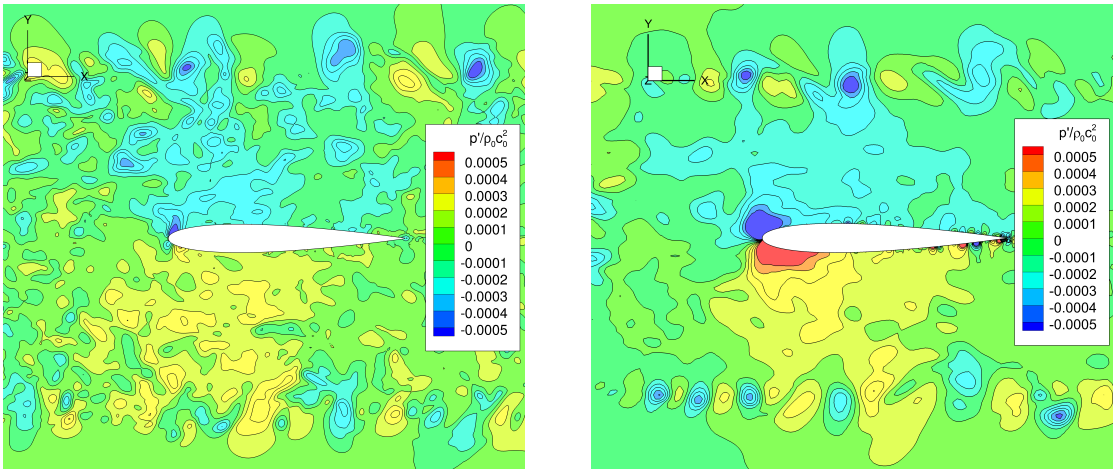

(a) Baseline case. (b) Derefined case.

Figure D.7: Comparison of non-dimensional instantaneous pressure of the baseline and derefined case.

It is immediately apparent from Figure D.7 (a) and (b) that the instantaneous pressure contours associated with the turbulent eddies are much coarser in the derefined case than in the baseline, which is expected. Areas of elevated or depressed instantaneous pressure, which are attributable with acoustic waves, are clearly observable in both cases, indicating that the noise production mechanism of turbulence interaction noise is exhibited by both cases. However, similar to the interaction case without a buffer domain, the generation of strong pressure fluctuations on the aerofoil surface is observable towards the trailing edge in the derefined case, indicating that this un-physical phenomenon may be triggered by a change in boundary conditions as well as by a change in refinement. The development of the temporally and spatially averaged axial velocity, $\overline{\langle U_1 \rangle}$ as well as of the RST quantities, $\overline{u_{11}}$, $\overline{u_{22}}$, $\overline{u_{33}}$ is further investigated quantitatively in Figures D.8 (a) and (b), respectively. Spanwise averaging was used to improve convergence, and to compensate for any remaining flow inhomogeneity effects.

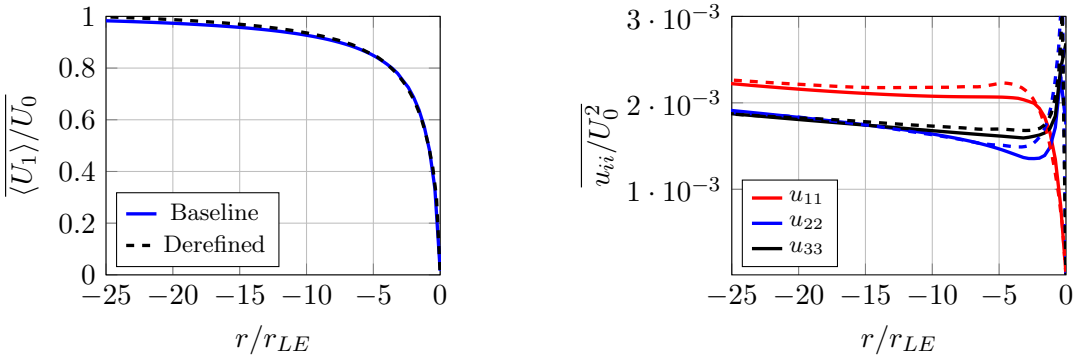

(a) Mean axial velocity. (b) RST components.

Figure D.8: Development of the transversally averaged velocity quantities towards the leading edge for the baseline case (solid) and derefined case (dashed).

From Figure D.8 (a) it is apparent that the development of $\overline{\langle U_1 \rangle}$ is not affected to a significant degree by the mesh refinement. This is expected, as the development of $\overline{\langle U_1 \rangle}$ is determined by the potential effect of the aerofoil, and as such is influenced by the aerofoil geometry as well as potentially the boundary conditions. As the aerofoil geometry is unchanged, minor differences are related to small deviations in terms of the mean flow quantities, which are caused by differences in the turbulent mixing upstream of the aerofoil at the inlet grid boundary condition, as well as at the interface of the turbulent jet to the steady far-field.
Larger differences between the baseline and the derefined case are observed in Figure D.8 (b) in case of the RST components $\overline{u_{11}}$, $\overline{u_{22}}$, $\overline{u_{33}}$. As the derefinement of the mesh leads to a considerable reduction in terms of the resolved turbulent scales, deviations in the RST are to be expected. However, it is apparent that the qualitative development of the three normal RST components is similar between the two cases. It is concluded that since even the derefined case exhibits a development of RST components as expected for the interaction of a turbulent flow with a leading edge, the more highly refined baseline case is sufficiently refined to be used for the investigation of this noise production mechanism.

Appendix E

Supporting investigations

This appendix documents investigations of LES results supporting the main text.

E.1 Assessment of flow homogeneity in the transverse directions

In order to support the assessment of the flow homogeneity conducted in Section 3.3, the inhomogeneity as defined by Eqn. (3.23) was computed for $\langle U_1 \rangle$ and u_{11} on three planes normal to the streamwise direction at the distances $x/G_p = 5$, 10 and 15 downstream of the inlet grid. Figures E.1 (a) - (c) show the results for the turbulence development case discussed in Chapters 3 and 4.

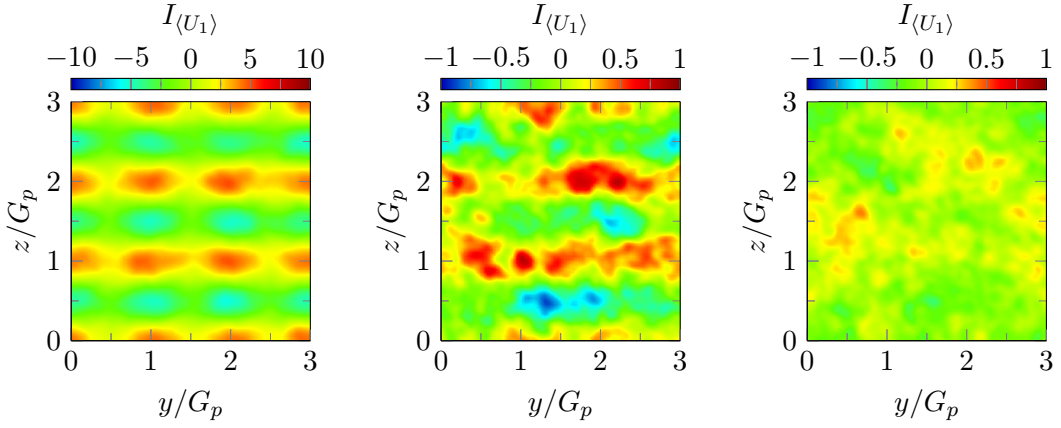

(a) $x/G_p = 5$. (b) $x/G_p = 10$. (c) $x/G_p = 15$.

Figure E.1: Homogeneities of the streamwise velocity downstream of the inlet grid in transverse planes extracted from the turbulence development case.

From Figures E.1 (a) - (c) it is apparent that while the inhomogeneity parameter $I_{\langle U_1 \rangle}$ is at distances of up to $x/G_p = 10$ still showing traces of the initial grid geometry, at distances of $x/G_p \geq 15$ the inhomogeneities in the flow have attained a random distribution, and are at values less than 0.5, which is considered a homogeneous flow in terms of $\langle U_1 \rangle$.

Figures E.2 (a) - (c) illustrate the behaviour of $I_{\langle U_1 \rangle}$ for the turbulence interaction case discussed in Chapter 5. The results shown are extracted from the background simulation, i.e. using the domain illustrated by Figure 5.1, but with the aerofoil removed. Dotted lines indicate the outlines of the removed aerofoil for the purpose of context.

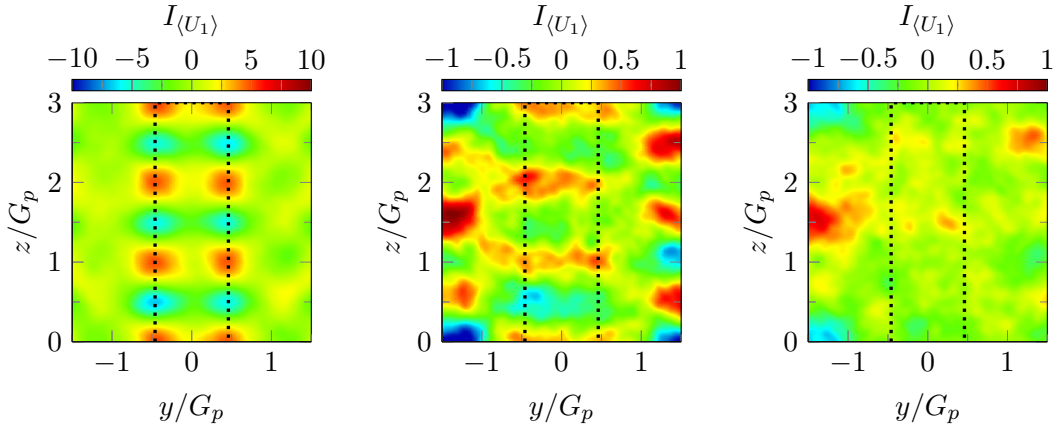

(a) $x/G_p = 5$. (b) $x/G_p = 10$. (c) $x/G_p = 15$.

Figure E.2: Homogeneities of the streamwise velocity downstream of the inlet grid in transverse planes extracted from the turbulence interaction case.

In Figures E.2 (a) - (c), the behaviour of $I_{\langle U_1 \rangle}$ is observed to be qualitatively very similar for the turbulence interaction case as for the turbulence development case. The main differences consist in a changed pattern of $I_{\langle U_1 \rangle}$ close to the inlet at $x/G_p = 5$, where the shear layer of the turbulent jet influences the distribution of $\langle U_1 \rangle$, as well as slightly elevated values of random inhomogeneity further downstream at $x/G_p = 15$, as observed in Figure E.2 (c). However, as $I_{\langle U_1 \rangle}$ does not exceed 1 and as any elevated values are well separated from the aerofoil, the effects associated to these inhomogeneities are considered negligible.

The homogeneity of the RST component u_{11} is illustrated for the turbulence development case in Figures E.3 (a) - (c).

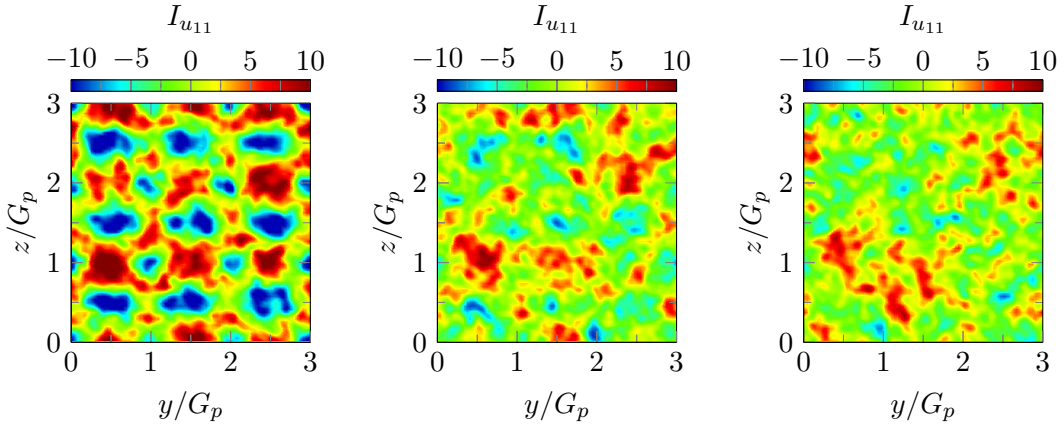

(a) $x/G_p = 5$. (b) $x/G_p = 10$. (c) $x/G_p = 15$.

Figure E.3: Homogeneities of the RST component u_{11} downstream of the inlet grid in transverse planes extracted from the turbulence development case.

From Figures E.3 (a) - (c) it is observed that the inhomogeneity of the streamwise RST component u_{11} is retained to a larger degree as for the mean streamwise velocity U_1, with $I_{u_{11}}$ approaching 10 even for distances of $x/G \geq 15$. However, even close to the grid an identification of the imprint of the grid geometry is difficult. These results are in qualitative agreement with the experimental studies of Ertunc *et al.* [56] as well as the DNS results of Laizet and Vassilicos [57].
The inhomogeneity parameter $I_{u_{11}}$ is shown for the turbulence interaction case in Figures E.4 (a) - (c), as extracted from the background simulation.

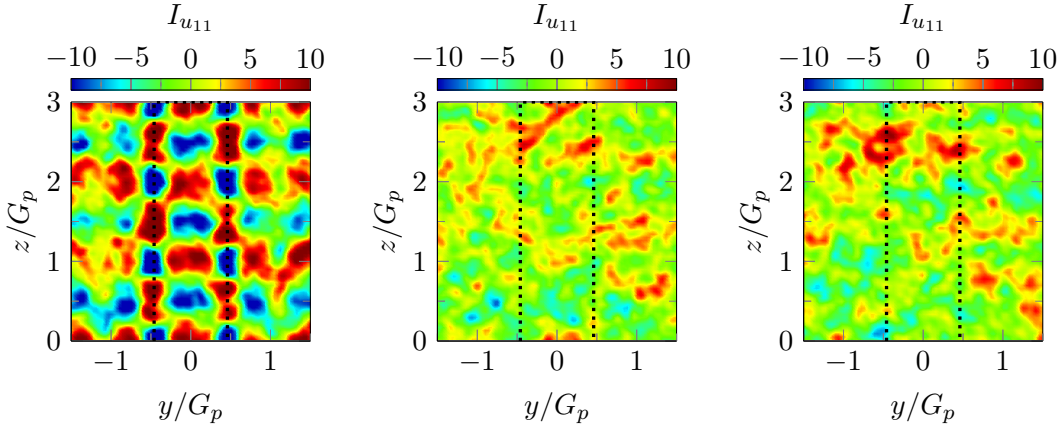

(a) $x/G_p = 5$. (b) $x/G_p = 10$. (c) $x/G_p = 15$.

Figure E.4: Homogeneities of the RST component u_{11} downstream of the inlet grid in transverse planes extracted from the turbulence interaction case.

When comparing the development of $I_{u_{11}}$ with streamwise distance in the turbulence development case, shown in Figures E.3 (a) - (c) and the turbulence interaction case, shown in Figures E.4 (a) - (c), very limited differences are observed, which are constrained to the transverse plane closest to the flow at $x/G_p = 5$. It is concluded that in

terms of $I_{u_{11}}$, there is no significant difference between the two simulation cases.

E.2 Assessment of the fluctuating pressure in the steady domain

As discussed in Section 6.1, in order to minimise the influence of boundary conditions on the turbulence interaction noise produced by the finite aerofoil, while simultaneously maintaining acceptable computational cost, a setup was selected where the turbulent flow is limited to the tip-most sections of the finite aerofoil, and the majority of the aerofoil is exposed to a steady flow. However, as the flow in the entire domain is computed using LES, it was observed that developing boundary layers on the late suction side of the aerofoil would lead to resolved unsteady pressure fluctuations on sections of the aerofoil immersed in steady flow. While flow transition under steady conditions is a well-known phenomenon, in this case, the developing turbulent boundary layers are not considered to be physical, considering the low quality of the near-wall mesh as well as the limited capabilities of the DES modelling approach [192]. It is emphasised that the accurate modelling of the boundary layers was not the primary focus of this study, considering the dominating contribution of the leading edge interaction noise to the total noise emissions in the frequencies of interest [12; 94].
In order to reduce the computed far-field noise spectra to contributions from the sections of the finite aerofoil which are interacting with turbulent flow only, a blanking step was conducted during post-processing, as discussed in Section 6.3. This consisted of setting the pressure signals of the sections of the aerofoil immersed in steady flow to zero during export to the aeroacoustic post-processor provided by the commercial software FLUENT. While this procedure eliminates directly radiated noise from the steady parts to the far-field observer position, it is conceivable that potential effects as well as scattered acoustic waves from the steady sections introduce an error to the results even post the blanking step.

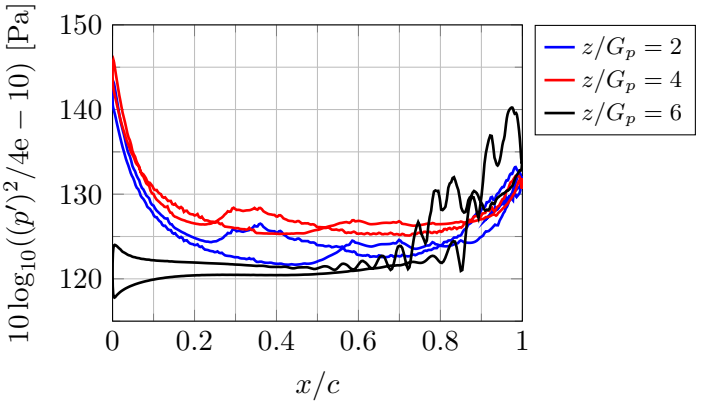

Figure E.5: Mean squared pressure on aerofoil surface for different crosssections.

In order to assess this potential source of error, the mean squared fluctuating pressure along three sections at different positions along the span is shown in Figure E.5. The positions $z_0/G_p = 2$, 4 and 6 were chosen as they represent a position within the homogeneous turbulent flow, within the turbulent shear layer towards the steady domain, and within the steady domain, respectively.

From Figure E.5 it is apparent that the pressure fluctuations at the leading edge are significantly higher for the positions $z_0/G_p = 2$ and 4 than for $z_0/G_p = 6$, which is expected. However, $(p')^2$ increases strongly towards the trailing edge for the section at $z_0/G_p = 2$, which is hypothesised to be caused by the steady flow being numerically tripped. The strongly oscillating pattern is interpreted to be the result of resolved fluctuations being amplified by tetrahedral cells as they are propagated downstream, since the tetrahedral cells have been noted as sensitive to fluctuations also in the turbulent domain, as shown in Figure 6.22 . As there is no random fluctuation in the flow conditions in the steady domain compared to the turbulent domain, harmonic excitation may occur, increasing fluctuation amplitude considerably.

In order to investigate whether these un-physical fluctuations have a detrimental effect on the fluctuating pressure within the steady domain, the pressure cross-correlation R_{pp} was computed for several points $z_0/G_p = 2, 3, 4, 5, 6$ along a line at $x_0/c = 0.956$, which corresponds to the largest peak of $(p')^2$ in the $z_0/G_p = 6$ section shown in Figure E.5. For reference, the approximate position of the shear layer z_s and the position of the edge of the refined turbulent domain z_f are indicated by the dotted and dashed lines, respectively.

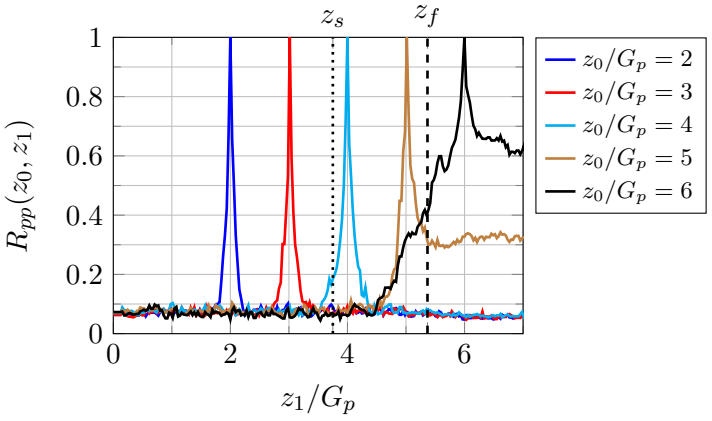

Figure E.6: Spanwise pressure cross-correlation relative to different origins z_0 for a chordwise position of $x_0/c = 0.95$.

From Figure E.6 it is apparent that the extent of the pressure cross-correlation varies significantly along span. Whereas for the sections $z_0/G_p = 2$, 3 and 4 within the turbulent domain, the spatial extent of correlation is relatively small, and does not exceed $0.5G_p$, the sections in the steady domain $z_0/G_p = 5$ and 6 show significantly increased spanwise correlation extends, particularly towards sections further away from the tip i.e. $z_1/G_p > 5$. This is expected, as the steady conditions should produce very

high levels of cross-correlation. However, the levels of R_{pp} relative to $z_0/G_p = 5$ and 6 decline rapidly with decreasing z_1, and by $z_1/G_p \leq 4.5$ the cross-correlation relative to these points has reduced to the level considered to be background noise. It is concluded that the pressure fluctuations within the turbulent domain are not correlated to any significant degree with the pressure fluctuations on the late suction side of the steady domain.

Considering that the fluctuations on the late suction side, i.e. $x_0/c = 0.95$, are observed to exhibit the largest magnitude, and are simultaneously not observed to be correlated to the pressure fluctuations in the turbulent domain, it is concluded that all other pressure fluctuations observable in the steady domain of lesser magnitude are also not correlated to the pressure fluctuations in the turbulent domain. As such, blanking the pressure fluctuations of the aerofoil in the steady domain is considered an effective methodology to minimize error introduced by the numerical phenomena exhibited by the steady domain.

E.3 Comparison of finite aerofoil surface pressure to experiment

In order to provide further context to the observation of reduced mean flow gradients upstream of the leading edge of the aerofoil, comparison of the surface pressure coefficient c_p at a number of sections along the span is conducted with the experimental measurements of McAlister and Takahashi [135]. The wing in their experiments had a constant profile a NACA 0015 and could be fitted with square and round tips, allowing qualitative comparisons.

As the experimental data is only provided for angles of attack equal to and in excess of 4 degrees, an estimation of the surface pressure coefficient distributions was computed for a NACA 0012 at 3 degrees and a NACA 0015 at 4 degrees using the panel method implemented in *XFOIL* [253], and is shown in Figure E.7, allowing to estimate the differences caused by change in profile and angle of attack.

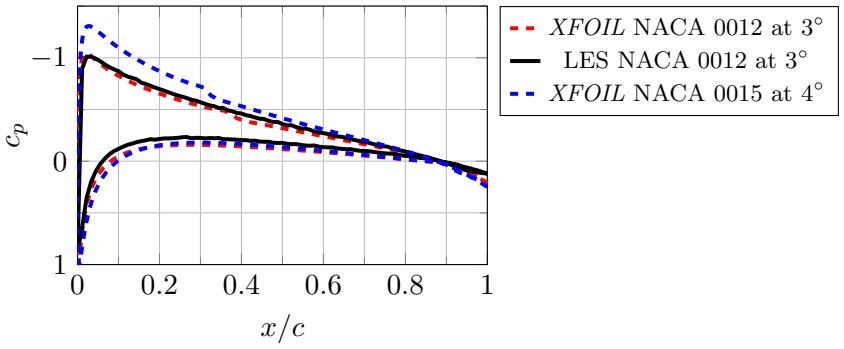

Figure E.7: Comparison of pressure coefficient results for the loaded infinite aerofoil to approximate solution using a panel method as implemented in *XFOIL*[253].

From Figure E.7, it is observed that the agreement between the results of the panel method based *XFOIL* and the LES results for the loaded infinite aerofoil discussed in Section 5.4.3 with the same angle of attack and of equal profile is slightly better for the suction side than for the pressure side. It is hypothesised that the domain setup illustrated in Figure 5.1, featuring a turbulent flow of a slightly higher mean flow velocity than in the surrounding steady domain, may lead to a slight deviation from the free stream conditions assumed in *XFOIL* if an aerofoil with an angle of attack is introduced, which implies a deflection of the turbulent flow [100]. However, the deviations between the panel method and the LES results are considered to be relatively small.

Considering the difference of the panel method predictions when a NACA 0015 at a slightly higher angle of attack is computed, it is qualitatively observed that the c_p distribution of the thicker aerofoil at 4° angle of attack envelops the c_p distribution of the thinner NACA 0012 aerofoil at 3°. Quantitatively, the largest difference is observed to be at the suction peak, where c_p for the NACA 0015 is found to be higher by a value of approximately 0.25.

With the context of the effect of the changes in terms of aerofoil thickness and angle of attack, the c_p distributions as obtained from the finite aerofoil are compared to the experimental values of McAlister and Takahashi [135] for a finite aerofoil with a round tip at an angle of attack of 4° in steady flow conditions in Figures E.8 (a) - (d) at four sections along the span.

From Figures E.8 (a) - (d) it is apparent that the experimental values are consistently above those obtained from LES. Taking into account the differences associated with aerofoil thickness as well as angle of attack, as illustrated by Figure E.7, it is observed that the deviation is of the order of 0.15 at the suction peak, with the deviation increasing for sections further inboard.

It is noted that their experiments took place in a closed wind tunnel, which is known to increase lift measured on aerofoils. However, as the most inboard measurement roughly aligns with the solution obtained from *XFOIL* as shown in Figure E.8 (d), this effect is considered minor. As such, the present analysis indicates that the finite aerofoil discussed in Chapter 6 exhibits a slightly decreased lift for an isolated aerofoil. It is hypothesised that this is partially due to the coarse mesh of the buffer domain being relatively close to the aerofoil geometry in the steady sections, as shown in Figure 6.1. Further assessment, using mesh refinement studies as well as experimental investigation using the test rig documented in Appendix A, is recommended to better quantify the under-prediction and its consequences. For the purpose of the far-field noise emissions discussed in this thesis however, this discrepancy is considered to be of minor effect, as the interaction noise is primarily determined by the turbulent quantities as well as the leading edge geometry [93; 94; 98].

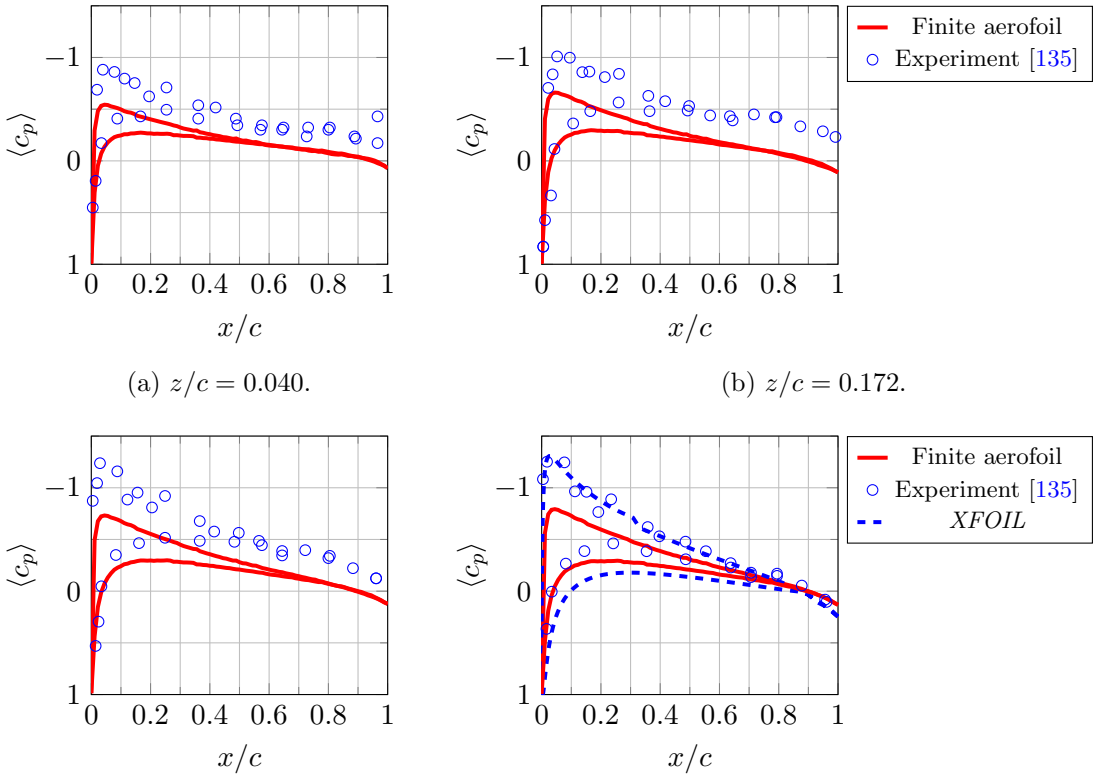

(a) $z/c = 0.040$.

(b) $z/c = 0.172$.

(c) $z/c = 0.370$.

(d) $z/c = 0.666$.

Figure E.8: Comparison of surface pressure coefficient with equivalent experiment of McAlister and Takahashi [135] of a finite NACA 0015 aerofoil with a round tip at an angle of attack of 4°.

Bibliography

[1] ACARE, "WG1 Contribution to the Strategic Research and Innovation Agenda," 2012.

[2] W. C. Strack, G. Knip, A. L. Weisbrich, J. Godston, and E. Bradley, "Technology and Benefits of Aircraft Counter Rotation Propellers," Tech. Rep. 82983, NASA, 1981.

[3] S. A. Khalid, D. Lurie, A. Breeze-Stringfellow, T. Wood, K. Ramakrishnan, U. Paliath, J. Wojno, B. Janardan, T. Goerig, A. Opalski, and J. Barrett, "Open Rotor Engine Aeroacoustic Technology Final Report," Tech. Rep. 4, General Electric, 2014.

[4] F. Brooks, D. Stuart, and A. Marcolini, *Airfoil Self-Noise and Prediction*. Hampton, Virginia: NASA, Office of Management, Scientific and Technical Information Division, 1989.

[5] G. E. Hoff, "Experimental Performance and Acoustic Investigation of Modern, Counterrotating Blade Concepts," tech. rep., GE Aircraft Engines, 1990.

[6] V. Blandeau, *Aerodynamic Broadband Noise from Contra-Rotating Open Rotors*. PhD thesis, University of Southampton, 2011.

[7] J. Gill, *Broadband Noise Generation of a Contra-Rotating Open Rotor Blade*. PhD thesis, University of Southampton, 2015.

[8] J. Giez, L. Vion, M. Roger, and S. Moreau, "Effect of the Edge and Tip Vortex on Airfoil Self Noise and Turbulence Impingement Noise," in *22nd AIAA/CEAS Aeroacoustics Conference*, AIAA 2016-2996, (Lyon, France), 2016.

[9] J. Ricouard, E. Julliard, M. Omais, V. Regnier, A. Parry, and S. Baralon, "Installation Effects on Contra-Rotating Open Rotor Noise," in *16th AIAA/CEAS Aeroacoustics Conference*, AIAA 2010-3795, (Stockholm, Sweden), 2010.

[10] T. Sinnige, K. P. Lynch, D. Ragni, G. Eitelberg, and L. L. M. Veldhuis, "Aerodynamic and Aeroacoustic Effects of Pylon Trailing Edge Blowing on Pusher Propeller Installation," in *21st AIAA/CEAS Aeroacoustics conference*, AIAA 2015-2356, (Dallas, TX, USA), 2015.

[11] T. Sinnige, D. Ragni, G. Eitelberg, and L. L. M. Veldhuis, "Pusher-Propeller Installation Effects in Angular Inflow," in *22nd AIAA/CEAS Aeroacoustics Conference*, AIAA 2016-2875, (Lyon, France), 2016.

[12] M. Roger and S. Moreau, "Extensions and limitations of analytical airfoil broadband noise models," *International Journal of Aeroacoustics*, vol. 9, no. 3, pp. 273–306, 2010.

[13] T. Blackmore, W. M. Batten, and A. S. Bahaj, "Inlet grid-generated turbulence for large-eddy simulations," *International Journal of Computational Fluid Dynamics*, vol. 27, no. 6-7, pp. 307–315, 2013.

[14] S. A. Petrikat, R. Karve, and D. Angland, "Broadband leading edge interaction noise prediction using simulated grid turbulence," in *24th AIAA/CEAS Aeroacoustics Conference*, AIAA 2018-3286, 2018.

[15] R. Amiet, "Acoustic radiation from an airfoil in a turbulent stream," *Journal of Sound and Vibration*, vol. 41, no. 4, pp. 407–420, 1975.

[16] S. B. Pope, *Turbulent Flows*. Cambridge University Press, 6 ed., 2000.

[17] G. I. Taylor, "The spectrum of turbulence," *Proceedings of the Royal Society A: Mathematical, Physical and Engineering Science1*, vol. 164, no. 919, 1938.

[18] L. Djenidi, S. F. Tardu, and R. A. Antonia, "Relationship between temporal and spatial averages in grid turbulence," *Journal of Fluid Mechanics*, vol. 730, pp. 593–606, 2013.

[19] C. Tong and Z. Warhaft, "Passive scalar dispersion and mixing in a turbulent jet," *Journal of Fluid Mechanics*, vol. 292, pp. 1–38, 1995.

[20] J. L. Lumley, "Interpretation of time spectra measured in high-intensity shear flows," *Physics of Fluids*, vol. 8, no. 6, pp. 1056–1062, 1965.

[21] C. C. Lin, "On Taylor's hypothesis and the acceleration terms in the Navier-Stokes equation," *Quarterly of applied Mathematics*, vol. 10, no. 4, pp. 295–306, 1953.

[22] T. von Karman and L. Howarth, "On the statistical theory of isotropic turbulence," in *Proceedings of the Royal Society A: Mathematical, Physical and Engineering Science*, vol. 164, pp. 192–215, 1938.

[23] P. Lavoie, P. Burattini, L. Djenidi, and R. A. Antonia, "Effect of initial conditions on decaying grid turbulence at low Rλ," *Experiments in Fluids*, vol. 39, no. 5, pp. 865–874, 2005.

[24] P. Lavoie, L. Djenidi, and R. A. Antonia, "Effects of initial conditions in decaying turbulence generated by passive grids," *Journal of Fluid Mechanics*, vol. 585, pp. 395–420, 2007.

[25] L. B. Esteban, J. S. Shrimpton, and B. Ganapathisubramani, "Laboratory experiments on the temporal decay of homogeneous anisotropic turbulence," *Journal of Fluid Mechanics*, vol. 862, pp. 99–127, 2019.

[26] G. Comte-Bellot and S. Corrsin, "The Use of a Contraction to Improve the Isotropy of Grid-Generated Turbulence," *Journal of Fluid Mechanics*, vol. 25, no. 4, pp. 657–682, 1966.

[27] M. S. Uberoi and P. Freymuth, "Turbulent energy balance and spectra of the axisymmetric wake," *Physics of Fluids*, vol. 13, pp. 2205–2210, 1970.

[28] F. H. Champagne, Y. H. Pao, and I. J. Wygnanski, "On the two-dimensional mixing region," *Journal of Fluid Mechanics*, vol. 74, pp. 209–250, 1976.

[29] S. G. Saddoughi and S. V. Veeravalli, "Local isotropy in turbulent boundary layers at high Reynolds number," *Journal of Fluid Mechanics*, vol. 268, pp. 333–372, 1994.

[30] G. R. Tabor and M. H. Baba-Ahmadi, "Inlet conditions for large eddy simulation: A review," *Computers and Fluids*, vol. 39, no. 4, pp. 553–567, 2010.

[31] A. M. Obukhov, "The spectral energy distribution in a turbulent flow," *Dokl. Adad. Nauk. SSSR*, vol. 32, pp. 22–24, 1941.

[32] W. Heisenberg, "On the theory of statistical and isotropic turbulence," *Proc. R. Soc. A*, vol. 195, pp. 402–406, 1948.

[33] Y. H. Pao, "Structure of turbulent velocity and scalar fields at large wavenumbers," *Physics of Fluids*, vol. 8, no. 6, pp. 1063–1075, 1965.

[34] S. Panchev, *Random Functions and Turbulence*. Oxford: Pergamon Press, 1971.

[35] H. W. Liepmann, J. Laufer, and K. Liepmann, "On the Spectrum of Isotropic Turbulence," Tech. Rep. 2473, 1951.

[36] M. Dieste and G. Gabard, "Random particle methods applied to broadband fan interaction noise," *Journal of Computational Physics*, vol. 231, no. 24, pp. 8133–8151, 2012.

[37] M. K. Chung and S. K. Kim, "A nonlinear return-to-isotropy model with Reynolds number and anisotropy dependency," *Physics of Fluids*, vol. 7, no. 6, pp. 1425–1437, 1995.

[38] P. Spalart and S. R. Allmaras, "A one-equation turbulence model for aerodynamic flows," *La Rech. Aerospatiale*, vol. 1, pp. 5–21, 1994.

[39] J. L. Lumley and G. R. Newman, "The return to isotropy of homogenous turbulence," *Journal of Fluid Mechanics*, vol. 82, no. 1, pp. 161–178, 1977.

[40] J. Rotta, "Statistische Theorie nichthomogener Turbulenz," *Zeitschrift fuer Physik*, vol. 129, no. 6, pp. 547–572, 1951.

[41] K. S. Choi and J. L. Lumley, "The return to isotropy of homogeneous turbulence," *Journal of Fluid Mechanics*, vol. 436, pp. 59–84, 2001.

[42] L. Djenidi and S. F. Tardu, "On the anisotropy of a low-Reynolds-number grid turbulence," *Journal of Fluid Mechanics*, vol. 702, pp. 332–353, 2012.

[43] C. J. Zusi and J. B. Perot, "Simulation and modeling of turbulence subjected to a period of axisymmetric contraction or expansion," *Physics of Fluids*, vol. 26, no. 11, 2014.

[44] G. I. Taylor, "Statistical theory of turbulence," in *Proceedings of the Royal Society London*, no. 151, pp. 412–478, 1935.

[45] A. N. Kolmogorov, "The local structure of turbulence in incompressible viscous fluid for very large Reynolds numbers," *Dokl. Adad. Nauk. SSSR.*, vol. 30, no. 4, pp. 299–303, 1941.

[46] M. S. Mohamed and J. C. Larue, "The decay power law in grid-generated turbulence," *Journal of Fluid Mechanics*, vol. 219, p. 195, 1990.

[47] W. K. George, *The decay of homogeneous turbulence.* Hemisphere, 1988.

[48] J. C. Vassilicos, "Dissipation in Turbulent Flows," *Annual Review of Fluid Mechanics*, vol. 47, no. 1, pp. 95–114, 2015.

[49] W. K. George, "The decay of homogeneous isotropic turbulence," *Physics of Fluids A*, vol. 4, no. 7, pp. 1492–1509, 1992.

[50] E. R. Seoud and C. J. Vassilicos, "Dissipation and decay of fractal-generated turbulence," *Physics of Fluids*, vol. 19, no. 10, 2007.

[51] P. C. Valente and J. C. Vassilicos, "The decay of turbulence generated by a class of multiscale grids," *Journal of Fluid Mechanics*, vol. 687, pp. 300–340, 2011.

[52] P. C. Valente and J. C. Vassilicos, "Universal dissipation scaling for nonequilibrium turbulence," *Physical Review Letters*, vol. 108, no. 21, pp. 1–5, 2012.

[53] P. Å. Krogstad and P. A. Davidson, "Freely decaying, homogeneous turbulence generated by multi-scale grids," *Journal of Fluid Mechanics*, vol. 680, pp. 417–434, 2011.

[54] P. C. Valente and J. C. Vassilicos, "Dependence of decaying homogeneous isotropic turbulence on inflow conditions," *Physics Letters, Section A: General, Atomic and Solid State Physics*, vol. 376, no. 4, pp. 510–514, 2012.

[55] H. L. Grant and I. C. T. Nisbet, "The inhomogeneity of grid turbulence," *Journal of Fluid Mechanics*, vol. 2, no. 3, pp. 263–272, 1957.

[56] Ö. Ertunç, N. Özyilmaz, H. Lienhart, F. Durst, and K. Beronov, "Homogeneity of turbulence generated by static-grid structures," *Journal of Fluid Mechanics*, vol. 654, pp. 473–500, 2010.

[57] S. Laizet and J. C. Vassilicos, "DNS of fractal-generated turbulence," *Flow, Turbulence and Combustion*, vol. 87, no. 4, pp. 673–705, 2011.

[58] M. Gad-el Hak and S. Corrsin, "Measurements of the nearly isotropic turbulence behind a uniform jet grid," *Journal of Fluid Mechanics*, vol. 62, no. 1, pp. 115–143, 1974.

[59] P. Lavoie, L. Djenidi, and R. A. Antonia, "Effect of initial conditions on the generation of coherent structures in grid turbulence," in *Whither Turbulence Prediction and Control Conference*, (Seoul), 2006.

[60] S. Discetti, I. B. Ziskin, T. Astarita, R. J. Adrian, and K. P. Prestridge, "PIV measurements of anisotropy and inhomogeneity in decaying fractal generated turbulence," *Fluid Dynamics Research*, vol. 45, no. 6, 2013.

[61] P. C. Valente and J. C. Vassilicos, "The non-equilibrium region of grid-generated decaying turbulence," *Journal of Fluid Mechanics*, vol. 744, pp. 5–37, 2014.

[62] X. Wu, "Inflow Turbulence Generation Methods," *Annual Review of Fluid Mechanics*, vol. 49, pp. 23–49, 2017.

[63] N. S. Dhamankar, G. A. Blaisdell, and A. S. Lyrintzis, "Overview of turbulent inflow boundary conditions for large-eddy simulations," *AIAA Journal*, vol. 56, no. 4, pp. 1317–1334, 2018.

[64] R. Poletto, T. Craft, and A. Revell, "A New Divergence Free Synthetic Eddy Method for the Reproduction of Inlet Flow Conditions for LES," *Flow, Turbulence and Combustion*, vol. 91, no. 3, pp. 519–539, 2013.

[65] Y. Kim, I. P. Castro, and Z. T. Xie, "Divergence-free turbulence inflow conditions for large-eddy simulations with incompressible flow solvers," *Computers and Fluids*, vol. 84, no. 0, pp. 56–68, 2013.

[66] M. L. Shur, P. R. Spalart, M. K. Strelets, and A. K. Travin, "Synthetic turbulence generators for RANS-LES interfaces in zonal simulations of aerodynamic and aeroacoustic problems," *Flow, Turbulence and Combustion*, vol. 93, no. 1, pp. 63–92, 2014.

[67] R. H. Kraichnan, "Diffusion by a Random Velocity Field," *Physics of Fluids*, vol. 13, no. 1, pp. 22–31, 1970.

[68] M. Karweit, P. Blanc-Benon, D. Juvé, and G. Comte-Bellot, "Simulation of the Propagation of an Acoustic Wave through a Turbulent Velocity Field: A study of Phase Variance," *Journal of the Acoustical Society of America*, vol. 89, no. 1, pp. 52–62, 1991.

[69] A. Smirnov, S. Shi, and I. Celik, "Random Flow Generation Technique for Large Eddy Simulations and Particle-Dynamics Modeling," *Journal of Fluids Engineering*, vol. 123, no. 2, pp. 359–371, 2001.

[70] S. Huang, Q. Li, and S. Xu, "Numerical Evaluation of Wind Effects on a Tall Steel Building by CFD," *Journal of Constructional Steel Research*, vol. 63, no. 5, pp. 612–627, 2007.

[71] E. Riber, V. Moureau, M. García, T. J. Poinsot, and O. Simonin, "Evaluation of Numerical Strategies for Large Eddy Simulation of Particulate Two-Phase Recirculating Flows," *Journal of Computational Physics*, vol. 228, no. 2, pp. 539–564, 2009.

[72] K. Elsayed and C. Lacor, "Numerical Modeling of the Flow Field and Performance in Cyclones of Different Cone-Tip Diameters," *Computers & Fluids*, vol. 51, no. 1, pp. 48–59, 2011.

[73] P. Batten, U. Goldberg, and S. Chakravarthy, "Interfacing Statistical Turbulence Closures with Large-Eddy Simulation," *AIAA Journal*, vol. 42, no. 3, pp. 485–492, 2004.

[74] S. H. Huang, Q. S. Li, and J. R. Wu, "A General Inflow Turbulence Generator for Large Eddy Simulation," *Journal of Wind Engineering and Industrial Aerodynamics*, vol. 98, no. 10, pp. 600–617, 2010.

[75] H. G. Castro and R. R. Paz, "A Time and Space Correlated Turbulence Synthesis Method for Large Eddy Simulations," *Journal of Computational Physics*, vol. 235, pp. 742–763, 2013.

[76] R. Yu and X. S. Bai, "A fully divergence-free method for generation of inhomogeneous and anisotropic turbulence with large spatial variation," *Journal of Computational Physics*, vol. 256, pp. 234–253, 2014.

[77] H. Le, P. Moin, and J. Kim, "Direct numerical simulation of turbulent flow over a backward-facing step," *Journal of Fluid Mechanics*, vol. 330, pp. 349–374, 1997.

[78] A. Keating, U. Piomelli, E. Balaras, and H. J. Kaltenbach, "A posteriori tests of inflow conditions for large-eddy simulation," *Physics of Fluids*, vol. 16, no. 12, pp. 4696–4712, 2004.

[79] M. Klein, A. Sadiki, and J. Janicka, "A digital filter based generation of inflow data for spatially developing direct numerical or large eddy simulations," *Journal of Computational Physics*, vol. 186, no. 2, pp. 652–665, 2003.

[80] L. di Mare, M. Klein, W. P. Jones, and J. Janicka, "Synthetic turbulence inflow conditions for large-eddy simulation," *Physics of Fluids*, vol. 18, no. 2, 2006.

[81] Z. T. Xie and I. P. Castro, "Efficient generation of inflow conditions for large eddy simulation of street-scale flows," *Flow, Turbulence and Combustion*, vol. 81, no. 3, pp. 449–470, 2008.

[82] K. M. Bercin, Z. T. Xie, and S. R. Turnock, "Exploration of digital-filter and forward-stepwise synthetic turbulence generators and an improvement for their skewness-kurtosis," *Computers and Fluids*, vol. 172, pp. 443–466, 2018.

[83] E. Sergent, *Vers une Méthodologie de Couplage entre la Simulation des Grandes Échelles et les Modèles Statistiques*. PhD thesis, École Centrale de Lyon, 2002.

[84] S. Benhamadouche, N. Jarrin, Y. Addad, and D. Laurence, "Synthetic turbulent inflow conditions based on a vortex method for large-eddy simulation," *Progress in Computational Fluid Dynamics*, vol. 6, no. 1-3, pp. 50–57, 2006.

[85] N. Jarrin, S. Benhamadouche, D. Laurence, and R. Prosser, "A Synthetic-Eddy-Method for Generating Inflow Conditions for Large-Eddy Simulations," *International Journal of Heat and Fluid Flow*, vol. 27, no. 4, pp. 585–593, 2006.

[86] N. Jarrin, R. Prosser, J.-C. Uribe, S. Benhamadouche, and D. Laurence, "Reconstruction of Turbulent Fluctuations for Hybrid RANS/LES Simulations Using a Synthetic-Eddy Method," *International Journal of Heat and Fluid Flow*, vol. 30, no. 3, pp. 435–442, 2009.

[87] M. Pamiès, P. É. Weiss, E. Garnier, S. Deck, and P. Sagaut, "Generation of synthetic turbulent inflow data for large eddy simulation of spatially evolving wall-bounded flows," *Physics of Fluids*, vol. 21, no. 4, 2009.

[88] A. Uzun and M. Hussaini, "Some Issues in Large-Eddy Simulations for Chevron Nozzle Jet Flows," *Journal of Propulsion and Power*, vol. 28, no. 2, pp. 246–258, 2012.

[89] M. Wang and P. Moin, "Computation of trailing-edge flow and noise using large-eddy simulation," *AIAA journal*, vol. 38, no. 12, pp. 2201–2209, 2000.

[90] H. F. Fasel, U. Rist, and U. Konzelmann, "Numerical investigation of the Three-Dimensional Development in Boundary-Layer Transition," *AIAA Journal*, vol. 28, no. 1, pp. 29–37, 1990.

[91] X. Gloerfelt and J. Berland, "Direct computation of turbulent boundary layer noise," in *15th AIAA/CEAS Aeroacoustics Conference*, AIAA 2009-3401, (Miami, Florida, USA), 2009.

[92] X. I. A. Yang, J. Sadique, R. Mittal, and C. Meneveau, "Integral Wall Model for Large Eddy Simulations of Wall-Bounded Turbulent Flows," *Physics of Fluids*, vol. 27, no. 2, 2015.

[93] R. W. Paterson and R. K. Amiet, "Noise and surface pressure response of an airfoil to incident turbulence," *Journal of Aircraft*, vol. 14, no. 8, pp. 729–736, 1977.

[94] P. Chaitanya, J. Gill, S. Narayanan, P. Joseph, and C. Vanderwel, "Aerofoil geometry effects on turbulence interaction noise," in *21st AIAA/CEAS Aeroacoustics conference*, AIAA 2015-2830, (Dallas, TX, USA), 2015.

[95] S. Moreau and M. Roger, "Competing Broadband Noise Mechanisms in Low-Speed Axial Fans," *AIAA Journal*, vol. 45, no. 1, pp. 48–57, 2007.

[96] A. S. Hersh and W. C. Meecham, "Sound directivity pattern radiated from small airfoils," *Journal of the Acoustical Society of America*, vol. 53, no. 2, pp. 602–606, 1973.

[97] R. W. Paterson and R. K. Amiet, "Acoustic Radiation and Surface Pressure Characteristics of an Airfoil due to Incident Turbulence," Tech. Rep. 2733, NASA, East Hartford, Conn, USA, sep 1976.

[98] S. Moreau, M. Roger, and V. Jurdic, "Effect of Angle of Attack and Airfoil Shape on Turbulence-Interaction noise," in *11th AIAA/CEAS Aeroacoustics Conference*, AIAA 2005-2973, (Monterey, California), 2005.

[99] J. K. Staubs, *Real Airfoil Effects on Leading Edge Noise*. PhD thesis, Virginia Polytechnic Institute and State University, 2008.

[100] W. J. Devenport, J. K. Staubs, and S. A. Glegg, "Sound radiation from real airfoils in turbulence," *Journal of Sound and Vibration*, vol. 329, no. 17, pp. 3470–3483, 2010.

[101] L. D. Santana, J. Christophe, C. Schram, and W. Desmet, "A Rapid Distortion Theory modified turbulence spectra for semi-analytical airfoil noise prediction," *Journal of Sound and Vibration*, vol. 383, pp. 349–363, 2016.

[102] T. Hainaut, G. Gabard, and V. Clair, "A CAA Study of Turbulence Distortion in Broadband Fan Interaction Noise," in *22nd AIAA/CEAS Aeroacoustics Conference*, AIAA 2016-2839, (Lyon, France), 2016.

[103] F. Gea-Aguilera, *Aerodynamic and aeroacoustic modelling of engine fan broadband noise*. PhD thesis, University of Southampton, 2017.

[104] C. Polacsek, G. Reboul, V. Clair, T. L. Garrec, and H. Deniau, "Turbulence-airfoil interaction noise reduction using wavy leading edge: An experimental and numerical study," in *Proc. of Inter-Noise*, 2011.

[105] S. Haeri, J. W. Kim, S. Narayanan, and P. Joseph, "3D calculations of aerofoil-turbulence interaction noise and the effect of wavy leading edges," in *20th AIAA/-CEAS Aeroacoustics Conference*, AIAA 2014-2325, (Atlanta, GA, USA), 2014.

[106] S. Narayanan, P. Joseph, S. Haeri, J. W. Kim, P. Chaitanya, and C. Polacsek, "Noise reduction studies from the leading edge of serrated flat plates," in *20th AIAA/CEAS Aeroacoustics Conference*, AIAA 2014-2320, (Atlanta, GA, USA), pp. 1–14, 2014.

[107] M. Roger and S. Moreau, "Airfoil Turbulence-Impingement Noise Reduction by Porosity or Wavy Leading-Edge Cut : Experimental Investigations," in *Inter-Noise 2016*, no. 2, pp. 6006–6015, 2016.

[108] W. R. Sears, "Some Aspects of Non-Stationary Airfoil Theory and its Practical Application," *Journal of the Aeronautical Sciences*, vol. 8, no. 3, pp. 104–108, 1941.

[109] R. K. Amiet, "Compressibility Effects in Unsteady Thin-Airfoil Theory," *AIAA Journal*, vol. 12, no. 2, pp. 252–255, 1974.

[110] H. Lamb, *Hydrodynamics*. New York: Dover Publications, 6th editio ed., 1932.

[111] N. Curle, "The influence of solid boundaries upon aerodynamic sound," *Proceedings of the Royal Society A: Mathematical and Physical Sciences*, vol. 231, no. 1187, pp. 505–514, 1955.

[112] V. P. Blandeau, P. F. Joseph, G. Jenkins, and C. J. Powles, "Comparison of sound power radiation from isolated airfoils and cascades in a turbulent flow," *The Journal of the Acoustical Society of America*, vol. 129, no. 6, pp. 3521–3530, 2011.

[113] F. Gea-Aguilera, J. Gill, X. Chen, and T. Nod, "Leading Edge Noise Predictions Using Anisotropic Synthetic Turbulence," in *21th AIAA/CEAS Aeroacoustics Conference*, AIAA 2016-2840, (Lyon, France), 2016.

[114] J. Gershfeld, "Leading Edge Noise From Thick Foils in Turbulent Flows," *Journal of the Acoustical Society of America*, vol. 116, no. 3, pp. 1416–1426, 2004.

[115] J. C. Hunt, "A theory of turbulent flow round two-dimensional bluff bodies," *Journal of Fluid Mechanics*, vol. 61, no. 4, pp. 625–706, 1973.

[116] R. Amiet, "High Frequency Thin-Airfoil theory for subsonic Flow," *AIAA Journal*, vol. 14, no. 8, pp. 1076–1082, 1976.

[117] M. J. Lighthill, "The effect of compressibility on Turbulence," *Gas Dynamics of Cosmic Clouds*, vol. 2, pp. 121–131, 1955.

[118] J. F. Williams and D. L. Hawkings, "Sound generation by turbulence and surfaces in arbitrary motion," *Philosophical Transactions of the Royal Society of London A: Mathematical, Physical and Engineering Sciences*, vol. 264, no. 1151, pp. 321–342, 1969.

[119] H. Atassi, S. Subramaniam, and J. Scott, "Acoustic radiation from lifting airfoils in compressible subsonic flow," in *13th Aeroacoustics conference*, p. 3911, 1990.

[120] D. P. Lockard and P. J. Morris, "Radiated noise from airfoils in realistic mean flows," *AIAA Journal*, vol. 36, no. 6, pp. 907–914, 1998.

[121] J. Gill, X. Zhang, and P. Joseph, "Symmetric airfoil geometry effects on leading edge noise," *The Journal of the Acoustical Society of America*, vol. 134, no. 4, pp. 2669–2680, 2013.

[122] D. Casalino, M. Jacob, and M. Roger, "Prediction of rod-airfoil interaction noise using the Ffowcs-Williams-Hawkings analogy," *AIAA Journal*, vol. 41, no. 2, pp. 182–191, 2003.

[123] J.-C. Giret, A. Sengissen, S. Moreau, M. Sanjosé, and J.-c. Jouhaud, "Prediction of the sound generated by a rod-airfoil configuration using a compressible unstructured LES solver and a FW-H analogy," in *18th AIAA/CEAS Aeroacoustics Conference*, AIAA 2012-2058, (Colorado Springs, CO, USA), 2012.

[124] J. Christophe, *Application of Hybrid Methods To High Frequency Aeroacoustics*. PhD thesis, Vrije Universiteit Brussels, 2011.

[125] H. Deniau, G. Dufour, J. F. Boussuge, C. Polacsek, and S. Moreau, "Affordable compressible LES of airfoil-turbulence interaction in a free jet," in *17th AIAA/-CEAS Aeroacoustics Conference 2011*, AIAA 2011-2707, (Portland, OR, USA), 2011.

[126] M. Sevik, "Sound Radiation from a Subsonic Rotor Subjected to Turbulence," in *Proceedings of the International Symposium on Fluid Mechanics and Designs of Turbomachinery*, (State College, PA, USA), pp. 493–512, NASA, 1974.

[127] U. W. Ganz, P. D. Joppa, T. J. Patten, and D. F. Scharpf, "Boeing 18-Inch Fan Rig Broadband Noise Test," Tech. Rep. 1998-208704, NASA, Office of Management, Scientific and Technical Information Division, 1998.

[128] E. J. Kerschen and P. R. Gliebe, "Noise Caused by the Interaction of a Rotor with Anisotropic Turbulence," *AIAA Journal*, vol. 19, no. 6, pp. 717–723, 1981.

[129] D. B. Hanson, "Spectrum of Rotor Noise Caused by Atmospheric Turbulence," *The Journal of the Acoustical Society of America*, vol. 56, no. 1, pp. 110–126, 1974.

[130] H. Posson, S. Moreau, and M. Roger, "Broadband noise prediction of fan outlet guide vane using a cascade response function," *Journal of Sound and Vibration*, vol. 330, no. 25, pp. 6153–6183, 2011.

[131] A. Uzun, M. Y. Hussaini, and C. L. Streett, "Large-Eddy Simulation of a Wing Tip Vortex on Overset Grids," *AIAA Journal*, vol. 44, no. 6, pp. 1229–1242, 2008.

[132] D. Kolomenskiy, R. Paoli, and J.-F. Boussuge, "Hybrid RANS–LES Simulation of Wingtip Vortex Dynamics," in *ASME 2014 4th Joint US-European Fluids Engineering Division Summer Meeting collocated with the ASME 2014 12th International Conference on Nanochannels, Microchannels, and Minichannels*, American Society of Mechanical Engineers, 2014.

[133] J.-E. W. Lombard, D. Moxey, S. J. Sherwin, J. F. A. Hoessler, S. Dhandapani, and M. J. Taylor, "Implicit Large-Eddy Simulation of a Wingtip Vortex," *AIAA Journal*, vol. 54, no. 2, pp. 506–518, 2015.

[134] S. I. Green and A. J. Acosta, "Unsteady flow in trailing vortices," *Journal of Fluid Mechanics*, vol. 227, pp. 107–134, 1991.

[135] K. W. McAlister and R. K. Takahashi, "NACA 0015 Wing pressure and Trailing Vortex Measurements," Tech. Rep. 91-A-003, NASA, 1992.

[136] W. J. Devenport, M. C. Rife, S. I. Liapis, and G. J. Follin, "The structure and development of a wing-tip vortex," *Journal of Fluid Mechanics*, vol. 312, pp. 67–106, 1996.

[137] V. R. Corsiglia, R. G. Schwind, and N. A. Chigier, "Rapid scanning, three-dimensional hot-wire anemometer surveys of wing-tip vortices," *Journal of Aircraft*, vol. 10, no. 12, pp. 752–757, 1973.

[138] H.-T. Liu, "Effects of ambient turbulence on the decay of a trailing vortex wake," *Journal of Aircraft*, vol. 29, no. 2, pp. 255–263, 1992.

[139] M. L. Beninati and J. S. Marshall, "An experimental study of the effect of free-stream turbulence on a trailing vortex," *Experiments in Fluids*, vol. 38, no. 2, pp. 244–257, 2005.

[140] S. C. Bailey, *The interaction of a Wing-Tip Vortex and Free-Stream Turbulence.* PhD thesis, University of Ottawa, 2007.

[141] V. J. Rossow, "Lift-generated vortex wakes of subsonic transport aircraft," *Progress in Aerospace Sciences*, vol. 35, no. 6, pp. 507–660, 1999.

[142] J. N. Hallock and F. Holzäpfel, "A review of recent wake vortex research for increasing airport capacity," *Progress in Aerospace Sciences*, vol. 98, no. December 2017, pp. 27–36, 2018.

[143] S. I. Green, *Fluid Vortices*. Kluwer Academic Publishers, 1995.

[144] J. Katz and J. Galdo, "Effect of roughness on rollup of tip vortices on a rectangular hydrofoil," *Journal of Aircraft*, vol. 26, no. 3, pp. 247–253, 1989.

[145] W. Philips, "The turbulent trailing vortex during Roll up," *Journal of Fluid Mechanics*, vol. 105, pp. 451–467, 1981.

[146] A. Shekarriz, T. Fu, J. Katz, and T. Huang, "Near-field behavior of a tip vortex," *AIAA Journal*, vol. 31, no. 1, pp. 112–118, 1993.

[147] B. R. Ramaprian and Y. Zheng, "Measurements in rollup region of the tip vortex from a rectangular wing," *AIAA Journal*, vol. 35, no. 12, pp. 1837–1843, 1997.

[148] G. K. Batchelor, "Axial flow in trailing line vortices," *Journal of Fluid Mechanics*, vol. 20, pp. 645–658, 1964.

[149] E. A. Anderson and T. A. Lawton, "Correlation between vortex strength and axial velocity in a trailing vortex," *Journal of Aircraft*, vol. 40, no. 4, pp. 699–704, 2003.

[150] M. V. Melander and F. Hussain, "Coupling between a coherent structure and fine-scale turbulence," *Physical Review E*, vol. 48, no. 4, pp. 2669–2689, 1993.

[151] J. S. Chow, *Turbulence measurements in the near-field of a wingtip vortex*. PhD thesis, 1995.

[152] P. Bradshaw, "The analogy between streamline curvature and buoyancy in turbulent shear flow," *Journal of Fluid Mechanics*, vol. 36, no. 1, pp. 177–191, 1969.

[153] P. R. Bandyopadhyay, D. J. Stead, and R. L. Ash, "Organized nature of a turbulent trailing vortex," *AIAA Journal*, vol. 29, no. 10, pp. 1627–1633, 1991.

[154] J. Dacles-Mariani, G. G. Zilliac, J. S. Chow, and P. Bradshaw, "Numerical/experimental study of a wingtip vortex in the near field," *AIAA Journal*, vol. 33, no. 9, pp. 1561–1568, 1995.

[155] P. Spalart, W.-H. Jou, M. K. Strelets, and S. Allmaras, "Comments on the Feasibility of LES for Wings, and on a Hybrid RANS / LES Approach," in *Proceedings of the first AFOSR international conference on DNS/LES*, no. July 2017, (Ruston, LA, USA), Greyden Press, 1997.

[156] M. J. Churchfield and G. A. Blaisdell, "Numerical Simulations of a Wingtip Vortex in the Near Field," *Journal of Aircraft*, vol. 46, no. 1, pp. 230–243, 2009.

[157] F. Holzäpfel, T. Hofbauer, D. Darracq, H. Moet, F. Garnier, and C. Gago, "Analysis of wake vortex decay mechanisms in the atmosphere," *Aerospace Science and Technology*, vol. 7, pp. 263–275, 2003.

[158] R. H. Kraichnan, "Inertial ranges in two-dimensional turbulence," *Physics of Fluids*, vol. 10, no. 7, pp. 1417–1423, 1967.

[159] P. G. Tucker, "Computation of unsteady turbomachinery flows: Part 2-LES and hybrids," *Progress in Aerospace Sciences*, vol. 47, no. 7, pp. 546–569, 2011.

[160] Z. Yang, "Large eddy simulation of fully developed turbulent flow in a rotating pipe," *International Journal for Numerical Methods in Fluids*, vol. 33, pp. 681–694, 2000.

[161] A. Javadi and H. Nilsson, "LES and DES of strongly swirling turbulent flow through a suddenly expanding circular pipe," *Computers and Fluids*, vol. 107, pp. 301–313, 2015.

[162] F. Holzäpfel, "Adjustment of subgrid-scale parameterizations to strong streamline curvature," *AIAA Journal*, vol. 42, no. 7, pp. 1369–1377, 2004.

[163] J. S. Marshall and M. L. Beninati, "External turbulence interaction with a columnar vortex," *Journal of Fluid Mechanics*, vol. 540, pp. 221–245, 2005.

[164] F. Risso, A. Corjon, and A. Stoessel, "Direct numerical simulations of wake vortices in intense homogeneous turbulence," *AIAA Journal*, vol. 35, no. 6, pp. 1030–1040, 1997.

[165] V. Blandeau and P. F. Joseph, "Broadband Noise Due to Rotor-Wake/Rotor Interaction in Contra-Rotating Open Rotors," *AIAA Journal*, vol. 48, no. 11, pp. 2674–2686, 2010.

[166] D. J. Moreau, C. J. Doolan, W. N. Alexander, T. W. Meyers, and W. J. Devenport, "Wall-Mounted Finite Airfoil-Noise Production and Prediction," *AIAA Journal*, vol. 54, no. 5, pp. 1637–1651, 2016.

[167] T. F. Brooks and A. Marcolini, "Airfoil Tip Vortex Formation Noise," *AIAA Journal*, vol. 24, no. 2, pp. 246–252, 1986.

[168] E. Envia, D. L. Tweedt, R. P. Woodward, D. M. Elliott, E. B. Fite, C. E. Hughes, G. G. Podboy, and D. L. Sutliff, "An assessment of current fan noise prediction capability," in *14th AIAA/CEAS Aeroacoustics Conference*, AIAA 2008-2991, (Vancouver, Canada), 2008.

[169] S. Moreau, "Turbomachinery Noise Predictions: Present and Future," *Acoustics*, vol. 1, no. 1, pp. 92–116, 2019.

[170] B. Mühlbauer, B. Noll, R. Ewert, O. Kornow, and M. Aigner, *Combustion Noise*. Berlin: Springer, 2009.

[171] A. Wohlbrandt, C. Kissner, and S. Guérin, "Impact of cyclostationarity on fan broadband noise prediction," *Journal of Sound and Vibration*, vol. 420, pp. 142–164, 2018.

[172] R. Ewert, J. Dierke, J. Siebert, A. Neifeld, C. Appel, M. Siefert, and O. Kornow, "CAA broadband noise prediction for aeroacoustic design," *Journal of Sound and Vibration*, vol. 330, no. 17, pp. 4139–4160, 2011.

[173] M. Siefert and R. Ewert, "Sweeping sound generation in jets realized with a random particle-mesh method," in *15th AIAA/CEAS Aeroacoustics Conference*, AIAA 2009-3369, (Miami, FL, USA), 2009.

[174] N. J. Georgiadis, D. P. Rizzetta, and C. Fureby, "Large-Eddy Simulation: Current Capabilities, Recommended Practices, and Future Research," *AIAA Journal*, vol. 48, no. 8, pp. 1772–1784, 2010.

[175] S. Lele and J. W. Nichols, "A second golden age for aeroacustics?," *Philosophical Transactions of the Royal Society A: Mathematical, Physical and Engineering Sciences*, vol. 372, no. 2022, 2014.

[176] P. Kholodov, "Identification of Noise Sources in a Realistic Turbofan Rotor Using Large Eddy Simulation," *Acoustics*, vol. 2, pp. 691–706, 2020.

[177] J. Smagorinsky, "General circulation experiments with the primitive equations: I. The basic experiment," *Monthly weather review*, vol. 91, no. 3, pp. 99–164, 1963.

[178] D. Wilcox, *Turbulence Modelling for CFD*. La Canada, CA: DCW Industries, 1998.

[179] U. Piomelli, "Wall-layer models for large-eddy simulations," *Progress in Aerospace Sciences*, vol. 44, no. 6, pp. 437–446, 2008.

[180] N. Okong'o, D. D. Knight, and G. Zhou, "Large Eddy Simulations Using an Unstructured Grid Compressible Navier-Stokes Algorithm," *International Journal of Computational Fluid Dynamics*, vol. 13, no. 4, pp. 303–326, 2000.

[181] H. S. Kang, S. Chester, and C. Meneveau, "Decaying turbulence in an active-grid-generated flow and comparisons with large-eddy simulation," *Journal of Fluid Mechanics*, vol. 480, no. 480, pp. 129–160, 2003.

[182] U. Piomelli, "Large eddy simulations in 2030 and beyond," *Philosophical Transactions of the Royal Society A: Mathematical, Physical and Engineering Sciences*, vol. 372, no. 2022, 2014.

[183] A. Favre, "Equations de gaz turbulents compressibles," *J. de Mecanique*, vol. 4(3), 1965.

[184] U. Piomelli, "Large-eddy simulation : achievements and challenges," *Progress in Aerospace Sciences*, vol. 35, pp. 335–362, 1999.

[185] J. LARSSON, S. KAWAI, J. BODART, and I. BERMEJO-MORENO, "Large eddy simulation with modeled wall-stress: recent progress and future directions," *Mechanical Engineering Reviews*, vol. 3, no. 1, pp. 15–00418–15–00418, 2016.

[186] E. Balaras and C. Benocci, "Subgrid-scale models in finite-difference simulations of complex wall bounded flows," *AGARD CP*, vol. 551, pp. 1–5, 1994.

[187] F. Nicoud, J. S. Baggett, P. Moin, and W. Cabot, "Large eddy simulation wall-modeling based on suboptimal control theory and linear stochastic estimation," *Physics of Fluids*, vol. 13, no. 10, pp. 2968–2984, 2001.

[188] U. Schumann, "Subgrid-scale model for finite difference simulation of turbulent flows in plane channels and annuli," *Journal of Computational Physics*, vol. 18, pp. 376–404, 1975.

[189] M. K. Strelets, "Detached Eddy Simulation of Massively Seperated Flows," in *39th Aerospace sciences meeting and exhibit*, (Reno, NV, USA), p. 879, 2001.

[190] A. Leonard, "Energy Cascade in Large-eddy simulations of turbulent fluid flows," *Advances in Geophysics*, vol. 18, pp. 237–248, 1975.

[191] P. R. Spalart, A. K. Travin, M. L. Shur, and M. K. Strelets, "Initial Noise Predictions for Open Rotors Using First Principles," in *16th AIAA/CEAS Aeroacoustics Conference*, (Stockholm, Schweden), AIAA 2010-3793, 2010.

[192] P. R. Spalart, S. Deck, M. L. Shur, K. Squires, M. K. Strelets, and A. K. Travin, "A New Version of Detached-eddy Simulation, Resistant to Ambiguous Grid Densities," *Theoretical and Computational Fluid Dynamics*, vol. 20, no. 3, pp. 181–195, 2006.

[193] M. L. Shur, P. Spalart, M. K. Strelets, and A. K. Travin, "A hybrid RANS-LES model with delayed DES and wall-modeled LES capabilities," *International Journal of Heat and Fluid Flow*, vol. 29, pp. 1638–1649, 2008.

[194] M. L. Shur, P. R. Spalart, M. Strelets, and A. Travin, "Detached-Eddy Simulation of an airfoil at High Angle of Attack," *Engineering Modelling and Experiments*, vol. 4, pp. 669–678, 1999.

[195] P. Spalart, L. Hedges, M. Shur, and A. Travin, "Simulation of Active Flow Control on a Stalled Airfoil," *Flow, Turbulence and Combustion*, vol. 71, no. 1-4, pp. 361–373, 2003.

[196] F. Farassat, "Derivation of Formulations 1 and 1A of Farassat," tech. rep., 2007.

[197] M. C. M. Wright and C. L. Morfey, "On the Extrapolation of Acoustic Waves from Flow Simulations with Vortical out Flow," *International Journal of Aeroacoustics*, vol. 14, no. 1-2, pp. 217–227, 2015.

[198] E. DeVilliers, *The Potential of Large Eddy Simulation for the Modeling of Wall Bounded Flows*. PhD thesis, Imperial College of Science, Technology and Medicine, 2006.

[199] H. Jasak, A. Jemcov, and T. Zeljko, "OpenFOAM : A C ++ Library for Complex Physics Simulations," *International workshop on coupled methods in numerical dynamics*, vol. 1000, pp. 1–20, 2007.

[200] D. A. Lysenko, I. S. Ertesvåg, and K. E. Rian, "Modeling of turbulent separated flows using OpenFOAM," *Computers & Fluids*, vol. 80, pp. 408–422, 2013.

[201] R. I. Issa, "Solution of the implicitly discretised fluid flow equations by operator-splitting," *Journal of Computational Physics*, vol. 62, no. 1, pp. 40–65, 1986.

[202] S. V. Patankar and D. B. Spalding, "A calculation procedure for heat, mass and momentum transfer in three-dimensional parabolic flows," *International Journal of Heat and Mass Transfer*, vol. 15, no. 10, pp. 1787–1806, 1972.

[203] W. K. George, P. D. Beuther, and J. L. Lumley, "Processing of random signals," in *Proceedings of the Dynamic Flow Conference 1979 on Dynamic Measurements in Unsteady Flows*, (Dordrecht), pp. 757–800, Springer, 1978.

[204] C. Hirsch, *Numerical computation of internal and external flows: The fundamentals of computational fluid dynamics*. Elsevier, 2007.

[205] P. Beaudan and P. Moin, "Numerical experiments on the flow past a circular cylinder at sub-critical Reynolds number," Tech. Rep. TF-62, Stanford Univ. CA Termosciences Div., 1994.

[206] S. A. Karabasov and V. M. Goloviznin, "Compact Accurately Boundary-Adjusting high-REsolution Technique for fluid dynamics," *Journal of Computational Physics*, vol. 228, no. 19, pp. 7426–7451, 2009.

[207] G. A. Faranosov, V. M. Goloviznin, S. A. Karabasov, V. G. Kondakov, V. F. Kopiev, and M. A. Zaitsev, "CABARET method on unstructured hexahedral grids for jet noise computation," *Computers and Fluids*, vol. 88, pp. 165–179, 2013.

[208] R. Mittal and P. Moin, "Suitability of Upwind-Biased Finite Difference Schemes for Large-Eddy Simulation of Turbulent Flows," *AIAA Journal*, vol. 35, no. 8, pp. 1415–1417, 1995.

[209] O. Colin and M. Rudgyard, "Development of High-Order Taylor-Galerkin Schemes for LES," *Journal of Computational Physics*, vol. 162, no. 2, pp. 338–371, 2000.

[210] Y. Cao and T. Tamura, "Large-eddy simulations of flow past a square cylinder using structured and unstructured grids," *Computers and Fluids*, vol. 137, pp. 36–54, 2016.

[211] L. Mydlarski and Z. Warhaft, "On the onset of high-Reynolds-number grid-generated wind tunnel turbulence," *Journal of Fluid Mechanics*, vol. 320, pp. 331–368, 1996.

[212] M. Breuer, J. Bernsdorf, T. Zeiser, and F. Durst, "Accurate computations of the laminar flow past a square cylinder based on two different methods: lattice-Boltzmann and finite-volume," *International Journal of Heat and Fluid Flow*, vol. 21, pp. 186–196, 2000.

[213] C. Bogey and C. Bailly, "Large eddy simulations of round free jets using explicit filtering with/without dynamic Smagorinsky model," *International Journal of Heat and Fluid Flow*, vol. 27, no. 4, pp. 603–610, 2006.

[214] J. Schedvin, G. R. Stegen, and C. H. Gibson, "Universal similarity at high grid Reynolds numbers," *Journal of Fluid Mechanics*, vol. 65, no. 3, pp. 561–579, 1974.

[215] T. Kurian and J. H. Fransson, "Grid-generated turbulence revisited," *Fluid Dynamics Research*, vol. 41, no. 2, pp. 0–32, 2009.

[216] A. J. Simonsen and P. Å. Krogstad, "Turbulent stress invariant analysis: Clarification of existing terminology," *Physics of Fluids*, vol. 17, no. 8, pp. 1–4, 2005.

[217] A. Mukhopadhyay and T. Sundararajan, "Numerical investigation of confined wakes behind a square cylinder in a channel," *International Journal for Numerical Methods in Fluids*, vol. 14, no. 12, pp. 1473–1484, 1992.

[218] J. R. Chasnov, "The decay of axisymmetric homogeneous turbulence," *Physics of Fluids*, vol. 7, no. 600, pp. 600–605, 1995.

[219] G. Comte-Bellot and S. Corrsin, "Simple Eulerian time correlation of full-and narrow-band velocity signals in grid-generated, 'isotropic' turbulence," *Journal of Fluid Mechanics*, vol. 48, no. 2, p. 273, 1971.

[220] Z. Warhaft and J. L. Lumley, "An experimental Study of Temperature Fluctuations in Grid-Generated Turbulence," *Journal of Fluid Mechanics*, vol. 88, pp. 659–684, 1978.

[221] R. A. Antonia, R. Smalley, T. Zhou, F. Anselmet, and L. Danaila, "Similarity of Energy Structure Functions in Decaying Homogeneous Isotropic Turbulence," *Journal of Fluid Mechanics*, vol. 487, pp. 245–269, 2003.

[222] A. L. Kistler and T. Vrebalovich, "Grid turbulence at large Reynolds numbers," *Journal of Fluid Mechanics*, vol. 26, no. 1, pp. 37–47, 1966.

[223] W. K. George, "Asymptotic Effect of Initial and Upstream Conditions on Turbulence," *Journal of Fluids Engineering*, vol. 134, no. 6, p. 061203, 2012.

[224] G. K. Batchelor, *The theory of homogeneous turbulence*. Cambridge University Press, 1953.

[225] W. K. George, H. Wang, C. Wollblad, and T. Johannson, "Homogeneous Turbulence and its Relation to Realizable Flows," in *Proceedings of the 14th Australasian Fluid Mechanics Conference*, (Adelaide, S. Australia), pp. 47–48, 2001.

[226] S. C. Ling and C. A. Wan, "Decay of isotropic turbulence generated by a mechanically agitated grid," *Physics of Fluids*, vol. 15, no. 8, pp. 1363–1369, 1972.

[227] J. R. Chasnov, "Similarity states of passive scalar transport in isotropic turbulence," *Physics of Fluids*, vol. 6, no. 2, pp. 1036–1051, 1994.

[228] F. van der Bos and B. J. Geurts, "Commutator errors in the filtering approach to large-eddy simulation," *Physics of Fluids*, vol. 17, no. 3, 2005.

[229] T. J. Poinsot and S. K. Lele, "Boundary conditions for direct simulations of compressible viscous flows," *Journal of Computational Physics*, vol. 101, no. 1, pp. 104–129, 1992.

[230] S. Pröbsting, F. Scarano, and S. C. Morris, "Regimes of tonal noise on an airfoil at moderate Reynolds number," *Journal of Fluid Mechanics*, vol. 780, pp. 407–438, 2015.

[231] M. Lowson, A. McAlpine, and E. Nash, "The generation of boundary layer instability noise on aerofoils," in *36th AIAA Aerospace Sciences Meeting & Exhibit*, AIAA 98-0627, (Reno, NV, USA), 1998.

[232] H. Tucker, "The distortion of turbulence by irrotational strain," *Mechanical Engineering*, vol. 70, no. 7, 1970.

[233] P. F. Mish and W. J. Devenport, "An experimental investigation of unsteady surface pressure on an airfoil in turbulence—Part 2: Sources and prediction of mean loading effects," *Journal of Sound and Vibration*, vol. 296, no. 3, pp. 447–460, 2006.

[234] N. Gregory and C. O'Reilly, "Low-Speed Aerodynamic Characteristics of NACA 0012 Aerofoil Sections, including the Effects of Upper-Surface Roughness Simulation Hoar Frost," Tech. Rep. 3726, NPL Aerodynamics Division, jan 1973.

[235] R. Karve, D. Angland, and T. Nodé-Langlois, "An analytical model for predicting rotor broadband noise due to turbulent boundary layer ingestion," *Journal of Sound and Vibration*, vol. 436, pp. 62–80, 2018.

[236] R. Karve, *Modelling Counter Rotating Open Rotor Installation Noise Sources.* PhD thesis, University of Southampton, 2018.

[237] V. P. Blandeau and P. F. Joseph, "Validity of Amiet's Model for Propeller Trailing-Edge Noise," *AIAA Journal*, vol. 49, no. 5, pp. 1057–1066, 2011.

[238] P. F. Mish, *An Experimental Investigation of Unsteady Surface Pressure on an Airfoil in Turbulence.* PhD thesis, Virginia Polytechnic, 2003.

[239] L. Jiang, J. Cai, and C. Liu, "Large-eddy simulation of wing tip vortex in the near field," *International Journal of Computational Fluid Dynamics*, vol. 22, no. 5, pp. 289–330, 2008.

[240] K. Kucukcoskun, J. Christophe, C. Schram, and T. Michel, "Broadband scattering of the turbulence-interaction noise of a stationary airfoil : experimental validation of a semi-analytical model," *International Journal of Aeroacoustics*, vol. 12, no. 1-2, pp. 83–102, 2013.

[241] P. L. O'Neill, D. Nicolaides, D. Honnery, and J. Soria, "Autocorrelation Functions and the Determination of Integral Length with Reference to Experimental and Numerical Data," in *15th Australasian Fluid Mechanics Conference*, (Sydney, Australia), pp. 13–17, 2004.

[242] S. C. Bailey and S. Tavoularis, "Measurements of the velocity field of a wing-tip vortex, wandering in grid turbulence," *Journal of Fluid Mechanics*, vol. 601, pp. 281–315, 2008.

[243] A. Heyes, R. Jones, and D. Smith, "Wandering of wing-tip vortices," in *Proceedings of the 12th International Symposium on the Application of Laser Techniques to Fluid Mechanics*, (Lisbon, Portugal), 2004.

[244] S. C. Bailey, S. Pentelow, H. C. Ghimire, B. Estejab, M. A. Green, and S. Tavoularis, "Experimental investigation of the scaling of vortex wandering in turbulent surroundings," *Journal of Fluid Mechanics*, vol. 843, pp. 722–747, 2018.

[245] J. Boudet, A. Cahuzac, P. Kausche, and M. C. Jacob, "Zonal large-eddy simulation of a fan tip-clearance flow, with evidence of vortex wandering," *Journal of Turbomachinery*, vol. 137, no. 6, 2015.

[246] J. S. Chow, G. G. Zilliac, and P. Bradshaw, "Mean and turbulence measurements in the near field of a wingtip vortex," *AIAA Journal*, vol. 35, no. 10, pp. 1561–1567, 1997.

[247] R. Karve, J. R. Gill, F. Gea Aguilera, D. Angland, and T. Node-Langlois, "Including Wall Effects in Analytical Leading Edge Noise Predictions," in *23rd AIAA/-CEAS Aeroacoustics Conference*, AIAA 2017-3198, (Denver, CO, USA), 2017.

[248] J. D. Anderson and J. Wendt, *Computational fluid dynamics*. New York: McGraw-Hill, 3rd ed., 1995.

[249] F. Q. Hu, M. Y. Hussaini, and J. L. Manthey, "Low-dissipation and low-dispersion Runge-Kutta schemes for computational acoustics," *Journal of Computational Physics*, vol. 124, no. 1, pp. 177–191, 1996.

[250] C. Bogey and C. Bailly, "A family of low dispersive and low dissipative explicit schemes for flow and noise computations," *Journal of Computational Physics*, vol. 194, no. 1, pp. 194–214, 2004.

[251] A. Najafi-Yazdi and L. Mongeau, "A low-dispersion and low-dissipation implicit runge-kutta scheme," *Journal of Computational Physics*, vol. 233, no. 1, pp. 315–323, 2013.

[252] J. Hardin, J. Ristorcelli, and C. K. W. Tam, "ICASE / LaRC Workshop on Benchmark Problems in Computational Aeroacoustics (CAA)," Tech. Rep. 3000, NASA, Hampton, Virginia, USA, 1995.

[253] M. Drela, "XFOIL: An analysis and design system for low Reynolds number airfoils," *Low Reynolds number aerodynamics*, pp. 1–12, 1989.